STARS

2019

Vibration Reduction of Mistuned Bladed Disks via Piezoelectric-Based Resonance Frequency Detuning

Garrett Lopp
University of Central Florida

Showcase of Text, Archives, Research & Scholarship

Vibration Reduction of Mistuned Bladed Disks via Piezoelectric-Based Resonance Frequency Detuning

by

Garrett K. Lopp
B.S. University of Central Florida, 2013
M.S. University of Central Florida, 2015

A dissertation submitted in partial fulfillment of the requirements
for the degree of Doctor of Philosophy
in the Department of Mechanical and Aerospace Engineering
in the College of Engineering and Computer Science
at the University of Central Florida
Orlando, Florida

Spring Term
2019

Major Professor: Jeffrey L. Kauffman

ABSTRACT

Recent trends in turbomachinery blade technology have led to increased use of monolithically constructed bladed disks (blisks). Although offering a wealth of performance benefits, this construction removes the blade-attachment interface present in the conventional design, thus unintentionally removing a source of friction-based damping needed to counteract large vibrations during resonance passages. This issue is further exacerbated in the presence of blade mistuning that arises from small imperfections from otherwise identical blades and are unavoidable as they originate from manufacturing tolerances and operational wear over the lifespan of the engine. Mistuning is known to induce vibration localization with large vibration amplitudes that render blades susceptible to failure induced by high-cycle fatigue. The resonance frequency detuning (RFD) method reduces vibration associated with resonance crossings by selectively altering the blades structural response. This method utilizes the variable stiffness properties of piezoelectric materials to switch between available stiffness states at some optimal time as the excitation frequency sweeps through a resonance. For a single-degree-of-freedom (SDOF) system, RFD performance is well defined. This research provides the framework to extend RFD to more realistic applications when the SDOF assumption breaks down, such as in cases of blade mistuning. Mistuning is inherently random; thus, a Monte Carlo analysis performed on a computationally cheap lumped-parameter model provides insight into RFD performance for various test parameters. Application

of a genetic algorithm reduces the computational expense required to identify the optimal set of stiffness-state switches. This research also develops a low-order blisk model with blade-mounted piezoelectric patches as a tractable first step to apply RFD to more realistic systems. Application of a multi-objective optimization algorithm produces Pareto fronts that aid in the selection of the optimized patch parameters. Experimental tests utilizing the academic blisk with the optimized patches provides validation.

ACKNOWLEDGMENTS

I would like to extend my deepest gratitude to Dr. Jeff Kauffman for playing a pivotal role as my academic advisor during my time as a graduate student at the University of Central Florida. Dr. Kauffman took me on as a graduate student during a transitional period in my early career following the completion of my undergraduate degree, where I still had questions and uncertainties surrounding my future career path, and led me to a more research-orientated path with challenging and fulfilling projects, both presented in this dissertation and extending beyond. I am extremely grateful for his guidance and insight during our weekly research meetings, the opportunities he provided for me to attend conferences domestic and abroad, and the welcoming and enjoyable research environment that he provided within the lab, all of which have stimulated my development as both a researcher and a more, well-rounded individual. I could not have envisioned a more fulfilling experience when beginning graduate school, and I look forward to our future interactions.

Next, I would like to thank my committee members Dr. Raghavan, Dr. Viana, and Dr. Catbas. Although we did not meet often, I am very grateful for their role in reviewing my dissertation and for providing their unique perspectives and areas of expertise.

I would also like to extend my gratitude to the members of the Structural and Thermal Systems Branch at NASA Langley Research Center and the members of the Experimental Structural Dynamics Department at Sandia National Labs. Both of these groups provided me with summer internships complete with engaging projects extending beyond my dissertation research. The location of these internships also provided me the opportunity to explore vastly different regions of the country and build memories that I will cherish throughout my life.

Thank you to my fellow members of the Structural Dynamics and Adaptive Structures Lab, specifically Daniel Geiyer, Chris Kelley, Brandi McPherson, Andres Rodriguez, James Little, and Christian Vazquez. I thoroughly enjoyed my time spent with them over the last few years, whether it be through our interactions in the lab, attending conferences, playing intramural sports, or any number of various activities.

Thank you to my parents. They always enabled me the freedom to pursue my own path through life and offered their support every step of the way. Thank you to all of my other family and friends. Often times, the many aspects of graduate school have taken priority and I would like to thank them for their patience and support.

Finally, thank you to Tiffany who has been by my side the last three years. She has been a constant source of motivation and support through all of the long hours spent working and I look forward to all of our future experiences together.

TABLE OF CONTENTS

LIST OF FIGURES

LIST OF TABLES

CHAPTER 1
INTRODUCTION

This chapter serves as an introduction for the primary focus of this research effort. Section 1.1 begins the chapter with an introduction to the loads experienced by turbomachinery blades and the external dynamic forcing mechanism. Section 1.2 introduces the bladed disk (blisk), also referred to as an integrally bladed rotor (IBR), with an accompanying discussion highlighting the advantages and drawbacks of the blisk compared to conventional turbomachinery technology. Section 1.3 describes the problem of high-cycle fatigue (HCF), the leading cause of jet engine component failure. Section 1.4 defines the phenomena of blade mistuning, or random deviations in the nominal blade properties, that can cause vibration-energy confinement that can lead to the failure of a small number of "rogue" blades. Section 1.5 presents the resonance frequency detuning (RFD) concept, the strategy adopted in this research proposal to reduce blade vibrations. Section 1.6 concludes the chapter with a discussion of the key aspects investigated in this research effort.

1.1   Turbomachinery Blade Vibration

Turbomachinery blisks operate in extremely harsh and highly stressed environments that subject the blades to both large static and dynamic loads. Under typical operating conditions, the large

static loads arise through thermal gradients and centrifugal forces. Dynamic loads arise from rotations of the rotor blades through pressure disturbances in the flow field introduced by the wakes generated from upstream stator vanes. Rotation through these essentially static pressure disturbances generates a periodic forcing on the rotor blades, referred to as engine-order excitation. From this point forward, the naming convention when discussing engine-order excitations is nEO, where n is the total number pressure disturbance encountered during a single revolution of the rotor, and corresponds to the number stator vanes in the upstream row. The excitation frequency experienced by the rotor blades is thus $f = n \times (\text{RPM}/60)$ Hz.

Typically, designers use a so-called Campbell diagram to ensure the intended blade design does not experience resonance near normal operating conditions. Figure 1.1 shows an example Campbell diagram for a single blade that shows the blade's natural frequencies (solid curves) as a function of the engine rotation speed. The '1T', '1B', and '2S' labels, for example, denote the blade natural frequencies associated with the 1st torsion, 1st bending, and 2-stripe modes, respectively. Typically, increasing engine RPM induces centrifugal forces that stiffen the blade's natural frequencies; however, in some cases, for example, the torsion modes of twisted blades, these forces tend to untwist the initial blade curvature resulting in a softening effect. Also shown are the linearly varying excitation frequencies, or "speed lines," corresponding to various engine orders (gray dashed lines). Resonance occurs at rotation speeds where these speed lines and blade natural frequencies intersect, for example, at the intersection of the 10EO speed line with the 2S mode near 4000 RPM. For typical operating conditions, blade designs avoid these resonant conditions; how-

ever, resonance is unavoidable during spool-up or spool-down of the engine, thus resulting in large

dynamic stresses associated with the increased vibration levels.
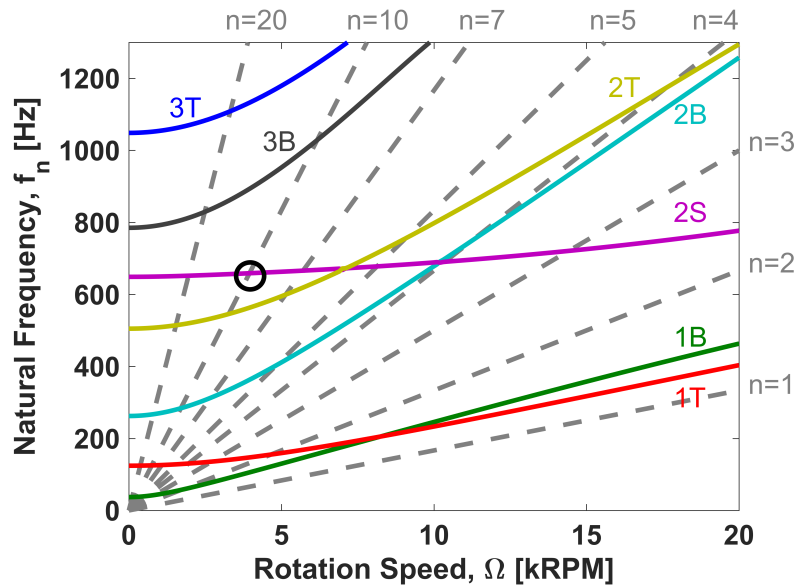
Figure 1.1: Example of a Campbell diagram showing rotation-dependent blade natural frequencies (solid lines) and speed lines corresponding to various engine order excitations (gray dashed lines) (from [3])

1.2 Monolithic Blisks

Over the last couple of decades, advances in turbomachinery technology have led to increased

use of bladed disks, or blisks [4]. Conventional designs incorporate the individual blades into the

disk through dovetail attachments, whereas blisks are monolithically constructed from a single

piece of material. Figure 1.2a shows the monolithic construction of a blisk and Fig. 1.2 shows the

conventional design. The monolithic construction offers performance benefits over their conven-

3

tional counterparts that include increased aerodynamic efficiency, and decreased parts count and complexity, thus resulting in a higher-performance, more light-weight design.

(a) Compressor blisk manufacture by GE.
(from [5])
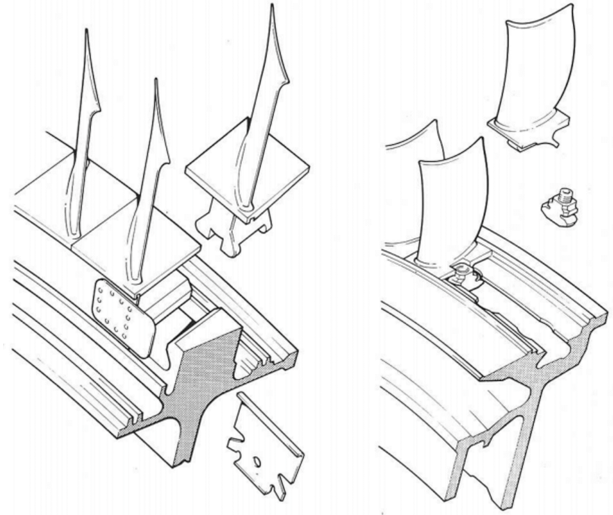
(b) Individual blades attached to the disk.
(from [6])

Figure 1.2: Turbomachinery blade construction examples.

Although offering many benefits, blisks aren't without their disadvantages. For example, replacing a damaged blade, although a straightforward procedure for the conventional design by inserting replacement blades, can be a labor-intensive process for the blisk. For minor damages (e.g., scratches, dents, etc.) incurred through foreign-object damage, repairing the damage requires the "blending" repair process to smooth the sharp edges that can lead to stress concentrations [7]. More serious damages may require welding a replacement blade to the blisk or replacing the blisk entirely [4]. Furthermore, the dovetail attachment found in conventional designs provides a natural source of friction-based damping induced by the relative motion between the blades and the disk. Blisks lack this attachment interface, thus removing this natural damping mechanism that

significantly lowers the inherent damping. As such, these designs no longer have the necessary damping to counteract the large vibratory motions generated from repeated resonance crossings and are highly susceptible to blade failure induced by high-cycle fatigue (HCF).

1.3 High-Cycle Fatigue

Repeated vibratory stresses under the yield stress of a material and over a large number of cycles can lead to failure induced by HCF. This failure mode is one of the leading causes of engine component failure and accounts for nearly 25% of failures, where blades are the leading component suffering from HCF [8]. Figure 1.3a shows that HCF is especially troublesome as the initial crack remains below the inspection limit for nearly the entire fatigue life of the blade and, consequently, there is rapid crack propagation and growth near the end of the blade's life. As operating conditions can cause blades to vibrate in the kHz range, a large number of vibratory cycles with stresses over the fatigue limit incur within a short period of time, thus causing rapid crack growth that can lead to failure within minutes.

Figure 1.3b shows a Modified Goodman Diagram that designers use to avoid issues pertaining to HCF. The abscissa corresponds to the dynamic vibratory stresses whereas the ordinate corresponds to the mean or steady stresses typically attributed to centrifugal loading. Creating such diagrams involve testing coupons over a large number of cycles, typically $> 10^7$, at various non-zero static stress states. These diagrams can also be created using experimental data obtained from vibration shaker tests of specific blade designs. Including a margin of safety on the maximum

allowable vibratory stress results in the safe life region where HCF will not be problematic over the blade's life span. Utilizing such an approach, however, can lead to over-conservative blade designs that are heavier and reduce overall performance. Furthermore, some damage types, such as foreign-object damage and fretting fatigue, significantly reduce the blade's fatigue strength. Lastly, as covered in more detail in the proceeding section, blade mistuning can result in vibration localized to a small region of blades, thus significantly increasing the vibratory stresses compared to the intended design.

(a) Differences between low- and high-cycle fatigue.

(b) Modified Goodman Diagram of a typical turbomachinery blade.
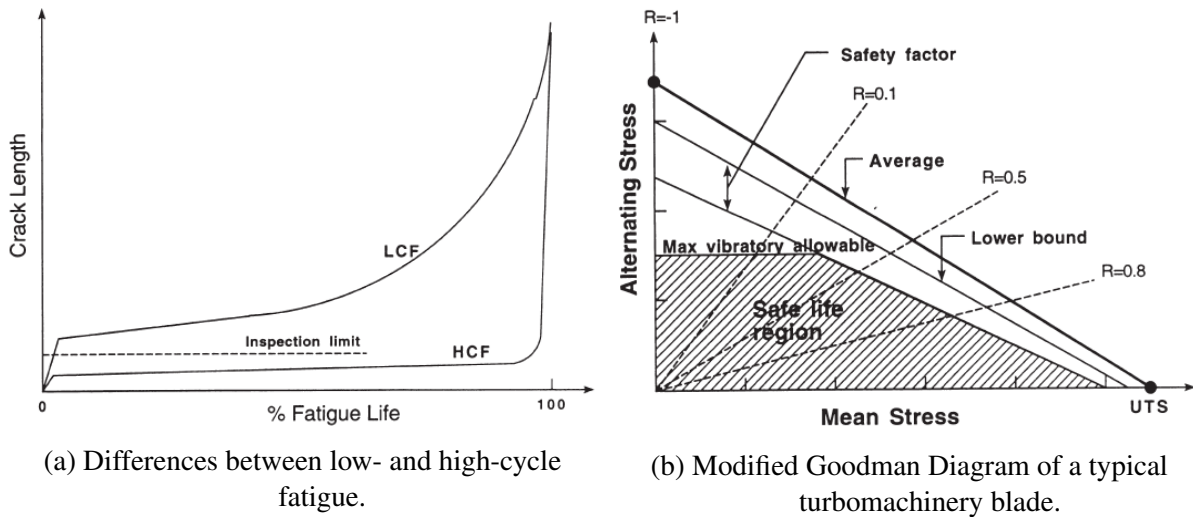
Figure 1.3: Characteristics of high-cycle fatigue. (from [1])

1.4 Mistuning Defined

Ideally, blisks are systems with identical blades distributed circumferentially around the disk. In such an ideal state, the blisk is referred to as tuned. Each blade is coupled to the neighboring blades mechanically (e.g., through the disk or the shroud casing and snubbers, if present) or aerodynami-

6

cally through the flow field, thus producing a cyclically symmetric structure. Cyclically symmetric structures composed of N_s identical substructures have mode shapes composed of a single spatial harmonic wrapped around the structure's circumference [9]. These mode shapes are readily identified by the number of nodal diameters running across the blisk. The number of nodal diameters (ND) occurs between $ND = 0$ to a maximum $ND_{max} = N/2$ for an even number of substructures, and $ND_{max} = (N-1)/2$ for an odd number of substructures. Similar to the naming convention used for the engine order, the convention used to identify the nodal diameter henceforth is hND. Most modes, the 0ND and (N/2)ND modes excluded, occur in degenerate orthogonal pairs, with each pair corresponding to mode shapes rotated by an angle $\pi/2h$ relative to each other. As each tuned mode shape corresponds to a single nodal diameter value, nEO excitation will only excite the hND mode when $h = n$ due to the orthogonality of all other mode shapes to the forcing configuration. Furthermore, each of the substructures will respond at the same magnitude when forced by nEO excitation.

Physical construction of a blisk, however, will have small blade-to-blade variations, referred to as mistuning, that arise from slight imperfections induced by the manufacturing process or uneven wear and foreign-object damage over the lifespan of the engine. Such unavoidable variations destroy the cyclic symmetry of the system and can split the natural frequencies of the degenerate pair, as well as induce response amplitudes that are much larger than that of their tuned counterpart [10]. Furthermore, the mistuned mode shapes no longer contain a single spatial harmonic, but are instead composed of a distrubution of all of the spatial harmonics. As an example, Figure 1.4a shows the 3ND tuned mode shape, while Fig. 1.4b shows a mistuned mode with localized vibration. Because

each mode shape contains a distribution of spatial-harmonic content, nEO excitation can excite all

modes with a magnitude dependent on the harmonic content present within the mode shape (i.e.,

nEO excitation strongly excites a mode containing a large contribution of the nND shape).
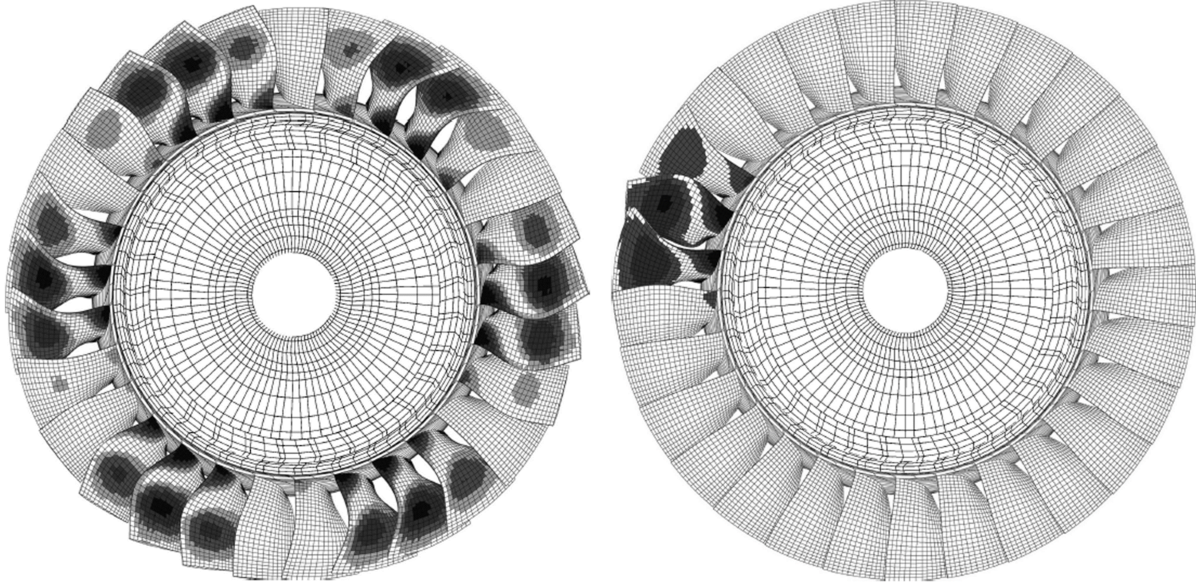
(a) 3ND mode shape of a tuned blisk.   (b) Localized mode shape of a mistuned blisk.

Figure 1.4: Example mode shapes of a blisk. (from [2])

Although the maximum blade response is system dependent, in as early as 1966, Whitehead

derived a theoretical maximum of the amplification factor (AF), the ratio of the maximum re-

sponse of all blades of the mistuned blisk to the maximum blade response of the tuned blisk.

This maximum factor is $AF_{\max} = \frac{1}{2}(1 + \sqrt{N_b})$ and depends on the total number of blades N_b [11].

This limiting amplification factor is only attainable under very specific circumstances that are not

likely achievable in operation; however, it shows the potential danger that arises from mistuning

in that some blades may experience much larger vibratory stresses than initially expected from a

8

tuned-system analysis. Thus, these larger vibratory stresses, if unaccounted for, can lead to HCF occurring prematurely, thus significantly reducing blade life.
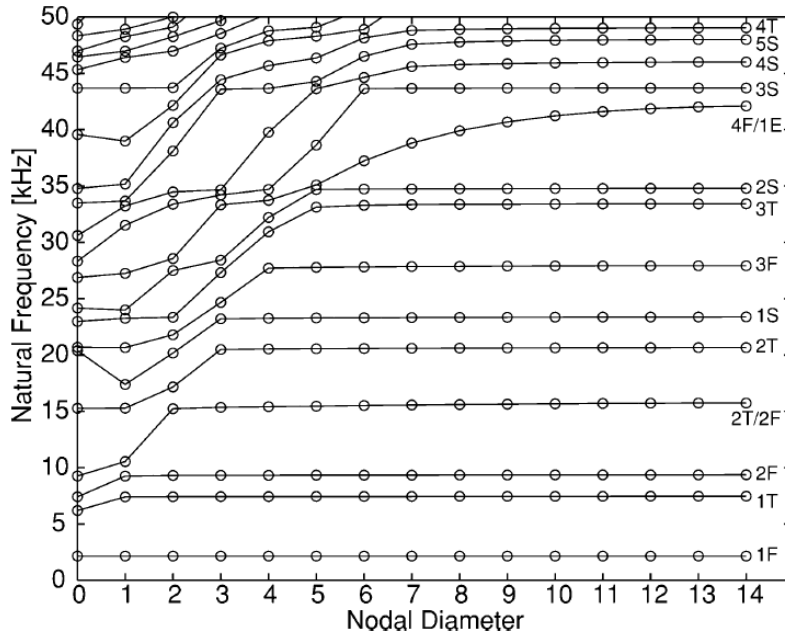
Figure 1.5: Tuned blisk natural frequencies as a function of the number of nodal diameters (spatial harmonic number) of the corresponding mode shape. (from [2])

For an un-shrouded blisk, the blade-to-blade coupling predominantly arises as mechanical coupling through the disk. For blade-dominated modes, most of the motion and corresponding strain energy for a particular mode is confined within the blades and there is minimal coupling between neighboring blades. For disk-dominated modes, most of the strain energy is confined within the disk. Figure 1.5 shows a commonly used plot of the natural frequency versus the nodal diameter that is used to identify these blade-dominated and disk-dominated regions for a tuned system. Each line corresponds to a family of blade modes where, for example, the $1F$ line corresponds to the 1st-flexural mode family, the $1T$ corresponds to the 1st-torsional mode family, etc. For the blade-dominated modes, there is little sensitivity in the natural frequencies as the nodal diame-

9

ter increases, thus resulting in relatively flat curves. Conversely, for the disk-dominated modes, the natural frequencies rapidly increase as nodal diameter increases, thus resulting in the sloped curves. In regions where there is a veering between the curves of two mode families, there is a considerable interaction between the disk and the blades. As a result, these regions are the most susceptible to localized vibration corresponding with the largest response magnitudes [2].

1.5   Resonance Frequency Detuning

Over the last few decades, researchers have continuously investigated methods to counteract these large vibratory stresses induced within turbomachinery blades. Such methods include friction-based dampers, tuned vibration absorbers, impact dampers, viscoelastic-layer dampers, and eddy-current dampers, to name a few; Ch. 2 provides a more thorough background of these methods. Piezoelectric-based vibration reduction has also garnered widespread interest over the last few decades due to their inherent adaptability to ever-changing environments. This research effort specifically focuses on developing further the RFD concept, a piezoelectric-based vibration reduction approach designed specifically for turbomachinery environments.

Originally developed by Kauffman and Lesieutre, RFD reduces vibration associated with transient passages through resonance [3]. The working concept behind RFD is to avoid resonance crossings by perturbing the blade stiffness at some optimal time. For example, Fig. 1.6 shows a zoomed window around the resonance crossing of the previously discussed Campbell diagram in Fig. 1.1. As the engine spools up, the excitation frequency increases, and the blade operates in a

high-stiffness state ($2S_1$). At some optimal engine speed or, by proxy, excitation frequency, the blade switches to a lower stiffness state ($2S_0$). Switching in this manner results in the excitation frequency having already surpassed the softened blade natural frequency, thus avoiding resonance and reducing vibration.
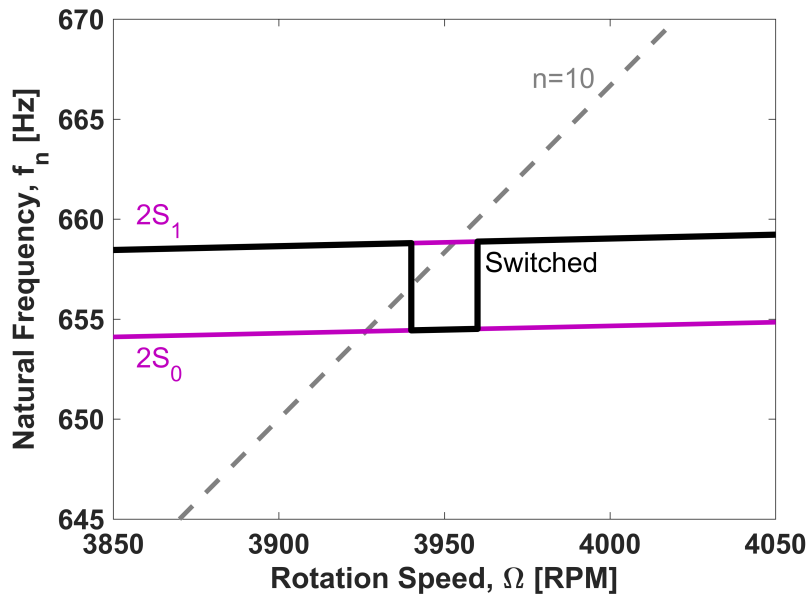
Figure 1.6: RFD concept shown on a zoomed view around the resonance crossing (black circle in Fig. 1.1) near 3950 RPM. (from [3])

To initiate the stiffness modulation, RFD employs piezoelectric materials due to their rapid response times. Researchers have also employed shape memory alloys to initiate this variable-stiffness effect that, although offering larger potential differences between available stiffness states, appear limited by their slow response times when considering transient excitations [12, 13]. By exploiting this variable-stiffness effect, RFD provides robust performance to any unexpected parameter variations and has the ability to target vibration for a number of resonance crossings, provided the piezoelectric elements remain located in a region of high modal strain. Kauffman

and Lesieutre's initial analysis focused on a single, well-separated mode of an academic blade, and showed that the excitation sweep rate, the inherent blade damping, the electromechanical coupling, and the timing of the stiffness modulation, were the primary parameters governing vibration reduction performance [3]. Experimental tests conducted on an academic blade, idealized as a trapezoidal plate, validated the RFD concept. In a subsequent study, Lopp and Kauffman showed that the electromechanical coupling was the primary parameter governing the timing of the optimal stiffness modulation. [14]

1.6 Dissertation Objectives

The ultimate goal of this research effort is to provide a method to reduce, and ideally eliminate, the harmful effects associated with HCF. Successful development and implementation of this method will extend blade life, reduce maintenance costs, increase passenger safety, as well as decrease conservatism, thus leading to higher-performance blade designs. To achieve this goal, RFD shows promise but, as it currently stands, requires further development to ultimately prove its viability. For example, previous studies focused the analysis of RFD towards a sufficiently well-separated vibration mode of a blade detached from the disk; however, for a built blisk, the coupling between neighboring blades, in conjunction with blade mistuning, causes this previously well-separated blade mode to now reside in a region of high modal density. As such, the SDOF assumption breaks down.

First and foremost, extending RFD towards blisk applications requires developing a representative model that can capture the relevant dynamics. In their simplest form, lumped-parameter models facilitate a computationally cheap method for employing the large-scale statistical investigations necessitated by the inherently random nature of mistuning. A natural progression then consists of the development of a more complex blisk model that includes the electrical influence of the piezoelectric materials. Development of such a model enables the application of a multi-objective optimization procedure to identify the piezoelectric patch parameters that maximize the electromechanical coupling, a key parameter that influences RFD performance.

The success of RFD also requires the identification of the optimal time to trigger the stiffness-state perturbation, referred to henceforth as simply the trigger. Previously, RFD only required identifying a single optimal trigger and utilized an exhaustive-search strategy to do so. For mis-tuned blisks, however, multiple modes influence the forced response such that RFD may require multiple triggers to maximize performance. Due to the increased number of parameters to opti-mize, an exhaustive-search strategy is not feasible to complete in a timely manner. As such, the identification of these optimal triggers requires application of a more computationally efficient optimization procedure.

Furthermore, experimental validation of the RFD concept only exists for a single blade de-tached from the disk. As such, experimental validation should also include testing of a built blisk. Complexity does arise in simulating the operating environment of a blisk, particularly in develop-ing a test rig capable of providing the necessary rotation speeds. Instead, this research tests a blisk in the stationary frame subjected to traveling-wave excitation. Although piezoelectric materials

provide the necessary stiffness modulations for RFD, these materials will also serve as the actuating mechanism to generate the traveling waves associated with specified engine-order excitations.

1.7   Dissertation Overview

This dissertation serves to guide the reader by providing the necessary details for the extension of RFD to reduce harmful vibrations of mistuned blisks. An outline of the subsequent chapters is as follows:

Chapter 2 provides a review of blade-damping technology conducive to familiarize the interested reader with the current state-of-the-art. It includes the background on piezoelectricity and its history and application in vibration control necessary for understanding the underlying concept of the proposed approach. It also provides a subsequent discussion that identifies potential limitations of piezoelectric elements as utilized in a turbomachinery application.

Chapter 3 presents the lumped-parameter blisk model with the blade-mounted piezoelectric elements utilized in this analysis. It focuses on the electromechanical coupling coefficient, an important parameter for RFD, and the qualitative behavior for both tuned and mistuned blisks. It then presents a semi-analytical solution for transient excitation adapted to include the stiffness-state switching.

Chapter 4 provides an analysis of the RFD concept with the corresponding application towards the lumped-parameter model. It provides a discussion regarding identification of the optimal sets of switch triggers; for mistuned blisks, this requires application of a genetic algorithm due to the

large computational expense of an exhaustive search. It also presents the results of Monte Carlo simulations to identify performance trends for several key parameters.

Chapter 5 is part one of a two-chapter analysis that focuses on the application of RFD towards a more physically representative blisk. It develops a low-order, numerical model of an academic blisk with blade-mounted piezoelectric elements. It also details the application of a multi-objective optimization algorithm used to optimize electromechanical coupling for several vibration modes of interest.

Chapter 6 is part two of the two-chapter analysis that focuses on the experimental testing of the academic blisk. It begins with a discussion of the test setup, as well as the methods utilized to experimentally characterize the blisk. It then presents a hybrid model that utilizes the the experimentally obtained modal data to identify the optimal sets of triggers. It then presents the results from both the numerical simulations and experimental tests.

Chapter 7 offers concluding remarks that highlights the key findings and significant contributions of this research effort specific not only to RFD, but also for the turbomachinery community as a whole. It also outlines some remaining questions as well as offers a discussion on potential paths forward.

CHAPTER 2
BACKGROUND REVIEW

This chapter discusses the background necessary for the reader to familiarize themselves with the concepts presented in this research. Section 2.1 outlines a number of damping strategies utilized to reduce vibration of turbomachinery blades. Section 2.2 introduces piezoelectric materials and discusses their role in vibration control applications. It also highlights some of the current limitations of the more classical piezoelectric-based vibration reduction strategies as applied to turbomachinery environments.

2.1   Overview of the Vibration Reduction of Bladed Disks

2.1.1   Friction Dampers

One of the most well-known methods for reducing blisk vibrations is through friction-based damping. These approaches dissipate the vibration energy as heat through relative motion between two contacting surfaces. For turbomachinery applications, these approaches typically introduce this friction-based damping mechanism using the relative motion between the blades and the disk, or between neighboring blades [15]. Conventional blade designs inherently contain a natural source

of friction-based damping through the contact interface between the blade and the disk introduced by the dovetail attachment. Under-platform dampers are also a popular method of increasing damping in conventional designs and rely on centrifugal loading of "cottage-roof" shaped dampers to induce a friction force between neighboring blades. Figure 2.1a shows an example of this under-platform damping concept.
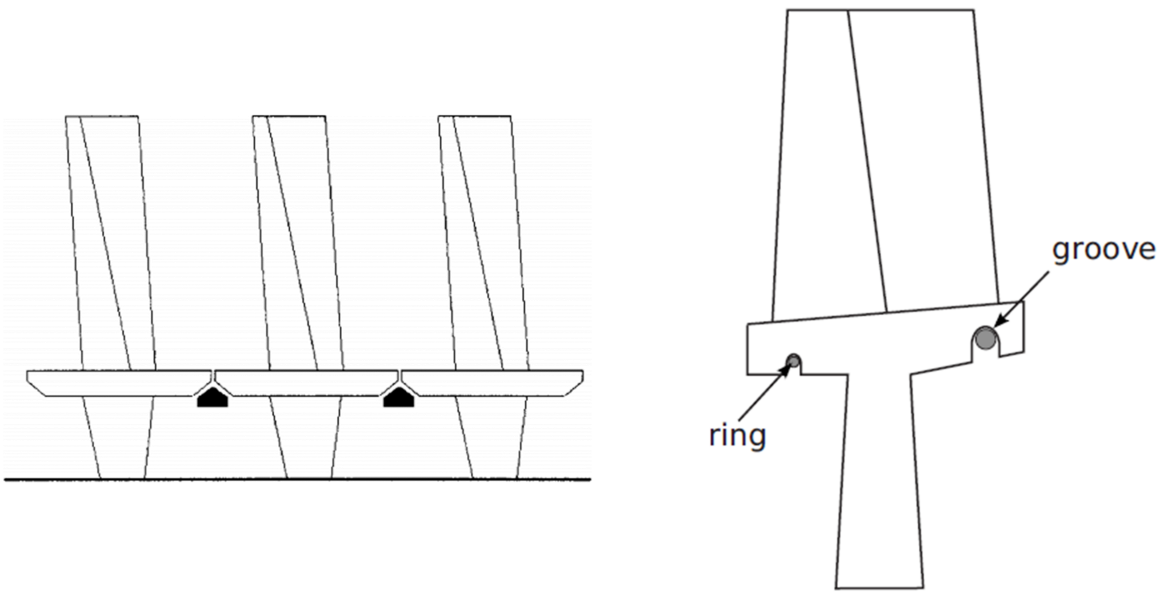
(a) Under-platform damper.
(from [16])

(b) Friction-ring damper.
(from [17]

Figure 2.1: Diagrams of friction-based damping designs.

The monolithic construction of blisks removes any joints and friction interfaces, thus leading researchers to pursue friction-ring dampers. Figure 2.1b shows an example of one of these friciton-ring dampers that sit within a groove on the underside of the disk. Laxalde et al. utilized both a lumped-parameter model, and a higher-fidelity finite element model to analyze friction-ring dampers [18, 17]. Both studies showed that friction-ring damping performance depends on the relative motion between the blades and the disk, thus requiring large bladed-disk coupling. Conse-

quently, these friction rings introduce minimal damping for modes with weak blade-disk coupling, a characteristic of the blade-dominated modes. Furthermore, these approaches largely depend on the centrifugal loading and consequently, the rotation speed of the engine; too small of a centrifugal load results in small friction forces and minimal damping, but too large of a centrifugal load results in the damper sticking with no relative motion. Furthermore, due to the nonlinear nature of such friction-based mechanisms, the theoretical analysis and optimization of these designs remains a difficult procedure.

2.1.2   Dynamic Vibration Absorbers and Impact Dampers

A dynamic vibration absorber (DVA) is a small oscillating mass attached to a vibrating host structure that is tuned to counteract the vibration amplitudes. Tuning the undamped DVA frequency to the forcing frequency localizes the vibration in the DVA that generates a spring force to completely cancel vibrations of the host structure at that frequency. As such, tuning the undamped DVA to match the host structure's natural frequency completely cancels resonant vibrations. The additional degree-of-freedom introduced by the DVA does, however, couple with the main system and produces two resonance peaks around the initial resonance, thus reducing performance for a non-stationary excitation. Introducing damping in the DVA offers a means to generate a damping force to reduce these resonant amplitudes from infinity in the undamped case, to some finite value. If the damping value approaches zero, the system operates in the undamped state with two resonant peaks at an infinite amplitude; conversely, if the damping value approaches infinity, there is zero

relative motion between the DVA and the host structure, thus generating only a single resonant peak, again with infinite amplitude. Between these limiting cases, there exists an optimal damping value that minimizes the maximum system response. Damped DVAs also increase performance bandwidth compared to undamped DVAs and is more robust to the frequency scattering associated with mistuning.

Typically, a single tuned DVA can only target a single mode of vibration, thus, reduced vibrations for a blisk is only achievable for a single resonance crossing. To enhance performance for multiple resonance crossings, Hollkamp et al. introduced a tunable DVA that consists of a pendulum contained in a hollow cavity within the blade [19]. Leveraging artificial gravity induced by rotation-based centrifugal forces resulted in a DVA with a rotation-dependent natural frequency. By appropriately sizing the pendulum, the DVA tracks a speed line associated with a chosen engine order, thus reducing vibration at multiple resonance crossings. Figure 2.2a shows a diagram of this order-tuned DVA concept. Hollkamp et al. also discussed several practical implementation concerns: The blade must contain a hollow cavity large enough to house the pendulum assembly without impacting the sides. Detuning of the pendulum can occur due to degrading parameters during operation, thus causing the DVA to no longer track the target speed line. Lastly, multiple engine orders can excite the blades over a given operating range, thus requiring multiple pendulum absorbers to fully attenuate vibration [19].

Building on this order-tuned DVA concept, Duffy et al. replaced the pendulum with a ball traversing a spherical trough that mitigates vibration through impacts with the sides of the cavity [20]. Figure 2.2b shows a diagram of this concept. Shaw and Pierre conducted a follow-up

study to provide further analytical insight to the complicated dynamics associated with the impacts [21]. Similar to the pendulum DVA, the impact damper utilizes centrifugal effects to obtain a linear dependence of the damper natural frequency with the rotor angular velocity. As such, controlling the ball's radial distance from the center of rotation, the ball's radius, and the radius of the spherical trough, the damper frequency directly tracks the engine-order excitation frequency. For small excitation levels, Shaw and Pierre showed the damper operates in the linear regime without impacting the cavity walls [21]. While operating in this regime, slightly under-tuning the damper results in resonance avoidance during a resonance crossing; however, Gozen et al. showed that for multiple modes in the blade model, this so-called "no-resonance zone" only exists for the first resonance crossing [22]. Furthermore, the absorber amplitude is inversely proportional to the ratio of the absorber mass to system mass, which is typically small. As such, there is only a small range of forcing amplitudes before the damper begins impacting the cavity sidewalls. For impacting operation, energy dissipation during sidewall impacts and the resulting response is nonlinear, thus leading to amplitude-dependent damping performance [20]. Optimal damping performance then requires an adequate estimate of the response amplitudes, which can lead to performance losses due to unexpected vibration localization caused by mistuning.

In a separate approach, Hartung et al. utilized small masses located within blade cavities to function as "impulse mistuners." [23] As these impulse mistuners are small, they do not dissipate much energy through sliding friction or from impacts with the sides of the cavity. Instead, the working principle of this concept is that when operating at certain frequencies, the impacts effectively alter the blade's stiffness and, consequently, the blade's natural frequencies, thus avoiding

a strong resonant condition. Hartung et al. likened this observed detuning effect to that of RFD, though emerging from a mechanical-based avenue, rather than a piezoelectric-based one.

(a) Order-tuned DVA as designed by Hollkamp.
(from [19])

(b) Order-tuned DVA as designed by Duffy et al. .
(from [20])
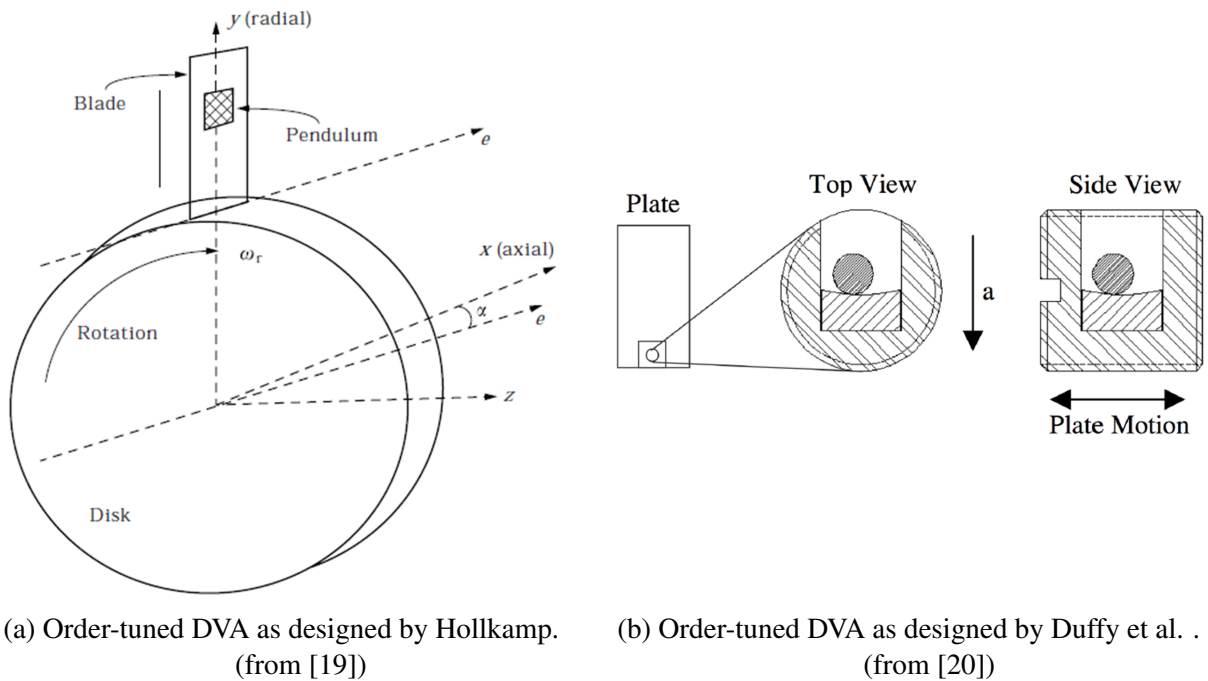
Figure 2.2: Diagrams of order-tuned DVA concepts.

2.1.3 Viscoelastic-Layer Damping

A viscoelastic material has the tendency to behave as both an elastic solid and viscous fluid when undergoing deformation. Upon removal of a stress, the elastic behavior allows the material to return to its undeformed state, while the viscous behavior causes this return to occur more slowly than the typical elastic case. When subjected to harmonic excitation, this viscoelastic behavior causes the induced strain to lag behind the applied stress, thus resulting in a hysteresis loop and an increase in the loss factor, or damping. The elastic modulus and loss factors of these materials show

21

strong temperature and frequency dependency, with the largest loss factors occurring within the transition region between the glassy and rubbery states. For damping treatments, these materials can be layered on a free surface, referred to as free-layer damping, or sandwiched between two panels, referred to as constrained-layer damping. [24] Figure 2.4a shows the differences between these two different configurations.

Near the turn of the century, these viscoelastic damping treatments were investigated for use in advanced turbofan blade concepts developed at NASA. [25, 26, 27, 28] In their initial analysis, Kosmatka et al. provided the damping treatment to composite fan blades idealized with both flat and pre-twisted plates and with viscoelastic patches sandwiched between two composite sheets. [25] Figure 2.3b shows the construction of their test article that included a border around the viscoelastic patch to prevent the damping material from flowing under centrifugal loading. They showed both numerically and experimentally that selectively choosing the patch shapes and locating them in regions of large modal strain increased the loss factors for the targeted modes. A subsequent analysis showed that the patches provided an order of magnitude increase in the loss factor for a total patch volume less than 10% of the blade volume. [26] In both these studies, however, the finite-element models significantly over-predicted the experimentally measured loss factors. Biggerstaff and Kosmatka showed that these discrepancies arose from the epoxy resin penetrating the damping material during the curing process [29]. Including a polyamide film as a barrier between these two layers prohibited the epoxy resin from interacting with the damping material, thus resulting in the expected loss factors. Kosmatka and Mehmed also experimentally analyzed the performance of these composite blades in the presence of rotation-based centrifugal

forces [27]. For modes that stiffened due to the centrifugal force, the loss factors decreased, and vice versa. The authors postulated that this effect occurred due to the increased energy storage capacity of the stiffened blades; a result that Lesieutre later verified analytically. [30]
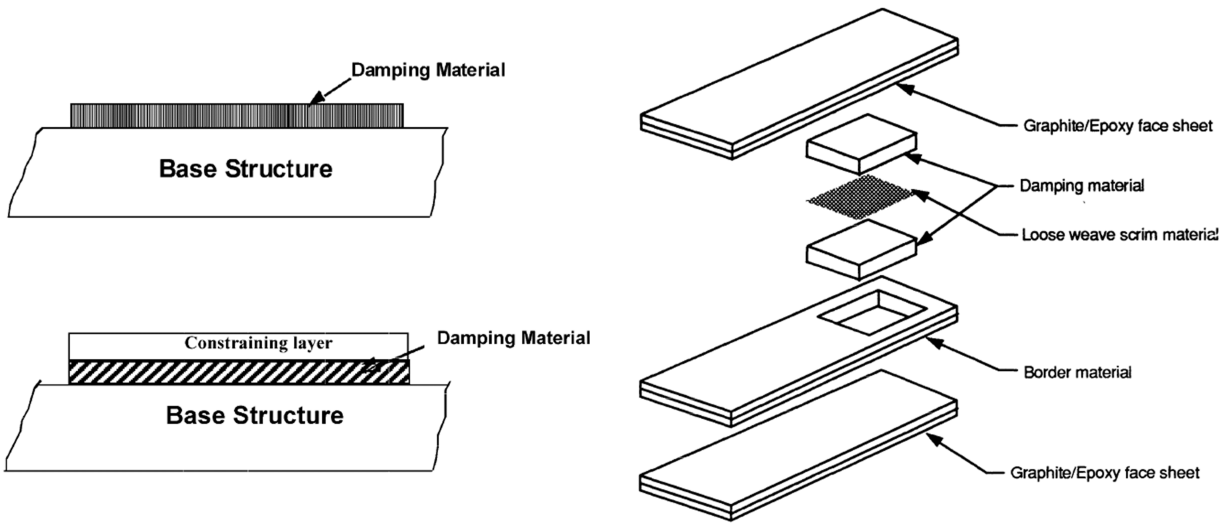
(a) Configuration of free-layer damping (top) and constrained-layer damping (bottom). (from [24])

(b) Constrained-layer damping of a representative turbomachinery blade idealized as a plate. (from [25])

Figure 2.3: Diagrams of viscoelastic-layer damping concepts.

2.1.4 Eddy-Current Damping

Movement of a nonmagnetic conductor relative to a magnetic field continually generates eddy currents via a changing magnetic flux, thus generating an electromotive force (EMF). In turn, these eddy currents produce their own magnetic fields with an opposing polarity than that of the initial magnetic field, thus providing a repulsive force with a magnitude proportional to the velocity,

similar to a viscous damper. Eddy currents are generated either through a motional EMF or transformer EMF. A motional EMF arises from motion of a conductor through a stationary magnetic field, whereas transformer EMF arises from a stationary conductor subject to a time-varying magnetic field. Graves et al. theoretically showed that both of these methods of producing an EMF generate a damping force [31]. Bae et al. used eddy currents to damp vibrations in a beam induced by a transformer EMF. Connecting permanent magnets to the beam tip using a flexible linkage enabled the motion of the magnets around a conductor fixed on the beam tip [32]. Although providing significant damping increases, the eddy-current damper's location on the beam tip drastically altered the beam's dynamics. Sodano et al. presented a noncontact method to damp vibrations of a beam using the motional EMF [33]. This method required locating a conductive patch on the beam tip that oscillated over a fixed permanent magnet. Decreasing the initial gap between the conductive patch and the magnet significantly increased damping performance. Sodano and Bae provide a more comprehensive review on the concept of eddy-current damping and their role in damping structural vibrations. [34]

Laborenz et al. investigated two eddy-current damping concepts to damp blade vibrations by using the relative motion between neighboring blade tips [35]. The first concept utilized a copper plate located on one blade tip situated across from a permanent magnet on the neighboring blade tip, and the second concept utilized a permanent magnet fixed behind a copper plate on one blade tip with a mirrored version of the same assembly on the neighboring blade tip. Figure 2.4b shows their two-blade experimental setup as well as their two proposed damper configurations. While

these concepts show promise, they may require relatively large magnets situated in the flow-stream

to provide adequate damping performance.
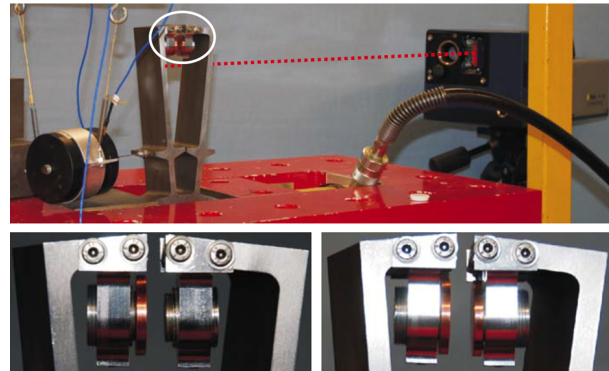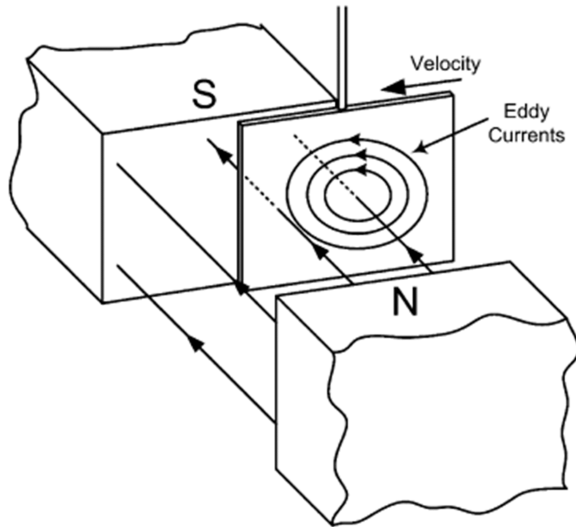
(a) The generation of eddy currents in a conductive material passing through a magnetic field. (from [34])

(b) Two-blade experiment used by Laborenz et al. to investigate eddy-current dampers. (from [35])

Figure 2.4: Eddy-current damper concept.

2.1.5 Intentional Mistuning

A tuned blisk is highly sensitive to mistuning such that even small perturbations from the nom-

inal blade design can lead to significant increases in the vibratory response; however, for highly

mistuned systems, both the maximum response levels and the sensitivity to additional mistuning

tapers off. [2] Researches have exploited this phenomena by incorporating intentional mistuning

into blisk designs. Whereas random mistuning refers to the inherently random blade-to-blade vari-

ations present in physical blisks, intentional mistuning refers to the inclusion of mistuning in a deliberate and systematic manner. Griffin and Hoosac first showed numerically that placing blades with a high and a low stiffness in an alternating pattern around the blisk can reduce the peak response compared to the randomly mistuned case [36].
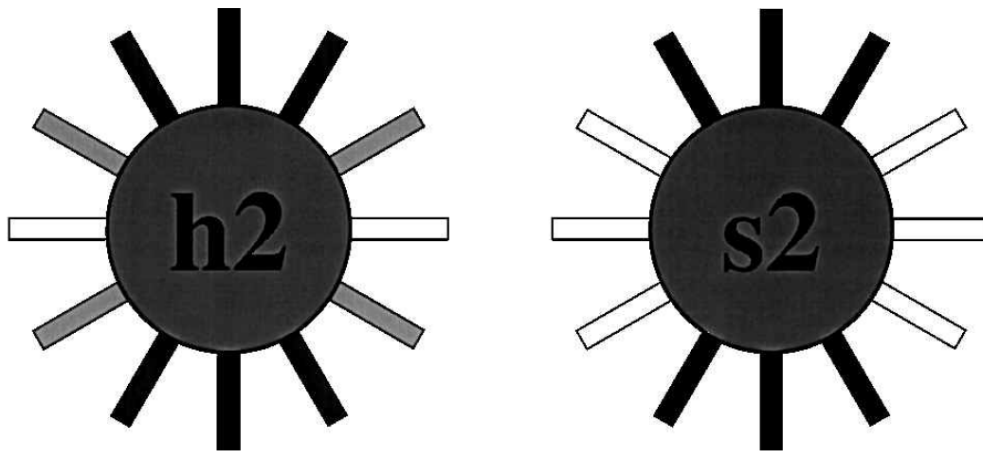
Figure 2.5: Intentionally mistuned blisk with harmonic (left) and square-wave mistuning (right). (from [37])

Building on this intentional mistuning concept, Castanier and Pierre showed that including harmonic mistuning patterns can reduce the maximum peak response while also reducing the sensitivity to random mistuning [37]. Including blades in harmonic patterns would significantly increase manufacturing costs by requiring numerous blade designs with the required stiffness (or mass) variations. As such, they also showed that representing the harmonic patterns with only two different blade designs, effectively produce square-wave mistuning patterns around the blisk, can achieve similar performance. Figure 2.5 shows examples of both a harmonic and a square-wave mistuning pattern. Intentionally mistuning the blisk with harmonic patterns, however, is not the only means of achieving this reduced vibration and sensitivity towards mistuning. Instead, Choi et al. incor-

26

porated a genetic algorithm to identify the optimal mistuning configuration when considering only two different blade designs. [38]

2.1.6 Piezoectric-Shunt Damping

Researchers have also shown a growing interest in utilizing the energy-conversion properties of piezoelectric materials to damp structural vibrations. These materials rely on the piezoelectric effect that enables the conversion of energy between the mechanical to electrical domains. These methods incorporate piezoelectric materials mounted on, or embedded in, a vibrating host structure. As the structure vibrates, the piezoelectric material converts a percentage of the mechanical strain energy to the electrical domain. Attaching the piezoelectric material to a shunt circuit enables the manipulation of this transformed electrical energy, including energy dissipation for damping applications. The following section provides a more thorough overview of the concept of piezo-electricity, including a discussion outlining their use in the vibration reduction of bladed disks.

2.2 Piezoelectric-Shunt Damping

2.2.1 Piezoelectricity

"Smart" or "intelligent" materials are a certain class of materials that exhibit a coupling between two domains. Piezoelectric materials are a subset of these materials that exhibit a two-way coupling

between the mechanical and electric domains. The direct piezoelectric effect refers to the property that enables the material to produce an electric charge when stimulated by mechanical pressure. In 1880, the Curie brothers originally discovered this piezoelectric effect present in various types of natural crystals [39]. A few years later, Lippman theoretically predicted that these crystals should also exhibit the inverse piezoelectric effect, or mechanical deformation due to an electrical stimulus; the Curie brothers experimentally verified this inverse effect the following year. The piezoelectric effect occurs in many natural or synthetic forms. Crystals such as quartz, topaz, and Rochalle salt, to name a few, naturally exhibit the piezoelectric effect but lack the energy conversion capabilities to be effective in vibration control applications. Over time, advances in material technology lead to synthetic ceramics, such as the commonly used zirconate titanate (PZT), that exhibit much stronger coupling, thus making them ideal candidates for many piezoelectric-based applications [40].

2.2.2   Constitutive Equations

For piezoelectric materials, the piezoelectric effect arises from a net dipole within the unit cell at temperatures below the Curie temperature. Joining these unit cells together results in local regions with a net polarity that are randomly distributed throughout the material. During the poling process, the application of a large electric field aligns these dipoles along a single axis, thus generating a permanent polarity for the entire material. Piezoelectric materials are generally transversely isotropic where the plane of isotropy is perpendicular to the poling axis. Typical convention aligns

the 3-axis (or z-axis) with the poling axis and the isotropic plane corresponds to 12-plane. Figure 2.6 shows a diagram of a typical piezoelectric patch with electrodes on the top and bottom surfaces and poled through the patch thickness.
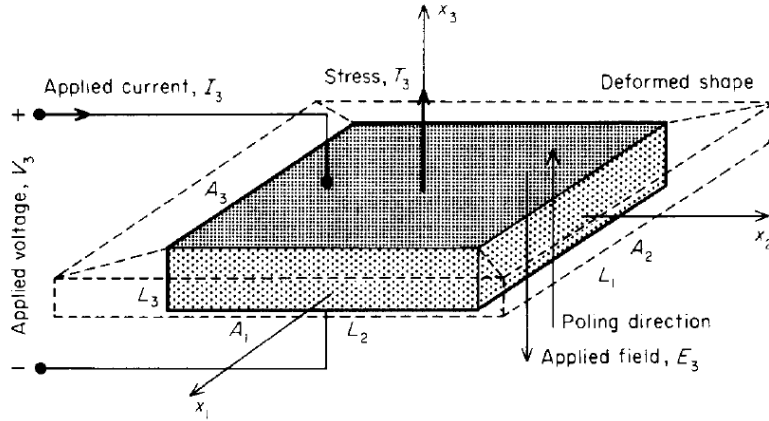
Figure 2.6: Diagram of a rectangular piezoelectric patch with electrodes on the top and bottom surface and poled through the patch thickness. (from [41])

The constitutive equations governing the electromechanical coupling behavior exist in various forms; one such form relates the stress **T** and electric displacement **D** vectors to the strain **S** and the electric field **E** vectors such that [42]

$$
\begin{bmatrix} \mathbf{T} \\ \mathbf{D} \end{bmatrix} = \begin{bmatrix} \mathbf{c}^E & -\mathbf{e}^t \\ \mathbf{e} & \boldsymbol{\varepsilon}^S \end{bmatrix} \begin{bmatrix} \mathbf{S} \\ \mathbf{E} \end{bmatrix}
\tag{2.1}
$$

29

where the stress, strain, electric displacement, and electric field vectors in expanded form are

$$\mathbf{T} = \begin{bmatrix} T_{11} \\ T_{22} \\ T_{33} \\ T_{23} \\ T_{13} \\ T_{12} \end{bmatrix} = \begin{bmatrix} T_1 \\ T_2 \\ T_3 \\ T_4 \\ T_5 \\ T_6 \end{bmatrix}, \quad \mathbf{S} = \begin{bmatrix} S_{11} \\ S_{22} \\ S_{33} \\ 2S_{23} \\ 2S_{13} \\ 2S_{12} \end{bmatrix} = \begin{bmatrix} S_1 \\ S_2 \\ S_3 \\ S_4 \\ S_5 \\ S_6 \end{bmatrix}, \quad \mathbf{D} = \begin{bmatrix} D_1 \\ D_2 \\ D_3 \end{bmatrix}, \quad \mathbf{E} = \begin{bmatrix} E_1 \\ E_2 \\ E_3 \end{bmatrix} \tag{2.2}$$

Furthermore, $\mathbf{c}$ is the stiffness tensor relating the stress and strain; $\mathbf{e}$ is the electromechanical coupling tensor relating the stress to the electric field and the electric displacement to the strain; and $\boldsymbol{\varepsilon}$ is the dielectric tensor relating the electric displacement to the electric field. The superscript t denotes the transpose operator, whereas the superscripts S, T, E, and D denote quantities measured at the various mechanical and electrical boundary conditions. For example, the above constitutive equations contain quantities measured at zero electric field (i.e., the short-circuit state) denoted with the superscript E, and quantities at zero strain (i.e., the strain-free state) denoted with the superscript S. The other forms of the constitutive equations utilize quantities measured at zero electric displacement (i.e., the open-circuit state) denoted with the superscript D, and quantities measured at zero stress (i.e., the stress-free state) denoted with a superscript T. One such example is the open-circuit stiffness tensor

$$\mathbf{c}^D = \mathbf{c}^E + \mathbf{e}^t (\boldsymbol{\varepsilon}^T)^{-1} \mathbf{e} \tag{2.3}$$

that relates the open-circuit stiffness tensor to the short-circuit stiffness tensor. Note here that the electromechanical coupling effect induces an additional stiffness (second term on the right-hand-side of the equation). A separate example is the stress-free dielectric tensor

$$\boldsymbol{\varepsilon}^T = \boldsymbol{\varepsilon}^S + \mathbf{e}(\mathbf{c}^E)^{-1}\mathbf{e}^t \tag{2.4}$$

that relates the stress-free dielectric tensor to the strain-free dielectric tensor.

2.2.3 Electromechanical Coupling Coefficients

Piezoelectric elements commonly operate with a single poling axis and a load applied in a single direction. These common modes of operation include the longitudinal case (poling and strain aligned in the same direction), the transverse case (poling in one direction with a force in a perpendicular direction), and the shear case, (poling in one direction with a shear force acting on the plane perpendicular to that direction). [41] For the poling axis in the i direction and a force in the j direction, the constitutive equations reduce to a set of scalar equations

$$T_j = c_{jj}^E S_j - e_{ij}E_i \tag{2.5}$$

$$D_i = e_{ij}S_j + \varepsilon_{ii}^S \tag{2.6}$$

A more intuitive approach to identifying the electromechanical coupling behavior in such cases is through the electromechanical coupling coefficient that, when squared, is the amount of imposed

31

mechanical work converted to electrical energy, and vise versa. This coefficient depends on either the difference between the open- and short-circuit stiffness values, or the difference between the stress-free and strain-free dielectric permittivity values such that [42]

$$k_{ij}^2 = \frac{c_{jj}^D - c_{jj}^E}{c_{jj}^D} = \frac{\varepsilon_{ii}^T - \varepsilon_{ii}^S}{\varepsilon_{ii}^T} = \frac{e_{ij}^2}{\varepsilon_{ii}^T c_{jj}^E - e_{ij}^2} \tag{2.7}$$

Complete and perfect energy conversion results in $k_{ij}^2 = 1$, and no energy conversion results in $k_{ij}^2 = 0$. For example, using the material properties for PZT-5A, a commonly used piezoceramic, the longitudinal coupling coefficient is $k_{33}^2 = 0.49$, and the transverse coupling coefficient is $k_{31}^2 = 0.12$. For built systems, the piezoelectric elements are in parallel with some other stiffness, resulting in a smaller percentage of strain energy converted to electric energy and, consequently, smaller coupling coefficients. For dynamic systems, the electromechanical coupling behavior depends on the vibration mode of interest. As such, the dynamic form of the coupling coefficient, known as the effective electromechanical coupling coefficient, depends on the open- and short-circuit natural frequencies of the rth vibration mode [42]

$$k_{\text{eff,r}}^2 = \frac{\omega_{\text{oc},r}^2 - \omega_{\text{sc},r}^2}{\omega_{\text{oc},r}^2} \tag{2.8}$$

2.2.4 Passive Shunts

The most classical method of piezoelectric shunt damping consists of passive circuit elements dissipating the transformed electrical energy as heat through a resistor. Forward originally attached a shunt circuit consisting of both a resistor and inductor that, when combined with the capacitance of the piezoelectric element, produced a resonant circuit [43]. An experimental test on a resonant bar reduced the Q factor by a factor of 10 compared to the undamped system. Over a decade later, Hagood and von Flotow developed the theoretical framework for damping vibrations via passive shunts utilizing both a resistive shunt and resonant shunt [41]. They showed that resistive shunts produce a frequency-dependent stiffness and loss factor similar to that of viscoelastic materials operating in the transition region between the glassy and rubbery states. For a single mode, they presented a closed-form solution for the optimal shunt resistance to maximize damping at a specific operating frequency. Furthermore, Hagood and von Flotow showed that incorporating an inductor into the circuit forms a resonant circuit, where proper choice of the inductance tunes the electrical natural frequency to match that of the system natural frequency, thus producing similar behavior to a DVA. Using principles from DVA design, they presented a closed-form solution for the optimal resistor to maximized damping performance Figure 2.7 shows an example of these two passive shunts as applied to a SDOF system using PZT-5A with $k_{31}^2 = 0.12$. The resonant shunt shows significant damping increases compared to the resistive shunt, though at the expense of operating bandwidth.

(a) Resistive (R) shunt.

(b) Resonant (RL) shunt.

(c) Frequency response magnitude for the shunts
with optimized parameters.
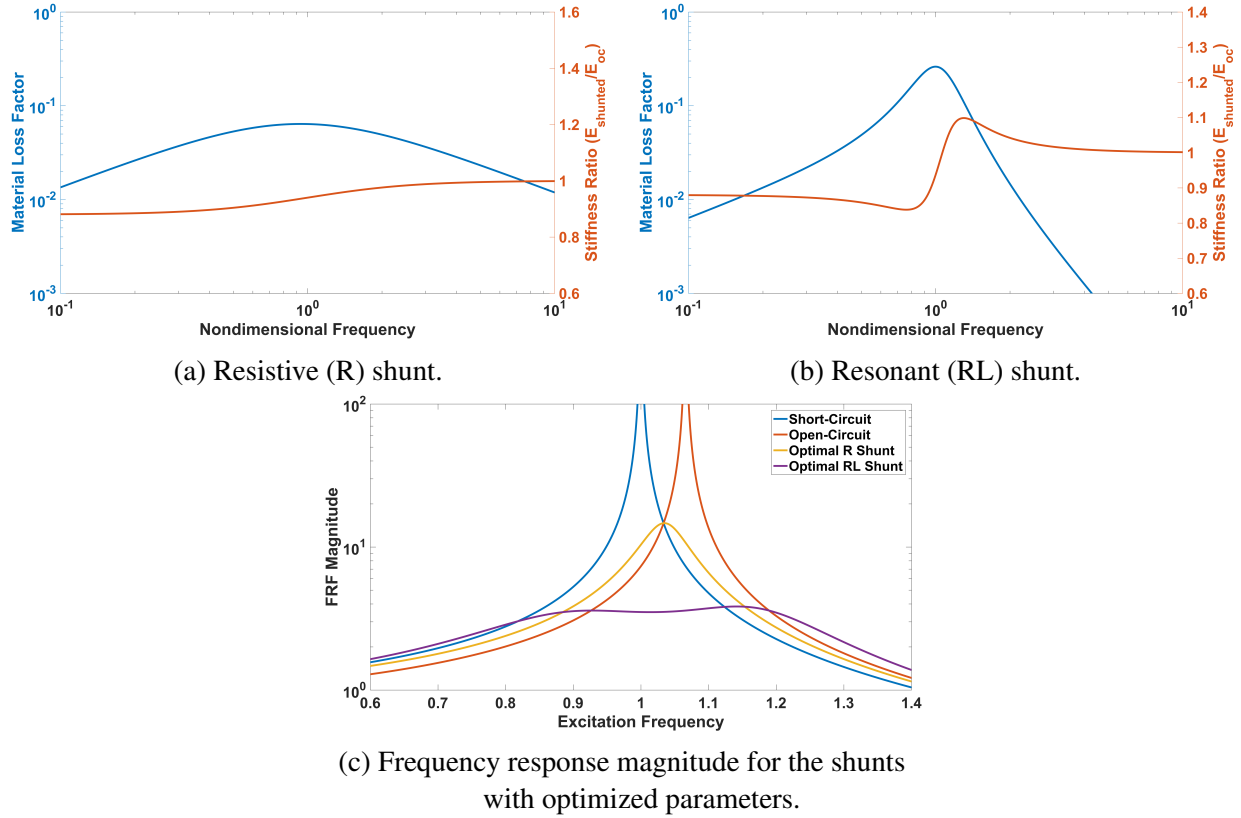
Figure 2.7: Performance characteristics of passive shunts for a piezoelectric material with $k_{31}^2 = 0.12$.
These curves are generated using the equations derived in Ref. [41]

Beginning in the early 2000s, researchers have incorporated passive shunts into turbomachin-

ery blade applications. Cross and Fleeter experimentally investigated passive shunts for reducing

resonant vibrations of a stator blade subjected to a periodic forcing induced by wakes shed from

upstream rotor blades [44]. They mounted four piezoelectric elements on the stator blade and

tuned the shunt circuit parameters to target the vibrations of the first chord-wise bending mode.

Although the tuned resistive shunt showed minimal performance, the resonant showed showed a

40% reduction in amplitude compared to the baseline case with no shunt. Schwarzendahl et al.

embedded the piezoelectric element within a cavity of a representative turbomachinery blade at a

location optimized to target the first chord-wise bending mode; tuning the resonant circuit to target this same mode reduced the amplitude by a factor of 11. [45]

These two previous efforts investigated damping performance for a single blade decoupled from the disk; however, researchers have also turned their attention to blisk assemblies. Yu and Wang employed resonant shunts to target vibration of an entire mode family [46, 47]. Using a SDOF-per-sector model, they showed that for independent resonant shunts attached to each blade, the optimally tuned inductance depends on the nodal diameter associated with the target mode, thus resulting in degraded performance for all other nodal-diameter modes within the mode family. They further showed that coupling the circuits together with an analytically derived optimal capacitor effectively removes this nodal-diameter dependence on the inductor, thus resulting in vibration reduction across the entire mode family [46]. Yu and Wang presented a subsequent study that incorporated a 2DOF-per-sector model to include the flexibility of the disk that captured the curve veering phenomena [47]. Similar to their previous study, they showed that an optimally tuned capacitor that links the various resonant shunts reduced vibration across all modes within the mode family. To supplement the numerical results, they provided an experimental study with a setup that incorporated cantilever beams connected through coupling springs to simulate the blisk dynamics. Utilizing piezoelectric actuators to force each of the beams according to the prescribed engine order, they validated their numerical results across all engine-order excitations. Hohl et al. used a resonant shunt tuned to reduce vibrations of the 4ND mode of an 8-blade academic blisk subjected to 4EO excitation [48]. Using a similar excitation strategy as Yu and Wang to simulate engine-order excitations, both numerical and experimental results showed significant damping

performance for the target mode. They showed the potential of further damping improvements by incorporating a negative-capacitance shunt, though such implementation would require op-amps that require some power to operate.

The previous strategies to reduce blisk vibrations incorporated piezoelectric patches mounted on the blades. Separate research efforts have investigated damping strategies with the piezoelectric patches located on the disk portion of the blisk and away from the flow field. Mokrani et al. distributed piezoelectric elements on the underside of the disk and analyzed two separate resonant shunt configurations [49]: The first configuration employed independent resonant circuits attached to each piezoelectric element with the shunt circuit parameters tuned to target a single mode. The second configuration placed multiple patches in parallel with the electrical connections in a systematic manner that targets a mode with a specified nodal diameter; this parallel configuration reduced inductance requirements compared to the independent shunts. A numerical analysis on a tuned blisk showed that the independent shunts showed vibration across most modes of a mode family, with performance degrading for the higher-frequency, blade-dominated modes; conversely, the parallel shunt showed increased damping solely for the target mode. The experimental analysis showed that the independent shunts again offered better damping performance, but now the parallel shunt showed increased damping for multiple modes, as mistuning caused a dispersion of spatial harmonic content across the modes of the family. Zhou et al. located independently shunted piezoelectric elements in parallel to the coupling springs that connected the disk components of a 3DOF-per-sector model [50]. Citing the problems associated with operational wear that can induce time-dependent mistuning patterns, they employed a strategy to adaptively control each shunt's

inductance components to continuously minimize vibration in the presence of any operational uncertainties. This method showed promising performance for the modes with appreciable disk motion, but did not show significant damping for the blade-dominated modes.

Although passive shunts, resonant shunts specifically, have shown increased attention for reducing vibrations of both stand-alone blades and full blisk, such approaches require tight tuning of circuit parameters, thus limiting their operating bandwidth to a small range of frequencies surrounding the target mode. To address this issue, Hollkamp introduced additional RLC branches to the resonant circuit for each additional mode targeted; however, with this updated circuit, the SDOF tuning of the circuit elements no longer applies [51]. Instead, minimizing a cost function using the vibration amplitudes as the performance measure enabled identification of the optimally tuned values of the circuit elements. An experimental analysis showed the multi-mode shunt suppressed the second and third bending modes of a cantilever beam and provided similar damping performance to that of the single-mode circuit tuned to target the second bending mode. In a separate but similar manner, Wu developed a "blocking" circuit capable of damping multiple modes [52]. Each branch of the circuit consisted of a resonant shunt tuned to a single mode, but also consisted of a series of inductors and capacitors in parallel, tuned to operate as bandstop filters for all others modal frequencies. Experimental results on a cantilever beam showed increased damping for three modes. Although these methods show excellent multi-modal damping performance, they require separate circuit branches for each additional target mode. Due to the increase in the size and complexity of the circuit when targeting additional modes and considering the stringent geometric constraints

imposed by a turbomachinery application, such approaches may not be feasible for a physical implementation.

2.2.5 Switched Shunts

To address the aforementioned bandwidth limitations imposed by the passive shunts, researchers have since developed switched shunts. These techniques reduce vibration by switching the piezo-electric patch onto a shunt circuit synchronously with the vibration cycle of the host structure. They are semi-active by nature due to the small amount of power required to periodically perform the swtich. Typically, the patch operates in the open-circuit state as the system moves away from equilibrium, thus generating a voltage proportional to the displacement. Switching the patch onto the shunt at a displacement extremum rapidly dissipates this stored electrical energy. Furthermore, the circuit elements and the amount of time the piezoelectric element remains attached to the circuit depends on the approach employed.

Clark initially developed a switching strategy where the patch switched to a short circuit in quarter-cycle increments (i.e., closing the switch at displacement extrema and opening the switch at displacement equilibria.) [53] A numerical simulation showed promising damping performance for the impulse response of a single oscillator. A follow-up numerical study showed that this state-switching concept provided similar damping performance to that of a passive resistive shunt; this study also showed switching onto an optimally tuned resistor in the shunt circuit offered better performance [54].

Around the same time, Richard et al. introduced synchronized switch damping on a short circuit (SSDS), a similar switching concept but with a switching strategy that opens the circuit immediately after the switch to a short circuit [55]. Switching in this manner generates a piezo-electric voltage with a square wave component that opposes the system velocity, thus generating a damping force. A year later, Richard et al. showed that placing an inductor in the shunt circuit, an approach termed synchronized switch damping on an inductor (SSDI), to invert the piezoelectric voltage offers better performance [56]. The role of the inductor is to induce a resonant response with the piezoelectric capacitance that enables a voltage inversion. The patch then switches onto the inductive shunt just long enough for the voltage to invert, then reopens the circuit; the only limitation on the inductor is that it must be small enough to invert the voltage at a much higher fre-quency than the vibration. Similar to SSDS, the generated piezoelectric voltage contains a square wave component that opposes the system velocity but larger in magnitude, thus leading to a larger damping force. The magnitude of this opposing force depends on the voltage generated across the electrodes of the piezoelectric patches. As such, the effectiveness of SSDI depends on the quality of the voltage inversion; however, there are voltage losses in the circuit that limits the performance. Lefeuvre et al. offered further improvements by including a constant voltage source in the shunt circuit, an approach termed synchronized switch damping on a voltage source (SSDV). The ap-proach is similar to that of SSDI, but the presence of the voltage source increases the voltage on the patch, thus increasing the damping force [57]. Further building on the SSDV concept, Badel et al. used a voltage source that supplies a voltage with a magnitude dependent on the vibration amplitude, thus increasing the stability [58].

As a low-power alternative to increasing SSDI performance, Ji et al. developed an approach, termed synchronized switch damping on a negative capacitance, that replaced the inductor in the shunt circuit with a negative capacitance element [59]. Although the shunt circuit no longer resonates, the inclusion of the negative capacitance still enables a voltage inversion, though in a different manner, provided the magnitude of the negative capacitance is larger than the piezoelectric capacitance. The shunt also includes a resistor so that when the patch switches onto the shunt, the negative capacitance inverts the voltage in an exponential manner; the magnitude of this inversion depends on the ratio of the piezoelectric capacitance to the difference between the negative capacitance and the piezoelectric capacitance. Maximizing this voltage inversion then requires choosing a negative capacitance with a magnitude slightly larger than the piezoelectric capacitance; however, as the negative capacitance is an active element, the system becomes unstable if the negative capacitance has a magnitude equal to or less than the piezoelectric capacitance.

Figure 2.8 shows the performance of several of these switched shunts in both the time and frequency domains. Figure 2.8a shows that for the un-switched, open-circuit case, the voltage oscillates with the displacement. When switching, the voltage immediately dissipates of inverts, thus creating a square wave component that opposes the velocity that provides the damping force. Figure 2.8b shows the dependence of the damping on the generated voltage, where larger voltages provide the greatest performance.

Citing the performance benefits of the SSDNC approach, Liu et al. applied the approach to reduce vibration in tuned and mistuned blisks modeled using lumped-parameter elements [60, 61]. In their initial analysis, they showed that SSDNC offers excellent performance when considering

multiple modes and is not susceptible to environmental drift that can alter the system frequencies, both of which are advantages over a tuned RL shunt. [60] As the switching circuit is nonlinear, they also applied a nonlinear component mode synthesis approach to decrease the computation time required to obtain the steady-state response magnitude. [61] This solution approach enabled a performance analysis of a mistuned blisk via Monte Carlo simulations that showed that SSDNC offered excellent vibration-reduction potential over all engine-order excitations and mistuning strengths tested.

(a) Time response.

(b) Frequency response.
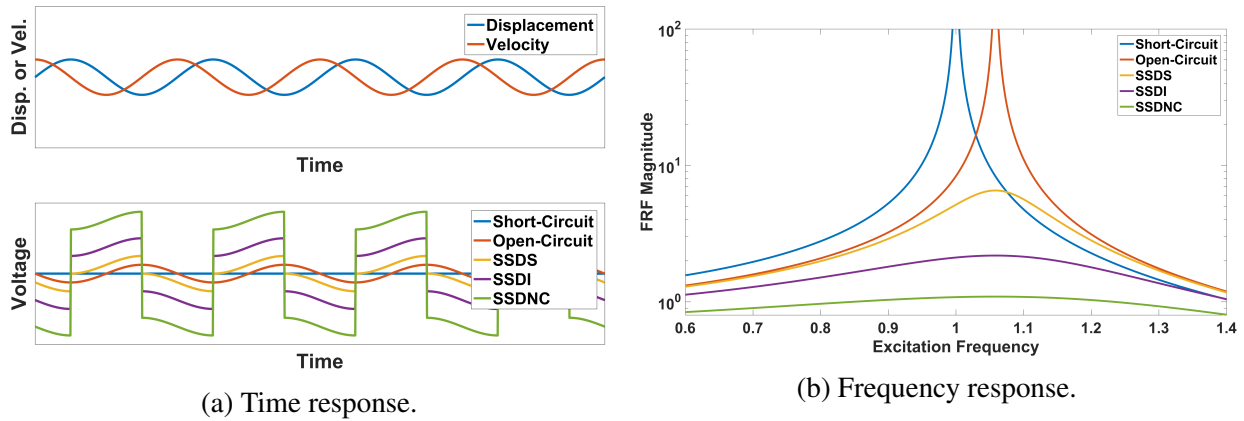
Figure 2.8: Performance characteristics of switched shunts for a piezoelectric material with $k_{31}^2 = 0.12$. These curves are generated using the equations derived in Refs. [58] and [59]

As with the passive shunts, there are some inherent drawbacks associated with these switching approaches. One such drawback is that the square wave component of the piezoelectric voltage is composed of a superposition of sinusoidal waves oscillating at the vibrating frequency and an infinite number of the higher-frequency odd harmonics. Consequently, the voltage will excite the system if one of the system's natural frequencies occurs near one of these higher harmonics. Furthermore, Larson et al. showed experimentally on a switched underwater transducer that the rapid voltage dissipation accompanying the switch from the open-circuit state to the shunt-circuit state

effectively acts as an impulsive force capable of exciting high-frequency modes [62]. Acknowledging the potential harm in exciting these transients, a class of state-switched vibration absorbers developed by Cunefare et al. constrained the switch to occur at zero displacement, or when the piezoelectric voltage is effectively zero [63]. Such switching logic, however, is not applicable to synchronized switching approaches that must switch at, or near, a displacement extremum. These approaches also require four switching events per vibration cycle, and perhaps more when considering a multi-modal response. As many resonance crossings associated with turbomachinery blades may occur in the kHz range, this would require thousands of switches per crossing. Such high switching demands may be prohibitive for typical relays; specifically, electromechanical relays utilize a mechanical armature to open and close the circuit that may also be susceptible to failure induced by high-cycle fatigue.

Both passive and switched shunts offer excellent vibration reduction potential. In fact, both the tuned RL shunt and SSDI approaches outperform RFD when considering transient excitation [64]; however, RFD trades performance for a more feasible turbomachinery implementation. Compared to passive approaches, RFD provides a more broadband approach as the underlying mechanism relies solely on a perturbation in the modal stiffness, thus enabling a means of reducing vibration for all modes, providing some electromechanical coupling exists. Compared to the synchronized switching approaches, RFD reduces the switching demands by only requiring a minimal number of switches per resonance crossing and does not rely on switching at a certain point within the vibration cycle.

2.2.6 Implementation Considerations

Turbomachinery blades operate in an extremely harsh environment with stringent geometric constraints. The design and implementation of any vibration-reduction system requires careful consideration to ensure the system's effectiveness and survivability over the lifespan of the engine. Specifically, for piezoelectric materials, this requires focusing special attention towards their temperature limitations and possible on-blade implementations.

The piezoelectric effect arises due to a lack of symmetry in the material's crystal structure at temperatures below the Curie temperature. At larger temperatures, the crystal structure becomes symmetric, thus losing its piezoelectric properties. Common piezoceramics have Curie temperatures below 350°; some higher-temperature materials exist, but typically have reduced electromechanical coupling properties. [65] As such, the fan blades and cold-side of the compressor are ideal locations for a piezoelectric-based application.

The possible on-blade implementations also requires some discussion. Piezoceramics are brittle by nature, thus cannot undergo the strains necessary to conform to the curved surfaces typical of blades. Advances in piezoelectric technology have led to the developments of piezoelectric fiber composites (PFC) that utilize piezoelectric fibers embedded in a compliant matrix. [66, 67] The matrix material increases the flexibility of the patch, thus enabling the large static strains required to conform to curved surfaces, while also offering protection for the brittle piezoelectric fibers. These designs can also incorporate interdigitated electrodes to exploit the high d_{33} mode of coupling for the material that offers improved performance.

For a blade-mounted application, an external mounting location on the blade may not be feasible due to the shear forces exerted by the air flow and the risk of damage induced by foreign-object strikes. To bypass this limitation, some researchers have investigated systems that locate the piezo-electrics on the disk and away from the blades. [49, 50] This off-blade location, however, is unable to target modes where the vibration is predominantly located on the blades. A second approach may involve locating the piezoelectric materials in a cavity within the blade. [45] In such an approach, care must be taken that this internal cavity does not adversely affect the structural integrity of the blade.
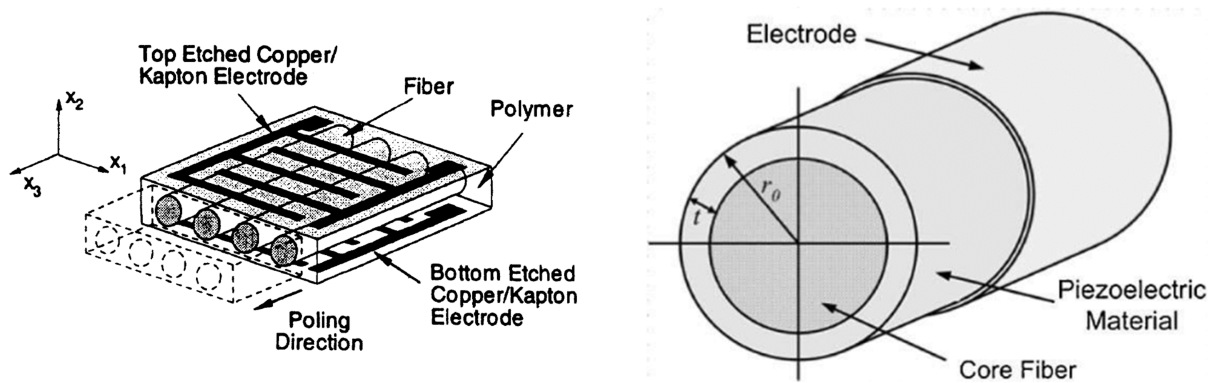
(a) Piezoelectric fiber composite.
(from [66])

(b) Piezoelectric-coated fiber.
(from [68]

Figure 2.9: Examples of piezoelectric-based composites.

The introduction and continued interest of composites as materials for fan and compressor blades offers a promising avenue for implementation. [69, 70] As the piezoelectric fibers in PFCs offer a fraction of the tensile stiffness as typical fiber reinforcements, embedding them within a

44

composite blade may lead to structural integrity concerns. Citing these structural concerns, Lin and Sodano recently developed an active fiber concept that coats a conducting fiber with piezo-electric material for use within a composite layup. [71, 68] Figure 2.9b shows a diagram of this piezoelectric fiber.

CHAPTER 3
LUMPED-PARAMETER BLISK MODEL AND APPLICATIONS

Ultimately validating RFD as a viable approach to reduce blisk vibrations requires confidence of successful performance over a range of various design parameters. As such, numerical analysis requires adequate modeling that captures the mistuning phenomena. This chapter presents a lumped-parameter blisk model typically employed when qualitatively analyzing blisk vibrations; this model includes the electrical dynamics introduced by with blade-mounted piezoelectric elements. Section 3.1 derives the lumped-parameter blisk model that considers only a single-degree-of-freedom (SDOF) per sector; a corresponding nondimensionalization generalizes the analysis. Section 3.2 uses modal analysis to provide information about the free- and forced-response characteristics associated with the tuned and mistuned systems. It considers for the forced response both harmonic and transient excitation, the latter idealized with constant acceleration frequency sweeps. It then presents the adaptation of a semi-analytical solution to swept excitation for the model used here.

3.1 Model Development

Due to the stochastic nature of mistuning, analysis via Monte Carlo simulations provides an excellent tool for identifying key design parameters. Griffin and Hoosac first utilized a lumped-parameter blisk model as a computationally cheap means to perform large-scale statistical analysis [36]; thus, as a first step, modeling each blade sector as a single oscillator can provide fundamental insight towards RFD performance towards mistuned blisks. Figure 3.1 shows a diagram of the lumped-parameter model where each oscillator represents the blade corresponding to the jth sector of an N_s-sector blisk. Each blade has a nominal mass m, damping c, and stiffness k_0 and is grounded to a rigid disk. Furthermore, RFD is a blade-mounted approach, thus required the placement of piezoelectric elements in parallel with the damping and stiffness elements of each blade. The springs k_c represent the coupling between neighboring blades that enable the flow of vibration energy around the disk.
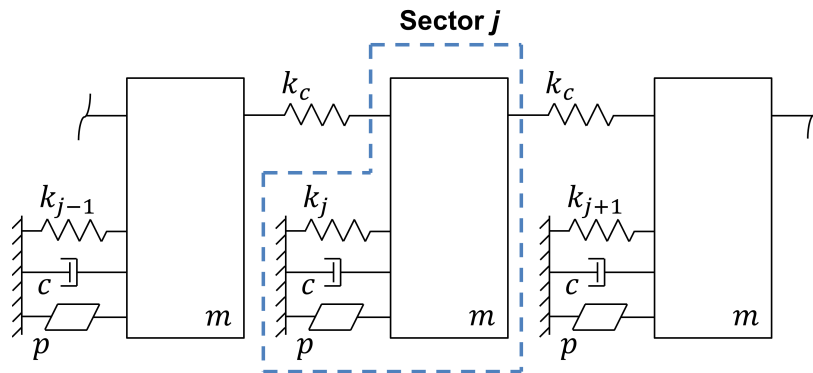
Figure 3.1: SDOF-per-sector blisk model.

3.1.1   Equations of Motion

The derivation of the electromechanical equations of motion begins with balancing the forces on the each oscillator such that

$$m\ddot{x}_j + c\dot{x}_s - k_c x_{j-1} + (k_j + k_{p,j} + 2k_c)x_j - k_c x_{j+1} - \theta V_j = f_{m,j} \tag{3.1}$$

$$\theta x_j + C_p V_j = Q_j, \quad \text{for } j = 0, \cdots, N_s - 1 \tag{3.2}$$

where the j subscript denotes a quantity associated with the jth blade. The variable k_p is the stiffness of the piezoelectric element in the short-circuit state, θ is the electromechanical coupling term, C_p is the piezoelectric capacitance, V is the piezoelectric voltage, and Q is the generated charge. For a tuned system with the piezoelectric elements shorted, there is zero voltage generated by each element such that $V_j = 0$ for $j = 0, \cdots, N_s - 1$, and the nominal blade and piezoelectric stiffness in the short-circuit state are k_0 and $k_{p,0}$; the short-circuit stiffness of the nominal blade that includes the stiffness contribution of the piezoelectric element is $k_{sc,0} = k_0 + k_{p,0}$. Slight blade-to-blade variations break the cyclic symmetry of the system, thereby inducing mistuning. For the lumped-parameter model, representing these variations as small perturbations in each blade's nominal stiffness provides a similar effect. Each modified blade stiffness is then

$$k_{sc,j} = k_{sc,0}(1 + \delta_{mis,sc,j}) \tag{3.3}$$

where $\delta_{\mathrm{mis,sc},j}$ is the short-circuit stiffness perturbation induced by mistuning and that is a random sample of a normal distribution with zero mean and a user-assigned standard deviation σ_{mis}.

With each piezoelectric element's electrodes open, there is a constant charge that depends on the initial displacement at the time of the switch x_{sw} such that $Q_{\mathrm{sw},j} = \theta x_{\mathrm{sw},j}$ for $j = 0, \cdots, N_s - 1$. [72] As such, the generated voltage for the jth element is proportional to the blade displacement plus a constant term:

$$V_j = \frac{\theta}{C_p} x_{\mathrm{sw},j} - \frac{\theta}{C_p} x_j \tag{3.4}$$

Inserting this voltage into Eq. 3.1 results in

$$m\ddot{x}_j + c\dot{x}_j - k_c x_{j-1} + \left(k_{\mathrm{sc},j} + \frac{\theta^2}{C_p} + 2k_c\right)x_j - k_c x_{j+1} = f_{m,j} + \frac{\theta^2}{C_p} x_{\mathrm{sw},j} \tag{3.5}$$

where there is a constant forcing term arising from the initial charge when switching to the open-circuit state that depends on the initial displacement. Furthermore, the modified stiffness term associated with x_j is the blade stiffness in the open-circuit state

$$k_{\mathrm{oc},j} = k_{\mathrm{sc},j} + \frac{\theta^2}{C_p} \tag{3.6}$$

and is always greater than the short-circuit stiffness, provided there is non-zero electromechanical coupling. Subtracting the short-circuit stiffness from the open-circuit stiffness results in

$$\Delta k_p = k_{\mathrm{oc},j} - k_{\mathrm{sc},j} = \frac{\theta^2}{C_p} \tag{3.7}$$

49

where Δk_p is the stiffness perturbation when switching between the open- and short-circuit state and is constant for each blade. During spool-up of the engine, the blades operate in the higher, open-circuit stiffness state for the majority of the operation and only switches to the short-circuit state during resonance passages. As such, recast the previously derived equations into open-circuit form by rearranging Eq. 3.2 to solve for V_j such that

$$-\frac{\theta}{C_p}x_j + \frac{1}{C_p}Q_j = V_j \tag{3.8}$$

Inserting the above voltage into Eq. 3.1 results in

$$m\ddot{x}_j + c\dot{x}_j - k_c x_{j-1} + (k_{\mathrm{oc},j} + 2k_c)x_j - k_c x_{j+1} - \frac{\theta}{C_p}Q_j = f_{m,j} \tag{3.9}$$

Representing the equations in open-circuit form also requires setting the stiffness perturbations with respect to the open-circuit blade stiffness; this is done by substituting the short-circuit stiffness of Eq. 3.3 into the open-circuit stiffness of Eq. 3.6 such that

$$k_{\mathrm{oc},j} = k_{\mathrm{oc},0}(1 + \frac{k_{\mathrm{sc},0}}{k_{\mathrm{oc},0}}\delta_{\mathrm{mis,sc},j}) = k_{\mathrm{oc},0}(1 + \delta_{\mathrm{mis,oc},j}) \tag{3.10}$$

The perturbation to the open-circuit blade stiffness from mistuning relates to the perturbation to the short-circuit blade stiffness as

$$\delta_{\mathrm{mis,oc},j} = \frac{k_{\mathrm{sc},0}}{k_{\mathrm{oc},0}}\delta_{\mathrm{mis,sc},j} = (1 - \frac{\Delta k_p}{k_{\mathrm{oc},0}})\delta_{\mathrm{mis,sc},j} = (1 - \delta_p)\delta_{\mathrm{mis,sc},j} \tag{3.11}$$

50

where δ_p is the switch-induced stiffness perturbation normalized by the nominal open-circuit blade stiffness.

3.1.1.1 Engine-Order Excitation

RFD is inherently a transient approach that reduces vibration induced from engine-order excitations that sweep through resonance. Although in turbomachinery operation, engine-order excitation refers to the blades rotating through essentially static pressure disturbances, the analysis here assumes a stationary blisk with a traveling-wave excitation. As such, a linear frequency sweep idealizes the excitation with constant amplitude $f_{m,0}$ and a blade-dependent phase; thus, the force applied to the jth blade is

$$f_{m,j} = f_{m,0} \sin \varphi_j(t)$$
$$\varphi_j(t) = \frac{\omega_{\text{rate}}}{2} t^2 + \omega_0 t + \gamma_j$$

(3.12)

where ω_{rate} is the linear frequency sweep rate and ω_0 is the initial operating frequency (taken as zero at start-up). The traveling-wave excitation arises through inclusion of the constant, blade-dependent phase γ_j that varies linearly around the disk circumference according to

$$\gamma_j = \frac{2\pi n(j-1)}{N_s}$$

(3.13)

and is an integer multiple $(j-1)$ of the interblade phase angle (IBPA)

$$\text{IBPA} = \frac{2\pi n}{N_s} \tag{3.14}$$

The IBPA is a constant that depends on the engine order and the total number of blades.

3.1.2 Nondimensional Equations of Motion

Nondimensionalizing the equations of motion both generalizes the analysis and reduces the number of independent variables, thus facilitating a parametric study over various design parameters. The nondimensional variables with respect to parameters in the open-circuit state are

$$\bar{t} = \sqrt{\frac{k_{\text{oc},0}}{m}}(t - t_0) = \omega_{\text{oc},0}(t - t_0) \tag{3.15}$$

$$\bar{x}_j = \frac{k_{\text{oc},0}}{f_{m,0}}x_j \tag{3.16}$$

$$\zeta_0 = \frac{c}{2\sqrt{k_{\text{oc},0}m}} \tag{3.17}$$

$$\bar{V}_j = \frac{\theta}{f_{m,0}}V_j \tag{3.18}$$

$$\bar{Q}_j = \frac{\theta}{C_p f_{m,0}}Q_j \tag{3.19}$$

$$\bar{\omega}_{\text{rate}} = \frac{\omega_{\text{rate}}}{\omega_{\text{oc},0}^2} \tag{3.20}$$

$$\bar{\omega}_0 = \frac{\omega_0 + \omega_{\text{rate}}t_0}{\omega_{\text{oc},0}} \tag{3.21}$$

where the overbar corresponds to a nondimensional variable. The resulting nondimensional equations of motion for the jth blade are

$$\bar{x}_j'' + 2\zeta_0 \bar{x}_j' - \bar{k}_c \bar{x}_{j-1} + (1 + \delta_{\text{mis,oc},j} + 2\bar{k}_c)\bar{x}_j - \bar{k}_c \bar{x}_{j-1} - \bar{Q}_j = \bar{f}_{m,j} \tag{3.22}$$

$$-\delta_p \bar{x}_j + \bar{Q}_j = \bar{V}_j \tag{3.23}$$

where $()'$ indicates a derivative with respect to the nondimensional time. Also, the nondimensional mechanical force is

$$\bar{f}_{m,j} = \sin\left(\frac{1}{2}\bar{\omega}_{\text{rate}}\bar{t}^2 + \bar{\omega}_0\bar{t} + \frac{1}{2}\omega_{\text{rate}}t_0^2 + \omega_0 t_0 + \gamma_j\right) \tag{3.24}$$

where the last three terms are the constant portion of the phase that depends not only on γ_j, but also the initial time of operation t_0.

3.1.2.1   Stiffness-State Switching

When operating in the open-circuit state, the nondimensional equations are

$$\bar{x}_j'' + 2\zeta_0 \bar{x}_j' - \bar{k}_c \bar{x}_{j-1} + (1 + \delta_{\text{mis,oc},j} + 2\bar{k}_c)\bar{x}_j - \bar{k}_c \bar{x}_{j-1} = \bar{f}_j + \delta_p \bar{x}_{\text{sw},j} \tag{3.25}$$

$$-\delta_p \bar{x}_j = \bar{V}_j \tag{3.26}$$

Conversely, when operating in the short-circuit state, the nondimensional equations are

$$\bar{x}_j'' + 2\zeta_0\bar{x}_j' - \bar{k}_c\bar{x}_{j-1} + (1 - \delta_p + \delta_{\text{mis,oc},j} + 2\bar{k}_c)\bar{x}_j - \bar{k}_c\bar{x}_{j-1} = \bar{f}_j \qquad (3.27)$$

$$\delta_p\bar{x}_j = \bar{Q}_j \qquad (3.28)$$

In a physical implementation, a typical relay opens/closes the shunt circuit attached to the electrodes of the piezoelectric element to provide a means of rapidly switching between the open- and short-circuit states. Typical bandwidth of relays can be on the order of microseconds, and is much faster than a period of vibration for the blisk with vibration frequencies expected in the kHz range. Such reasoning enables use of a discrete switching model to instantaneously switch between the open- and short-circuit states, thereby decoupling the equations of motion into purely mechanical form:

$$\bar{x}_j'' + 2\zeta_0\bar{x}_j' - \bar{k}_c\bar{x}_{j-1} + \left[1 + 2\bar{k}_c + \delta_{\text{mis,oc},j} - (1 - s_j)\delta_p\right]\bar{x}_j - \bar{k}_c\bar{x}_{j-1} = \bar{f}_{m,j} + s_j\delta_p\bar{x}_{\text{sw},j} \qquad (3.29)$$

where s_j is a binary number that depends on the stiffness state of the jth piezoelectric element such that

$$s_j = \begin{cases} 0, & \text{short-circuit state} \\ \\ 1, & \text{open-circuit state} \end{cases} \qquad (3.30)$$

Note here that the use of a discrete switching model leads to a discontinuity in the system dynamics when switching between stiffness states. For example, when switching from the open- to the short-circuit state, there is initially a voltage generated across the piezoelectric immediately pre-

ceding the switch. The discrete switching model assumes this voltage dissipates instantaneously immediately following the switch. This rapid voltage dissipation results in an impulsive-like force capable of exciting high-frequency modes and that results in high-frequency transients observed in the acceleration response [62, 73, 74]. Similar to impulses, the duration of this voltage dissipation dictates the frequency content excited when switching. Controlling the shunt circuit's time constant by including an appropriately-sized resistor can significantly reduce any developed mechanical transients [75].

3.1.2.2 Equations of Motion in Matrix Form

In matrix form, the nondimensional equations of motion in matrix form are

$$\bar{\mathbf{M}}\bar{\mathbf{x}}'' + \bar{\mathbf{C}}\bar{\mathbf{x}}' + \bar{\mathbf{K}}\bar{\mathbf{x}} = \bar{\mathbf{F}}_{\mathbf{m}} + \bar{\mathbf{F}}_{\mathbf{sw}} \tag{3.31}$$

where the mass, damping, and stiffness matrices, as well as the mechanical and switch-induced forcing vectors are

$$\bar{\mathbf{M}} = \mathbf{I} \tag{3.32}$$

$$\bar{\mathbf{C}} = 2\zeta_0 \mathbf{I} \tag{3.33}$$

$$\bar{\mathbf{K}} = \mathbf{I} + \bar{\mathbf{K}}_{\mathbf{c}} + \mathbf{\Delta}\bar{\mathbf{K}}_{\mathbf{mis,oc}} - [\mathbf{I} - \mathbf{S}]\mathbf{\Delta}\bar{\mathbf{K}}_{\mathbf{p}} \tag{3.34}$$

$$\bar{\mathbf{F}}_{\mathbf{m}} = \begin{bmatrix} \bar{f}_{m,0} & \cdots & \bar{f}_{m,N_s-1} \end{bmatrix}^t \tag{3.35}$$

$$\bar{\mathbf{F}}_{\mathbf{sw}} = \mathbf{S}\mathbf{\Delta}\bar{\mathbf{K}}_{\mathbf{p}}\bar{\mathbf{x}}_{\mathbf{sw}} \tag{3.36}$$

where $\mathbf{I}$ is the $N_s \times N_s$ identity matrix. Four components comprise the stiffness matrix: 1) The first component is the identity matrix that corresponds to the open-circuit stiffness of the nominal blade. 2) The second component corresponds to the stiffness elements coupling the blades:

$$\bar{\mathbf{K}}_{\mathbf{c}} = \bar{k}_c \begin{bmatrix}
2 & -1 & 0 & \cdots & & & & \cdots & 0 & -1 \\
-1 & 2 & -1 & 0 & \cdots & & & & \cdots & 0 \\
0 & -1 & 2 & -1 & 0 & \cdots & & & \cdots & 0 \\
\vdots & & & \ddots & & & & & & \vdots \\
& & & & & & & & & \\
\vdots & & & & & \ddots & & & & \vdots \\
0 & \cdots & & & & \cdots & 0 & -1 & 2 & -1 & 0 \\
0 & \cdots & & & & & \cdots & 0 & -1 & 2 & -1 \\
-1 & 0 & \cdots & & & & & \cdots & 0 & -1 & 2
\end{bmatrix} \tag{3.37}$$

56

3) The third component is a diagonal matrix that corresponds to the stiffness perturbations induced by the blade mistuning:

$$\mathbf{\Delta \bar{K}_{mis,oc}} = \mathbf{diag}(\delta_{\mathrm{mis,oc},0}, \cdots, \delta_{\mathrm{mis,oc},N_s-1}) \tag{3.38}$$

4) The fourth component corresponds to the perturbations induced by the stiffness-state switching where $\mathbf{S}$ is the switching matrix and $\mathbf{\Delta \bar{K}_p}$ is the stiffness perturbation between the open- and short-circuit states:

$$\mathbf{S} = \mathbf{diag}(s_0, \cdots, s_{N_s-1}) \tag{3.39}$$

$$\mathbf{\Delta \bar{K}_p} = \delta_p \mathbf{I} \tag{3.40}$$

where $\mathbf{S} = \mathbf{0}$ for all blades operating in the short-circuit state and $\mathbf{S} = \mathbf{I}$ for all blades operating in the open-circuit state.

3.2   Modal Response

As is typical for many second-order, MDOF systems, coupling exists between the degrees of freedom; here, this coupling arises through the stiffness components linking neighboring blades. This coupling stiffness matrix is circulant, thus also resulting in a circulant stiffness matrix for the tuned system. A property of such systems enables a transformation using the Fourier matrix $\mathbf{F}$ to decouple the equations of motion. [76] I.e., a real-valued Fourier series comprises each blade's

displacement such that

$$\bar{x}_j = \frac{1}{\sqrt{N_s}}\tilde{x}^{(0)} + \sqrt{\frac{2}{N_s}}\sum_{h=1}^{\kappa}\left[\cos(jh\alpha)\tilde{x}^{(h,c)} + \sin(jh\alpha)\tilde{x}^{(h,s)}\right] + \frac{(-1)^j}{\sqrt{N_s}}\tilde{x}^{(N_s/2)} \qquad (3.41)$$

where α is the angle between neighboring sectors on the blisk that takes the value of $\alpha = 2\pi/N_s$, κ is a quantity that takes the value of $\kappa = N_s/2 - 1$ for an even number of sectors, or $\kappa = (N_s - 1)/2$ for an odd number of sectors, $\tilde{x}$ is the response of a reference sector in the cyclic domain, and the superscript denotes the associated spatial harmonic; e.g., (0) denotes the zeroth harmonic, (h,c) and (h,s) denote the cosine and sine components of the hth harmonic, and $(N_s/2)$ denotes the component of the $(N_s/2)^{\text{th}}$ harmonic and is present only if N_s is even. Stacking each sector's transverse displacement into a single column vector and expanding the summation leads to the displacement in matrix form

$$\bar{\mathbf{x}} = \mathbf{F}\tilde{\mathbf{x}} \qquad (3.42)$$

where

$$\bar{\mathbf{x}} = \begin{bmatrix} \bar{x}_0 & \cdots & \bar{x}_{N_s-1} \end{bmatrix}^t \qquad (3.43)$$

$$\tilde{\mathbf{x}} = \begin{bmatrix} \tilde{x}^{(0)} & \tilde{x}^{(1,c)} & \tilde{x}^{(1,s)} & \cdots & \tilde{x}^{(\kappa,c)} & \tilde{x}^{(\kappa,s)} & \tilde{x}^{(N_s/2)} \end{bmatrix}^t \qquad (3.44)$$

and $\mathbf{F}$ is the Fourier transformation matrix

$$
\mathbf{F} = \frac{1}{\sqrt{N_s}}
\begin{bmatrix}
1 & \sqrt{2} & 0 & \cdots & 0 & 1 \\
1 & \sqrt{2}\cos\alpha & \sqrt{2}\sin\alpha & \cdots & \sqrt{2}\sin\kappa\alpha & -1 \\
1 & \sqrt{2}\cos 2\alpha & \sqrt{2}\sin 2\alpha & \cdots & \sqrt{2}\sin 2\kappa\alpha & 1 \\
\vdots & \vdots & \vdots & & \vdots & \vdots \\
1 & \sqrt{2}\cos(N_s-1)\alpha & \sqrt{2}\sin(N_s-1)\alpha & \cdots & \sqrt{2}\sin(N_s-1)\kappa\alpha & (-1)^{N_s-1}
\end{bmatrix}
\tag{3.45}
$$

The columns of $\mathbf{F}$, denoted by $\mathbf{F}^{(h)}$, correspond to the specified spatial harmonic. The 1st column, denoted by $\mathbf{F}^{(0)}$, corresponds to the 0th harmonic, whereas the last column, denoted by $F^{(N_s/2)}$, corresponds to the $(N_s/2)^{\text{th}}$ harmonic, and only exists if N_s is even. All other harmonics contain both cosine and sine components such that there are two columns in $\mathbf{F}$ for each harmonic; these columns correspond to the cosine component, denoted by $\mathbf{F}^{(h,c)}$, and the sine component, denoted by $\mathbf{F}^{(h,s)}$. Furthermore, $\mathbf{F}$ is a unitary matrix with the defining property $\mathbf{F}^t\mathbf{F} = \mathbf{I}$.

Next, insert the transformation in Eq. 3.42 into Eq. 3.31 and premultiplying by $\mathbf{F}^t$ to obtain the equations of motion in the cyclic domain

$$
\tilde{\mathbf{M}}\tilde{\mathbf{x}}'' + \tilde{\mathbf{C}}\tilde{\mathbf{x}}' + \tilde{\mathbf{K}}\tilde{\mathbf{x}} = \tilde{\mathbf{F}}_{\mathbf{m}} + \tilde{\mathbf{F}}_{\mathbf{sw}}
\tag{3.46}
$$

where the cyclic mass, damping, and stiffness matrix, as well as the cyclic forcing vectors are

$$\tilde{\mathbf{M}} = \mathbf{I} \tag{3.47}$$

$$\tilde{\mathbf{C}} = 2\zeta_0\mathbf{I} \tag{3.48}$$

$$\tilde{\mathbf{K}} = \mathbf{I} + \mathbf{F}^t\bar{\mathbf{K}}_{\mathbf{c}}\mathbf{F} + \mathbf{F}^t\Delta\bar{\mathbf{K}}_{\mathbf{mis,oc}}\mathbf{F} - \delta_p\mathbf{F}^t[\mathbf{I} - \mathbf{S}]\mathbf{F} \tag{3.49}$$

$$\tilde{\mathbf{F}}_{\mathbf{m}} = \mathbf{F}^t\mathbf{F}_{\mathbf{m}} \tag{3.50}$$

$$\tilde{\mathbf{F}}_{\mathbf{sw}} = \delta_p\mathbf{F}^t\mathbf{S}\mathbf{F}\tilde{\mathbf{x}}_{\mathbf{sw}} \tag{3.51}$$

3.2.1   Tuned System

3.2.1.1   Free Response Characteristics

Consider the case of the tuned system with all blades operating in the open-circuit state. As the system is tuned, there is no stiffness perturbation induced by mistuning such that $\Delta\bar{\mathbf{K}}_{\mathbf{mis,oc}} = \mathbf{0}$. Neglecting the influence of damping and any applied forces, Eq. 3.46 reduces to

$$\tilde{\mathbf{M}}\tilde{\mathbf{x}}'' + \tilde{\mathbf{K}}_0\tilde{\mathbf{x}} = \mathbf{0} \tag{3.52}$$

where $\tilde{\mathbf{K}}_0$ is the tuned stiffness matrix:

$$\tilde{\mathbf{K}}_0 = \mathbf{I} + \mathbf{F}^t\bar{\mathbf{K}}_{\mathbf{c}}\mathbf{F} - \delta_p\mathbf{F}^t[\mathbf{I} - \mathbf{S}]\mathbf{F} \tag{3.53}$$

The second term $\mathbf{F}^t \mathbf{K_c} \mathbf{F}$ is a diagonal matrix with the diagonal components defined for each spatial harmonic. Assuming no switch-induced stiffness perturbation such that $\mathbf{S} = \mathbf{I}$, Eq. 3.52 reduces to

$$\tilde{\mathbf{M}} \tilde{\mathbf{x}}'' + \tilde{\mathbf{K}}_{\mathbf{0,oc}} \tilde{\mathbf{x}} = \mathbf{0} \tag{3.54}$$

where $\tilde{\mathbf{K}}_{\mathbf{0,oc}}$ is the open-circuit, tuned stiffness matrix that is diagonal where the components are the squared, open-circuit, tuned natural frequencies:

$$\tilde{\mathbf{K}}_{\mathbf{0,oc}} = \mathbf{diag}\left(\bar{\omega}_{0,oc}^{(0)^2}, \bar{\omega}_{0,oc}^{(1,c)^2}, \bar{\omega}_{0,oc}^{(1,s)^2}, \cdots, \bar{\omega}_{0,oc}^{(\kappa,c)^2}, \bar{\omega}_{0,oc}^{(\kappa,s)^2}, \bar{\omega}_{0,oc}^{(N_s/2)^2} \right) \tag{3.55}$$

The squared natural frequencies for the 0th and $(N_s/2)^{\text{th}}$ harmonics are

$$\bar{\omega}_{0,oc}^{(0)^2} = 1 \tag{3.56}$$

$$\bar{\omega}_{0,oc}^{(N_s/2)^2} = 1 + 4\bar{k}_c \tag{3.57}$$

All other harmonics occur in degenerate pairs where the squared natural frequencies are

$$\bar{\omega}_{0,oc}^{(h,c)^2} = \bar{\omega}_{0,oc}^{(h,s)^2} = 1 + 2\bar{k}_c(1 - \cos h\alpha) \tag{3.58}$$

Furthermore, as $\tilde{\mathbf{M}}$ and $\tilde{\mathbf{K}}_{\mathbf{0,oc}}$ are diagonal and because $\tilde{\mathbf{M}} = \mathbf{I}$, the columns of $\mathbf{F}$ correspond to the mass-normalized mode shapes.

Next, consider the case with all blades operating in the short-circuit state such that the switching matrix is $\mathbf{S} = \mathbf{0}$, Eq. 3.52 becomes

$$\tilde{\mathbf{M}}\tilde{\mathbf{x}}'' + \tilde{\mathbf{K}}_{0,sc}\tilde{\mathbf{x}} = \mathbf{0} \tag{3.59}$$

where $\tilde{\mathbf{K}}_{0,sc}$ is the short-circuit, tuned stiffness matrix:

$$\tilde{\mathbf{K}}_{0,sc} = \tilde{\mathbf{K}}_{0,oc} - \delta_p \mathbf{I} \tag{3.60}$$

that is also diagonal where the components are the squared, short-circuit, tuned natural frequencies:

$$\tilde{\mathbf{K}}_{0,sc} = \mathbf{diag}\left(\bar{\omega}_{0,sc}^{(0)^2}, \bar{\omega}_{0,sc}^{(1,c)^2}, \bar{\omega}_{0,sc}^{(1,s)^2}, \cdots, \bar{\omega}_{0,sc}^{(\kappa,c)^2}, \bar{\omega}_{0,sc}^{(\kappa,s)^2}, \bar{\omega}_{0,sc}^{(N_s/2)^2}\right) \tag{3.61}$$

The short-circuit, tuned natural frequencies relate to the open-circuit, tuned frequencies by

$$\bar{\omega}_{0,sc}^{(h)^2} = \bar{\omega}_{0,oc}^{(h)^2} - \delta_p \tag{3.62}$$

The above relation shows that compared to the open-circuit case, there is a uniform decrease in the short-circuit modal stiffness (squared natural frequencies) by an amount δ_p for all harmonics. Furthermore, as $\delta_p \mathbf{I}$ is proportional to the mass matrix, or the identity matrix, the mode shapes between these two operating states remain unchanged. To obtain the electromechanical coupling coefficients, substitute the analytical values for the open- and short-circuit, tuned natural frequencies into Eq. 2.8 such that

$$k_{\text{eff}}^{(h)^2} = \frac{\bar{\omega}_{0,oc}^{(h)^2} - \bar{\omega}_{0,sc}^{(h)^2}}{\bar{\omega}_{0,oc}^{(h)^2}} = \frac{\delta_p}{\bar{\omega}_{0,oc}^{(h)^2}} \tag{3.63}$$

62

or

$$
k_{\text{eff}}^{(h)^2} = \begin{cases} \delta_p, & h = 0 \\[2ex] \dfrac{\delta_p}{1+4\bar{k}_c}, & h = \dfrac{N_s}{2} \\[2ex] \dfrac{\delta_p}{1+2\bar{k}_c(1-\cos h\alpha)}, & \text{all other } h \end{cases} \tag{3.64}
$$

If, instead of all blades uniformly operating in one of the stiffness states, there is an arbitrary arrangement of blades operating in either stiffness states such that $\mathbf{S} \neq \mathbf{I}, \mathbf{0}$, the term $\mathbf{F}^t[\mathbf{I} - \mathbf{S}]\mathbf{F}$ appearing in $\tilde{\mathbf{K}}_0$ is, in general, no longer diagonal, thus resulting in the coupling of the various spatial harmonics; i.e., the blades no longer operate uniformly with an equal stiffness around the blisk, thus breaking the cyclic symmetry of the system, thus inducing a switch-dependent stiffness pattern capable of mistuning an otherwise tuned system. The coupling of the various harmonics for the mistuned blisk requires solving an eigenvalue problem to extract the mistuned natural frequencies and mode shapes, a topic covered in the following section.

As an example, consider a 13-sector system with parameters $\bar{k}_c = 0.02$ and $\delta_p = 0.05$. Table 3.1 shows the natural frequencies with all blades operating in either the open- or short-circuit states. As there is an odd number of blades, all harmonics occur in degenerate orthogonal pairs except for the 0ND harmonic. This table also shows the coupling coefficients for each mode evaluated using Eq. 3.64; these coefficients exhibit a slight decrease in coupling with increasing harmonic number; however, because $\bar{k}_c \ll 1$, this decrease is small and $k_{\text{eff}}^2 \approx \delta_p$ for all harmonics. Figure 3.2 shows the tuned mode shapes obtained from the columns of $\mathbf{F}$ (left plots) where the ordinate corresponds to the blade number. It also shows the magnitude of the Fourier components associated with each mode shape (right bar plots) where the ordinate corresponds to the spatial harmonic(nodal

diameter). The tuned mode shapes include only a single spatial harmonic (single nodal diameter) as evidenced by the presence of a single Fourier component for each shape.

3.2.1.2 Harmonic Response to Engine-Order Excitation

Although RFD is a transient approach, analyzing the limiting case of zero sweep, or harmonic excitation, can provide a fundamental understanding of the underlying forced-response dynamics. Assuming the engine-order excitation is harmonic and neglecting any initial conditions, the nondimensional force acting on the jth blade is

$$\bar{f}_j = e^{i\omega\bar{t}}e^{i\gamma_j} \tag{3.65}$$

Obtaining the cyclic components of the forcing vector requires applying the inverse Fourier transform to the force acting on each of the blades such that

$$
\begin{aligned}
\tilde{f}_m^{(0)} &= \frac{1}{\sqrt{N_s}} \sum_{j=0}^{N_s-1} \bar{f}_j \\
\tilde{f}_m^{(h,c)} &= \sqrt{\frac{2}{N_s}} \sum_{j=0}^{N_s-1} \cos(jh\alpha)\bar{f}_j \\
\tilde{f}_m^{(h,s)} &= \sqrt{\frac{2}{N_s}} \sum_{j=0}^{N_s-1} \sin(jh\alpha)\bar{f}_j \\
\tilde{f}_m^{(N_s/2)} &= \frac{1}{\sqrt{N_s}} \sum_{j=0}^{N_s-1} (-1)^j \bar{f}_j
\end{aligned}
\tag{3.66}
$$

Table 3.1: Natural frequencies of the tuned blisk.

Mode, r	Harmonic, h	Natural Frequency, $\bar{\omega}_r^2$		Coupling Coeff., $k_{\text{eff},r}^2$
		Open-Circuit	Short-Circuit	
1	0	1.000	0.975	0.050
2	1,c	1.023	0.977	0.050
3	1,s	1.023	0.977	0.050
4	2,c	1.009	0.984	0.049
5	2,s	1.009	0.984	0.049
6	3,c	1.017	0.993	0.048
7	3,s	1.017	0.993	0.048
8	4,c	1.027	1.002	0.047
9	4,s	1.027	1.002	0.047
10	5,c	1.034	1.010	0.047
11	5,s	1.034	1.010	0.047
12	6,c	1.039	1.014	0.046
13	6,s	1.039	1.014	0.046
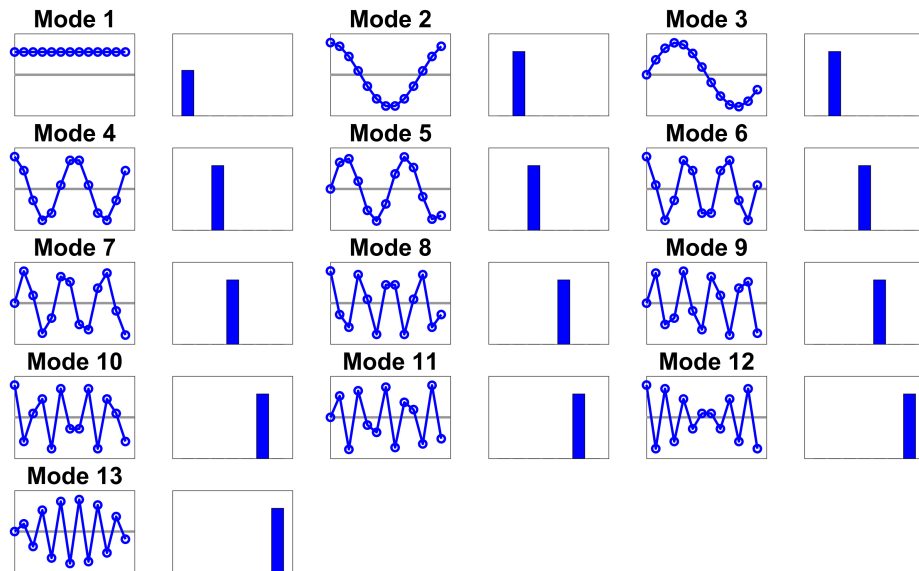
Figure 3.2: Unwrapped tuned-blisk mode shapes (left plots) where the ordinate corresponds to the blade number. Also shown is the magnitude of the Fourier components associated with each mode shape (right bar plots) where the ordinate corresponds to the spatial harmonic (nodal diameter).

A characteristic property of the tuned-blisk forced response is that the excitation only excites the modes with a harmonic number equal to the engine order due to orthogonality with all other harmonics (i.e., $\tilde{f}_m^{(h)} = 0$ if $h \neq n$). As such, the complex forced response of the jth blade is

$$\bar{H}_j^{(n)}(\bar{\omega}) = \frac{e^{ijn\alpha}}{\bar{\omega}_0^{(n)^2} - \bar{\omega}^2 + i2\zeta_0\bar{\omega}} \tag{3.67}$$

where $\omega_0^{(h)}$ is the tuned natural frequency for either the open- or short-circuit state derived previously. Although the numerator term $e^{ijh\alpha}$ indicates that the phase of the response is blade dependent, the magnitude is constant for all blades. As an example, consider again the blisk with parameters provided in the previous section with $\zeta_0 = 0.001$ and subjected to 3EO excitation. Figure 3.3 shows the frequency response of all blades of the tuned blisk in both the open- and short-circuit states. Only a single resonance exists at the natural frequencies of the 3ND mode pair corresponding to modes 6 and 7 shown in Table 3.1.
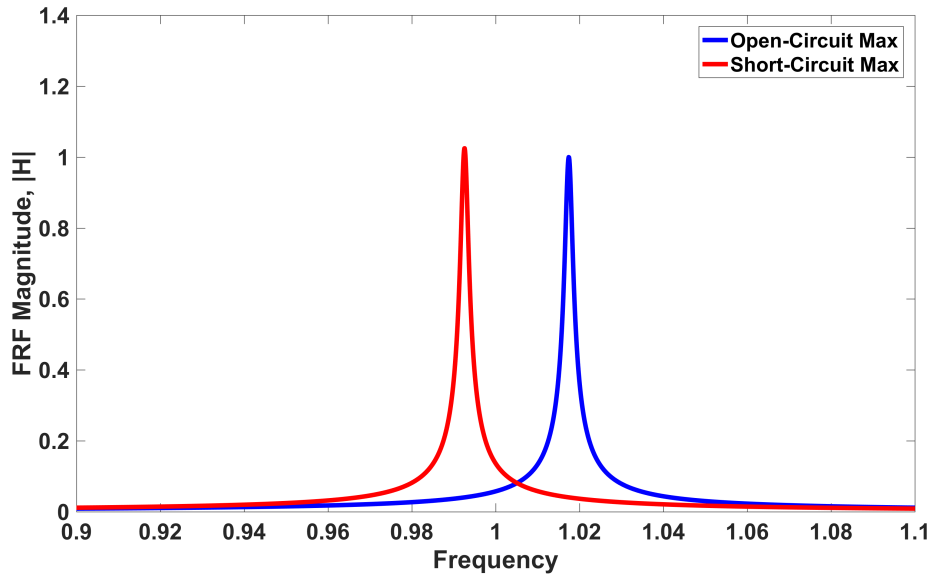
Figure 3.3: Frequency response of all blades of a tuned blisk subjected to 3EO excitation.

3.2.2 Mistuned System

3.2.2.1 Free Response Characteristics

Next, consider the mistuned system such that $\Delta\bar{\mathbf{K}}_{\mathbf{mis,oc}} \neq \mathbf{0}$. Again, neglecting the damping and external forces, the resulting unforced equations of motion in the cyclic domain are

$$\tilde{\mathbf{M}}\tilde{\mathbf{x}}'' + \tilde{\mathbf{K}}\tilde{\mathbf{x}} = \mathbf{0} \tag{3.68}$$

where $\tilde{\mathbf{K}}$ is the mistuned, cyclic stiffness matrix from Eq. 3.49 and rewritten here as

$$\tilde{\mathbf{K}} = \tilde{\mathbf{K}}_{\mathbf{0,oc}} + \mathbf{F}^t\Delta\bar{\mathbf{K}}_{\mathbf{mis,oc}}\mathbf{F} - \delta_p\mathbf{F}^t[\mathbf{I} - \mathbf{S}]\mathbf{F} \tag{3.69}$$

With all blades operating in the open-circuit state such that $\mathbf{S} = \mathbf{I}$, this equation reduces to

$$\tilde{\mathbf{M}}\tilde{\mathbf{x}}'' + \tilde{\mathbf{K}}_{\mathbf{oc}}\tilde{\mathbf{x}} = \mathbf{0} \tag{3.70}$$

where the open-circuit, mistuned cyclic stiffness matrix is

$$\tilde{\mathbf{K}}_{\mathbf{oc}} = \tilde{\mathbf{K}}_{\mathbf{0,oc}} + \mathbf{F}^t\Delta\bar{\mathbf{K}}_{\mathbf{mis,oc}}\mathbf{F} \tag{3.71}$$

Although $\tilde{\mathbf{K}}_{\mathbf{0,oc}}$ is diagonal, the matrix $\mathbf{F}^t\Delta\bar{\mathbf{K}}_{\mathbf{mis,oc}}\mathbf{F}$ is, in general, not diagonal, thus resulting in the coupling of the various spatial harmonics. As such, decoupling these equations requires solving

67

the eigenvalue problem

$$\left(\tilde{\mathbf{K}}_{\mathbf{oc}} - \lambda\tilde{\mathbf{M}}\right)\mathbf{P} = \mathbf{0} \tag{3.72}$$

where the eigenvalues correspond to the squared, open-circuit, mistuned natural frequencies ($\lambda_r = \omega_{\mathrm{oc},r}^2$). Also, assembling the associated eigenvectors ($\mathbf{P}_r$) column-wise produces the transformation matrix $\mathbf{P} = [\mathbf{P_1}, \cdots, \mathbf{P_{N_s}}]$. The mistuned-system mode shapes are then a linear combination of the tuned-system mode shapes

$$\mathbf{\Phi} = \mathbf{FP} \tag{3.73}$$

where $\mathbf{P_r}$ contains the associated weights for the rth mistuned mode. The above result indicates that the tuned mode shapes, containing a single spatial harmonic, form the basis of the mistuned mode shapes, that contain multiple spatial harmonics. Next, insert the transformation

$$\tilde{\mathbf{x}} = \mathbf{P}\boldsymbol{\eta} \tag{3.74}$$

into Eq. 3.68 and premultiply by $\mathbf{P}^t$ to obtain the modal equations of motion with respect to the open-circuit, mistuned system

$$\hat{\mathbf{M}}\boldsymbol{\eta}'' + \tilde{\mathbf{K}}\boldsymbol{\eta} = \mathbf{0} \tag{3.75}$$

where the modal mass matrix $\hat{\mathbf{M}}$ remains the $N_s \times N_s$ identity matrix. The mistuned modal stiffness matrix $\hat{\mathbf{K}}$ is

$$\hat{\mathbf{K}} = \hat{\mathbf{K}}_{\mathbf{oc}} - \delta_p\mathbf{\Phi}^t[\mathbf{I} - \mathbf{S}]\mathbf{\Phi} \tag{3.76}$$

where $\hat{\mathbf{K}}_{\mathbf{oc}}$ is the open-circuit, mistuned modal stiffness matrix that is diagonal where the components are the squared, open-circuit, mistuned natural frequencies:

$$\hat{\mathbf{K}}_{\mathbf{oc}} = \mathbf{diag}\left(\bar{\omega}_{\mathrm{oc},1}^2, \cdots, \bar{\omega}_{\mathrm{oc},N_s}^2\right) \tag{3.77}$$

When all blades operate in the short-circuit state such that $\mathbf{S} = \mathbf{0}$, Eq. 3.75 becomes

$$\hat{\mathbf{M}}\boldsymbol{\eta}'' + \hat{\mathbf{K}}_{\mathbf{sc}}\boldsymbol{\eta} = \mathbf{0} \tag{3.78}$$

where $\hat{\mathbf{K}}_{\mathbf{sc}}$ is the short-circuit, mistuned modal stiffness matrix that is also diagonal where the components are the squared, short-circuit, mistuned natural frequencies:

$$\hat{\mathbf{K}}_{\mathbf{sc}} = \mathbf{diag}\left(\bar{\omega}_{\mathrm{sc},1}^2, \cdots, \bar{\omega}_{\mathrm{sc},N_s}^2\right) \tag{3.79}$$

Similar to the tuned system, the short-circuit, mistuned natural frequencies relate to the open-circuit, mistuned natural frequencies by

$$\bar{\omega}_{\mathrm{sc},r}^2 = \bar{\omega}_{\mathrm{oc},r}^2 - \delta_p \tag{3.80}$$

resulting in the electromechanical coupling coefficients

$$k_{\mathrm{eff},r}^2 = \frac{\delta_p}{\bar{\omega}_{\mathrm{oc},r}^2} \tag{3.81}$$

69

Also similar to the tuned system, the mistuned mode shapes are identical in both the open-circuit and short-circuit operating states.

As an example, consider again the same blisk previously examined except with random stiffness perturbations generated using $\sigma_{\mathrm{mis}} = 0.03$. Table 3.2 shows the natural frequencies for both the open- and short-circuit cases. The mistuning splits the natural frequencies of all degenerate pairs of the tuned blisk. Also, similar to the tuned blisk, k_{eff}^2 decreases with increasing natural frequency. Figure 3.4 shows the mistuned mode shapes for each mode (left plots) where the ordinate corresponds to the blade number. This figure also shows the magnitude of the corresponding Fourier coefficients associated with each mode shape (right bar plots) where the ordinate corresponds to the spatial harmonic (nodal diameter). The various Fourier coefficients in each mistuned mode shape indicate that multiple spatial harmonics compose these shapes and these coefficients directly relate to the columns of $\mathbf{P}$. The mistuning also induces localized vibration for some of the modes (e.g., blades 10 and 11 in mode 1, blade 5 in mode 2, etc.)

3.2.2.2 Response to Harmonic Forcing

Next, consider the effects of the damping and applied force, the mistuned modal equations of motion are

$$\hat{\mathbf{M}}\boldsymbol{\eta}'' + \hat{\mathbf{C}}\boldsymbol{\eta}' + \hat{\mathbf{K}}\boldsymbol{\eta} = \hat{\mathbf{F}}_{\mathbf{m}} + \hat{\mathbf{F}}_{\mathbf{sw}} \tag{3.82}$$

Table 3.2: Natural frequencies of the mistuned blisk.

| Mode, r | Natural Frequency, $\bar{\omega}_r^2$ | | Coupling Coeff., $k_{\text{eff},r}^2$ |
	Open-Circuit	Short-Circuit	
1	0.990	0.964	0.051
2	0.990	0.965	0.051
3	1.003	0.978	0.050
4	1.008	0.983	0.049
5	1.016	0.991	0.048
6	1.021	0.996	0.047
7	1.030	1.005	0.047
8	1.033	1.008	0.047
9	1.038	1.014	0.046
10	1.042	1.018	0.046
11	1.045	1.020	0.046
12	1.050	1.026	0.045
13	1.065	1.041	0.044
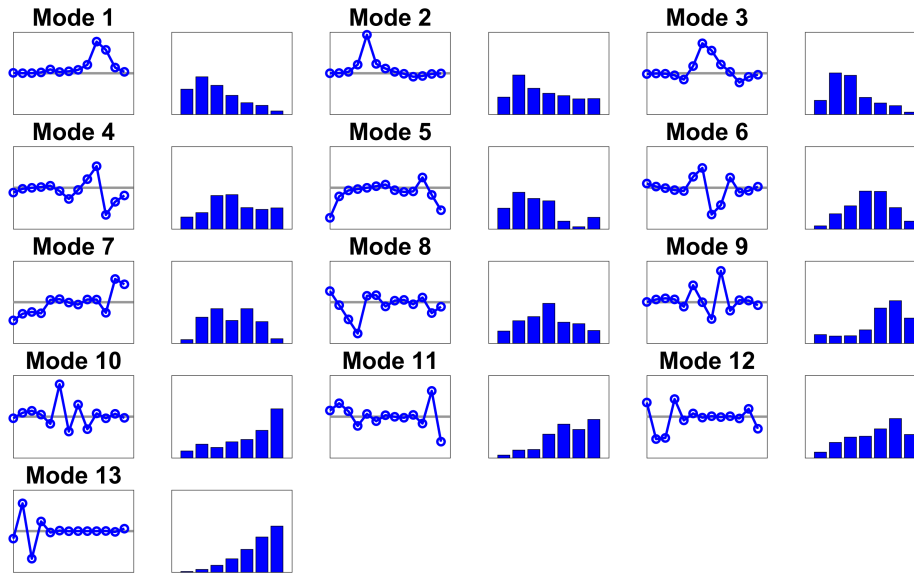
Figure 3.4: Unwrapped mistuned blade mode shapes (left plots) where the ordinate corresponds to the blade number. Also shown is the magnitude of the corresponding Fourier components associated with each mode shape (right bar plots) where the ordinate corresponds to the spatial harmonic (nodal diameter).

The corresponding modal matrices and force vectors are

$$\hat{\mathbf{M}} = \mathbf{I} \tag{3.83}$$

$$\hat{\mathbf{C}} = 2\zeta_0\mathbf{I} \tag{3.84}$$

$$\hat{\mathbf{K}} = \hat{\mathbf{K}}_{\mathbf{oc}} - \delta_p\mathbf{\Phi}^t[\mathbf{I} - \mathbf{S}]\mathbf{\Phi} \tag{3.85}$$

$$\hat{\mathbf{F}}_{\mathbf{m}} = \mathbf{P}^t\tilde{\mathbf{F}}_{\mathbf{m}} = \mathbf{\Phi}^t\mathbf{F}_{\mathbf{m}} \tag{3.86}$$

$$\hat{\mathbf{F}}_{\mathbf{sw}} = \mathbf{P}^t\tilde{\mathbf{F}}_{\mathbf{sw}}\mathbf{P} = \delta_p\mathbf{\Phi}^t\mathbf{S}\mathbf{\Phi}\boldsymbol{\eta}_{\mathbf{sw}} \tag{3.87}$$

In the tuned system, the only non-zero components of the cyclic force in Eq. 3.66 arise when the spatial harmonic equals the engine order. In the mistuned system, the premultiplication of $\tilde{\mathbf{F}}_{\mathbf{m}}$ by $\mathbf{P}^t$ enables a single engine order to excite all mistuned modes. As the columns of $\mathbf{P}$ directly relate to the Fourier components of each mistuned mode, the participation of each mistuned mode in the overall response directly depends on the magnitude of the Fourier coefficient associated with the spatial harmonic that equals the engine order. Neglecting any initial conditions, the complex frequency response of the jth blade is

$$\bar{H}_j(\bar{\omega}) = \sum_{r=1}^{N_s} \frac{\phi_{j,r}\sum_{j=0}^{N_s-1}\phi_{j,r}e^{i\gamma_j}}{\bar{\omega}_r^2 - \bar{\omega}^2 + i2\zeta_0\bar{\omega}} \tag{3.88}$$

As an example, consider again the blisk utilized previously. Figure 3.5 shows the frequency response of the mistuned blisk for both the open-circuit and short-circuit cases. The 3EO excitation now excites all modes because each mistuned mode shape contains many spatial harmonics, thus

inducing the region of high modal density. Furthermore, each of the blades respond with distinct magnitudes (light, thin curves) resulting in a larger maximum response of all blades (dark, thick curves) as compared to their respective tuned cases (dashed lines). Mode 8 contributes the largest response due to this mode containing the largest amount of 3ND content that matches the 3EO excitation.
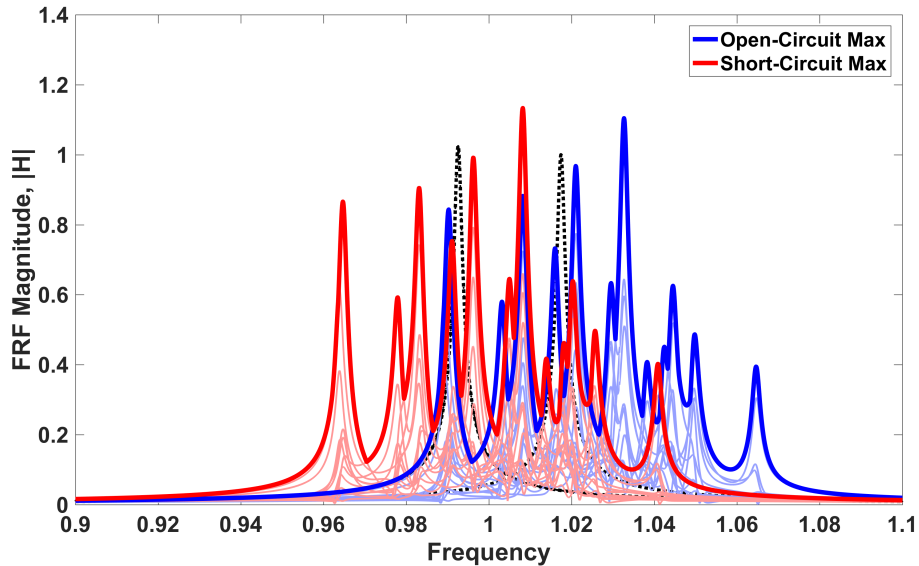
Figure 3.5: Frequency response magnitude of all blades of a mistuned blisk in the open-circuit (light blue) and short-circuit (light red) states. The thicker curves indicate the maximum blade response at each frequency line. Also shown is the tuned frequency response magnitudes (black dashed) for both stiffness states.

3.2.3 Response to Transient Excitation

The examples in the the preceding sections served to illustrate how regions of high modal density arise in the forced response of mistuned blisks. As RFD is a transient approach, this section considers the transient excitation with an idealized linear frequency sweep with constant amplitude.

This section also adapts a previously-derived, semi-analytical solution for use with swept excitation associated with a chosen engine order and when considering the switch-induced force. When solving for the response, numerical-integration schemes can lead to large computation times, particularly for large numbers of degrees of freedom or for slow sweeps due to the increased number of oscillations per resonance crossing. Fortunately, Markert and Seidler derived an analytical solution for a SDOF system subjected to swept excitation [77]. Analyzing RFD requires adapting their solution to a blisk subjected to engine-order excitation and begins with the forced modal equations of motion; for the rth mode, these equations are

$$\ddot{\eta}_r + 2\zeta_r \bar{\omega}_r \dot{\eta}_r + \bar{\omega}_r^2 \eta_r = \hat{f}_{m,r} + \hat{f}_{\text{sw},r} \tag{3.89}$$

where the mechanical modal force for the rth mode is

$$\hat{f}_{m,r} = \sum_{j=0}^{N_s-1} \phi_{j,r} \bar{f}_{m,j} \tag{3.90}$$

As such, $\hat{f}_{m,r}$ is a linear combination of swept sinusoidal waves with differing amplitudes and phases. An expression for this combination of sinusoidal waves represented as a single wave with amplitude $\hat{f}_{m,0,r}$ and phase Γ_r is

$$\hat{f}_{m,r} = \hat{f}_{m,0,r} \sin\left(\frac{1}{2}\bar{\omega}_{\text{rate}} t^2 + \bar{\omega}_0 \bar{t} + \Gamma_r\right) \tag{3.91}$$

where

$$\hat{f}_{m,0,r} = \sqrt{\left[\sum_{j=0}^{N_s-1} \phi_{j,r}\cos(\gamma_j)\right]^2 + \left[\sum_{j=0}^{N_s-1} \phi_{j,r}\sin(\gamma_j)\right]^2} \tag{3.92}$$

$$\Gamma_r = \tan^{-1}\left[\frac{\sum_{j=0}^{N_s-1} \phi_{j,r}\sin(\gamma_j)}{\sum_{j=0}^{N_s-1} \phi_{j,r}\cos(\gamma_j)}\right] \tag{3.93}$$

To stay consistent with the form of the equations derived in [77], scale the already nondimensional time such that

$$\check{t}_r = \bar{\omega}_r(\bar{t} - \bar{t}_0) \tag{3.94}$$

where $\check{(\,)}$ corresponds to a scaled variable. The quantity $\bar{t}_0$ is the initial time of operation in a particular stiffness state. For example, $\bar{t}_0 = 0$ at start-up with all blades operating in the open-circuit state, and $\bar{t}_0 = \bar{t}_{sw}$ following any switch to a separate stiffness state. The scaled phase of excitation is

$$\check{\phi}_r(\check{t}_r) = \frac{1}{2}\check{\omega}_{\mathrm{rate},r}\check{t}_r^2 + \check{\omega}_{0,r}\check{t}_r + \check{\Gamma}_r \tag{3.95}$$

where

$$\check{\omega}_{\mathrm{rate},r} = \frac{\bar{\omega}_{\mathrm{rate}}}{\bar{\omega}_r^2} \tag{3.96}$$

$$\check{\omega}_{0,r} = \frac{\bar{\omega}_{\mathrm{rate}}\bar{t}_0 + \bar{\omega}_0}{\bar{\omega}_r} \tag{3.97}$$

$$\check{\Gamma}_r = (\frac{1}{2}\bar{\omega}_{\mathrm{rate}}\bar{t}_0^2 + \bar{\omega}_0\bar{t}_0 + \Gamma_r) \tag{3.98}$$

and the scaled modal displacement is

$$\check{\eta}_r = \frac{\bar{\omega}_r^2}{\hat{f}_{m,0,r}} \eta_r \tag{3.99}$$

The resulting scaled modal equation of motion is

$$\mathring{\check{\eta}}_r + 2\zeta_r \mathring{\check{\eta}}_r + \check{\eta}_r = \sin\bar{\varphi}(\bar{t}_r) + \bar{f}_{sw,r} \tag{3.100}$$

where $\mathring{()}$ denotes a derivative with respect to the scaled time. The response for these equations of motion is a superposition of three solutions:

$$\check{\eta}_r = \check{\eta}_{c,r} + \check{\eta}_{p1,r} + \check{\eta}_{p2,r} \tag{3.101}$$

where $\check{\eta}_{c,r}$ is the complementary solution of the homogenous form of the modal equation

$$\check{\eta}_{c,r} = c_1 e^{\lambda_{1,r}\check{t}_r} + c_2 e^{\lambda_{2,r}\check{t}_r} \tag{3.102}$$

where λ_1 and λ_2 are the scaled eigenvalues for the rth mode such that $\lambda_{1,2} = -\zeta_r \pm \sqrt{1-\zeta_r^2}$; the constants c_1 and c_2 are determined from the initial conditions. Additionally, $\check{\eta}_{p1,r}$ is the particular solution for the swept excitation obtained from

$$\check{\eta}_{p1,r} = \frac{1}{\sqrt{1-\zeta_r^2}} \int_0^{\check{t}_r} \sin\check{\varphi}_r(\check{t}_r) e^{-\zeta_r(\check{t}_r-\tau)} \sin\sqrt{1-\zeta_r^2}(\check{t}_r-\tau)\mathrm{d}\tau \tag{3.103}$$

and $\check{\eta}_{p2,r}$ is the particular solution for the constant force induced by the switch from the short- to open-circuit state obtained from

$$\check{\eta}_{p2,r} = \frac{1}{\sqrt{1-\zeta_r^2}} \int_0^{\check{t}_r} \check{f}_{\mathrm{sw},r} e^{-\zeta_r(\check{t}_r-\tau)} \sin\sqrt{1-\zeta_r^2}(\check{t}_r-\tau)\mathrm{d}\tau \qquad (3.104)$$

The entirety of the steps required to obtain these solutions is omitted here for brevity. However, the derivation for the solution to the swept excitation that includes the initial conditions can be found in [77]; the solution to the constant forcing term can be found in typical textbooks on mechanical vibrations. As such, the scaled modal response is

$$\check{\eta}_r = |\check{N}_r(\check{t}_r)| \sin[\check{\phi}_r(\check{t}_r) + \check{\beta}_r(\check{t}_r)] + \check{f}_{\mathrm{sw}}\left[1 - \frac{e^{-\zeta_r\check{t}_r}}{\sqrt{1-\zeta_r^2}} \sin\left[\sqrt{1-\zeta_r^2}\check{t}_r + \tan^{-1}\left(\frac{\sqrt{1-\zeta_r^2}}{\zeta_r}\right)\right]\right] \qquad (3.105)$$

where $\check{N}_r(\check{t}_r)$ is a complex amplitude and $\check{\beta}_r(\check{t}_r)$ is the phase difference between the response and excitation. Note here that the first term on the right-hand-side takes a similar form as that of harmonic excitation; however, the present case shows a time dependency for both the magnitude and phase components.

Continuing with the previous mistuned blisk example, Fig. 3.6 shows the transient response generated from 3EO excitation for an increasing sweep rate and with all blades operating in the open-circuit state. Each curve corresponds to the maximum response of the set of blades at each time instant. For this case, sweeping through the resonance crossings delays the maximum response peaks past the harmonic resonance, causing the peaks to both broaden and decrease in amplitude. As the sweep rate slows, the maximum blade response approaches that of harmonic

excitation. For rapid sweeps, the excitation quickly passes through resonance, thus generating little vibration. Although not shown here, i some situations, sweeping through the closely-spaced modes of a mistuned blisk can result in an amplification of the maximum blisk response that is larger than the harmonic case. This effect arises due to a superposition of each modal response of the closely-space modes and has been observed in both numerical and experimental tests [78, 79].
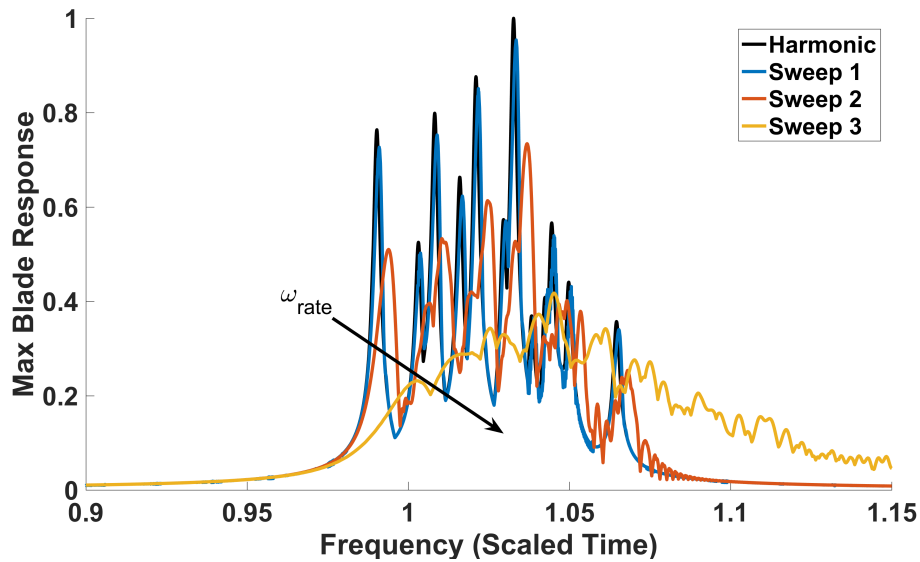
Figure 3.6: The effect of an increasing sweep rate on the maximum blisk response with all blades operating in the open-circuit state. Also shown is the limiting case of harmonic excitation, or zero sweep rate.

Using the solution obtained by numerical integration as a point of comparison can offer validation for the implementation of the solution as developed here. This solution utilizes MATLAB's built-in *ode45* function that uses an explicit Runge-Kutta formulation; using this function requires casting the equations of motion in Eq. 3.31 into first-order form. Defining the states as $\mathbf{y_1} = \mathbf{x}$ and

$\mathbf{y_2} = \mathbf{x}'$, the first-order equations of motion are

$$\begin{Bmatrix} \mathbf{y}'_1 \\ \mathbf{y}'_2 \end{Bmatrix} = \begin{bmatrix} \mathbf{0} & \mathbf{I} \\ -\bar{\mathbf{M}}^{-1}\bar{\mathbf{K}} & -\bar{\mathbf{M}}^{-1}\bar{\mathbf{C}} \end{bmatrix} \begin{Bmatrix} \mathbf{y}_1 \\ \mathbf{y}_2 \end{Bmatrix} + \begin{Bmatrix} \mathbf{0} \\ \bar{\mathbf{M}}^{-1}(\bar{\mathbf{F}}_\mathbf{m} + \bar{\mathbf{F}}_\mathbf{sw}) \end{Bmatrix} \qquad (3.106)$$

Continuing with the previous example system, Fig. 3.7 shows the time response of all blades of the blisk subjected to 3EO excitation with $\bar{\omega}_{\text{rate}} = 10^{-6}$. The piezoelectric elements on all of the blades initially begin in the open-circuit state, then followed by three switches: 1) the first switch occurs at $\bar{\omega}_{\text{sw},1} = 0.98$ to the short-circuit state, 2) the second switch occurs at $\bar{\omega}_{\text{sw},2} = 1.01$ returning to the open-circuit state, and 3) the final switch occurs at $\bar{\omega}_{\text{sw},3} = 1.04$ again returning to the short-circuit state. Figure 3.7 shows these three separate switches as vertical lines in each time response. This figure from the developed solution (red) superposed on the response obtained from MATLAB's *ode45* solver (black). The solutions are nearly identical, thus validating the implementation of the solution developed here. Furthermore, both simulations were performed using a personal computer with a 3.40 GHz Intel Core i7 processor with 8.00 GB of RAM. The total computation time using MATLAB's *ode45* solver was 133.803 s, while the computation time using the developed analytical solution was an order of magnitude less at 12.194 s. As the analytical solution significantly reduces the computational expense while offering similar accuracy, this is the chosen solution henceforth.
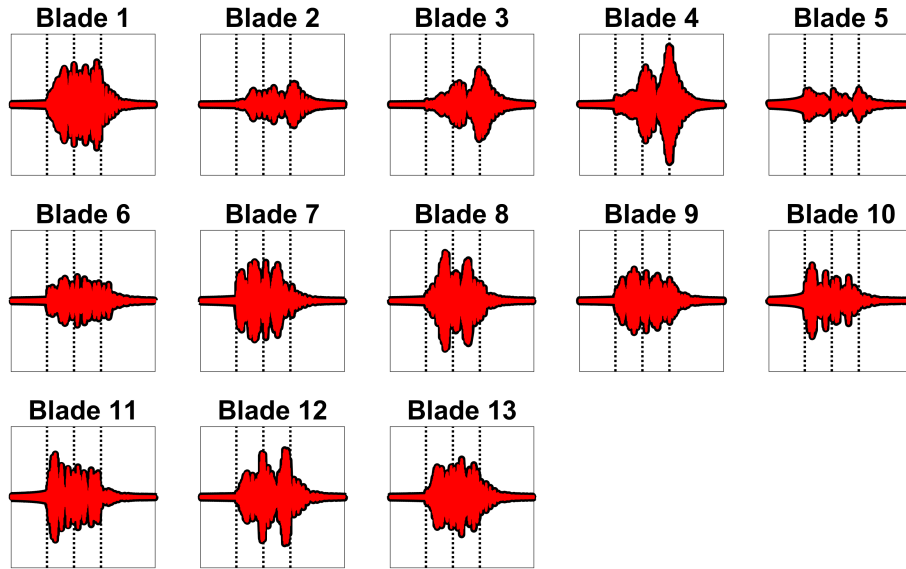
Figure 3.7: Comparison between the time responses of each blade obtained using MATLAB's *ode45* solver (black curves) and the developed solution (red curves). These plots also show the three arbitrarily chosen switch triggers (vertical dashed lines)

CHAPTER 4
VIBRATION REDUCTION VIA RESONANCE FREQUENCY

DETUNING

This chapter presents the RFD concept as applied to the lumped-parameter model. Section 4.1 discusses the identification of the optimal sets of switch triggers that optimize RFD vibration reduction performance. It begins with an analytical determination of the optimal triggers for the limiting case of harmonic excitation. It also presents the optimization procedure used to identify the optimal triggers when considering transient excitation. Section 4.2 presents the results of Monte Carlo simulations used to identify general trends for various design parameters.

4.1   Optimal Trigger Identification

The performance of RFD depends largely on when the switch between stiffness states initiates. When considering a mistuned system, RFD may require multiple switches to avoid the increased number of resonance peaks present in the forced response. As such, identification of these optimal switch triggers is paramount to RFD's success.

4.1.1 Limiting Case of Harmonic Excitation

Although RFD is a transient approach, the limiting of harmonic excitation, or zero sweep rate, offers fundamental insight into the identification of the optimal trigger sets. The analysis presented here considers three separate cases: 1) a tuned blisk, 2) a mistuned blisk with decoupled blades, and 3) a mistuned blisk that includes the interblade coupling.

4.1.1.1 Tuned Blisk

Consider first the case of a tuned blisk. As derived previously and shown in Eq. 3.67, the frequency response magnitudes for nEO excitation and with all blades operating in either the open- or short-circuit states are

$$|\bar{H}_{\text{oc}}| = \frac{1}{\sqrt{\left\{[1 + 2\bar{k}_c(1 - \cos n\alpha)] - \bar{\omega}^2\right\}^2 + (2\zeta_0\bar{\omega})^2}} \tag{4.1}$$

$$|\bar{H}_{\text{sc}}| = \frac{1}{\sqrt{\left\{[1 + 2\bar{k}_c(1 - \cos n\alpha)] - \delta_p - \bar{\omega}^2\right\}^2 + (2\zeta_0\bar{\omega})^2}} \tag{4.2}$$

In this case, the optimal switch triggers minimize the maximum blisk response. Similar to the SDOF case, there is only a single optimal trigger $\bar{\omega}_{\text{sw}}^*$ and it corresponds to the frequency where both the OC and SC response magnitudes intersect [80, 14]. Equating these response magnitudes

and solving for the frequency results in

$$\bar{\omega}_{sw}^* = \sqrt{[1 + 2\bar{k}_c(1 - \cos n\alpha)] - \frac{1}{2}\delta_p} \qquad (4.3)$$

where $\bar{\omega}_{sw}^*$ is a function of the coupling stiffness, the excitation order, and the amount of electromechanical coupling. Inserting $\bar{\omega}_{sw}^*$ back into Eq. 4.1 results in the optimal response magnitude

$$|\bar{H}^*| = \frac{2}{\sqrt{\delta_p^2 + 8\zeta_0^2\{2[1 + 2\bar{k}_c(1 - \cos n\alpha)] - \delta_p\}}} \qquad (4.4)$$

Typical δ_p values are on the order of 1% (i.e., $\delta_p \ll 2[1 + 2\bar{k}_c(1 - \cos n\alpha)]$) and there is light coupling between blades, (i.e., $\bar{k}_c \ll 1$). As such, the approximate response magnitude is

$$|\bar{H}^*| \approx \frac{2}{\sqrt{\delta_p^2 + 16\zeta_0^2}} \qquad (4.5)$$

For heavily damped blisks with minimal electromechanical coupling (i.e., $\zeta_0 \gg \delta_p$), the response magnitude is

$$|\bar{H}^*| \approx \frac{1}{2\zeta_0^2} \qquad (4.6)$$

Monolithic blisks, however, are typically lightly damped such that $\delta_p \gg \zeta_0$, and the response magnitude is

$$|\bar{H}^*| \approx \frac{2}{\delta_p} \qquad (4.7)$$

One measure of RFD performance is the amount of reduced vibration relative to the baseline case with no switching. As such, normalize the optimal RFD response with respect to the case when all blades operate in the OC state where, at resonance, the maximum response is $|\bar{H}_{\text{oc}}|_{\max} \approx 1/2\zeta_0$. The vibration reduction provided by RFD is then

$$\bar{H}_{\text{norm}}^* \approx \frac{4\zeta_0}{\delta_p} \tag{4.8}$$

The above equation shows that for a tuned blisk, RFD provides the most benefit for blisks with light damping and large electromechanical coupling. As δ_p increases, the short-circuit peak increasingly shifts away from the open-circuit peak, resulting in the earlier application of the optimal switch and a reduced peak magnitude.

As an example, Fig. 4.1 shows the response magnitudes of a tuned system subjected to nEO excitation. The open- and short-circuit peaks occur at frequencies defined by Eqs. 3.58 and 3.62 when $h = n$. This figure also shows the optimal response magnitude obtained by switching all blades' stiffness in accordance with Eq. 4.3. As the excitation frequency increases, the blades initially operate in the open-circuit state until $\bar{\omega}_{\text{sw}}^*$ when there is a trigger that initiates the switch to the short-circuit. As Eq. 4.8 predicts, there is a 92% reduction in the response compared to the un-switched, open-circuit baseline.
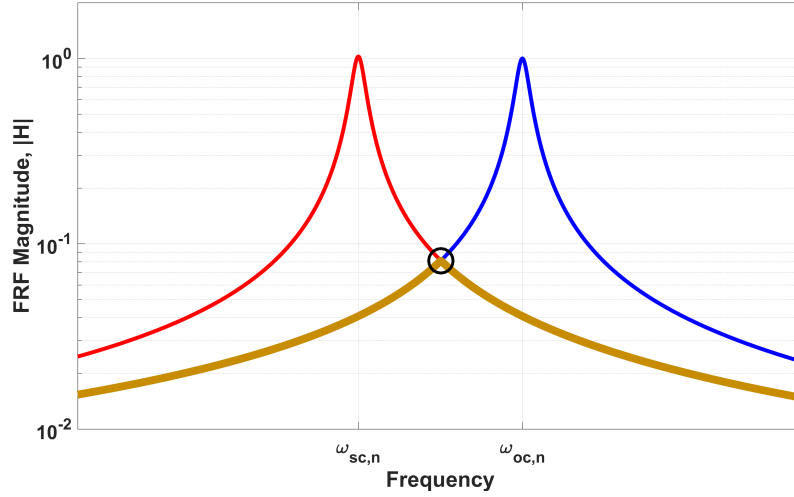
Figure 4.1: Example of RFD applied to a tuned system subjected to harmonic excitation. This figure shows the open-circuit response (blue), short-circuit response (red), and the optimal response (gold), as well as the optimal switch and corresponding maximum magnitude (black circle).

4.1.1.2 Mistuned Blisk with Decoupled Blades

Next, consider the case of a mistuned blisk with each blade decoupled from the neighboring blades such that $\bar{k}_c = 0$. Due to the mistuning, each blade has separate and distinct natural frequencies such that the jth blade's open- and short-circuit natural frequencies are $\bar{\omega}_{\text{oc},j}^2 = 1 + \delta_{\text{mis},j}$ and $\bar{\omega}_{\text{sc},j}^2 = 1 + \delta_{\text{mis},j} - \delta_p$, respectively. As such, the resulting response magnitudes in the frequency domain for the jth blade operating in either the open- or short-circuit state is

$$|\bar{H}_{\text{oc},j}| = \frac{1}{\sqrt{\left\{1 + \delta_{\text{mis},j} - \bar{\omega}^2\right\}^2 + (2\zeta_0\bar{\omega})^2}} \tag{4.9}$$

$$|\bar{H}_{\text{sc},j}| = \frac{1}{\sqrt{\left\{1 + \delta_{\text{mis},j} - \delta_p - \bar{\omega}^2\right\}^2 + (2\zeta_0\bar{\omega})^2}} \tag{4.10}$$

Using a similar procedure as with the tuned system, the optimal switch for the jth blade is

$$\bar{\omega}^*_{\text{sw},j} = \sqrt{1 + \delta_{\text{mis},j} - \frac{1}{2}\delta_p} \qquad (4.11)$$

As both $\delta_{\text{mis},j}$ and δ_p are small, the first-order approximation of this square root is

$$\bar{\omega}^*_{\text{sw},j} \approx 1 + \frac{1}{2}\delta_{\text{mis},j} - \frac{1}{4}\delta_p \qquad (4.12)$$

and varies linearly with the mistuning. The corresponding optimal response magnitude for the jth blade is

$$|\bar{H}^*_j| = \frac{2}{\sqrt{\delta_p^2 + 8\zeta_0^2\{2(1 + \delta_{\text{mis},j}) - \delta_p\}}} \qquad (4.13)$$

Using the assumption $\delta_p \gg \zeta_0$, the optimal response is

$$|\bar{H}^*_j| \approx \frac{2}{\delta_p} \qquad (4.14)$$

and the optimal response normalized by the maximum open-circuit response is

$$|\bar{H}^*_{\text{norm},j}| \approx \frac{4\zeta_0}{\delta_p} \qquad (4.15)$$

Similar to the tuned blisk, the jth blade's optimal switch and corresponding response magnitude are functions of δ_p. In the tuned system, however, the optimal trigger for all blades occurs at the

same frequency, whereas the optimal triggers for the mistuned blisk with decoupled blades are blade dependent and must account for the mistuning present in the blades.
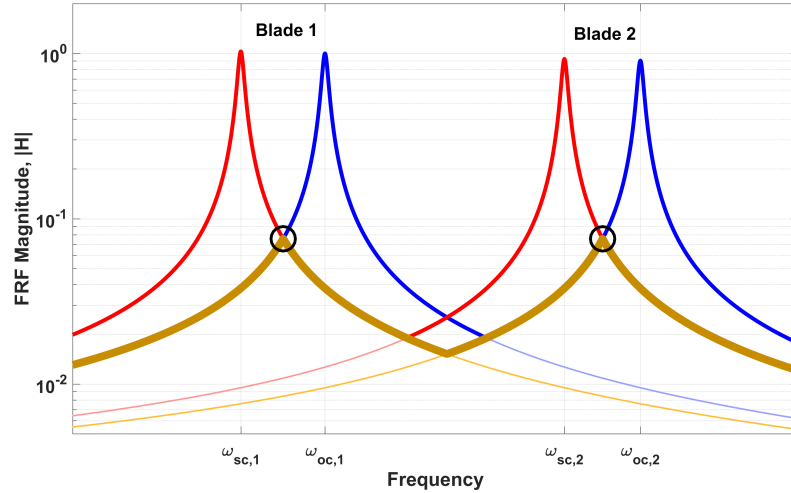
Figure 4.2: Example of RFD applied to a mistuned system with two decoupled blades and subjected to harmonic excitation. This figure shows the open-circuit response (blue), short-circuit response (red), and the optimal response (gold), as well as the optimal switch and corresponding maximum magnitude (black circles) for each blade. This figure also shows the response for each blade (light, thin curves) and the maximum response of either blade (dark, thick curves) at each frequency line.

As an example, Fig. 4.2 shows the frequency response of a mistuned blisk with two decoupled blades and subjected to harmonic excitation. The first pair of peaks corresponds to the 1st blade with the lower stiffness, and the second pair of peaks corresponds to the 2nd blade with the higher stiffness. This figure also shows the optimal response magnitude obtained by switching each blade's stiffness state at the intersection of the respective open- and short-circuit response magnitudes, as defined in Eq. 4.11. As the excitation frequency increases, each blade initially operates in the open-circuit state. Upon reaching $\omega_{sw,1}$, a trigger initiates the switch to the short-circuit state for the 1st blade. As the excitation frequency increases further, the second blade continues to operate in the open-circuit state. Upon reaching $\omega_{sw,2}$, a trigger initiates the switch to the short-circuit

state for the 2nd blade. As Eq. 4.15 predicts, there is a 92% reduction in the response of both blades compared to the un-switched, open-circuit baseline.

4.1.1.3   Mistuned Blisks Including the Interblade Coupling

As the two preceding sections show, the tuned system requires only one trigger application for all blades simultaneously, while the system with decoupled blades requires a blade-dependent trigger application for the N_s blades. In both these limiting cases, each blade will only experience a single resonance; however, when considering the effects of both the interblade coupling and the mistuning, the system behaves within these two limiting cases. For example, for blisks where the mistuning strength is small with respect to the interblade coupling (i.e., $\sigma_{mis} \ll \bar{k}_c$), the presence of the mistuning acts as a small perturbation to the tuned system; whereas for blisks where the mistuning strength is large with respect to the interblade coupling (i.e., $\sigma_{mis} \gg \bar{k}_c$), the presence of the mistuning acts as a small perturbation to the mistuned system with decoupled blades [81, 82]. As Fig. 3.5 showed previously, this combination of the interblade coupling with the mistuning will induce multiple resonances experienced by each blade, with each resonance occurring at the mistuned blisk's natural frequencies. As the blades experience each resonance simultaneously, RFD can reduce vibration by switching each blade's stiffness simultaneously.

The task then remains to identify the optimal set of switch triggers to reduce vibration for the mistuned blisks and requires the defining an appropriate objective function to optimize. For many vibration reduction approaches, the primary goal is to reduce the maximum response of the entire

blade set; however, solely focusing on reducing this maximum response potentially ignores other resonance peaks that may appreciably contribute to the total response. As such, a secondary goal is to reduce the total area under the response envelope curves to target these less-salient resonances. Considering these two goals, the objective function J that RFD seeks to minimize is

$$J = w_1 \frac{|\bar{X}_{\max}|}{|\bar{X}_{\text{oc,max}}|} + w_2 \frac{\sum_{j=0}^{N_s-1} \int_{t_1}^{t_2} |\bar{X}_j| \mathrm{d}t}{\sum_{j=0}^{N_s-1} \int_{t_1}^{t_2} |\bar{X}_{\text{oc},j}| \mathrm{d}t} \tag{4.16}$$

where w_i are the user-defined weights used to control the relative importance of the two objectives.

As an example, consider again the same 2-DOF system used in the two preceding sections with $\bar{k}_c = 0.02$, $\delta_{\text{mis},1} = -0.05$, and $\delta_{\text{mis},2} = 0.05$. Figure 4.3a shows the response envelopes for each blade with the system operating in either the open- or short-circuit state. As the excitation sweeps up in frequency, RFD requires three application of three triggers to minimize J: 1) the blades initially operate in the open-circuit state, then switch to the short-circuit state to avoid the first open-circuit resonance; 2) the blades operate in the short-circuit state, then switch to the open-circuit state to avoid the second short-circuit resonance; and 3) the blades operate in the open-circuit state, then switch to the short-circuit state to avoid the final open-circuit peak. Employing an exhaustive-search strategy to test all various combinations of triggers enables the identification of the optimal set. Figure 4.3b shows the objective function for each combination of the three triggers. The dark blue region corresponds to the optimal set of triggers that, for this system, corresponds to $\bar{\omega}_{\text{sw},1} = 0.979$, $\bar{\omega}_{\text{sw},2} = 1.001$, and $\bar{\omega}_{\text{sw},3} = 1.039$; though, there are other sets of switches that also offer excellent performance. Figure 4.3a also shows this optimal response with the vertical lines

indicating the frequencies of the optimal triggers. The optimal response shows a 91.2% reduction of the maximum response peak, as well reductions in the smaller peaks associated with the first resonance.

Figure 4.4 shows the effects that the mistuning has on the optimal system response and optimal switch triggers for the same 2-DOF system, but with the mistuning magnitude ranging from $\delta_{m,1} = [-0.15, 0]$ for the 1$^\text{th}$ blade, and $\delta_{m,2} = [0, 0.15]$ for the 2$^\text{nd}$ blade. Each figure shows quantities corresponding to the optimal trigger obtained when considering only a single switch from the open- to short-circuit state, as well as the optimal triggers obtained when considering multiple switches, as in the example shown in Fig. 4.3.

Figure 4.4a shows the influence of the mistuning strength on the optimal triggers and only shows the triggers that initiate the switch from the open- to short-circuit state, and not vice versa. When the mistuning is small, there is only a single resonance peak in either the open- or short-circuit states. As such, the optimal triggers converge to the tuned-system trigger predicted in Eq. 4.3. As the mistuning magnitude increases, multiple resonance peaks appear in the response and requires multiple switches to reduce vibration. These optimal triggers branch out to track the optimal triggers identified for the mistuned blisk with the decoupled blades that vary linearly as predicted in Eq. 4.12. When considering only a single trigger, the optimal curve tracks the top curve corresponding to the switch used to avoid the second pair of resonance peaks. This occurs due to the second open-circuit resonance peak exhibiting a larger magnitude than the first.

Figures 4.4b and 4.4c show the maximum peak response for the entire blade set as well as the total area under all response envelope curves, the two components making up J in Eq. 4.16. Both

of these figures show quantities normalized by the quantities obtained for the open-circuit, tuned system. For small mistuning strengths, the optimal response obtained when considering both a single trigger, or multiple triggers, converges to a single value corresponding to the tuned-system optimal response. As the mistuning increases, the optimal response obtained when considering multiple triggers remains relatively constant; however, the optimal response obtained when considering a single trigger diverges and performance deteriorates as the single trigger can only reduce vibration for a single resonance peak.
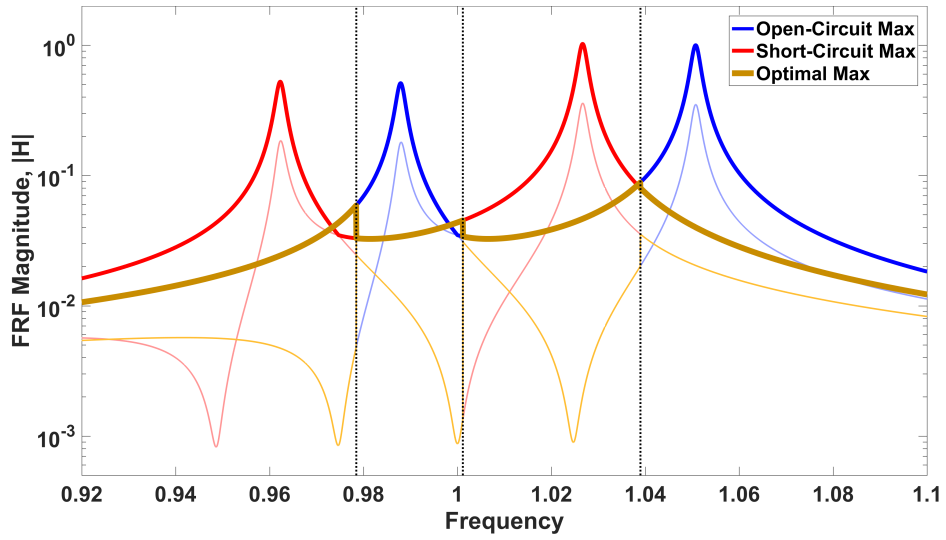
(a) Maximum response envelopes with vertical lines indicating the frequencies of the three optimal switches.
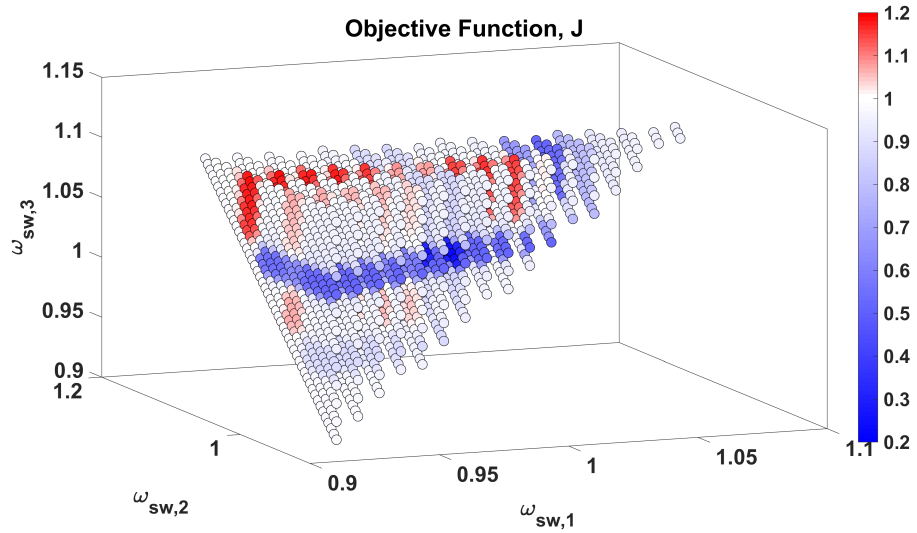
(b) Optimization function for each combination of switches.

Figure 4.3: Example of RFD applied to a mistuned 2-DOF system.
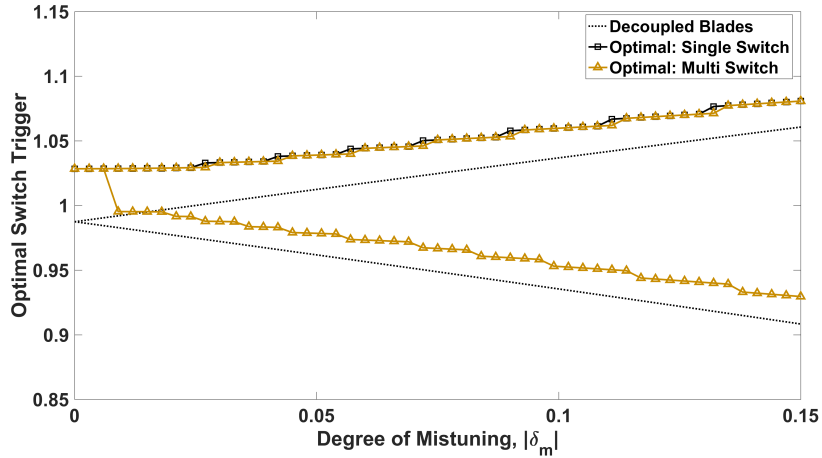
(a) Optimal switch triggers.
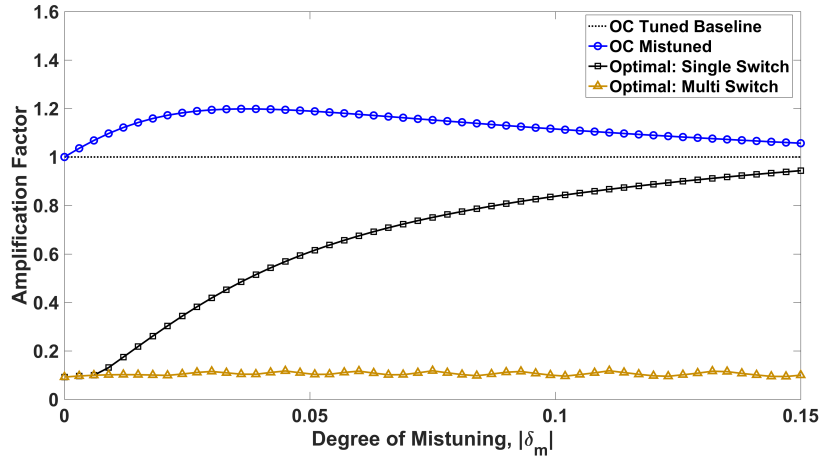
(b) Amplification factor.
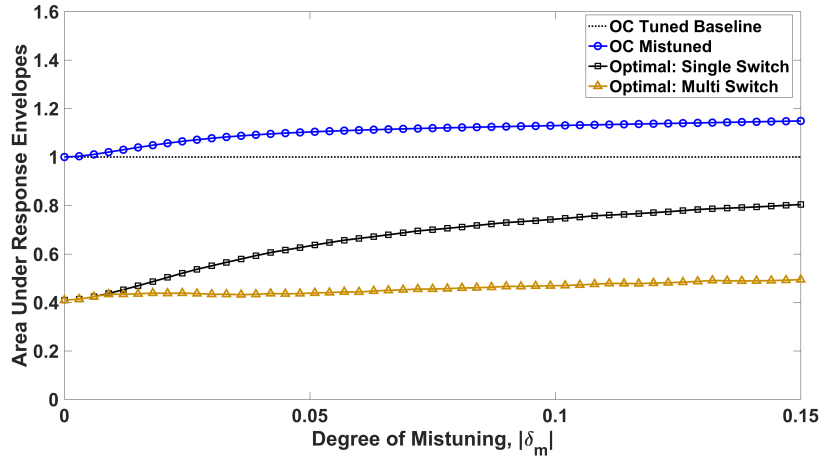
(c) Total area under response envelope curves.

Figure 4.4: The effects of mistuning strength for the 2-DOF mistuned system.

4.1.2 Optimal Trigger Identification for Transient Excitation

As the preceding section showed, a 2-sector mistuned blisk subjected to harmonic excitation required three switches to maximize RFD performance. In general, an N_s-sector blisk may require up to $2N_s - 1$ switches to maximize RFD performance. Furthermore, solving for the response from a linearly varying excitation requires numerically computing the complex error function to determine the time-dependent magnitude and phase components in Eq. 3.105, thus significantly increasing the computational expense compared to the harmonic case. As such, the exhaustive-search strategy employed in the previous example with harmonic excitation is not feasible for identification of the optimal triggers for blisks with many sectors and subjected to transient excitation. Rather, this analysis incorporates a more computationally efficient optimization procedure to more rapidly identify these optimal triggers.

The optimization procedure used here is the genetic algorithm. Darwin's theory of evolution forms the basis of this algorithm by simulating a natural selection process to produce the most fit solution from a population of candidate solutions. During each iteration, or generation, the candidate solutions are chosen for mating using a probabilistic approach and based on a measure of their fitness. As such, the solutions with the best fitness have the greatest chance to pass on their genes to the subsequent generation via application of genetic operators such as genetic crossover and mutation. Over numerous generations, the natural selection process increases the total fitness of the population, while simultaneously producing the most fit solution that ideally corresponds to the problem's global optimum.

As applied here, the candidate solutions contain the real-valued switch triggers as their genetic code. The process begins by randomly generating a total of N_{pop} initial candidates with switch triggers falling within user-defined upper and lower limits, $\bar{\omega}_{sw,U}$ and $\bar{\omega}_{sw,L}$, and generated in ascending order. After generating this initial population, each candidate's fitness is measured by evaluating a fitness function that corresponds to the inverse of the objective function defined in Eq. 4.16, or $1/J$. As such, the most fit individuals correspond to the individuals that offer the greatest vibration reduction performance. A tournament selection process then chooses the individual candidates for mating. After selecting two candidates in this manner, the candidates mate and perform a genetic crossover at a probability of P_{cross}. This analysis uses an arithmetic crossover to ensure that each offspring contains switch triggers that fall within the previously defined upper and lower limits. [83] Each gene will then mutate at a probability of P_{mut} with the mutated gene replaced by a randomly chosen switch trigger within the previously defined limits. The process iterates over a total of N_{gen}, or until satisfying a specified threshold.

As an example of the switch-trigger optimization procedure, consider again the 13-sector mistuned blisk previously discussed in Chapter 3 and with 6EO excitation sweeping through at $\bar{\omega}_{rate} = 10^{-5}$. The parameters used in the genetic algorithm are $N_{pop} = 50$, $N_{gen} = 50$, $P_{cross} = 0.80$, and $P_{mut} = 0.05$. To verify the implementation of the genetic algorithm, Fig. 4.5 shows the optimization results when considering only a single trigger. Figure 4.5a shows that the mean objective function for the entire population shows an immediate decrease and stabilizes near the optimal solution of $J_{opt} = 0.677$ within the first three generations. The resulting optimal trigger is $\bar{\omega}_{sw,opt} = 1.041$. Figure 4.5b shows the objective function obtained when employing the

exhaustive-search strategy to test a range of switch triggers between $\bar{\omega}_{\mathrm{sw}} = [0.92, 1.11]$. There is a clear minimum corresponding to the optimal trigger at $\bar{\omega}_{\mathrm{sw,opt}} = 1.041$ showing agreement with the optimal trigger obtained from the genetic algorithm. Figure 4.5c shows the response envelopes for the open-circuit, short-circuit, and optimal cases. In the short-circuit case, the second largest peak occurs at a frequency near the largest open-circuit peak. Consequently, although RFD reduces the maximum peak by 32.8%, these overlapping modes limit the performance.

Continuing with the previous example, Figure 4.6 shows the optimization results when considering $2N_s - 1$ switches. Figure 4.6a shows an overall decreasing trend for the mean objective function with each successive generation that begins to stabilize by the 15$^{\text{th}}$ generation. Furthermore, the optimal solution converges to $J_{\mathrm{opt}} = 0.529$, a 21.9% improvement when compared to the case of a single trigger. Figure 4.6b shows the response envelopes for the open-circuit, short-circuit, and optimal cases. Interestingly, the optimal switch triggers cluster near the largest open-circuit peak and further decreases the maximum response peak compared to the case of a single trigger. This trigger clustering shows noticeable increases in RFD performance in the event that open- and short-circuit resonances overlap. This seemingly promising result may arise since in these two stiffness states, the overlapping resonance frequencies will have different operating deflection shapes. As such, the near-periodic switching between these two states does not allow the response to reach a steady-state condition in any one state before undergoing a switch to the opposing state. Note here that this not the same effect as the synchronized-switch damping approaches discussed in the Section 2.2.5 that must switch synchronously with the system deflection (four times per vibration

cycle). Instead, the approach identified here can switch at any point in the vibration cycle at much longer time intervals.
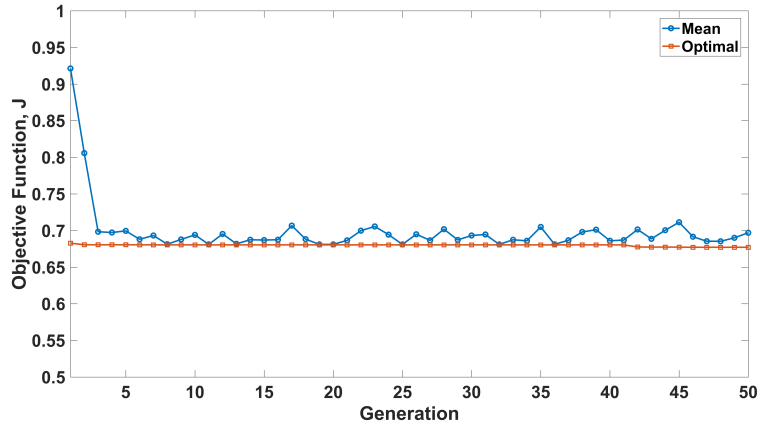
(a) Objective function for each generation.
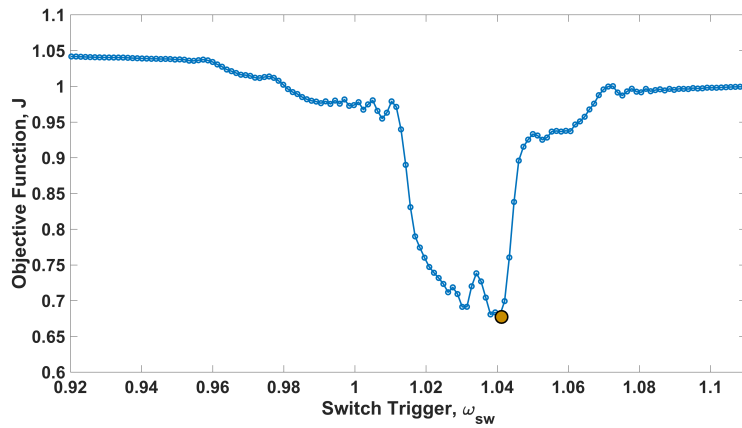
(b) The objective functions correspond to all switches tested and the optimal switch from the genetic algorithm.
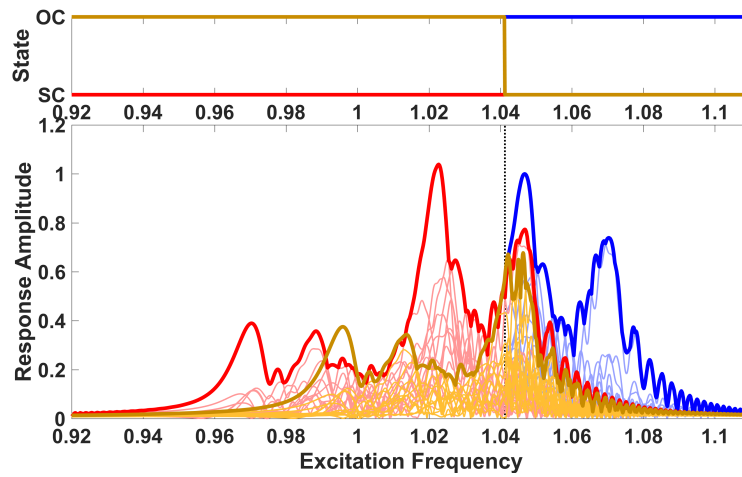
(c) Response envelopes for the open-circuit (blue), short-circuit (red), and optimal (gold) cases.

Figure 4.5: Optimization results when considering only a single switch trigger.
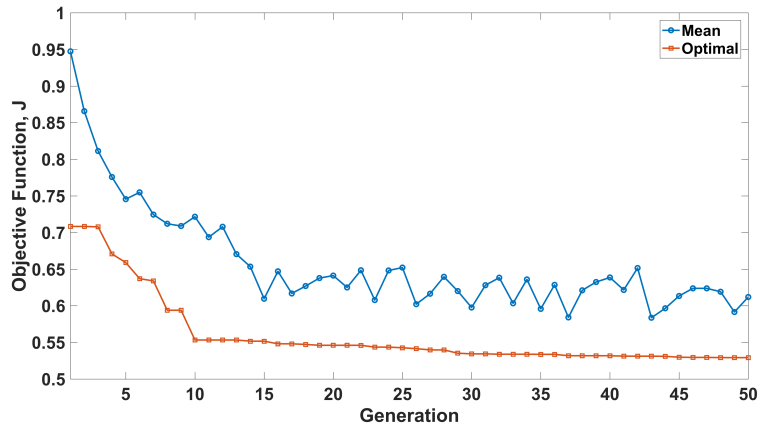
(a) Objective function for each generation.
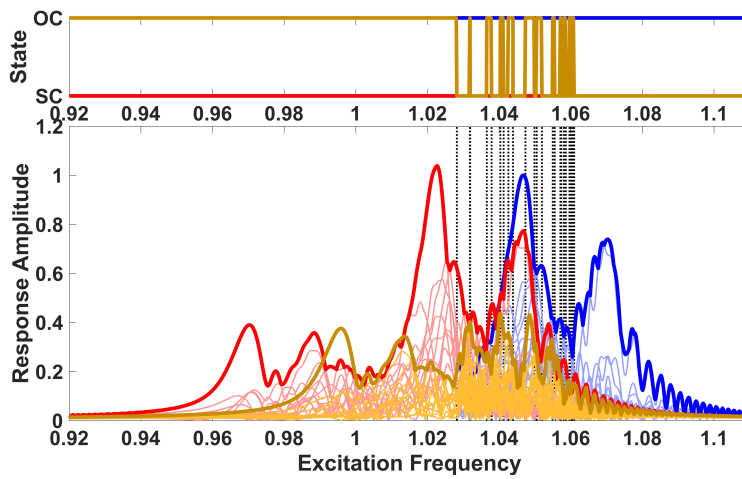
(b) Response envelopes for the open-circuit (blue), short-circuit
(red), and optimal (gold) cases.

Figure 4.6: Optimization results when considering multiple single switch triggers.

4.2   Parametric Study via Monte Carlo Simulations

As mistuning is inherently random, Monte Carlo simulations can provide insight on the underlying
fundamental effects of the various design parameters. These parameters may include the mistun-
ing strength, the excitation frequency sweep rate, the modal damping, and the electromechanical
coupling. A Monte Carlo statistical analysis requires performing a large number of simulations to
obtain a representative distribution for each design parameter. The process begins by generating
a system with the desired design parameters. Each generated system contains a different blade-
stiffness distribution randomly obtained from a normal distribution with zero mean and standard
deviation σ_{mis}. Applying the switch-trigger optimization procedure to each generated system pro-
duces the optimal response expected from RFD.

Although the genetic algorithm significantly reduces the computational expense for identifying
the optimal sets of switch triggers, the shear number of simulations required for obtaining a rep-
resentative distribution is not feasible to perform in a timely manner. The data set will, however,
trend towards a Weibull distribution, thus enabling the utilization of an accelerated Monte Carlo
analysis [84, 37]. This method requires fitting the cumulative distribution function for a three-
parameter Weibull distribution to a decreased number of data points, thus significantly reducing
the computation expense while still producing high-accuracy estimates. The results presented here
correspond to the 95th percentile of the amplification factors for the maximum peak response of the
entire system normalized by the open-circuit, tuned value(Max-Peak AF), as well as the total area
under all response envelope curves, also normalized by the open-circuit tuned value (Envelope-

Area AF). Furthermore, the 95$^{\text{th}}$ percentile for a data set refers to the value where only 5% of the data occurs with a greater value. The accelerated Monte Carlo simulations as used here only require generating and analyzing 50 systems per parameter set to produce estimates of the 95$^{\text{th}}$ percentile of the desired quantities. Furthermore, the genetic algorithm utilized the same parameters as in the preceding example; however, the optimization included a convergence threshold to speed up the trigger identification process. This threshold was satisfied when the optimal objective function decreased by less than one percent of the mean of the optimal objective function spanning the previous five generations.

Figures 4.7–4.10 show the results from the Monte Carlo simulations considering the effects of the mistuning strength, sweep rate, modal damping, and the difference in stiffness states (electromechanical coupling) on a 13-sector system. Each figure shows quantities corresponding to the tuned system that include the un-switched, open-circuit response used as the baseline and the optimal response provided by RFD. Each figure also shows quantities corresponding to the mistuned systems that include the open-circuit response, as well as the optimal responses provided by RFD when considering only a single trigger, or multiple triggers identified using the genetic algorithm.

Figure 4.7 shows the effect that the mistuning strength has on the response with the parameters $\bar{\omega}_{\text{rate}} = 10^{-5}$, $\zeta_0 = 0.001$, and $\delta_p = 0.05$ held constant for all runs. Figure 4.7a shows the effect that the mistuning strength has on the Max-Peak AF. For the tuned system, RFD reduces the Max-Peak AF by 67.4%. For the mistuned system operating in the open-circuit state, the response approaches that of the tuned system for small mistuning. As the mistuning strength increases, the Max-Peak AF sharply increases until a critical point, then steadily declines. This is a similar trend found

in the mistuning literature for harmonic excitation [2]. For all mistuning levels, RFD reduces the Max-Peak AF. For small mistuning levels, RFD performance for the mistuned system converges to that of the tuned system. As the mistuning increases, the slope of the Max-Peak AF curves for RFD is smaller than that of the open-circuit case, thus RFD reduces the system's sensitivity towards mistuning. Further increases in mistuning cause the performance when only considering a single trigger to diverge from the performance when considering multiple triggers since there are multiple resonance peaks present for highly mistuned systems. RFD performance also deteriorates for both cases in highly mistuned systems as there exists some overlap between the short- and open-circuit natural frequencies and, consequently, the corresponding resonance peaks can also overlap, thus hindering RFD performance. Figure 4.7b shows the effect that the mistuning strength has on the Envelope-Area AF. For the tuned system, RFD reduces the Envelope-Area AF by 62.8%. Similar to the Max-Peak AF curves, the Envelope-Area AF for the mistuned system approaches the tuned system for small mistuning and RFD performance also deteriorates for large mistuning. The performance for RFD for both switch configurations, however, shows an approximate one-to-one relation for all mistuning values. Although the Max-Peak AF decreases when applying multiple triggers, the transients developed following each switch may increase the lower-level vibration, thus causing this one-to-one relation.

Figure 4.8 shows the effect that the excitation sweep rate has on the response with the parameters $\sigma_m = 0.03$, $\zeta_0 = 0.001$, and $\delta_p = 0.05$ held constant for all runs. Figure 4.8a shows the effect that the sweep rate has on the Max-Peak AF. For the tuned case, RFD provides the most benefit for slow sweeps, consistent with previous results for a SDOF system [3]. The quick passage through

resonance for rapid sweeps generates minimal vibration, even for the un-switched, open-circuit case, thus limiting the benefits provided by RFD. Interestingly, for the open-circuit, mistuned case, an increasing sweep rate causes an increase in the Max-Peak AF up to a critical point, and only slightly decreases past this point. For slower sweeps, the response approaches that of harmonic excitation; however, as the sweep rate increases, there is a compounding effect due to the influence of the closely-spaced modes in the response that results in this increase in the Max-Peak AF [78, 79]. Similar to the tuned case, RFD shows excellent performance for the slow and intermediate sweep rates, and begins to degrade for the most rapid sweeps tested. Furthermore, RFD with multiple switches slightly outperforms RFD with only a single switch for all sweep rates tested. Figure 4.8b shows the effect that the sweep rate has on the Envelope-Area AF. Similar to the Max-Peak AF, RFD provides the greatest benefit for slow sweeps and degrades for quicker sweeps. Surprisingly, for the open-circuit mistuned case, the quicker sweeps result in a lower Envelope-Area AF than for the tuned case. This result suggests that although the mistuned maximum peak is larger than that of the tuned case, only a small number of blades experience these large magnitudes; conversely, all other blades respond with comparatively smaller amplitudes. Furthermore, at slower sweep rates, RFD exhibits better performance when only considering a single trigger due to the aforementioned transients that develop when considering an increased number of triggers; however, this effect diminishes for quicker sweeps.

Figure 4.9 shows the effect that the modal damping has on the response with the parameters $\sigma_m = 0.03$, $\omega_{\text{rate}} = 10^{-5}$, and $\delta_p = 0.05$ held constant for all runs. Figure 4.9a shows the effect that the modal damping has on the Max-Peak AF. For the tuned case, RFD provides the most benefit

for low modal damping, consistent with previous results for a SDOF system [3]. For the open-circuit, mistuned case, increasing the modal damping decreases the peak response with respect to the tuned case. As the damping increases, the closely-spaced resonance peaks broaden and may become indistinguishable from a single resonance peak, thus reducing the compounding effect when sweeping through the closely-spaced modes and, consequently, the Max-Peak AF. Similar to the tuned case, RFD provides the greatest benefit for lightly damped systems. Furthermore, RFD exhibits only marginally better performance when considering multiple triggers rather than a single optimal trigger. Figure 4.10b shows the effect that the modal damping has on the Envelope-Area AF. Similar to the Max-Peak AF, RFD provides the greatest benefit for lightly damped systems. For the open-circuit, mistuned case, the Envelope-Area AF remains relatively constant for all damping values. Furthermore, RFD again provides the greatest benefit for the lightly damped systems.

Figure 4.10 shows the effect that the difference in stiffness states (i.e., the electromechanical coupling) has on the response with the parameters $\sigma_m = 0.03$, $\omega_{\text{rate}} = 10^{-5}$, and $\zeta_0 = 0.001$ held constant for all runs. Figure 4.10a shows the effect that the difference in stiffness states has on the Max-Peak AF. For the tuned case, RFD provides the most benefit for large δ_p, consistent with previous results for a SDOF system [3]. For the open-circuit, mistuned case, the Max-Peak AF is relatively constant for all δ_p values as this quantity only has an effect when switching between stiffness states. The deviations from the otherwise constant curve arise due to the stochastic variability when using the Weibull fit on each of the various sets of 50 data points; including more data points would diminish this variability at the expense of increased computation time. Similar to the tuned case, RFD provides the greatest benefit for systems with large δ_p values as the

closely-spaced modes corresponding to the short-circuit state shift increasingly further away from the open-circuit modes. Figure 4.10b shows the effect that δ_p has on the Envelope-Area AF; the curves follow the same trends as the Max-Peak AF for all cases.

Overall, the results obtained from the Monte Carlo simulations show that RFD provides the greatest performance potential for lightly mistuned, lightly damped systems with large electrome-chanical coupling and excited by slow or moderate frequency sweeps. Utilizing multiple triggers with RFD offers greater performance for highly mistuned systems compared utilizing on a single optimized trigger; however, there are only marginal improvements for all other parameters. This result suggests that for some cases, there is premature convergence of the genetic algorithm on sets of triggers that correspond to a local minimum for the objective function. Due to the utilization of a reduced number of 50 data points with the Weibull fit, premature convergence for several of these points may skew the data, thus leading to an overestimation of the true optimal response. Such a drawback may be unavoidable when performing large-scale Monte Carlo simulations due to the large computational expense; however, applying RFD to a single system, as is the case in Fig. 4.6, enables the utilization of more computational resources to identify a more optimal set of switches.

(a) Maximum peak response.

(b) Total area under the response envelope curves.
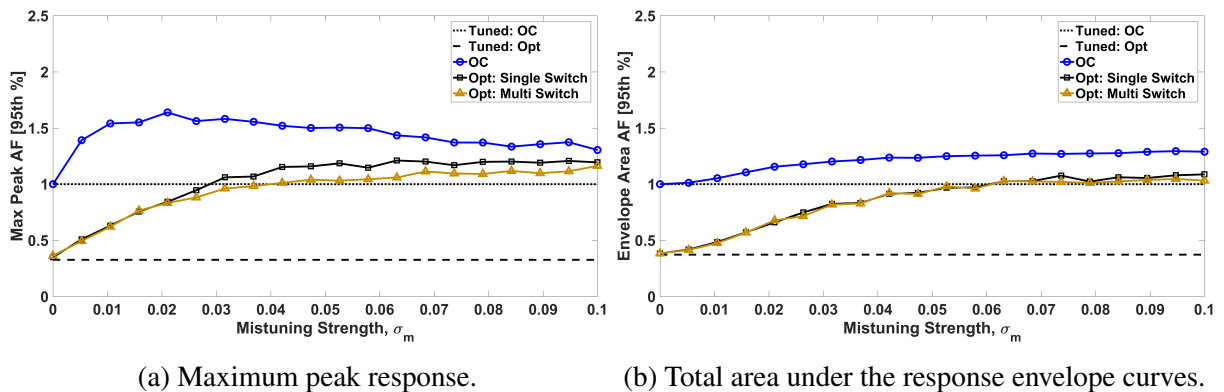
Figure 4.7: Monte Carlo simulation results showing the effect of the mistuning strength.
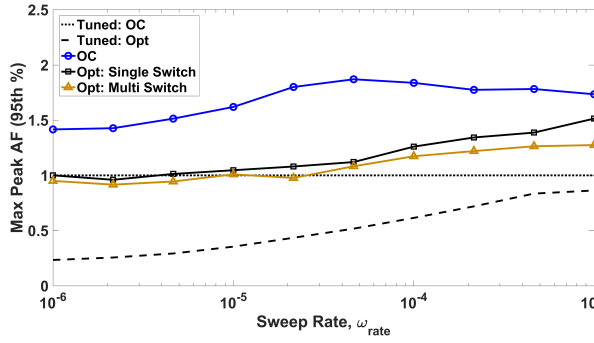
(a) Maximum peak response.
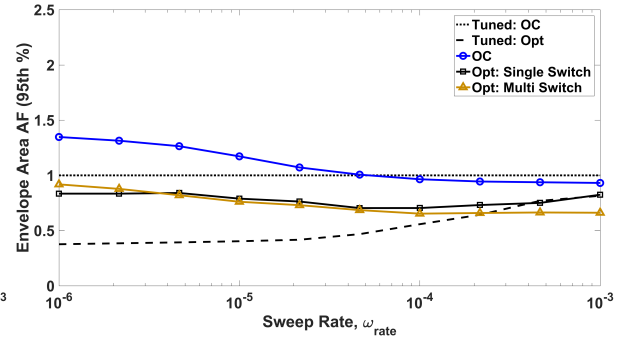
(b) Total area under the response envelope curves.

Figure 4.8: Monte Carlo simulation results showing the effect of the sweep rate.
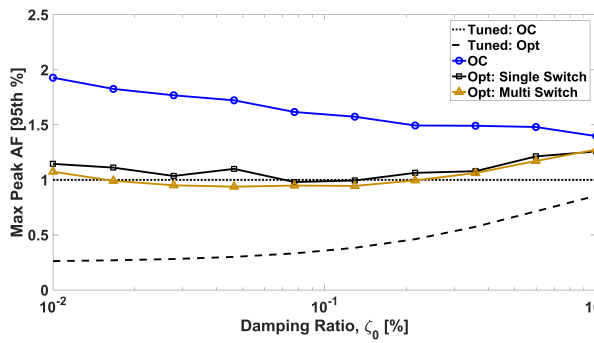
(a) Maximum peak response.
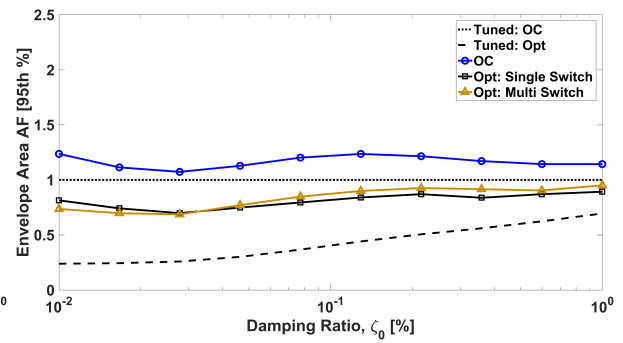
(b) Total area under the response envelope curves.

Figure 4.9: Monte Carlo simulation results showing the effect of the modal damping.
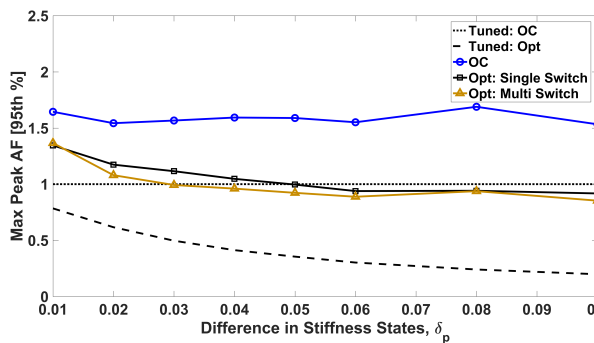
(a) Maximum peak response.
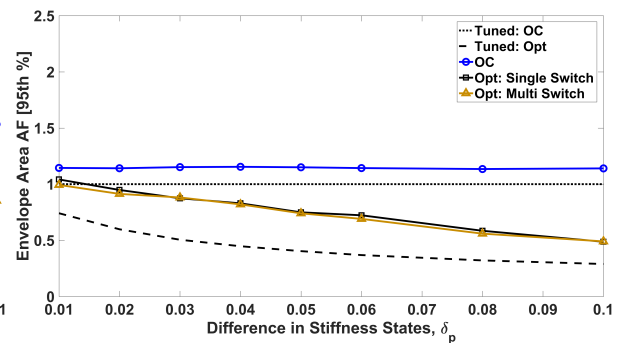
(b) Total area under the response envelope curves.

Figure 4.10: Monte Carlo simulation results showing the effects of the difference between the open- and short-circuit stiffness states (electromechanical coupling).

CHAPTER 5
APPLICATION TOWARDS AN ACADEMIC BLISK—PART 1:

MODELING AND OPTIMIZATION

The following two chapters provide an overview of extending the analysis of the RFD concept towards more realistic bladed disk models. This chapter details the numerical model development and the identification the optimal patch parameters, while the following chapter details the experimental test setup and corresponding experimental analysis. Section 5.1 begins with the development of an academic blisk model derived using the assumed-modes approach and that includes electrical influence of the blade-mounted piezoelectric patches. In a similar manner to blisk models developed using the finite-element approach, the model developed here exploits the cyclic symmetry of a tuned blisk to significantly reduce computational expense when performing modal analysis. Section 5.2 then details the application of multi-objective optimization procedure that aids in the selection of the optimal piezoelectric patch parameters using the electromechanical coupling coefficients as the performance measure.

5.1 Blisk Model Development

This section begins with the development of the academic blisk model that includes the blade-mounted piezoelectric elements. Although in practice, blisks have significantly more complex geometries, the blades have similar dynamics to and can be idealized with flat plates. Figure 5.1 shows the academic blisk geometry that is manufactured from a single material with a clamped boundary condition along the disk's inner radius. This relatively simple geometry facilitates the use of the low-order assumed-modes approach to model the blisk. Over the years, several studies utilized similar energy-based modeling strategies to analyze blisk vibrations [85, 86, 87]. Several studies also employed the to model piezoelectric-based systems, including a stand-alone turbomachinery blade detached from the disk [3, 80, 88]. No such studies exist, however, that utilize the assumed-modes approach, or a similar energy-based approach, to model a blisk that includes the influence of blade-mounted piezoelectric patches.

5.1.1 Total System Energy

Deriving the equations of motion using the assumed-modes approach requires calculating the total system energy. Several terms contribute to the total system energy: the total kinetic energy, the total potential energy, the internal electrical energy of the piezoelectric patches, and the non-conservative work performed on the system by the external mechanical forcing and the electric charge on the piezoelectric patches.
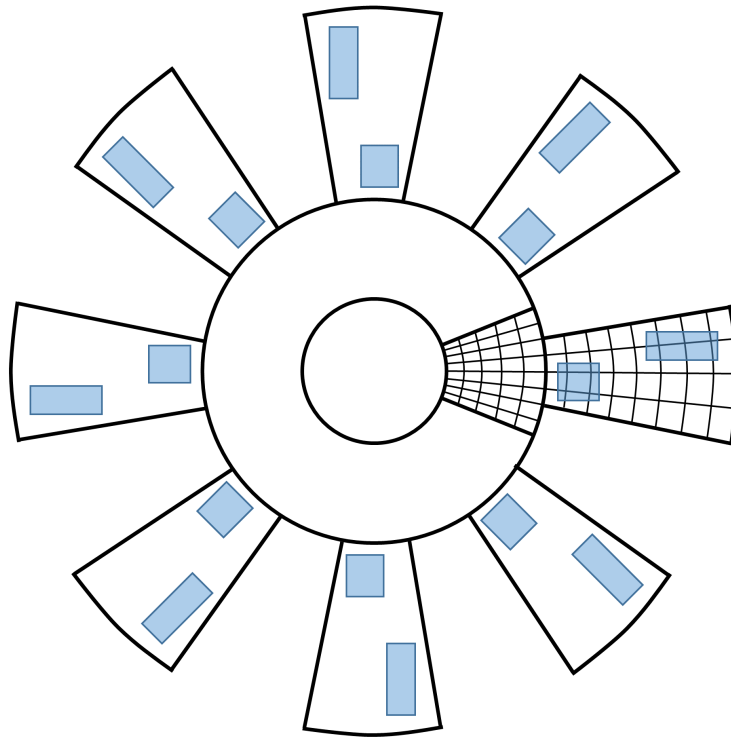
(a) Full blisk showing the reference sector with a course mesh.
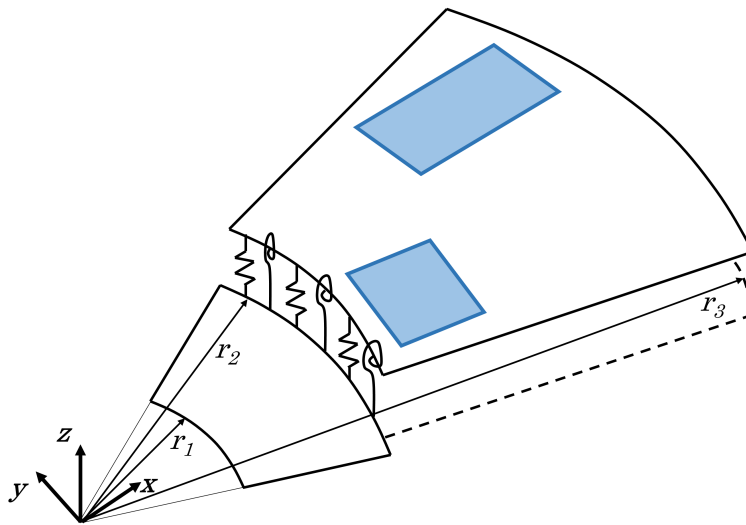
(b) Reference sector showing the distributed springs connecting the
blade and disk portions of the sector.

Figure 5.1: Diagram of the academic blisk with a clamped boundary condition along the inner disk
radius. The model also contains multiple piezoelectric patches (blue rectangles).

5.1.1.1 Kinetic Energy

The total system kinetic energy of the N_s sectors is

$$T_{\text{tot}} = \sum_{j=0}^{N_s-1} T_{d,j} + \sum_{j=0}^{N_s-1} T_{b,j} + \sum_{k=1}^{N_p} \sum_{j=0}^{N_s-1} T_{p,k,j} \tag{5.1}$$

where T_d, T_b, and T_p are the kinetic energies of the disk, blade, and the piezoelectric patches, respectively. The j subscript denotes a quantity associated with the jth sector, and the k subscript denotes a quantity associated with the kth piezoelectric patch on the jth sector. The corresponding kinetic energies associated with the jth sector are

$$T_{d,j} = \frac{1}{2} \int_{V_{d,j}} \rho_{d,j} \dot{w}_{d,j}^2 \mathrm{d}V \tag{5.2}$$

$$T_{b,j} = \frac{1}{2} \int_{V_{b,j}} \rho_{b,j} \dot{w}_{b,j}^2 \mathrm{d}V \tag{5.3}$$

$$T_{p,k,j} = \frac{1}{2} \int_{V_{p,k,j}} \rho_{p,k,j} \dot{w}_{p,k,j}^2 \mathrm{d}V \tag{5.4}$$

with the integrals evaluated over the volume of the disk, blade, and piezoelectric patches, respectively. The quantities ρ_d, ρ_b, and ρ_p are the densities of the disk, the blade, and the piezoelectric patches, respectively. This analysis assumes a perfect bond between the piezoelectric patches and the blades. As such, each patch's transverse displacement is equal to the blade's transverse displacement within the area enclosed by the patch (i.e., $w_{p,k,j} = w_{b,j}$).

5.1.1.2 Mechanical Potential Energy

The total system potential energy of the N_s sectors is

$$U_{\text{tot}} = \sum_{j=0}^{N_s-1} U_{d,j} + \sum_{j=0}^{N_s-1} U_{b,j} + \sum_{k=1}^{N_p} \sum_{j=0}^{N_s-1} U_{p,k,j} \tag{5.5}$$

where U_d, U_b, and U_p are the mechanical potential energies of the disk, blade, and the piezoelectric patches, respectively. The corresponding mechanical potential energies associated with the jth sector are

$$U_{d,j} = \frac{1}{2} \int_{V_{d,j}} \mathbf{T_d}^t \mathbf{S_d} dV \tag{5.6}$$

$$U_{b,j} = \frac{1}{2} \int_{V_{b,j}} \mathbf{T_b}^t \mathbf{S_b} dV \tag{5.7}$$

$$U_{p,k,j} = \frac{1}{2} \int_{V_{p,k,j}} \mathbf{T_p}^t \mathbf{S_p} dV \tag{5.8}$$

where $\mathbf{T}$ is a vector of stresses and $\mathbf{S}$ is a vector of strains. This analysis assumes that the thickness of the disk, the blades, and all of the piezoelectric patches are small compared to the other two dimensions, thus resulting in negligible out-of-plane stresses. First, consider the mechanical potential energy associated with the disk and blades. The proceeding analysis only considers the blade portion of the sector and omits the disk portion for brevity; however, the disk portion is similar to that of the blade, but uses the quantities corresponding to the disk. This analysis assumes the disk and blades are isotropic. The resulting constitutive equations for the three non-zero stress

components for the jth blade are

$$
\begin{Bmatrix} T_1 \\ T_2 \\ T_b \end{Bmatrix} = \begin{Bmatrix} T_{rr} \\ T_{\theta\theta} \\ T_{r\theta} \end{Bmatrix} = \frac{Y}{1-v^2} \begin{bmatrix} 1 & v & 0 \\ v & 1 & 0 \\ 0 & 0 & \frac{1-v}{2} \end{bmatrix} \begin{Bmatrix} S_1 \\ S_2 \\ S_6 \end{Bmatrix}
\tag{5.9}
$$

where Y and v are the Young's modulus and Poisson's ratio, respectively. Inserting the stress components into the blade's potential energy results in

$$
U_{b,j} = \frac{1}{2} \int_{V_{b,j}} \frac{Y_{b,j}}{1-v_{b,j}^2} \left(S_1^2 + S_2^2 + 2v_{b,j} S_1 S_2 + \frac{1-v_{b,j}}{2} S_6^2 \right) dV
\tag{5.10}
$$

Further, the three non-zero strain components are

$$
\begin{Bmatrix} S_1 \\ S_2 \\ S_6 \end{Bmatrix} = \begin{Bmatrix} S_{rr} \\ S_{\theta\theta} \\ 2S_{r\theta} \end{Bmatrix} = \begin{Bmatrix} \frac{\partial u_r}{\partial r} \\ \frac{u_r}{r} + \frac{1}{r}\frac{\partial u_\theta}{\partial \theta} \\ \frac{1}{r}\frac{\partial u_r}{\partial \theta} + \frac{\partial u_\theta}{\partial r} - \frac{u_\theta}{r} \end{Bmatrix}
\tag{5.11}
$$

For thin, plate-type structures, the cross-section remains nominally orthogonal to the neutral plane. As such, the in-plane displacements are related to the transverse displacement according to

$$
\mathbf{u} = \begin{bmatrix} -z\frac{\partial w}{\partial r} & -\frac{z}{r}\frac{\partial w}{\partial \theta} & w \end{bmatrix}
\tag{5.12}
$$

where z is the distance from the neutral plane. The resulting strain components as a function of the transverse displacement are

$$
\left\{ \begin{array}{c} S_1 \\ S_2 \\ S_6 \end{array} \right\} = \left\{ \begin{array}{c} -z\frac{\partial^2 w}{\partial r^2} \\ -z\left(\frac{1}{r}\frac{\partial w}{\partial r} + \frac{1}{r^2}\frac{\partial^2 w}{\partial \theta^2}\right) \\ -2z\left(\frac{1}{r}\frac{\partial^2 w}{\partial r\partial\theta} - \frac{1}{r^2}\frac{\partial w}{\partial\theta}\right) \end{array} \right\}
\tag{5.13}
$$

Utilizing the above strains, the jth blade's potential energy as a function of the displacement is

$$
\begin{aligned}
U_{b,j} = \frac{1}{2}\int_{V_{b,j}} \frac{Y_{b,j}z^2}{1 - v_{b,j}^2}\Bigg\{ &(\nabla w_{b,j})^2 - 2(1 - v_{b,j})\Bigg[\frac{1}{r}\left(\frac{\partial^2 w_{b,j}}{\partial r^2}\frac{\partial w_{b,j}}{\partial r}\right. \\
&+ \frac{1}{r}\frac{\partial^2 w_{b,j}}{\partial r^2}\frac{\partial^2 w_{b,j}}{\partial\theta^2}\bigg) - \frac{1}{r^2}\left(\frac{\partial^2 w_{b,j}}{\partial r\partial\theta} - \frac{1}{r}\frac{\partial w_{b,j}}{\partial\theta^2}\right)\Bigg] \Bigg\} dV
\end{aligned}
\tag{5.14}
$$

Next, consider the mechanical potential energy of the piezoelectric patches. Assuming the patches are transversely isotropic with the plane of symmetry orthogonal to the poling direction (typical convention aligns the poling with the 3-direction, or the z-axis used here), the constitutive equations for a thin patch are [89]

$$
\left[\begin{array}{c} T_1 \\ T_2 \\ T_6 \\ D_3 \end{array} \right] = \left[\begin{array}{cccc} \bar{c}_{11}^E & \bar{c}_{12}^E & 0 & -\bar{e}_{31} \\ \bar{c}_{12}^E & \bar{c}_{11}^E & 0 & -\bar{e}_{31} \\ 0 & 0 & \bar{c}_{66}^E & 0 \\ \bar{e}_{31} & \bar{e}_{31} & 0 & \bar{\varepsilon}_{33}^S \end{array} \right] \left[\begin{array}{c} S_1 \\ S_2 \\ S_6 \\ E_3 \end{array} \right]
\tag{5.15}
$$

where the reduced elastic, electromechanic, and permittivity constants are

$$\bar{c}_{11}^E = \frac{s_{11}^E}{(s_{11}^E + s_{12}^E)(s_{11}^E - s_{12}^E)} \tag{5.16}$$

$$\bar{c}_{12}^E = \frac{-s_{12}^E}{(s_{11}^E + s_{12}^E)(s_{11}^E - s_{12}^E)} \tag{5.17}$$

$$\bar{c}_{66} = \frac{1}{s_{66}^E} \tag{5.18}$$

$$\bar{e}_{31} = \frac{d_{31}}{s_{11}^E + s_{12}^E} \tag{5.19}$$

$$\bar{\varepsilon}_{33}^S = \varepsilon_{33}^T - \frac{2d_{31}^2}{s_{11}^E + s_{12}^E} \tag{5.20}$$

Inserting the stresses into Eq. 5.8 results in the mechanical potential energy for the kth patch on the jth blade such that

$$U_{p,k,j} = \frac{1}{2} \int_{V_{p,k,j}} \left(\bar{c}_{11,k,j}^E S_1^2 + \bar{c}_{11,k,j}^E S_2^2 + 2\bar{c}_{12,k,j}^E S_1 S_2 + \bar{c}_{66,k,j}^E S_6^2 \right) \mathrm{d}V - \frac{1}{2} \int_{V_{p,k,j}} \bar{e}_{31,k,j} \left(S_1 + S_2 \right) E_3 \mathrm{d}V$$

$$= U_{\text{strain},p,k,j} - U_{\text{coupled},k,j}$$

$$\tag{5.21}$$

where $U_{\text{strain},p,k,j}$ is the mechanical strain energy and $U_{\text{coupled},k,j}$ is a quantity that couples the energy between the mechanical and electrical domains. Assuming a perfect bond between the patch and the blade with a bond layer of negligible thickness, the strain components and displacements are the same as in Eqs. 5.12 and 5.13 while also using the displacement of the blade's neutral plane

as the reference. The mechanical strain potential energy is then

$$
\begin{aligned}
U_{\text{strain},p,k,j} = \frac{1}{2} \int_{V_{p,k,j}} z^2 \Bigg\{ & \bar{c}^E_{11,k,j} \left(\frac{\partial^2 w_{b,j}}{\partial r^2} \right)^2 + \frac{\bar{c}^E_{11,k,j}}{r^2} \left[\left(\frac{\partial^2 w_{b,j}}{\partial r^2} \right)^2 + \frac{2}{r} \left(\frac{\partial w_{b,j}}{\partial r} \right) \left(\frac{\partial^2 w_{b,j}}{\partial \theta^2} \right) \right. \\
& \left. + \frac{1}{r^2} \left(\frac{\partial^2 w_{b,j}}{\partial \theta^2} \right)^2 \right] + \frac{2 \bar{c}^E_{12,k,j}}{r} \left[\left(\frac{\partial^2 w_{b,j}}{\partial r^2} \right) \left(\frac{\partial w_{b,j}}{\partial r} \right) + \frac{1}{r} \left(\frac{\partial^2 w_{b,j}}{\partial r^2} \right) \left(\frac{\partial^2 w_{b,j}}{\partial \theta^2} \right) \right] \\
& + \frac{4 \bar{c}^E_{66,k,j}}{r^2} \left[\left(\frac{\partial^2 w_{b,j}}{\partial r \partial \theta} \right)^2 - \frac{2}{r} \left(\frac{\partial^2 w_{b,j}}{\partial r \partial \theta} \right) \left(\frac{\partial w_{b,j}}{\partial \theta} \right) + \frac{1}{r^2} \left(\frac{\partial w_{b,j}}{\partial \theta} \right)^2 \right] \Bigg\} dV
\end{aligned}
$$

$$(5.22)$$

Determining the coupling component of the mechanical energy requires the electric field produced by each piezoelectric element. Assuming that the top and bottom surfaces containing the conducting electrodes are parallel, the electric field arises from the variation of the voltage V through the patch thickness

$$
E_3 = -\frac{\partial V}{\partial z} \tag{5.23}
$$

Inserting the electric field and strains into the coupling term in Eq. 5.21 results in

$$
U_{\text{coupled},k,j} = \frac{1}{2} \int_{V_{p,k,j}} z e_{31,k,j} \left(\frac{\partial^2 w_{b,j}}{\partial r^2} + \frac{1}{r} \frac{\partial w_{b,j}}{\partial r} + \frac{1}{r^2} \frac{\partial^2 w_{b,j}}{\partial \theta^2} \right) \frac{\partial V_{k,j}}{\partial z} dV \tag{5.24}
$$

5.1.1.3 Internal Electrical Energy

The total internal electrical energy of all piezoelectric patches is

$$W_{\text{ie,tot}} = \sum_{k=1}^{N_p} \sum_{j=0}^{N_s-1} W_{\text{ie},k,j} \tag{5.25}$$

For a piezoelectric patch poled in the direction of the z-axis, the internal energy associated with the kth patch on the jth blade is

$$W_{\text{ie},k,j} = \frac{1}{2} \int_{V_{p,k,j}} D_3 E_3 \mathrm{d}V \tag{5.26}$$

Inserting into the above equation the electric displacement in Eq. 5.15 results in

$$W_{\text{ie},k,j} = \frac{1}{2} \int_{V_{p,k,j}} \bar{e}_{31,k,j}(S_1 + S_2) E_3 \mathrm{d}V + \frac{1}{2} \int_{V_{p,k,j}} \bar{\varepsilon}_{33,k,j} E_3^2 \mathrm{d}V$$

$$= U_{\text{coupled},k,j} + U_{\text{electric},k,j} \tag{5.27}$$

where the first term on the right-hand-side of the equation is the same coupling term provided in Eq. 5.24, and $U_{\text{electric},k,j}$ is the electrical potential energy stored within each patch. Substituting in the electric field results in

$$U_{\text{electric},k,j} = \frac{1}{2} \int_{V_{p,k,j}} \bar{\varepsilon}_{33,k,j}^S \left(\frac{\partial V_{k,j}}{\partial z}\right)^2 \mathrm{d}V \tag{5.28}$$

116

5.1.2 Continuity at Substructure Interfaces

Up to this point, the derivation does not include the coupling between the various substructures that include the blade and disk portions of a single sector, and also the coupling between neighboring sectors. In the assumed-modes approach, one method to synthesize the adjacent substructures and impose continuity at each interface is through the inclusion of artificial springs. [90, 91] Setting the spring stiffness to a large value compared to the stiffness of each of the substructures creates a rigid boundary, thereby enforcing both displacement and rotation continuity at each interface.

5.1.2.1 Continuity Between the Blade and Disk

Consider the rigid coupling between the disk and blade portions of a single sector. Figure 5.1b shows a diagram of the transverse springs $k_{\text{bdi},z}$ and the torsional springs $k_{\text{bdi},Tr}$ and $k_{\text{bdi},T\theta}$ that couple these two substructures where the "bdi" subscript denotes quantities corresponding to the "Blade-Disk Interface". The contribution of these springs to the potential energy of the entire system is

$$U_{\text{bdi,tot}} = \sum_{j=0}^{N_s-1} U_{\text{bdi},j} \tag{5.29}$$

where the spring energy associated with the jth sector is

$$
U_{\text{bdi},j} = \frac{1}{2} \int_{-\theta_{b1}}^{\theta_{b1}} \left[k_{\text{bdi},z} \left(w_{b,\text{bdi},j} - w_{d,\text{bdi},j} \right)^2 + k_{\text{bdi},Tr} \left(\frac{\partial w_{b,\text{bdi},j}}{\partial r} - \frac{\partial w_{d,\text{bdi},j}}{\partial r} \right)^2 \right.
$$
$$
\left. + k_{\text{bdi},T\theta} \left(\frac{1}{r_{\text{bdi}}} \frac{\partial w_{b,\text{bdi},j}}{\partial \theta} - \frac{1}{r_{\text{bdi}}} \frac{\partial w_{d,\text{bdi},j}}{\partial \theta} \right)^2 \right] r_{\text{bdi}} d\theta \tag{5.30}
$$

5.1.2.2 Continuity Between Neighboring Sectors

In this analysis, the intersector coupling arises between neighboring disk sectors; however, coupling can also arise between the blades through shrouds or snubbers, if present. Discrete springs can also simulate these additional sources of interblade coupling but is beyond the scope of this analysis. [86] Figure 5.2 shows a diagram of the transverse springs $k_{\mathrm{nsi},z}$ and the torsional springs $k_{\mathrm{nsi},Tr}$ and $k_{\mathrm{nsi},T\theta}$ that couple the neighboring sectors where the "nsi" subscript denotes quantities corresponding to the "Neighboring-Sector Interface". The contribution of these springs to the potential energy of the entire system is

$$U_{\mathrm{nsi,tot}} = \sum_{j=0}^{N_s-1} U_{\mathrm{nsi},j} \tag{5.31}$$

The spring energy associated with the jth sector refers to the sets of springs located at the interface of the left-hand-side of the jth sector and the right-hand-side of the $(j+1)^{\mathrm{th}}$ sector such that

$$U_{\mathrm{nsi},j} = \frac{1}{2} \int_{r_1}^{r_2} \left[k_{\mathrm{nsi},z} \left(w_{d,R,j+1} - w_{d,L,j} \right)^2 + k_{\mathrm{nsi},Tr} \left(\frac{\partial w_{d,R,j+1}}{\partial r} - \frac{\partial w_{d,L,j}}{\partial r} \right)^2 \right.$$
$$\left. + k_{\mathrm{nsi},T\theta} \left(\frac{1}{r} \frac{\partial w_{d,R,j+1}}{\partial \theta} - \frac{1}{r} \frac{\partial w_{d,L,j}}{\partial \theta} \right)^2 \right] r \mathrm{d}\theta \tag{5.32}$$

where the R and L subscripts denote quantities corresponding to the right- and left-disk-sector interface.
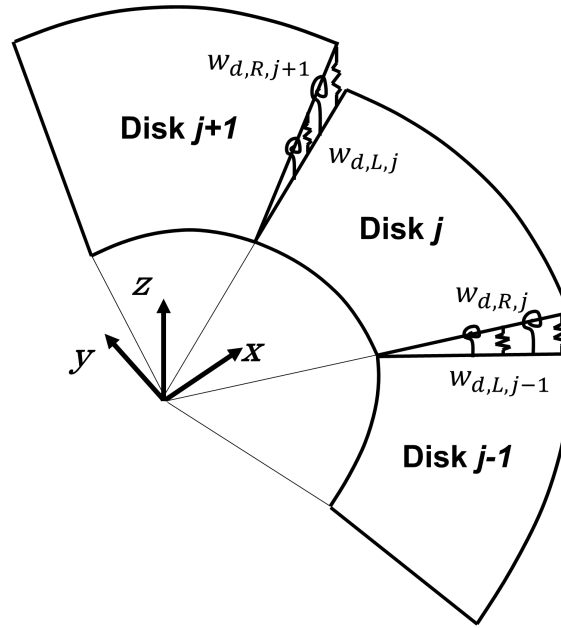
Figure 5.2: Disk diagram showing the artificial springs coupling the neighboring sectors.

5.1.3   Virtual Work due to External Forcing

5.1.3.1   Mechanical Forcing

The external mechanical forcing arises due to aerodynamic forces f_m acting on each sector. This force acts through a virtual displacement δw and performs virtual work δW_m. The mechanical virtual work corresponding to the jth sector is

$$\delta W_{m,j} = \int_{A,b} f_{m,j} \delta w_j \mathrm{d}A \tag{5.33}$$

The aerodynamic forcing can act over all components of the sector, including the disk, the blade, and all piezoelectric patches. As such, the virtual work acting over the entire system is

$$\delta W_{m,\text{tot}} = \sum_{j=0}^{N_s-1} \delta W_{m,d,j} + \sum_{j=0}^{N_s-1} \delta W_{m,b,j} + \sum_{k=1}^{N_p} \sum_{j=0}^{N_s-1} \delta W_{m,p,k,j} \tag{5.34}$$

5.1.3.2 Electrical Forcing

The piezoelectric patches also introduce an electrical forcing mechanism into the system. Similar to the external mechanical force, this electrical force acts through a virtual voltage δV and performs virtual work δW_e. The electrical virtual work corresponding to the kth patch on the jth blade is

$$\delta W_{e,k,j} = \int_{h_{p,k,j}} f_{e,k,j} \delta V_{k,j} \mathrm{d}z \tag{5.35}$$

where f_e is the electric-charge density. The total virtual work generated by all patches is

$$\delta W_{e,\text{tot}} = \sum_{k=1}^{N_p} \sum_{j=0}^{N_s-1} \delta W_{e,k,j} \tag{5.36}$$

5.1.4 Cyclic Symmetry of a Tuned Blisk

A tuned blisk is an example of a cyclically symmetric system that inherently contains certain desirable characteristics that enables the efficient computation of the eigenvalue problem of an

entire blisk by only requiring the system matrices from a single sector. [9] Each tuned mode shape is characterized by a spatial harmonic with a harmonic index ranging from 0 to $N_s/2$ for an even number of sectors and $(N_s - 1)/2$ for an odd number of sectors. As such, a real-valued Fourier series comprises the displacement of both the blade and disk portions of each sector [92, 93]

$$w_j = \frac{1}{\sqrt{N_s}}\tilde{w}^{(0)} + \sqrt{\frac{2}{N_s}}\sum_{h=1}^{\kappa}\left[\cos(jh\alpha)\tilde{w}^{(h,c)} + \sin(jh\alpha)\tilde{w}^{(h,s)}\right] + \frac{(-1)^j}{\sqrt{N_s}}\tilde{w}^{(N_s/2)} \qquad (5.37)$$

where $\tilde{w}$ is the transverse displacement of the reference sector in the cyclic coordinate system, $\alpha = 2\pi/N_s$, and κ is a quantity that takes the value of $\kappa = N_s/2 - 1$ for an even number of sectors or $\kappa = (N_s - 1)/2$ for an odd number of sectors. Further, the superscript denotes the associated spatial harmonic; e.g., (0) denotes the zeroth harmonic, (h, c) and (h, s) denote the cosine and sine components of the hth harmonic, and $(N_s/2)$ denotes the component of the $(N_s/2)^{\text{th}}$ harmonic and is present only if N_s is even. Stacking each sector's transverse displacement into a single column vector and expanding the summation leads to the displacement in matrix form

$$\mathbf{w} = \mathbf{F}\tilde{\mathbf{w}} \qquad (5.38)$$

where

$$\mathbf{w} = \begin{bmatrix} w_0 & w_1 & \cdots & w_{N_s-1} \end{bmatrix}^t \qquad (5.39)$$

$$\tilde{\mathbf{w}} = \begin{bmatrix} \tilde{w}^{(0)} & \tilde{w}^{(1,c)} & \tilde{w}^{(1,s)} & \cdots & \tilde{w}^{(\kappa,c)} & \tilde{w}^{(\kappa,s)} & \tilde{w}^{(N_s/2)} \end{bmatrix}^t \qquad (5.40)$$

and $\mathbf{F}$ is the Fourier transformation matrix defined previously in Eq. 3.45 and reproduced here as

$$\mathbf{F} = \frac{1}{\sqrt{N_s}} \begin{bmatrix} 1 & \sqrt{2} & 0 & \cdots & 0 & 1 \\ 1 & \sqrt{2}\cos\alpha & \sqrt{2}\sin\alpha & \cdots & \sqrt{2}\sin\kappa\alpha & -1 \\ 1 & \sqrt{2}\cos 2\alpha & \sqrt{2}\sin 2\alpha & \cdots & \sqrt{2}\sin 2\kappa\alpha & 1 \\ \vdots & \vdots & \vdots & & \vdots & \vdots \\ 1 & \sqrt{2}\cos(N_s-1)\alpha & \sqrt{2}\sin(N_s-1)\alpha & \cdots & \sqrt{2}\sin(N_s-1)\kappa\alpha & (-1)^{N_s-1} \end{bmatrix} \quad (5.41)$$

where the last column only exists if N_s is even.

For finite-element models, application of this transformation decouples the equations of motion such that the resulting system matrices, generated from a single reference sector, only couple quantities with similar spatial-harmonic content. A following step then imposes continuity between the reference sector and the neighboring sectors for spatial harmonic before solving the reduced eigenproblems to obtain the eigenvalues and eigenvectors. Essentially, this process reduces the eigenproblem from one that requires solving a large, computationally expensive problem, to one that requires solving several smaller, significantly cheaper eigenproblems. A tuned blisk modeled using the assumed-modes approach can similarly take advantage of the cyclically symmetric nature of a tuned blisk to reduce the computational expense as the proceeding section shows.

5.1.5 Assumed Displacement and Voltage Fields

To begin, the transverse displacement in cyclic coordinates is written as a linear combination of assumed mode shapes and the corresponding generalized coordinates where

$$\tilde{w}^{(0)}(r,\theta,t) = \sum_{f=0}^{M_f-1}\sum_{g=0}^{M_g-1} \tilde{q}_{m,fg}^{(0)}(t)\,\psi_{R,f}(r)\,\psi_{\Theta,g}(\theta) \tag{5.42}$$

$$\tilde{w}^{(h,c)}(r,\theta,t) = \sum_{f=0}^{M_f-1}\sum_{g=0}^{M_g-1} \tilde{q}_{m,fg}^{(h,c)}(t)\,\psi_{R,f}(r)\,\psi_{\Theta,g}(\theta) \tag{5.43}$$

$$\tilde{w}^{(h,s)}(r,\theta,t) = \sum_{f=0}^{M_f-1}\sum_{g=0}^{M_g-1} \tilde{q}_{m,fg}^{(h,s)}(t)\,\psi_{R,f}(r)\,\psi_{\Theta,g}(\theta) \tag{5.44}$$

$$\tilde{w}^{(N_s/2)}(r,\theta,t) = \sum_{f=0}^{M_f-1}\sum_{g=0}^{M_g-1} \tilde{q}_{m,fg}^{(N_s/2)}(t)\,\psi_{R,f}(r)\,\psi_{\Theta,g}(\theta) \tag{5.45}$$

where $\tilde{q}_m$ is the time-dependent generalized coordinate corresponding to the specified harmonic, M_f and M_g are the number of assumed shapes chosen in each direction, and ψ are the assumed mode shapes defined at the specified spatial position and that must satisfy the geometric boundary conditions of the disk or blade. For the disk, the assumed shape requires a clamped condition (i.e., zero displacement and slope) at the inner radius. The other boundaries of the disk incorporate artificial springs at the neighboring-sector interface and the blade-disk interface, thus requiring a free boundary condition. For the blade, the artificial springs at the blade-disk interface, and those at the free edges on all other boundaries, similarly require a free boundary condition. These sets of assumed shapes can incorporate simple polynomials as in Ref [80]; however, such sets can suffer numerical stability problems when including high-order modes. [94] Instead, this analysis

utilizes orthogonal polynomials generated using the Gram-Schmidt orthogonalization procedure, as first applied to structural systems by Bhat, to alleviate any numerical stability concerns. [95] The Gram-Schmidt procedure begins by first defining an initial shape that satisfies the geometric boundary conditions; for the disk and the blade, these initial shapes are

$$\psi_{R,d,0}(r) = \left(\frac{r - r_1}{r_2 - r_1}\right)^2 \tag{5.46}$$

$$\psi_{\Theta,d,0}(\theta) = 1 \tag{5.47}$$

$$\psi_{R,b,0}(r) = 1 \tag{5.48}$$

$$\psi_{\Theta,b,0}(\theta) = 1 \tag{5.49}$$

The algorithm to obtain subsequent orthogonal shapes for either the disk or blade is as follows:

$$\psi_1 = (x - A_1)\psi_0$$
$$\psi_l = (x - A_l)\psi_{l-1} - B_l\psi_{l-2} \tag{5.50}$$

where

$$A_l = \frac{\int_a^b x\psi_{l-1}^2(x)\mathrm{d}x}{\int_a^b \psi_{l-1}^2(x)\mathrm{d}x}$$
$$B_l = \frac{\int_a^b x\psi_{l-1}(x)\psi_{l-2}(x)\mathrm{d}x}{\int_a^b \psi_{l-2}^2(x)\mathrm{d}x} \tag{5.51}$$

and x is any spatial variable in the interval $a \leq x \leq b$. After independently generating mode shapes in the two principle directions, combining the shapes into a single function results in the displace-

ments:

$$\tilde{w}^{(0)}(r,\theta,t) = \sum_{l=0}^{M_l-1} \tilde{q}_{m,l}^{(0)}(t)\psi_l(r,\theta) \tag{5.52}$$

$$\tilde{w}^{(h,c)}(r,\theta,t) = \sum_{l=0}^{M_l-1} \tilde{q}_{m,l}^{(h,c)}(t)\psi_l(r,\theta) \tag{5.53}$$

$$\tilde{w}^{(h,s)}(r,\theta,t) = \sum_{l=0}^{M_l-1} \tilde{q}_{m,l}^{(h,s)}(t)\psi_l(r,\theta) \tag{5.54}$$

$$\tilde{w}^{(N_s/2)}(r,\theta,t) = \sum_{l=0}^{M_l-1} \tilde{q}_{m,l}^{(N_s/2)}(t)\psi_l(r,\theta) \tag{5.55}$$

where

$$\psi_l(r,\theta) = \psi_{R,f}(r)\psi_{\Theta,g}(\theta)$$
$$l = fM_g + g \tag{5.56}$$

Next, writing the displacements in vector form

$$\tilde{w}^{(0)}(r,\theta,t) = \boldsymbol{\Psi}(r,\theta)\tilde{\mathbf{q}}_{\mathbf{m}}^{(0)}(t) \tag{5.57}$$

$$\tilde{w}^{(h,c)}(r,\theta,t) = \boldsymbol{\Psi}(r,\theta)\tilde{\mathbf{q}}_{\mathbf{m}}^{(h,c)}(t) \tag{5.58}$$

$$\tilde{w}^{(h,s)}(r,\theta,t) = \boldsymbol{\Psi}(r,\theta)\tilde{\mathbf{q}}_{\mathbf{m}}^{(h,s)}(t) \tag{5.59}$$

$$\tilde{w}^{(N_s/2)}(r,\theta,t) = \boldsymbol{\Psi}(r,\theta)\tilde{\mathbf{q}}_{\mathbf{m}}^{(N_s/2)}(t) \tag{5.60}$$

and substituting into Eq. 5.38 results in

$$\mathbf{w} = [\mathbf{F}\otimes\boldsymbol{\Psi}]\tilde{\mathbf{q}}_{\mathbf{m}} \tag{5.61}$$

where

$$\tilde{\mathbf{q}}_{\mathbf{m}} = \left[\tilde{\mathbf{q}}_{\mathbf{m}}^{(0)^t} \quad \tilde{\mathbf{q}}_{\mathbf{m}}^{(1,c)^t} \quad \tilde{\mathbf{q}}_{\mathbf{m}}^{(1,s)^t} \quad \cdots \quad \tilde{\mathbf{q}}_{\mathbf{m}}^{(\kappa,c)^t} \quad \tilde{\mathbf{q}}_{\mathbf{m}}^{(\kappa,s)^t} \quad \tilde{\mathbf{q}}_{\mathbf{m}}^{(N_s/2)^t} \right]^t \tag{5.62}$$

and $\otimes$ is the Kronecker product. The above expression pertains to both the disk and blade portions of the sector such that

$$\mathbf{w_d} = [\mathbf{F} \otimes \mathbf{\Psi_d}] \tilde{\mathbf{q}}_{\mathbf{d}} \tag{5.63}$$

$$\mathbf{w_b} = [\mathbf{F} \otimes \mathbf{\Psi_b}] \tilde{\mathbf{q}}_{\mathbf{b}} \tag{5.64}$$

Furthermore, assuming that the voltage generated in each piezoelectric patch linearly varies through the patch's thickness and the poling direction is orientate such that there is zero potential at the interface with the blade, the voltage for the kth patch on the jth blade is

$$V_{k,j}(z,t) = \frac{z - z_{p1,k,j}}{z_{p2,k,j} - z_{p1,k,j}} q_{e,k,j}(t) \tag{5.65}$$

where q_e is a time-dependent, generalized coordinate corresponding to the piezoelectric voltage and z_{p1} and z_{p2} are the locations of the patch's surface electrodes with respect to the neutral plane at the blade interface, and the opposing surface, respectively.

5.1.6 System Matrices

This section derives the system matrices using the system energies in combination with the displacement fields in Eqs. 5.63 and 5.63, as well as the voltage fields in Eq. 5.63. For brevity, this section only presents those quantities corresponding to the blades, while omitting those corresponding to the disk, which are similar in form.

5.1.6.1 Mechanical Mass Matrix

To obtain the blade's mechanical mass matrix, substitute the first time derivative of the jth blade's displacement into Eq. 5.4 to obtain the kinetic energy:

$$T_{b,j} = \frac{1}{2}\mathring{\mathbf{q}}_{\mathbf{b}}^{t}\left[\left(\mathbf{F_j}{}^{t}\mathbf{F_j}\right)\otimes\mathbf{M_{bb,j}}\right]\mathring{\mathbf{q}}_{\mathbf{b}} \tag{5.66}$$

where $\mathbf{F_j}$ is the jth row of the Fourier transformation matrix in Eq. 3.45 and the components of the blade mass matrix $\mathbf{M_{bb,j}}$ are

$$M_{bb,j,ls} = \int_{V_{b,j}} \rho_{b,j}\psi_{b,l}\psi_{b,s}\mathrm{d}V \tag{5.67}$$

The total kinetic energy for all blades is thus

$$
\begin{aligned}
T_{\text{tot},b} &= \sum_{j=0}^{N_s-1} T_{b,j} \\
&= \frac{1}{2}\dot{\tilde{\mathbf{q}}}_{\mathbf{b}}^t\left[\left(\mathbf{F}_{\mathbf{0}}^t\mathbf{F}_{\mathbf{0}}\right)\otimes\mathbf{M}_{\mathbf{bb,0}}\right]\dot{\tilde{\mathbf{q}}}_{\mathbf{b}} + \cdots + \frac{1}{2}\dot{\tilde{\mathbf{q}}}_{\mathbf{b}}^t\left[\left(\mathbf{F}_{\mathbf{N_s-1}}^t\mathbf{F}_{\mathbf{N_s-1}}\right)\otimes\mathbf{M}_{\mathbf{bb,N_s-1}}\right]\dot{\tilde{\mathbf{q}}}_{\mathbf{b}} \\
&= \frac{1}{2}\dot{\tilde{\mathbf{q}}}_{\mathbf{b}}^t\tilde{\mathbf{M}}_{\mathbf{bb}}\dot{\tilde{\mathbf{q}}}_{\mathbf{b}}
\end{aligned}
\tag{5.68}
$$

where the mass matrix $\tilde{\mathbf{M}}_{\mathbf{bb}}$ associated with the cyclic coordinates is

$$
\tilde{\mathbf{M}}_{\mathbf{bb}} = \left[\left(\mathbf{F}_{\mathbf{0}}^t\mathbf{F}_{\mathbf{0}}\right)\otimes\mathbf{M}_{\mathbf{bb,0}} + \cdots + \left(\mathbf{F}_{\mathbf{N_s-1}}^t\mathbf{F}_{\mathbf{N_s-1}}\right)\otimes\mathbf{M}_{\mathbf{bb,N_s-1}}\right]
\tag{5.69}
$$

Similarly, for the disk, the total kinetic energy is

$$
T_{\text{tot},d} = \frac{1}{2}\dot{\tilde{\mathbf{q}}}_{\mathbf{d}}^t\tilde{\mathbf{M}}_{\mathbf{dd}}\dot{\tilde{\mathbf{q}}}_{\mathbf{d}}
\tag{5.70}
$$

where

$$
\tilde{\mathbf{M}}_{\mathbf{dd}} = \left[\left(\mathbf{F}_{\mathbf{0}}^t\mathbf{F}_{\mathbf{0}}\right)\otimes\mathbf{M}_{\mathbf{dd,0}} + \cdots + \left(\mathbf{F}_{\mathbf{N_s-1}}^t\mathbf{F}_{\mathbf{N_s-1}}\right)\otimes\mathbf{M}_{\mathbf{dd,N_s-1}}\right]
\tag{5.71}
$$

and

$$
M_{dd,j,ls} = \int_{V_{d,j}} \rho_{d,j}\psi_{d,l}\psi_{d,s}\mathrm{d}V
\tag{5.72}
$$

Furthermore, the piezoelectric patches also contribute to the total system kinetic energy; the total kinetic energy of all of the kth patches is

$$T_{\text{tot},p,k} = \frac{1}{2}\dot{\tilde{\mathbf{q}}}_{\mathbf{b}}^t \tilde{\mathbf{M}}_{\mathbf{bb},\mathbf{p},\mathbf{k}}\dot{\tilde{\mathbf{q}}}_{\mathbf{b}} \tag{5.73}$$

where

$$\tilde{\mathbf{M}}_{\mathbf{bb},\mathbf{p},\mathbf{k}} = \left[\left(\mathbf{F}_{\mathbf{0}}^t \mathbf{F}_{\mathbf{0}}\right) \otimes \mathbf{M}_{\mathbf{bb},\mathbf{p},\mathbf{k},\mathbf{0}} + \cdots + \left(\mathbf{F}_{\mathbf{N_s-1}}^t \mathbf{F}_{\mathbf{N_s-1}}\right) \otimes \mathbf{M}_{\mathbf{bb},\mathbf{p},\mathbf{k},\mathbf{N_s-1}} \right] \tag{5.74}$$

and

$$M_{bb,p,k,j,ls} = \int_{V_{p,k,j}} \rho_{p,k,j}\psi_{b,l}\psi_{b,s}\mathrm{d}V \tag{5.75}$$

5.1.6.2   Mechanical Stiffness Matrix

To obtain the blade's mechanical stiffness matrix, first substitute the jth blade's displacement into Eq. 5.14 to obtain the strain energy:

$$U_{b,j} = \frac{1}{2}\tilde{\mathbf{q}}_{\mathbf{b}}^t \left[\left(\mathbf{F}_{\mathbf{j}}^t \mathbf{F}_{\mathbf{j}}\right) \otimes \mathbf{K}_{\mathbf{bb},\mathbf{j}} \right] \tilde{\mathbf{q}}_{\mathbf{b}} \tag{5.76}$$

where the components of the blade stiffness matrix $\mathbf{K_{bb,j}}$ are

$$
\begin{aligned}
K_{bb,j,ls} = \int_{V_{b,j}} \frac{Y_{b,j} z^2}{1 - v_{b,j}^2} & \left\{ \frac{\partial^2 \psi_{b,l}}{\partial r^2} \frac{\partial^2 \psi_{b,s}}{\partial r^2} + \frac{1}{r^2} \frac{\partial \psi_{b,l}}{\partial r} \frac{\partial \psi_{b,s}}{\partial r} + \frac{1}{r^4} \frac{\partial^2 \psi_{b,l}}{\partial \theta^2} \frac{\partial^2 \psi_{b,s}}{\partial \theta^2} \right. \\
& + \frac{1}{r} \frac{\partial^2 \psi_{b,l}}{\partial r^2} \frac{\partial \psi_{b,s}}{\partial r} + \frac{1}{r} \frac{\partial \psi_{b,l}}{\partial r} \frac{\partial^2 \psi_{b,s}}{\partial r^2} + \frac{1}{r^2} \frac{\partial^2 \psi_{b,l}}{\partial r^2} \frac{\partial^2 \psi_{b,s}}{\partial \theta^2} \\
& + \frac{1}{r^2} \frac{\partial^2 \psi_{b,l}}{\partial \theta^2} \frac{\partial^2 \psi_{b,s}}{\partial r^2} + \frac{1}{r^3} \frac{\partial \psi_{b,l}}{\partial r} \frac{\partial^2 \psi_{b,s}}{\partial \theta^2} + \frac{1}{r^3} \frac{\partial^2 \psi_{b,l}}{\partial \theta^2} \frac{\partial \psi_{b,s}}{\partial r} \\
& - 2(1 - v_{b,j}) \left[\frac{1}{2r} \left(\frac{\partial^2 \psi_{b,l}}{\partial r^2} \frac{\partial \psi_{b,s}}{\partial r} + \frac{\partial \psi_{b,l}}{\partial r} \frac{\partial^2 \psi_{b,s}}{\partial r^2} \right. \right. \\
& + \frac{1}{r} \frac{\partial^2 \psi_{b,l}}{\partial r^2} \frac{\partial^2 \psi_{b,s}}{\partial \theta^2} + \frac{1}{r} \frac{\partial^2 \psi_{b,l}}{\partial \theta^2} \frac{\partial^2 \psi_{b,s}}{\partial r^2} \left. \right) - \frac{1}{r^2} \left(\frac{\partial^2 \psi_{b,l}}{\partial r \partial \theta} \frac{\partial^2 \psi_{b,s}}{\partial r \partial \theta} \right. \\
& \left. \left. \left. - \frac{1}{r} \frac{\partial^2 \psi_{b,l}}{\partial r \partial \theta} \frac{\partial \psi_{b,s}}{\partial \theta} - \frac{1}{r} \frac{\partial \psi_{b,l}}{\partial \theta} \frac{\partial^2 \psi_{b,s}}{\partial r \partial \theta} + \frac{1}{r^2} \frac{\partial \psi_{b,l}}{\partial \theta} \frac{\partial \psi_{b,s}}{\partial \theta} \right) \right] \right\} dV
\end{aligned}
\tag{5.77}
$$

The total strain energy for all the blades is thus

$$
\begin{aligned}
U_{\text{tot},b} &= \sum_{j=0}^{N_s-1} U_{b,j} \\
&= \frac{1}{2} \tilde{\mathbf{q}}_{\mathbf{b}}^t \left[(\mathbf{F}_{\mathbf{0}}^t \mathbf{F}_{\mathbf{0}}) \otimes \mathbf{K_{bb,0}} \right] \tilde{\mathbf{q}}_{\mathbf{b}} + \cdots + \frac{1}{2} \tilde{\mathbf{q}}_{\mathbf{b}}^t \left[(\mathbf{F}_{\mathbf{N_s-1}}^t \mathbf{F}_{\mathbf{N_s-1}}) \otimes \mathbf{K_{bb,N_s-1}} \right] \tilde{\mathbf{q}}_{\mathbf{b}} \\
&= \frac{1}{2} \tilde{\mathbf{q}}_{\mathbf{b}}^t \tilde{\mathbf{K}}_{\mathbf{bb}} \tilde{\mathbf{q}}_{\mathbf{b}}
\end{aligned}
\tag{5.78}
$$

where the blade stiffness matrix $\tilde{\mathbf{K}}_{\mathbf{bb}}$ associated with the cyclic coordinates is

$$
\tilde{\mathbf{K}}_{\mathbf{bb}} = \left[(\mathbf{F}_{\mathbf{0}}^t \mathbf{F}_{\mathbf{0}}) \otimes \mathbf{K_{bb,0}} + \cdots + (\mathbf{F}_{\mathbf{N_s-1}}^t \mathbf{F}_{\mathbf{N_s-1}}) \otimes \mathbf{K_{bb,N_s-1}} \right]
\tag{5.79}
$$

Similarly, for the disk, the total strain energy is

$$
U_d = \frac{1}{2} \tilde{\mathbf{q}}_{\mathbf{d}}^t \tilde{\mathbf{K}}_{\mathbf{dd}} \tilde{\mathbf{q}}_{\mathbf{d}}
\tag{5.80}
$$

130

where

$$\tilde{\mathbf{K}}_{\mathbf{dd}} = \left[\left(\mathbf{F}_{\mathbf{0}}^t \mathbf{F}_{\mathbf{0}} \right) \otimes \mathbf{K}_{\mathbf{dd,0}} + \cdots + \left(\mathbf{F}_{\mathbf{N_s-1}}^t \mathbf{F}_{\mathbf{N_s-1}} \right) \otimes \mathbf{K}_{\mathbf{dd,N_s-1}} \right] \tag{5.81}$$

and

$$
\begin{aligned}
K_{dd,j,ls} = \int_{V_{d,j}} \frac{Y_{d,j} z^2}{1 - v_{d,j}^2} &\left\{ \frac{\partial^2 \psi_{d,l}}{\partial r^2} \frac{\partial^2 \psi_{d,s}}{\partial r^2} + \frac{1}{r^2} \frac{\partial \psi_{d,l}}{\partial r} \frac{\partial \psi_{d,s}}{\partial r} + \frac{1}{r^4} \frac{\partial^2 \psi_{d,l}}{\partial \theta^2} \frac{\partial^2 \psi_{d,s}}{\partial \theta^2} \right. \\
&+ \frac{1}{r} \frac{\partial^2 \psi_{d,l}}{\partial r^2} \frac{\partial \psi_{d,s}}{\partial r} + \frac{1}{r} \frac{\partial \psi_{d,l}}{\partial r} \frac{\partial^2 \psi_{d,s}}{\partial r^2} + \frac{1}{r^2} \frac{\partial^2 \psi_{d,l}}{\partial r^2} \frac{\partial^2 \psi_{d,s}}{\partial \theta^2} \\
&+ \frac{1}{r^2} \frac{\partial^2 \psi_{d,l}}{\partial \theta^2} \frac{\partial^2 \psi_{d,s}}{\partial r^2} + \frac{1}{r^3} \frac{\partial \psi_{d,l}}{\partial r} \frac{\partial^2 \psi_{d,s}}{\partial \theta^2} + \frac{1}{r^3} \frac{\partial^2 \psi_{d,l}}{\partial \theta^2} \frac{\partial \psi_{d,s}}{\partial r} \\
&- 2(1 - v_{d,j}) \left[\frac{1}{2r} \left(\frac{\partial^2 \psi_{d,l}}{\partial r^2} \frac{\partial \psi_{d,s}}{\partial r} + \frac{\partial \psi_{d,l}}{\partial r} \frac{\partial^2 \psi_{d,s}}{\partial r^2} \right. \right. \\
&+ \frac{1}{r} \frac{\partial^2 \psi_{d,l}}{\partial r^2} \frac{\partial^2 \psi_{d,s}}{\partial \theta^2} + \frac{1}{r} \frac{\partial^2 \psi_{d,l}}{\partial \theta^2} \frac{\partial^2 \psi_{d,s}}{\partial r^2} \right) - \frac{1}{r^2} \left(\frac{\partial^2 \psi_{d,l}}{\partial r \partial \theta} \frac{\partial^2 \psi_{d,s}}{\partial r \partial \theta} \right. \\
&\left. \left. \left. - \frac{1}{r} \frac{\partial^2 \psi_{d,l}}{\partial r \partial \theta} \frac{\partial \psi_{d,s}}{\partial \theta} - \frac{1}{r} \frac{\partial \psi_{d,l}}{\partial \theta} \frac{\partial^2 \psi_{d,s}}{\partial r \partial \theta} + \frac{1}{r^2} \frac{\partial \psi_{d,l}}{\partial \theta} \frac{\partial \psi_{d,s}}{\partial \theta} \right) \right] \right\} dV
\end{aligned}
\tag{5.82}
$$

Furthermore, the piezoelectric patches also contribute to the total system strain energy; the total strain energy of all of the kth patches is

$$U_{\text{strain},p,k} = \frac{1}{2} \tilde{\mathbf{q}}_{\mathbf{b}}^t \tilde{\mathbf{K}}_{\mathbf{bb,p,k}} \tilde{\mathbf{q}}_{\mathbf{b}} \tag{5.83}$$

where

$$\tilde{\mathbf{K}}_{\mathbf{bb,p,k}} = \left[\left(\mathbf{F}_{\mathbf{0}}^t \mathbf{F}_{\mathbf{0}} \right) \otimes \mathbf{K}_{\mathbf{bb,p,k,0}} + \cdots + \left(\mathbf{F}_{\mathbf{N_s-1}}^t \mathbf{F}_{\mathbf{N_s-1}} \right) \otimes \mathbf{K}_{\mathbf{bb,p,k,N_s-1}} \right] \tag{5.84}$$

and

$$
\begin{aligned}
K_{bb,p,k,j,ls} = \int_{V_{p,k,j}} z^2 \Bigg\{ & \bar{c}_{11,k,j}^E \frac{\partial^2 \psi_{b,l}}{\partial r^2} \frac{\partial^2 \psi_{b,s}}{\partial r^2} + \frac{\bar{c}_{11,k,j}^E}{r^2} \left[\frac{\partial \psi_{b,l}}{\partial r} \frac{\partial \psi_{b,s}}{\partial r} + \frac{1}{r} \frac{\partial \psi_{b,l}}{\partial r} \frac{\partial^2 \psi_{b,s}}{\partial \theta^2} \right. \\
& \left. + \frac{1}{r} \frac{\partial^2 \psi_{b,l}}{\partial \theta^2} \frac{\partial \psi_{b,s}}{\partial r} + \frac{1}{r^2} \frac{\partial^2 \psi_{b,l}}{\partial \theta^2} \frac{\partial^2 \psi_{b,s}}{\partial \theta^2} \right] + \frac{2\bar{c}_{12,k,j}^E}{r} \left[\frac{\partial^2 \psi_{b,l}}{\partial r^2} \frac{\partial \psi_{b,s}}{\partial r} \right. \\
& \left. + \frac{\partial \psi_{b,l}}{\partial r} \frac{\partial^2 \psi_{b,s}}{\partial r^2} + \frac{1}{r} \frac{\partial^2 \psi_{b,l}}{\partial r^2} \frac{\partial^2 \psi_{b,s}}{\partial \theta^2} + \frac{1}{r} \frac{\partial^2 \psi_{b,l}}{\partial \theta^2} \frac{\partial^2 \psi_{b,s}}{\partial r^2} \right] \\
& + \frac{4\bar{c}_{66,k,j}^E}{r^2} \left[\left(\frac{\partial^2 \psi_{b,l}}{\partial r \partial \theta} \frac{\partial^2 \psi_{b,s}}{\partial r \partial \theta} - \frac{1}{r} \frac{\partial^2 \psi_{b,l}}{\partial r \partial \theta} \frac{\partial \psi_{b,s}}{\partial \theta} \right. \right. \\
& \left. \left. - \frac{1}{r} \frac{\partial \psi_{b,l}}{\partial \theta} \frac{\partial^2 \psi_{b,s}}{\partial r \partial \theta} + \frac{1}{r^2} \frac{\partial \psi_{b,l}}{\partial \theta} \frac{\partial \psi_{b,s}}{\partial \theta} \right] \Bigg\} dV
\end{aligned}
\tag{5.85}
$$

The potential energy arising from the artificial springs also contribute to the system's stiffness. To obtain the stiffness matrix corresponding to the artificial springs located along the blade-disk interface, substitute the blade and disk's displacements into Eq. 5.30 such that

$$
\begin{aligned}
U_{\mathrm{bdi,j}} = {} & \frac{1}{2} \tilde{\mathbf{q}}_{\mathbf{b}}^t \left[\left(\mathbf{F_j}{}^t \mathbf{F_j} \right) \otimes \mathbf{K_{bb,bdi}} \right] \tilde{\mathbf{q}}_{\mathbf{b}} + \frac{1}{2} \tilde{\mathbf{q}}_{\mathbf{d}}^t \left[\left(\mathbf{F_j}{}^t \mathbf{F_j} \right) \otimes \mathbf{K_{dd,bdi}} \right] \tilde{\mathbf{q}}_{\mathbf{d}} \\
& - \frac{1}{2} \tilde{\mathbf{q}}_{\mathbf{b}}^t \left[\left(\mathbf{F_j}{}^t \mathbf{F_j} \right) \otimes \mathbf{K_{bd,bdi}} \right] \tilde{\mathbf{q}}_{\mathbf{d}} - \frac{1}{2} \tilde{\mathbf{q}}_{\mathbf{d}}^t \left[\left(\mathbf{F_j}{}^t \mathbf{F_j} \right) \otimes \mathbf{K_{db,bdi}} \right] \tilde{\mathbf{q}}_{\mathbf{b}}
\end{aligned}
\tag{5.86}
$$

where the components of the spring stiffness matrices are

$$
\begin{aligned}
K_{bb,\text{bdi},ls} = \int_{-\theta_{b1}}^{\theta_{b1}} \Bigg(& k_{\text{bdi},z}\psi_{b,\text{bdi},l}\psi_{b,\text{bdi},s} + k_{\text{bdi},Tr}\frac{\partial\psi_{b,\text{bdi},l}}{\partial r}\frac{\partial\psi_{b,\text{bdi},s}}{\partial r} \\
& + \frac{k_{\text{bdi},T\theta}}{r_{\text{bdi}}^2}\frac{\partial\psi_{b,\text{bdi},l}}{\partial\theta}\frac{\partial\psi_{b,\text{bdi},s}}{\partial\theta}\Bigg)r_{\text{bdi}}\mathrm{d}\theta
\end{aligned}
\tag{5.87}
$$

$$
\begin{aligned}
K_{dd,\text{bdi},ls} = \int_{-\theta_{b1}}^{\theta_{b1}} \Bigg(& k_{\text{bdi},z}\psi_{d,\text{bdi},l}\psi_{d,\text{bdi},s} + k_{\text{bdi},Tr}\frac{\partial\psi_{d,\text{bdi},l}}{\partial r}\frac{\partial\psi_{d,\text{bdi},s}}{\partial r} \\
& + \frac{k_{\text{bdi},T\theta}}{r_{\text{bdi}}^2}\frac{\partial\psi_{d,\text{bdi},l}}{\partial\theta}\frac{\partial\psi_{d,\text{bdi},s}}{\partial\theta}\Bigg)r_{\text{bdi}}\mathrm{d}\theta
\end{aligned}
\tag{5.88}
$$

$$
\begin{aligned}
K_{bd,\text{bdi},ls} = \int_{-\theta_{b1}}^{\theta_{b1}} \Bigg(& k_{\text{bdi},z}\psi_{b,\text{bdi},l}\psi_{d,\text{bdi},s} + k_{\text{bdi},Tr}\frac{\partial\psi_{b,\text{bdi},l}}{\partial r}\frac{\partial\psi_{d,\text{bdi},s}}{\partial r} \\
& + \frac{k_{\text{bdi},T\theta}}{r_{\text{bdi}}^2}\frac{\partial\psi_{b,\text{bdi},l}}{\partial\theta}\frac{\partial\psi_{d,\text{bdi},s}}{\partial\theta}\Bigg)r_{\text{bdi}}\mathrm{d}\theta
\end{aligned}
\tag{5.89}
$$

$$
\begin{aligned}
K_{db,\text{bdi},ls} = \int_{-\theta_{b1}}^{\theta_{b1}} \Bigg(& k_{\text{bdi},z}\psi_{d,\text{bdi},l}\psi_{b,\text{bdi},s} + k_{\text{bdi},Tr}\frac{\partial\psi_{d,\text{bdi},l}}{\partial r}\frac{\partial\psi_{b,\text{bdi},s}}{\partial r} \\
& + \frac{k_{\text{bdi},T\theta}}{r_{\text{bdi}}^2}\frac{\partial\psi_{d,\text{bdi},l}}{\partial\theta}\frac{\partial\psi_{b,\text{bdi},s}}{\partial\theta}\Bigg)r_{\text{bdi}}\mathrm{d}\theta
\end{aligned}
\tag{5.90}
$$

Assuming identical blade-disk interfaces for all sectors, the total spring energy is

$$
\begin{aligned}
U_{\text{bdi}} &= \sum_{j=0}^{N_s-1} U_{\text{bdi},j} \\
&= \frac{1}{2}\tilde{\mathbf{q}}_{\mathbf{b}}^t\left[\mathbf{I}\otimes\mathbf{K}_{\mathbf{bb},\mathbf{bdi}}\right]\tilde{\mathbf{q}}_{\mathbf{b}} + \frac{1}{2}\tilde{\mathbf{q}}_{\mathbf{d}}^t\left[\mathbf{I}\otimes\mathbf{K}_{\mathbf{dd},\mathbf{bdi}}\right]\tilde{\mathbf{q}}_{\mathbf{d}} \\
&\quad - \frac{1}{2}\tilde{\mathbf{q}}_{\mathbf{b}}^t\left[\mathbf{I}\otimes\mathbf{K}_{\mathbf{bd},\mathbf{bdi}}\right]\tilde{\mathbf{q}}_{\mathbf{d}} - \frac{1}{2}\tilde{\mathbf{q}}_{\mathbf{d}}^t\left[\mathbf{I}\otimes\mathbf{K}_{\mathbf{db},\mathbf{bdi}}\right]\tilde{\mathbf{q}}_{\mathbf{b}}
\end{aligned}
\tag{5.91}
$$

To obtain the stiffness matrix corresponding to the artificial springs located along the neighboring-sector interface, substitute the disk's displacements into Eq. 5.32 such that

$$
U_{\text{nsi},j} = \frac{1}{2} \tilde{\mathbf{q}}_{\mathbf{d}}^t \Big[\big(\mathbf{F}_{\mathbf{j+1}}^t \mathbf{F}_{\mathbf{j+1}}\big) \otimes \mathbf{K}_{\mathbf{dd,RR}} + \big(\mathbf{F}_{\mathbf{j}}^t \mathbf{F}_{\mathbf{j}}\big) \otimes \mathbf{K}_{\mathbf{dd,LL}}
$$
$$
- \big(\mathbf{F}_{\mathbf{j+1}}^t \mathbf{F}_{\mathbf{j}}\big) \otimes \mathbf{K}_{\mathbf{dd,RL}} - \big(\mathbf{F}_{\mathbf{j}}^t \mathbf{F}_{\mathbf{j+1}}\big) \otimes \mathbf{K}_{\mathbf{dd,LR}} \Big] \tilde{\mathbf{q}}_{\mathbf{d}}
\tag{5.92}
$$

where the components of the spring stiffness matrices are

$$
K_{dd,RR,ls} = \int_{r_1}^{r_2} \left(k_{\text{nsi},z} \psi_{d,R,l} \psi_{d,R,s} + k_{\text{nsi},Tr} \frac{\partial \psi_{d,R,l}}{\partial r} \frac{\partial \psi_{R,s}}{\partial r} + \frac{k_{\text{nsi},T\theta}}{r^2} \frac{\partial \psi_{d,R,l}}{\partial \theta} \frac{\partial \psi_{d,R,s}}{\partial \theta} \right) dr \tag{5.93}
$$

$$
K_{dd,LL,ls} = \int_{r_1}^{r_2} \left(k_{\text{nsi},z} \psi_{d,L,l} \psi_{d,L,s} + k_{\text{nsi},Tr} \frac{\partial \psi_{d,L,l}}{\partial r} \frac{\partial \psi_{d,L,s}}{\partial r} + \frac{k_{\text{nsi},T\theta}}{r^2} \frac{\partial \psi_{d,L,l}}{\partial \theta} \frac{\partial \psi_{d,L,s}}{\partial \theta} \right) dr \tag{5.94}
$$

$$
K_{dd,RL,ls} = \int_{r_1}^{r_2} \left(k_{\text{nsi},z} \psi_{d,R,l} \psi_{d,L,s} + k_{\text{nsi},Tr} \frac{\partial \psi_{d,R,l}}{\partial r} \frac{\partial \psi_{d,L,s}}{\partial r} + \frac{k_{\text{nsi},T\theta}}{r^2} \frac{\partial \psi_{d,R,l}}{\partial \theta} \frac{\partial \psi_{d,L,s}}{\partial \theta} \right) dr \tag{5.95}
$$

$$
K_{dd,LR,ls} = \int_{r_1}^{r_2} \left(k_{\text{nsi},z} \psi_{d,L,r} \psi_{d,R,s} + k_{\text{nsi},Tr} \frac{\partial \psi_{d,L,l}}{\partial r} \frac{\partial \psi_{d,R,s}}{\partial r} + \frac{k_{\text{nsi},T\theta}}{r^2} \frac{\partial \psi_{d,L,l}}{\partial \theta} \frac{\partial \psi_{d,R,s}}{\partial \theta} \right) dr \tag{5.96}
$$

Assuming identical neighboring-sector interfaces for all sectors, the total spring energy is

$$
U_{\text{nsi}} = \sum_{j=0}^{N_s-1} U_{\text{nsi},j}
$$
$$
= \frac{1}{2} \tilde{\mathbf{q}}_{\mathbf{d}}^t \Big[\mathbf{I} \otimes \big(\mathbf{K}_{\mathbf{dd,RR}} + \mathbf{K}_{\mathbf{dd,LL}}\big) - \big(\mathbf{F}_{\mathbf{Rot}}^t \mathbf{F}\big) \otimes \mathbf{K}_{\mathbf{dd,RL}} - \big(\mathbf{F}^t \mathbf{F}_{\mathbf{Rot}}\big) \otimes \mathbf{K}_{\mathbf{dd,LR}} \Big] \tilde{\mathbf{q}}_{\mathbf{d}}
\tag{5.97}
$$

where $\mathbf{F_{Rot}}$ is the Fourier matrix rotated around one sector (i.e., each row of $\mathbf{F}$ shifted upwards) such that

$$\mathbf{F_{Rot}} = \begin{bmatrix} \mathbf{F_1} \\ \vdots \\ \mathbf{F_{N_s-1}} \\ \mathbf{F_0} \end{bmatrix} \tag{5.98}$$

The matrix product corresponding to the stiffness terms coupling the left and right sides of the reference sector is block diagonal where

$$\mathbf{F_{Rot}^t F} = \begin{bmatrix} 1 & 0 & 0 & \cdots & 0 & 0 & 0 \\ 0 & \cos\alpha & -\sin\alpha & \cdots & 0 & 0 & 0 \\ 0 & \sin\alpha & \cos\alpha & \cdots & 0 & 0 & 0 \\ \vdots & \vdots & \vdots & \ddots & \vdots & \vdots & \vdots \\ 0 & 0 & 0 & \cdots & \cos\kappa\alpha & -\sin\kappa\alpha & 0 \\ 0 & 0 & 0 & \cdots & \sin\kappa\alpha & \cos\kappa\alpha & 0 \\ 0 & 0 & 0 & \cdots & 0 & 0 & -1 \end{bmatrix} \tag{5.99}$$

and the last row and column only exist if N_s is even. This matrix introduces constraints between both the left and right sides of the reference sector in a similar manner to the constraints imposed in a tuned, finite-element model; [92, 93] however, rather than constraining the deflections, as is the case in the finite-element model, this matrix constrains the disk sector's generalized coordinates.

5.1.6.3 Mechanical Forcing Vector

To obtain the forcing vector corresponding to the aerodynamic forces acting on the blades, first substitute the jth blade's displacement into Eq. 5.33 resulting in

$$\delta W_{m,b,j} = \delta \tilde{\mathbf{q}}_{\mathbf{b}}^t \left(\mathbf{F}_{\mathbf{j}}^t \otimes \mathbf{F}_{\mathbf{m,b,j}} \right) \tag{5.100}$$

where the components of the forcing vector are

$$F_{m,b,j,l} = \int_{A_{b,j}} f_{m,b,j} \psi_{b,l} \mathrm{d}A \tag{5.101}$$

The total virtual work acting over all blades is thus

$$\begin{aligned}
\delta W_{m,\text{tot},b} &= \sum_{j=0}^{N_s-1} \delta W_{m,b,j} \\
&= \delta \tilde{\mathbf{q}}_{\mathbf{b}}^t \left(\mathbf{F}_{\mathbf{0}}^t \otimes \mathbf{F}_{\mathbf{m,b,0}} \right) + \cdots + \delta \tilde{\mathbf{q}}_{\mathbf{b}}^t \left(\mathbf{F}_{\mathbf{(N_s-1)}}^t \otimes \mathbf{F}_{\mathbf{m,b,N_s-1}} \right) \\
&= \delta \tilde{\mathbf{q}}_{\mathbf{b}}^t \left(\mathbf{F}^t \otimes \mathbf{I} \right) \mathbf{F}_{\mathbf{m,b}}
\end{aligned} \tag{5.102}$$

where

$$\mathbf{F}_{\mathbf{m,b}} = \left[\mathbf{F}_{\mathbf{m,b,0}}^t \quad \cdots \quad \mathbf{F}_{\mathbf{m,b,N_s-1}}^t \right]^t \tag{5.103}$$

Similarly, for the disk, the total virtual work due to the aerodynamic forcing is

$$
\begin{aligned}
\delta W_{m,\text{tot},d} &= \sum_{j=0}^{N_s-1} \delta W_{m,d,j} \\
&= \delta\tilde{\mathbf{q}}_{\mathbf{d}}^t \left(\mathbf{F}_{\mathbf{0}}^t \otimes \mathbf{F}_{\mathbf{m,d,0}} \right) + \cdots + \delta\tilde{\mathbf{q}}_{\mathbf{d}}^t \left(\mathbf{F}_{\mathbf{N_s-1}}^t \otimes \mathbf{F}_{\mathbf{m,d,N_s-1}} \right) \\
&= \delta\tilde{\mathbf{q}}_{\mathbf{b}}^t \left(\mathbf{F}^t \otimes \mathbf{I} \right) \mathbf{F}_{\mathbf{m,d}}
\end{aligned}
\tag{5.104}
$$

where

$$
F_{m,d,j,l} = \int_{A_{d,j}} f_{m,d,j} \psi_{d,l} \mathrm{d}A
\tag{5.105}
$$

If the aerodynamic forces act over the piezoelectric patches, the total virtual work performed over all of the kth patches is

$$
\begin{aligned}
\delta W_{m,\text{tot},p,k} &= \sum_{j=0}^{N_s-1} \delta W_{m,p,k,j} \\
&= \delta\tilde{\mathbf{q}}_{\mathbf{b}}^t \left(\mathbf{F}_{\mathbf{0}}^t \otimes \mathbf{F}_{\mathbf{m,p,k,0}} \right) + \cdots + \delta\tilde{\mathbf{q}}_{\mathbf{b}}^t \left(\mathbf{F}_{\mathbf{N_s-1}}^t \otimes \mathbf{F}_{\mathbf{m,p,k,N_s-1}} \right) \\
&= \delta\tilde{\mathbf{q}}_{\mathbf{b}}^t \left(\mathbf{F}^t \otimes \mathbf{I} \right) \mathbf{F}_{\mathbf{m,p,k}}
\end{aligned}
\tag{5.106}
$$

where

$$
F_{m,p,k,j,l} = \int_{A_{p,k,j}} f_{m,p,k,j} \psi_{b,l}^t \mathrm{d}A
\tag{5.107}
$$

5.1.6.4 Electrical Contributions and Electromechanical Coupling

To obtain the piezoelectric patch's electrical stiffness matrix, first substitute the voltage generated by the kth patch on the jth blade into Eq. 5.28 resulting in

$$U_{\text{electric,k,j}} = \frac{1}{2} K_{ee,k,j} q_{e,k,j}^2 \tag{5.108}$$

where the electrical stiffness term is

$$K_{ee,k,j} = \int_{V_{p,k,j}} \frac{\bar{\varepsilon}_{33,k,j}^S}{(z_{p2,k,j} - z_{p1,k,j})^2} dV \tag{5.109}$$

For a rectangular patch, this volume integral simplifies to the capacitance for a parallel plate capacitor

$$K_{ee,k,j} = \frac{\bar{\varepsilon}_{33,k,j}^S L_{p,k,j} b_{p,k,j}}{h_{p,k,j}} \tag{5.110}$$

The electrical energy for all of the kth patches is thus

$$
\begin{aligned}
U_{\text{electric},k} &= \sum_{j=0}^{N_s-1} U_{\text{electric},k,j} \\
&= \frac{1}{2} K_{ee,k,0} q_{e,k,0}^2 + \cdots + \frac{1}{2} K_{ee,k,N_s-1} q_{e,k,N_s-1}^2 \\
&= \frac{1}{2} \mathbf{q}_{e,k}^t \mathbf{K}_{ee,k} \mathbf{q}_{e,k}
\end{aligned}
\tag{5.111}
$$

where

$$\mathbf{q_{e,k}} = \begin{bmatrix} q_{e,k,0} & \cdots & q_{e,k,N_s-1} \end{bmatrix}^t \tag{5.112}$$

$$\mathbf{K_{ee,k}} = \begin{bmatrix} K_{ee,k,0} & & 0 \\ & \ddots & \\ 0 & & K_{ee,k,N_s-1} \end{bmatrix} \tag{5.113}$$

Summing over all N_p patches, the total electrical energy is

$$\begin{aligned} U_{\text{electric,tot}} &= \sum_{k=1}^{N_p} U_{\text{electric},k} \\ &= \frac{1}{2}\mathbf{q}_{\mathbf{e,1}}^t \mathbf{K_{ee,1}} \mathbf{q_{e,1}} + \cdots + \frac{1}{2}\mathbf{q}_{\mathbf{e,N_p}}^t \mathbf{K_{ee,N_p}} \mathbf{q_{e,N_p}} \\ &= \frac{1}{2}\mathbf{q_e}^t \mathbf{K_{ee}} \mathbf{q_e} \end{aligned} \tag{5.114}$$

where

$$\mathbf{q_e} = \begin{bmatrix} \mathbf{q}_{\mathbf{e,1}}^t & \cdots & \mathbf{q}_{\mathbf{e,N_p}}^t \end{bmatrix}^t \tag{5.115}$$

$$\mathbf{K_{ee}} = \begin{bmatrix} \mathbf{K_{ee,1}} & & \mathbf{0} \\ & \ddots & \\ \mathbf{0} & & \mathbf{K_{ee,N_p}} \end{bmatrix} \tag{5.116}$$

To obtain the matrix coupling the energy between the mechanical and electrical domains, sub-stitute both the jth blade's displacement and the voltage of the kth patch on the jth blade into

Eq. 5.24 resulting in

$$U_{\text{coupled},p,k,j} = \frac{1}{2}\tilde{\mathbf{q}}_{\mathbf{b}}^t \left[\mathbf{F_j}^t \otimes \mathbf{K_{be,k,j}} \right] q_{e,k,j} \tag{5.117}$$

where the components of the coupling stiffness vector are

$$K_{be,k,j,l} = \int_{V_{p,k,j}} \frac{\bar{e}_{31,k,j}z}{z_{p2,k,j} - z_{p1,k,j}} \left(\frac{\partial^2 \psi_{b,l}}{\partial r^2} + \frac{1}{r}\frac{\partial \psi_{b,l}}{\partial r} + \frac{1}{r^2}\frac{\partial^2 \psi_{b,l}}{\partial \theta^2} \right) \mathrm{d}V \tag{5.118}$$

Summing the coupling energy corresponding to the kth patch over all sectors results in

$$
\begin{aligned}
U_{\text{coupled},p,k} &= \sum_{j=0}^{N_s-1} U_{\text{coupled},p,k,j} \\
&= \frac{1}{2}\tilde{\mathbf{q}}_{\mathbf{b}}^t \left(\mathbf{F_0}^t \otimes \mathbf{K_{be,k,0}} \right) q_{e,k,0} + \cdots + \frac{1}{2}\tilde{\mathbf{q}}_{\mathbf{b}}^t \left(\mathbf{F_{N_s-1}}^t \otimes \mathbf{K_{be,k,N_s-1}} \right) q_{e,k,N_s-1} \\
&= \frac{1}{2}\tilde{\mathbf{q}}_{\mathbf{b}}^t \tilde{\mathbf{K}}_{\mathbf{be,k}} \mathbf{q_{e,k}}
\end{aligned}
\tag{5.119}
$$

where

$$\tilde{\mathbf{K}}_{\mathbf{be,k}} = \left(\mathbf{F}^t \otimes \mathbf{I} \right) \mathbf{K_{be,k}} \tag{5.120}$$

$$\mathbf{K_{be,k}} = \begin{bmatrix} \mathbf{K_{be,k,0}} & & \mathbf{0} \\ & \ddots & \\ \mathbf{0} & & \mathbf{K_{be,k,N_s-1}} \end{bmatrix} \tag{5.121}$$

Summing the coupling energy over all N_p patches, the total coupling energy is

$$
\begin{aligned}
U_{\text{coupled,tot}} &= \sum_{k=1}^{N_p} U_{\text{coupled},p,k} \\
&= \frac{1}{2}\tilde{\mathbf{q}}_{\mathbf{b}}^t \tilde{\mathbf{K}}_{\mathbf{be,1}} \mathbf{q}_{\mathbf{e,1}} + \cdots + \frac{1}{2}\tilde{\mathbf{q}}_{\mathbf{b}}^t \tilde{\mathbf{K}}_{\mathbf{be,N_p}} \mathbf{q}_{\mathbf{e,N_p}} \\
&= \frac{1}{2}\tilde{\mathbf{q}}_{\mathbf{b}}^t \tilde{\mathbf{K}}_{\mathbf{be}} \mathbf{q}_{\mathbf{e}}
\end{aligned}
\tag{5.122}
$$

where

$$
\tilde{\mathbf{K}}_{\mathbf{be}} = \begin{bmatrix} \tilde{\mathbf{K}}_{\mathbf{be,1}} & \cdots & \tilde{\mathbf{K}}_{\mathbf{be,N_p}} \end{bmatrix}
\tag{5.123}
$$

The piezoelectric patches also introduce an electrical forcing mechanism into the system. To obtain the electrical force vector, substitute the voltage of the kth patch on the jth blade into Eq. 5.35 such that

$$
\delta W_{e,k,j} = \delta q_{e,k,j} F_{e,k,j}
\tag{5.124}
$$

where the electrical forcing term is

$$
F_{e,k,j} = \int_{z_{p2,k,j}}^{z_{p1,k,j}} f_{e,k,j} \frac{z - z_{p1,k,j}}{z_{p2,k,j} - z_{p1,k,j}} \, \mathrm{d}z
\tag{5.125}
$$

The total virtual work of the kth patches acting over all blades is thus

$$
\begin{aligned}
\delta W_{e,k} &= \sum_{j=0}^{N_s-1} \delta W_{e,k,j} \\
&= \delta q_{e,k,0} F_{e,k,0} + \cdots + \delta q_{e,k,N_s-1} F_{e,k,N_s-1} \\
&= \delta \mathbf{q}_{\mathbf{e,k}}^t \mathbf{F}_{\mathbf{e,k}}
\end{aligned}
\tag{5.126}
$$

where

$$\mathbf{F_{e,k}} = \begin{bmatrix} F_{e,k,0} & \cdots & F_{e,k,N_s-1} \end{bmatrix}^t \tag{5.127}$$

Summing the virtual work performed by all N_p patches results in the total virtual work

$$\begin{aligned} \delta W_e &= \sum_{k=1}^{N_p} \delta W_{e,k} \\ &= \mathbf{q}_{e,1}^t \mathbf{F_{e,1}} + \cdots + \mathbf{q}_{e,N_p}^t \mathbf{F_{e,N_p}} \\ &= \mathbf{q}_e^t \mathbf{F_e} \end{aligned} \tag{5.128}$$

where

$$\mathbf{F_e} = \begin{bmatrix} \mathbf{F_{e,1}}^t & \cdots & \mathbf{F_{e,Np}} \end{bmatrix}^t \tag{5.129}$$

5.1.7 Lagrangian Equations of Motion

Writing the total system energies as a function of the generalized coordinates

$$T = T(\dot{\tilde{\mathbf{q}}}_\mathbf{d}, \dot{\tilde{\mathbf{q}}}_\mathbf{b}), \quad U = U(\tilde{\mathbf{q}}_\mathbf{d}, \tilde{\mathbf{q}}_\mathbf{b}, \mathbf{q_e}), \quad W_{ie} = W_{ie}(\tilde{\mathbf{q}}_\mathbf{b}, \mathbf{q_e}) \tag{5.130}$$

enables application of the electromechanical version of Lagrange's equations of motion [88]. As
applied here, these equations are

$$\frac{\mathrm{d}}{\mathrm{d}t}\left(\frac{\partial T}{\partial \dot{\tilde{\mathbf{q}}}_{\mathbf{d}}}\right) + \frac{\partial U}{\partial \tilde{\mathbf{q}}_{\mathbf{d}}} - \frac{\partial W_{\mathrm{ie}}}{\partial \tilde{\mathbf{q}}_{\mathbf{d}}} = \mathbf{Q_d}$$

$$\frac{\mathrm{d}}{\mathrm{d}t}\left(\frac{\partial T}{\partial \dot{\tilde{\mathbf{q}}}_{\mathbf{b}}}\right) + \frac{\partial U}{\partial \tilde{\mathbf{q}}_{\mathbf{b}}} - \frac{\partial W_{\mathrm{ie}}}{\partial \tilde{\mathbf{q}}_{\mathbf{b}}} = \mathbf{Q_b} \qquad (5.131)$$

$$\frac{\mathrm{d}}{\mathrm{d}t}\left(\frac{\partial T}{\partial \dot{\mathbf{q}}_{\mathbf{e}}}\right) + \frac{\partial U}{\partial \mathbf{q}_{\mathbf{e}}} - \frac{\partial W_{\mathrm{ie}}}{\partial \mathbf{q}_{\mathbf{e}}} = \mathbf{Q_e}$$

and the resulting system equations of motion

$$\begin{bmatrix} \tilde{\mathbf{M}}_{\mathbf{dd}} & \mathbf{0} & \mathbf{0} \\ \mathbf{0} & \tilde{\mathbf{M}}_{\mathbf{bb}} & \mathbf{0} \\ \mathbf{0} & \mathbf{0} & \mathbf{0} \end{bmatrix} \begin{Bmatrix} \ddot{\tilde{\mathbf{q}}}_{\mathbf{d}} \\ \ddot{\tilde{\mathbf{q}}}_{\mathbf{b}} \\ \ddot{\mathbf{q}}_{\mathbf{e}} \end{Bmatrix} + \begin{bmatrix} \tilde{\mathbf{C}}_{\mathbf{dd}} & \tilde{\mathbf{C}}_{\mathbf{db}} & \mathbf{0} \\ \tilde{\mathbf{C}}_{\mathbf{bd}} & \tilde{\mathbf{C}}_{\mathbf{bb}} & \mathbf{0} \\ \mathbf{0} & \mathbf{0} & \mathbf{0} \end{bmatrix} \begin{Bmatrix} \dot{\tilde{\mathbf{q}}}_{\mathbf{d}} \\ \dot{\tilde{\mathbf{q}}}_{\mathbf{b}} \\ \dot{\mathbf{q}}_{\mathbf{e}} \end{Bmatrix}$$
$$+ \begin{bmatrix} \tilde{\mathbf{K}}_{\mathbf{dd}} & \tilde{\mathbf{K}}_{\mathbf{db}} & \mathbf{0} \\ \tilde{\mathbf{K}}_{\mathbf{bd}} & \tilde{\mathbf{K}}_{\mathbf{bb}} & -\tilde{\mathbf{K}}_{\mathbf{be}} \\ \mathbf{0} & \tilde{\mathbf{K}}_{\mathbf{eb}} & \mathbf{K}_{\mathbf{ee}} \end{bmatrix} \begin{Bmatrix} \tilde{\mathbf{q}}_{\mathbf{d}} \\ \tilde{\mathbf{q}}_{\mathbf{b}} \\ \mathbf{q}_{\mathbf{e}} \end{Bmatrix} = \begin{Bmatrix} \tilde{\mathbf{F}}_{\mathbf{m,d}} \\ \tilde{\mathbf{F}}_{\mathbf{m,b}} \\ \mathbf{F_e} \end{Bmatrix} \qquad (5.132)$$

For mathematical convenience, the above equations of motion include a mechanical damping matrix $\tilde{\mathbf{C}}$ that is proportional to the mechanical mass and stiffness matrices. As such, the solution to the corresponding eigenvalue problem results in eigenvectors that produce normal vibration modes and eigenvalues that are the squared natural frequencies.

5.1.8 Spatial Fourier Transform of System Matrices

In general, there are slight variations between sectors that result in sector-dependent system matrices. Consider, for example, an arbitrary system matrix $\mathbf{A_j}$ corresponding to the jth sector. As the preceding section shows, the cyclic system matrix $\tilde{\mathbf{A}}$ is a linear combination of all sector-dependent system matrices such that

$$\tilde{\mathbf{A}} = \left(\mathbf{F_0^t F_0}\right) \otimes \mathbf{A_0} + \cdots + \left(\mathbf{F_{N_s-1}^t F_{N_s-1}}\right) \otimes \mathbf{A_{N_s-1}} \tag{5.133}$$

The above expression can also be expressed as

$$\tilde{\mathbf{A}} = \left(\mathbf{F}^t \otimes \mathbf{I}\right) \mathbf{A} \left(\mathbf{F} \otimes \mathbf{I}\right) \tag{5.134}$$

where

$$\mathbf{A} = \begin{bmatrix} \mathbf{A_0} & \cdots & \mathbf{0} & \cdots & \mathbf{0} \\ \vdots & \ddots & \vdots & & \vdots \\ \mathbf{0} & \cdots & \mathbf{A_j} & \cdots & \mathbf{0} \\ \vdots & & \vdots & \ddots & \vdots \\ \mathbf{0} & \cdots & \mathbf{0} & \cdots & \mathbf{A_{N_s-1}} \end{bmatrix} \tag{5.135}$$

Furthermore, each sector matrix can be expressed as the nominal matrix of the reference sector with some variation $\mathbf{\Delta A_j}$ such that

$$\mathbf{A_j} = \mathbf{A_0} + \mathbf{\Delta A_j} \tag{5.136}$$

and

$$
\mathbf{A} = \begin{bmatrix} \mathbf{A_0} & \cdots & \mathbf{0} & \cdots & \mathbf{0} \\ \vdots & \ddots & \vdots & & \vdots \\ \mathbf{0} & \cdots & \mathbf{A_0} & \cdots & \mathbf{0} \\ \vdots & & \vdots & \ddots & \vdots \\ \mathbf{0} & \cdots & \mathbf{0} & \cdots & \mathbf{A_0} \end{bmatrix} + \begin{bmatrix} \mathbf{\Delta A_0} & \cdots & \mathbf{0} & \cdots & \mathbf{0} \\ \vdots & \ddots & \vdots & & \vdots \\ \mathbf{0} & \cdots & \mathbf{\Delta A_j} & \cdots & \mathbf{0} \\ \vdots & & \vdots & \ddots & \vdots \\ \mathbf{0} & \cdots & \mathbf{0} & \cdots & \mathbf{\Delta A_{N_s-1}} \end{bmatrix}
\tag{5.137}
$$

The cyclic matrix is then

$$
\begin{aligned}
\tilde{\mathbf{A}} &= \left(\mathbf{F}^t \otimes \mathbf{I}\right)\left[\mathbf{I} \otimes \mathbf{A_0} + \mathbf{\Delta A}\right]\left(\mathbf{F} \otimes \mathbf{I}\right) \\
&= \mathbf{I} \otimes \mathbf{A_0} + \left(\mathbf{F}^t \otimes \mathbf{I}\right)\mathbf{\Delta A}\left(\mathbf{F} \otimes \mathbf{I}\right) \\
&= \tilde{\mathbf{A}}_0 + \mathbf{\Delta}\tilde{\mathbf{A}}
\end{aligned}
\tag{5.138}
$$

The first term on the right-hand-side in the above expression corresponds to the Fourier transform of the system matrix of the reference sector. This Fourier transformation results in the block diagonal matrix

$$
\tilde{\mathbf{A}}_0 = \begin{bmatrix} \mathbf{A_0} & \cdots & \mathbf{0} & \cdots & \mathbf{0} \\ \vdots & \ddots & \vdots & & \vdots \\ \mathbf{0} & \cdots & \mathbf{A_0} & \cdots & \mathbf{0} \\ \vdots & & \vdots & \ddots & \vdots \\ \mathbf{0} & \cdots & \mathbf{0} & \cdots & \mathbf{A_0} \end{bmatrix}
\tag{5.139}
$$

where the rows and columns correspond to the cosine and sine components of the various spatial harmonics. For the 0 and $N_s/2$ harmonics, no sine component exists, and the block component is

145

simply

$$\tilde{\mathbf{A}}^{(0)} = \tilde{\mathbf{A}}^{(N_s/2)} = \mathbf{A_0} \tag{5.140}$$

All other harmonics contain both cosine and sine components such that the associated blocks are

$$\tilde{\mathbf{A}}^{(h)} = \begin{bmatrix} \mathbf{A_0} & \mathbf{0} \\ \mathbf{0} & \mathbf{A_0} \end{bmatrix} \tag{5.141}$$

As the block-diagonal form of the tuned-system matrix suggests, there is no coupling between different harmonics. In general, however, the second term on the right-hand-side of Eq. 5.138 that corresponds to the mistuning matrix is not block diagonal. As such, the presence of mistuning results in a coupling between the different harmonics.

5.1.9 Modal Analysis for a Bare Blisk

Consider the case of a bladed disk with no piezoelectric patches. Excluding the external forces and the effects of damping, the equations of motion reduce to

$$\begin{bmatrix} \tilde{\mathbf{M}}_{\mathbf{dd}} & \mathbf{0} \\ \mathbf{0} & \tilde{\mathbf{M}}_{\mathbf{bb}} \end{bmatrix} \begin{Bmatrix} \ddot{\tilde{\mathbf{q}}}_{\mathbf{d}} \\ \ddot{\tilde{\mathbf{q}}}_{\mathbf{b}} \end{Bmatrix} + \begin{bmatrix} \tilde{\mathbf{K}}_{\mathbf{dd}} & \tilde{\mathbf{K}}_{\mathbf{db}} \\ \tilde{\mathbf{K}}_{\mathbf{bd}} & \tilde{\mathbf{K}}_{\mathbf{bb}} \end{bmatrix} \begin{Bmatrix} \tilde{\mathbf{q}}_{\mathbf{d}} \\ \tilde{\mathbf{q}}_{\mathbf{b}} \end{Bmatrix} = \begin{Bmatrix} \mathbf{0} \\ \mathbf{0} \end{Bmatrix} \tag{5.142}$$

where $\tilde{\mathbf{M}}_{\mathbf{bb}}$ and $\tilde{\mathbf{K}}_{\mathbf{bb}}$ do not contain the mass and stiffness contributions of any of the piezoelectric patches.

146

5.1.9.1 Tuned Blisk

For a tuned system, the block-diagonal form of the system matrices leads to equations of motion that are decoupled for the different spatial harmonics. This decoupling splits the full equations of motion into several, smaller equations, thus reducing the corresponding eigenvalue problems to

$$
\left[\begin{bmatrix} \tilde{\mathbf{K}}_{\mathbf{dd}}^{(h)} & \tilde{\mathbf{K}}_{\mathbf{db}}^{(h)} \\ \tilde{\mathbf{K}}_{\mathbf{bd}}^{(h)} & \tilde{\mathbf{K}}_{\mathbf{bb}}^{(h)} \end{bmatrix} - \omega^{(h)^2} \begin{bmatrix} \tilde{\mathbf{M}}_{\mathbf{dd}}^{(h)} & \mathbf{0} \\ \mathbf{0} & \tilde{\mathbf{M}}_{\mathbf{bb}}^{(h)} \end{bmatrix} \right] \left\{ \begin{matrix} \mathbf{V}_{\mathbf{d}}^{(h)} \\ \mathbf{V}_{\mathbf{b}}^{(h)} \end{matrix} \right\} = \left\{ \begin{matrix} \mathbf{0} \\ \mathbf{0} \end{matrix} \right\} \tag{5.143}
$$

where $\omega^{(h)^2}$ are the eigenvalues and $\mathbf{V}^{(h)} = \begin{bmatrix} \mathbf{V}_{\mathbf{d}}^{(h)^t} & \mathbf{V}_{\mathbf{b}}^{(h)^t} \end{bmatrix}^t$ are the eigenvectors corresponding to the hth harmonic. Utilizing the eigenvectors with Eq. 5.61 recovers the tuned mode shapes as

$$
\begin{aligned}
\mathbf{\Phi}_{\mathbf{d}}^{(h)} &= \begin{bmatrix} \mathbf{F}^{(h)} \otimes \mathbf{\Psi}_{\mathbf{d}} \end{bmatrix} \mathbf{V}_{\mathbf{d}}^{(h)} \\
\mathbf{\Phi}_{\mathbf{b}}^{(h)} &= \begin{bmatrix} \mathbf{F}^{(h)} \otimes \mathbf{\Psi}_{\mathbf{d}} \end{bmatrix} \mathbf{V}_{\mathbf{b}}^{(h)}
\end{aligned} \tag{5.144}
$$

where $\mathbf{F}^{(h)}$ are the columns of $\mathbf{F}$ corresponding to the hth harmonic.

5.1.9.2 Mistuned Blisk

With mistuning present, the system matrices where the mistuning occurs are no longer block diagonal, thereby coupling the various spatial harmonics and requiring the solution to the full eigenvalue

problem

$$
\left[\begin{bmatrix} \tilde{\mathbf{K}}_{\mathbf{dd}} & \tilde{\mathbf{K}}_{\mathbf{db}} \\ \tilde{\mathbf{K}}_{\mathbf{bd}} & \tilde{\mathbf{K}}_{\mathbf{bb}} \end{bmatrix} - \omega^2 \begin{bmatrix} \tilde{\mathbf{M}}_{\mathbf{dd}} & \mathbf{0} \\ \mathbf{0} & \tilde{\mathbf{M}}_{\mathbf{bb}} \end{bmatrix} \right] \left\{ \begin{matrix} \mathbf{V_d} \\ \mathbf{V_b} \end{matrix} \right\} = \left\{ \begin{matrix} \mathbf{0} \\ \mathbf{0} \end{matrix} \right\}
\tag{5.145}
$$

Utilizing the mistuned eigenvectors with the full Fourier transformation matrix recovers the mistuned mode shapes as

$$
\mathbf{\Phi_d} = \begin{bmatrix} \mathbf{F} \otimes \mathbf{\Psi_d} \end{bmatrix} \mathbf{V_d}
$$
$$
\mathbf{\Phi_b} = \begin{bmatrix} \mathbf{F} \otimes \mathbf{\Psi_d} \end{bmatrix} \mathbf{V_b}
\tag{5.146}
$$

5.1.9.3 Example Modal Characteristics

An example helps demonstrate this fundamental difference between the tuned and mistuned system analysis. Consider a tuned blisk absent any piezoelectric patches and with the parameters shown in Table 5.1; all artificial springs are set with a spring constant of 10^9. Figure 5.3 shows images of the mass and stiffness matrices with the colors corresponding to the $\log_{10}$ of the absolute value of the matrix components. As Eq. 5.142 shows, the upper-left and lower-right quadrants correspond to the disk and blade degrees-of-freedom, respectively, where there is zero coupling between different spatial harmonics. The upper-right and lower-left quadrants show the coupling between the blade and the disk provided by the artificial springs located at the blade-disk interface; this coupling only arises for similar spatial harmonic content (i.e., the hND disk coordinates couple with the hND blade coordinates). Solving the eigenvalue problem for each spatial harmonic generates the tuned-blisk natural frequencies and corresponding mode shapes. Figure 5.4 shows the nodal

diameter map (i.e., natural frequency vs. nodal diameter) for the tuned blisk with the stand-alone

sector mode shapes for the first six mode families. A finite-element model developed in NX 12.0

provided initial validation for the proposed modeling approach. The finite-element model utilized

10-point solid tetrahedral elements to model the blisk with the default Aluminum 6061 material

assigned to each element. Assigning a fixed constraint along the inner disk radius simulated the

clamped condition utilized in the assumed-modes model. Figure 5.4 also shows the nodal diameter

map generated from the finite-element model. Both the assumed-modes and finite-element results

show excellent agreement.

Table 5.1: Example blisk parameters.

Blisk (Aluminum)	
Thickness [mm]	1.59
Hub Outer Diameter [mm]	152.40
Hub Inner Diameter [mm]	101.60
Blade Length [mm]	127.00
Blade Root Chord [mm]	50.80
Blade Tip Chord [mm]	101.60

Next, consider the case of a mistuned blisk with the mistuning arising from random variations

in each blade's stiffness. Using Eq. 5.138, the blade stiffness matrix is

$$
\begin{aligned}
\tilde{\mathbf{K}}_{\mathbf{bb}} &= \mathbf{I} \otimes \mathbf{K}_{\mathbf{bb,0}} + \left(\mathbf{F}^{t} \otimes \mathbf{I}\right) \mathbf{\Delta K}_{\mathbf{bb}} \left(\mathbf{F} \otimes \mathbf{I}\right) \\
&= \mathbf{I} \otimes \mathbf{K}_{\mathbf{bb,0}} + \left(\mathbf{F}^{t} \otimes \mathbf{I}\right) \left(\mathbf{\Delta_{b}} \otimes \mathbf{K}_{\mathbf{bb,0}}\right) \left(\mathbf{F} \otimes \mathbf{I}\right) \\
&= \left(\mathbf{I} + \mathbf{F}^{t} \mathbf{\Delta_{b}} \mathbf{F}\right) \otimes \mathbf{K}_{\mathbf{bb,0}}
\end{aligned}
\tag{5.147}
$$

(a) Mass matrix	(b) Stiffness matrix
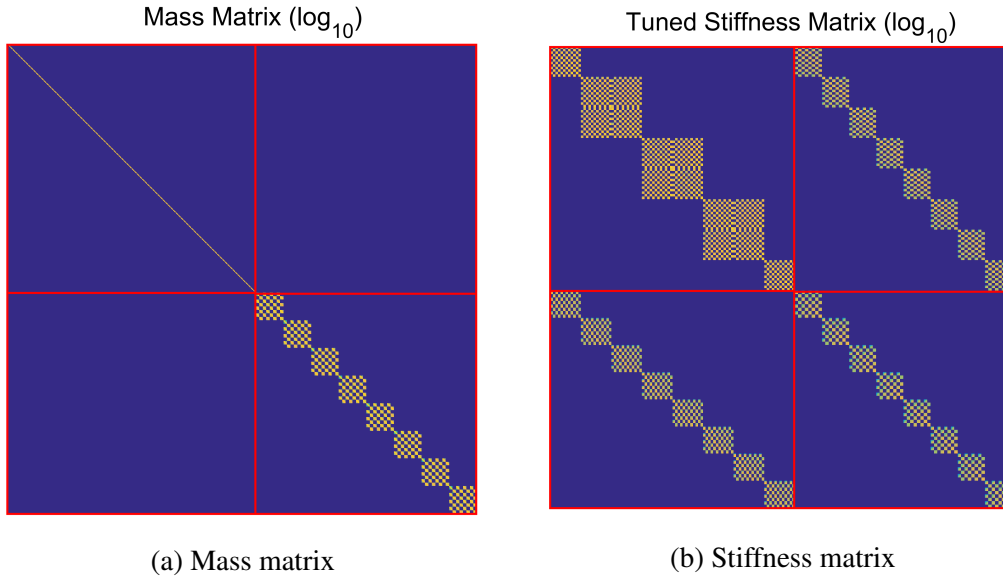
Figure 5.3: Images of the tuned system matrices. The upper-left and lower-right quadrants correspond to the disk and blade degrees-of-freedom, respectively, whereas the upper-right and lower-left quadrants correspond to the blade-disk coupling terms.

Figure 5.4: Nodal diameter map of the tuned academic blisk showing the stand-alone sector mode shapes for the first six mode families. Shown are both the natural frequencies obtained using the proposed assumed-modes model and a finite-element model.

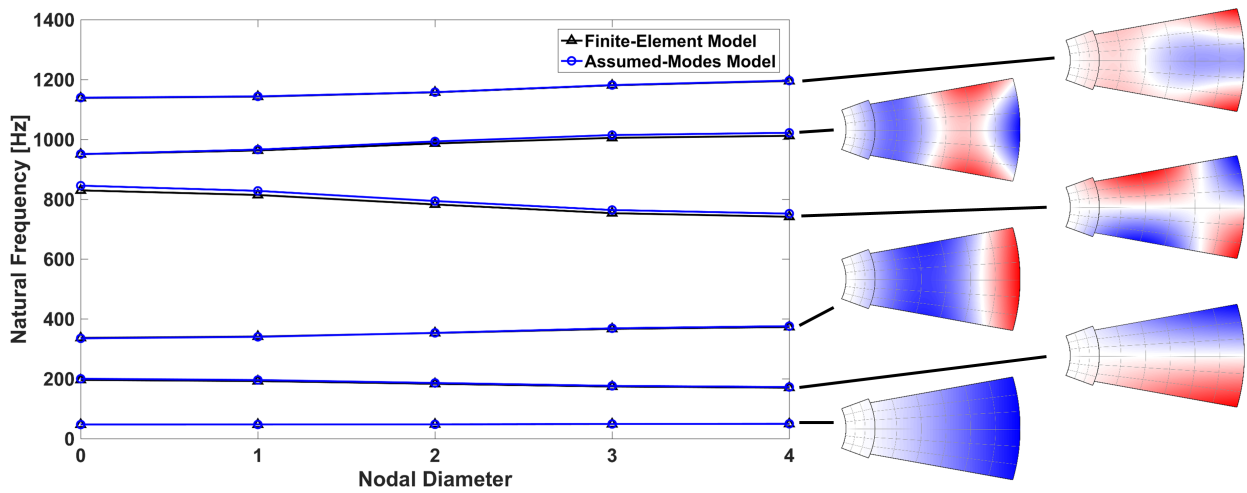The matrix $\mathbf{\Delta_b}$ is diagonal where the components correspond to the stiffness variations of each blade sector

$$\mathbf{\Delta_b} = \mathbf{diag}\big(\delta_{b,0}, \cdots, \delta_{b,N_s-1}\big) \tag{5.148}$$

The presence of the blade mistuning pollutes the block-diagonal, tuned matrix, thus resulting in the coupling of the various spatial harmonics. Continuing with the previous example, randomly assigning the blade perturbations using a normal distribution with zero mean and $\sigma_{\mathrm{mis}} = 0.03$ results in the mistuning distribution shown in Fig. 5.5a. Figure 5.5b shows an image of the corresponding mistuning stiffness matrix where there are off-diagonal components within the blade stiffness matrix, thereby requiring the solution of the eigenvalue problem for the entire blisk.

Furthermore, although the mistuning magnitudes are relatively small, this mistuning pattern can split the degenerate modes and induce localized vibration. Table 5.2 shows a comparison of the natural frequencies of the 6th mode family between the tuned and mistuned blisk obtained from both the assumed-modes and finite-element models. The tuned system contains three degenerate mode pairs, modes 2 and 3, modes 4 and 5, and modes 6 and 7, that correspond to the 1ND, 2ND, and 3ND modes, respectively; the mistuning splits these degenerate pairs. Furthermore, Fig. 5.6 shows an example of the 4ND mode shape for the 6th mode family where neighboring sectors show out-of-phase motion. Figure 5.7 shows an example of a mode shape for the same mode family, but for the mistuned blisk, that exhibits localized vibration. As this example shows, the assumed-modes model absent any piezoelectric patches accurately captures the dynamics for both tuned and mistuned systems. The following sections will incorporate the piezoelectric patches and provide further validation of the proposed modeling strategy.

(a) Mistuning distribution.
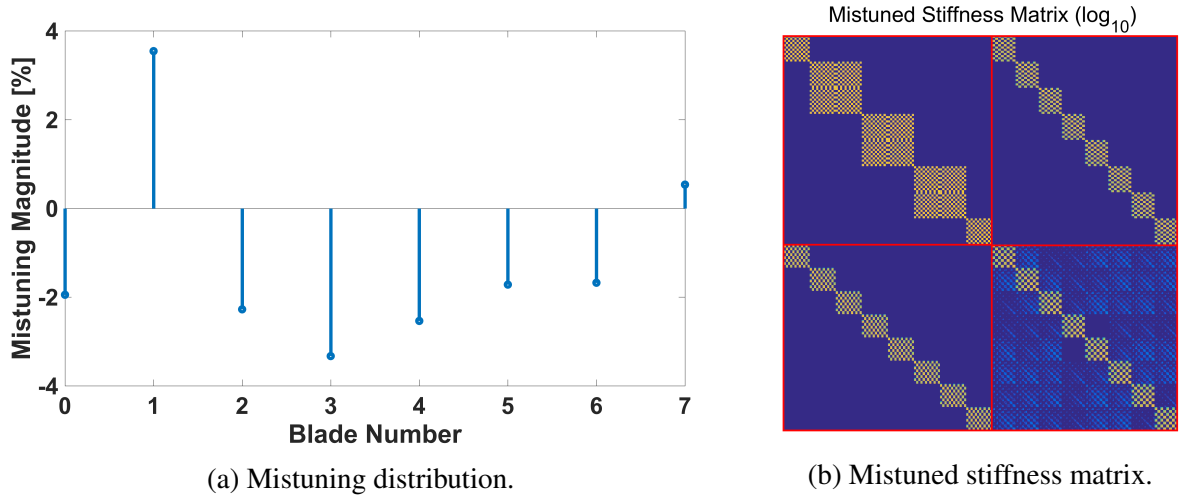

(b) Mistuned stiffness matrix.

Figure 5.5: The influence of mistuning on the academic blisk. Variations in the blade stiffness breaks the cyclic symmetry of the blisk resulting in the coupling of the spatial harmonics.

Table 5.2: Natural frequencies for the 6th mode family of the tuned and mistuned blisk.

Mode r	Tuned Natural Freqs. [kHz]			Mistuned Natural Freqs [kHz]		
	AMM	FEM	Error [%]	AMM	FEM	Error [%]
1	1.1396	1.1403	-0.0664	1.1271	1.1276	-0.0443
2	1.1438	1.1445	-0.0557	1.1349	1.1354	-0.0440
3	-	-	-	1.1397	1.1400	-0.0263
4	1.1580	1.1579	0.0038	1.1470	1.1468	0.0174
5	-	-	-	1.1553	1.1548	0.0433
6	1.1816	1.1798	0.1512	1.1717	1.1698	0.1624
7	-	-	-	1.1803	1.1785	0.1527
8	1.1966	1.1935	0.2623	1.1959	1.1933	0.2179
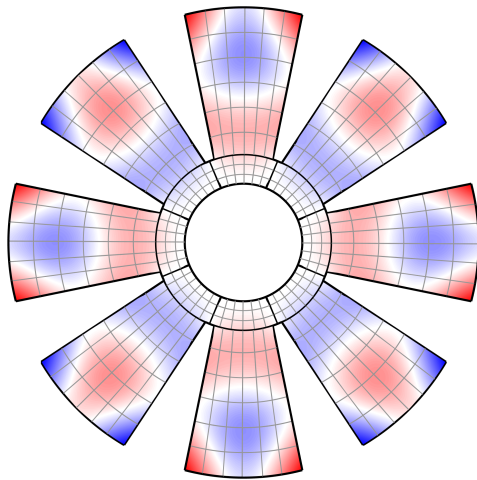
(a) Assumed-modes model.
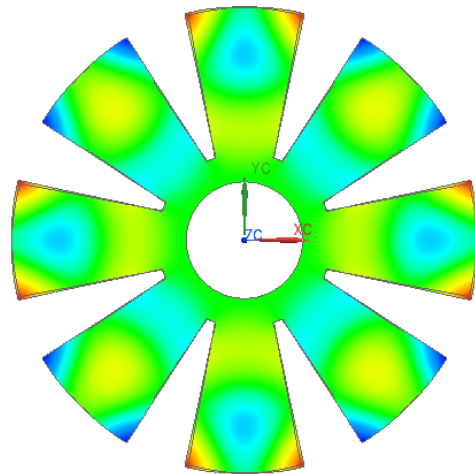
(b) Finite-element model.

Figure 5.6: Example mode shape for the tuned academic blisk. The mode shape corresponds to the 4ND mode of the 6th mode family.
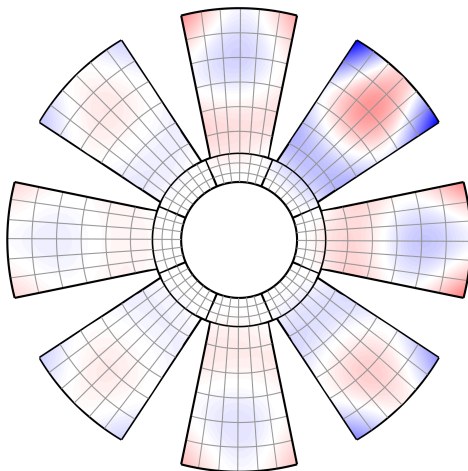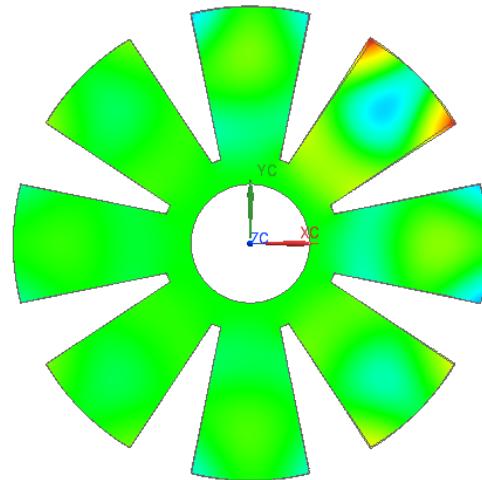

(a) Assumed-modes model.

(b) Finite-element model.

Figure 5.7: Example mode shape for the mistuned academic blisk showing localized vibration. The shape corresponds to the 8th mode of the 6th mode family.

5.1.10 Modal Analysis for the Blisk Including the Piezoelectric Patches

Next, consider the case of a blisk that includes the blade-mounted piezoelectric patches. Excluding the external force and the effects of damping, the equations of motion reduce to

$$
\begin{bmatrix} \tilde{\mathbf{M}}_{dd} & \mathbf{0} & \mathbf{0} \\ \mathbf{0} & \tilde{\mathbf{M}}_{bb} & \mathbf{0} \\ \mathbf{0} & \mathbf{0} & \mathbf{0} \end{bmatrix} \begin{Bmatrix} \ddot{\tilde{\mathbf{q}}}_d \\ \ddot{\tilde{\mathbf{q}}}_b \\ \ddot{\mathbf{q}}_e \end{Bmatrix} + \begin{bmatrix} \tilde{\mathbf{K}}_{dd} & \tilde{\mathbf{K}}_{db} & \mathbf{0} \\ \tilde{\mathbf{K}}_{bd} & \tilde{\mathbf{K}}_{bb} & -\tilde{\mathbf{K}}_{be} \\ \mathbf{0} & \tilde{\mathbf{K}}_{eb} & \mathbf{K}_{ee} \end{bmatrix} \begin{Bmatrix} \tilde{\mathbf{q}}_d \\ \tilde{\mathbf{q}}_b \\ \mathbf{q}_e \end{Bmatrix} = \begin{Bmatrix} \mathbf{0} \\ \mathbf{0} \\ \mathbf{F}_e \end{Bmatrix}
\tag{5.149}
$$

where $\tilde{\mathbf{M}}_{bb}$ and $\tilde{\mathbf{K}}_{bb}$ now contain the mass and stiffness contributions provided by the piezoelectric patches.

5.1.10.1 Short-Circuit Electrical Boundary Condition

With all of the piezoelectric patches operating with a short circuit between the electrodes, there is zero voltage developed across the piezoelectric patches (i.e., $\mathbf{q}_e = \mathbf{0}$). The resulting equations of motion reduce to

$$
\begin{bmatrix} \tilde{\mathbf{M}}_{dd} & \mathbf{0} \\ \mathbf{0} & \tilde{\mathbf{M}}_{bb} \end{bmatrix} \begin{Bmatrix} \ddot{\tilde{\mathbf{q}}}_d \\ \ddot{\tilde{\mathbf{q}}}_b \end{Bmatrix} + \begin{bmatrix} \tilde{\mathbf{K}}_{dd} & \tilde{\mathbf{K}}_{db} \\ \tilde{\mathbf{K}}_{bd} & \tilde{\mathbf{K}}_{bb,sc} \end{bmatrix} \begin{Bmatrix} \tilde{\mathbf{q}}_d \\ \tilde{\mathbf{q}}_b \end{Bmatrix} = \begin{Bmatrix} \mathbf{0} \\ \mathbf{0} \end{Bmatrix}
\tag{5.150}
$$

where the short-circuit blade stiffness matrix is

$$\tilde{\mathbf{K}}_{bb,sc} = \tilde{\mathbf{K}}_{bb} \tag{5.151}$$

Solving the eigenvalue problem for either the tuned or mistuned system in a similar manner as the previous section results in the short-circuit natural frequencies ω_{sc} and eigenvectors $\mathbf{V}_{sc}$.

5.1.10.2 Open-Circuit Electrical Boundary Condition

With all of the piezoelectric patches operating with an open circuit between the electrodes and neglecting any initial conditions, there is zero electric charge generated (i.e., $\mathbf{F_e} = \mathbf{0}$). The resulting piezoelectric voltage is proportional to the blade's mechanical response

$$\mathbf{q_e} = -\mathbf{K}_{ee}^{-1}\tilde{\mathbf{K}}_{eb}\tilde{\mathbf{q}}_b \tag{5.152}$$

and the mechanical equations of motion reduce to

$$\begin{bmatrix} \tilde{\mathbf{M}}_{dd} & \mathbf{0} \\ \mathbf{0} & \tilde{\mathbf{M}}_{bb} \end{bmatrix} \begin{Bmatrix} \ddot{\tilde{\mathbf{q}}}_d \\ \ddot{\tilde{\mathbf{q}}}_b \end{Bmatrix} + \begin{bmatrix} \tilde{\mathbf{K}}_{dd} & \tilde{\mathbf{K}}_{db} \\ \tilde{\mathbf{K}}_{bd} & \tilde{\mathbf{K}}_{bb,oc} \end{bmatrix} \begin{Bmatrix} \tilde{\mathbf{q}}_d \\ \tilde{\mathbf{q}}_b \end{Bmatrix} = \begin{Bmatrix} \mathbf{0} \\ \mathbf{0} \end{Bmatrix} \tag{5.153}$$

where the open-circuit blade stiffness matrix is

$$\tilde{\mathbf{K}}_{bb,oc} = \tilde{\mathbf{K}}_{bb,sc} + \Delta\tilde{\mathbf{K}}_p \tag{5.154}$$

155

The matrix $\boldsymbol{\Delta\tilde{K}_p}$ is the stiffness perturbation matrix resulting from a switch between the open- and short-circuit stiffness states

$$\boldsymbol{\Delta\tilde{K}_p} = \boldsymbol{\tilde{K}_{be}}\boldsymbol{K_{ee}^{-1}}\boldsymbol{\tilde{K}_{eb}} \tag{5.155}$$

Assuming each blade contains identical piezoelectric patches, the stiffness perturbation matrix becomes

$$\boldsymbol{\Delta\tilde{K}_p} = \begin{bmatrix} \boldsymbol{F^t} \otimes \boldsymbol{K_{be,1,0}} & \cdots & \boldsymbol{F^t} \otimes \boldsymbol{K_{be,N_p,0}} \end{bmatrix} \begin{bmatrix} K_{ee,1,0}\boldsymbol{I} & & \boldsymbol{0} \\ & \ddots & \\ \boldsymbol{0} & & K_{ee,N_p,0}\boldsymbol{I} \end{bmatrix}^{-1} \begin{bmatrix} \boldsymbol{F} \otimes \boldsymbol{K_{eb,1,0}} \\ \vdots \\ \boldsymbol{F} \otimes \boldsymbol{K_{eb,N_p,0}} \end{bmatrix} \tag{5.156}$$

$$= \boldsymbol{I} \otimes \boldsymbol{\Delta K_{p,1}} + \cdots + \boldsymbol{I} \otimes \boldsymbol{\Delta K_{p,N_p}}$$

where

$$\boldsymbol{\Delta K_{p,k}} = \frac{1}{K_{ee,k,0}}\boldsymbol{K_{be,k,0}}\boldsymbol{K_{eb,k,0}} \tag{5.157}$$

The above equation shows that for identical patches on each of the blades, the stiffness perturbation matrix induced by the voltage developed in all of the patches is block diagonal. This result signifies that there is a uniform stiffness variation across all spatial harmonics.

Solving the eigenvalue problem for either the tuned or mistuned system results in the open-circuit natural frequencies ω_{oc} and eigenvectors $\boldsymbol{V_{oc}}$. After obtaining both the open- and short-circuit natural frequencies for the blisk, the dynamic form of the effective coupling coefficient

given in Eq. 2.8 and reproduced here as

$$k_{\text{eff},r}^2 = \frac{\omega_{\text{oc},r}^2 - \omega_{\text{sc},r}^2}{\omega_{\text{oc,r}}^2} \tag{5.158}$$

enables a measure of the electromechanical coupling across the various modes.

5.1.10.3 Arbitrary Combinations of Open- and Short-Circuit Piezoelectric Patches

Next, consider the case where the piezoelectric patches on each blade can switch independently, thus resulting in arbitrary combinations of the blades operating in the open- and short-circuit stiffness states. As such, the voltage of the kth patch on the jth blade takes one of two values depending on the operating state:

$$q_{e,k,j} = -s_{k,j}\frac{1}{K_{ee,k,j}}\tilde{\mathbf{K}}_{\mathbf{eb,k,j}}\tilde{\mathbf{q}}_{\mathbf{b}} \tag{5.159}$$

where

$$s_{k,j} = \begin{cases} 0, & \text{short-circuit state} \\ \\ 1, & \text{open-circuit state} \end{cases} \tag{5.160}$$

Considering all of the piezoelectric patches, the voltage vector is

$$\mathbf{q_e} = -\mathbf{S}\mathbf{K}_{\mathbf{ee}}^{-1}\tilde{\mathbf{K}}_{\mathbf{eb}}\tilde{\mathbf{q}}_{\mathbf{b}} \tag{5.161}$$

where $\mathbf{S}$ is the switching matrix that is a diagonal matrix

$$\mathbf{S} = \begin{bmatrix} \mathbf{S_1} & & \mathbf{0} \\ & \ddots & \\ \mathbf{0} & & \mathbf{S_{N_p}} \end{bmatrix} \tag{5.162}$$

and where

$$\mathbf{S_k} = \mathbf{diag}(s_{k,0}, \cdots, s_{k,N_s-1}) \tag{5.163}$$

Each component corresponds to a distinct sector and takes the value of one or zero, depending on the blade in that sector operating in the open- or short-circuit state. Substituting the above voltage into Eq. 5.149 results in

$$\begin{bmatrix} \tilde{\mathbf{M}}_{\mathbf{dd}} & \mathbf{0} \\ \mathbf{0} & \tilde{\mathbf{M}}_{\mathbf{bb}} \end{bmatrix} \begin{Bmatrix} \ddot{\tilde{\mathbf{q}}}_{\mathbf{d}} \\ \ddot{\tilde{\mathbf{q}}}_{\mathbf{b}} \end{Bmatrix} + \begin{bmatrix} \tilde{\mathbf{K}}_{\mathbf{dd}} & \tilde{\mathbf{K}}_{\mathbf{db}} \\ \tilde{\mathbf{K}}_{\mathbf{bd}} & \tilde{\mathbf{K}}_{\mathbf{bb,as}} \end{bmatrix} \begin{Bmatrix} \tilde{\mathbf{q}}_{\mathbf{d}} \\ \tilde{\mathbf{q}}_{\mathbf{b}} \end{Bmatrix} = \begin{Bmatrix} \mathbf{0} \\ \mathbf{0} \end{Bmatrix} \tag{5.164}$$

where the updated blade stiffness matrix is

$$\tilde{\mathbf{K}}_{\mathbf{bb,as}} = \tilde{\mathbf{K}}_{\mathbf{bb,oc}} - \tilde{\mathbf{K}}_{\mathbf{be}}(\mathbf{I} - \mathbf{S})\mathbf{K}_{\mathbf{ee}}^{-1}\tilde{\mathbf{K}}_{\mathbf{eb}}$$

$$= \tilde{\mathbf{K}}_{\mathbf{bb,oc}} - \left[\tilde{\mathbf{K}}_{\mathbf{be,1}}(\mathbf{I} - \mathbf{S_1})\mathbf{K}_{\mathbf{ee,1}}^{-1}\tilde{\mathbf{K}}_{\mathbf{eb,1}} + \cdots + \tilde{\mathbf{K}}_{\mathbf{be,N_p}}(\mathbf{I} - \mathbf{S_{N_p}})\mathbf{K}_{\mathbf{ee,N_p}}^{-1}\tilde{\mathbf{K}}_{\mathbf{eb,N_p}}\right] \tag{5.165}$$

The subscript "as" denotes the blade stiffness when considering "Arbitrary Switches." By again assuming the kth patches are identical for all blades, the blade stiffness matrix reduces to

$$\tilde{\mathbf{K}}_{\mathbf{bb,as}} = \tilde{\mathbf{K}}_{\mathbf{bb,oc}} - \left[(\mathbf{I} - \mathbf{F}^t\mathbf{S_1}\mathbf{F}) \otimes \Delta\mathbf{K}_{\mathbf{p,1}} + \cdots + (\mathbf{I} - \mathbf{F}^t\mathbf{S_{N_p}}\mathbf{F}) \otimes \Delta\mathbf{K}_{\mathbf{p,N_p}}\right] \tag{5.166}$$

As the above equation shows, if all the switches are open (i.e., $\mathbf{S_k} = \mathbf{I}$ for $k = 1, \cdots, N_p$) or closed (i.e., $\mathbf{S_k} = \mathbf{0}$ for $k = 1, \cdots, N_p$), the blade stiffness matrix simplifies to the open-circuit or short-circuit stiffness matrix, respectively; however, an arbitrary combination of switches results in $\mathbf{F'S_kF}$ that is not block diagonal. As such, there is no uniform variation in blade stiffness throughout the blisk. Instead, an arbitrary distribution of switches can induce a new stiffness mistuning pattern capable of mistuning an otherwise tuned blisk, or alter an already existing mistuning pattern.

5.2 Piezoelectric Patch Optimization

Researchers have shown a wealth of interest with regards to utilizing piezoelectric materials for turbomachinery applications. In addition to the damping applications outlined previously in Section 2.2, there also exists potential applications as vibration actuators in test environments to excite blade vibrations [47, 48, 96, 97, 98], as well as dynamic strain sensors, due to their high signal to noise ratio with minimal signal conditioning [99, 100]. Successful implementation of any piezoelectric-based system requires the designer to pay special attention towards the size and location of the piezoelectric elements that ensures the efficient energy exchange between the mechanical and electrical domains. When optimizing a piezoelectric-based system, several objective measures exist depending on the application [101]. As RFD performance depends largely on the electromechanical coupling coefficients, the objective function chosen here corresponds to maximizing this coupling coefficient for the target modes of interest. As the disk dynamics can influence

the blades' dynamic response, this analysis considers the entire blisk in the optimization, rather than solely a stand-alone blade model utilized in previous patch optimization studies. [102, 103] Furthermore, as any optimization procedure must evaluate numerous design iterations, the optimization presented here will focus on the coupling coefficients for a tuned system, specifically maximizing the coupling coefficients for the tuned-system modes with a spatial harmonic equal to the expected engine order.

5.2.1 Evaluation of the Coupling Coefficients for a Truncated Set of Bare-Blisk Modes

Solving the eigenvalue problem for the full blisk with the piezoelectric patches in the open- and short-circuit state generates the natural frequencies required for evaluating the coupling coefficients; however, the large number of design iterations required for an optimization procedure results in large computation times, even when only considering a single spatial harmonic. Instead, using only a truncated set of bare-blisk modes further reduces the computational expense. To begin, consider the tuned-system equations of motion and neglect the external mechanical forcing and the effects of damping, the equations of motion for the hth harmonic are

$$
\begin{bmatrix} \tilde{\mathbf{M}}_{\mathbf{dd}}^{(h)} & \mathbf{0} & \mathbf{0} \\ \mathbf{0} & \tilde{\mathbf{M}}_{\mathbf{bb}}^{(h)} & \mathbf{0} \\ \mathbf{0} & \mathbf{0} & \mathbf{0} \end{bmatrix} \begin{Bmatrix} \ddot{\tilde{\mathbf{q}}}_{\mathbf{d}}^{(h)} \\ \ddot{\tilde{\mathbf{q}}}_{\mathbf{b}}^{(h)} \\ \ddot{\mathbf{q}}_{\mathbf{e}} \end{Bmatrix} + \begin{bmatrix} \tilde{\mathbf{K}}_{\mathbf{dd}}^{(h)} & \tilde{\mathbf{K}}_{\mathbf{db}}^{(h)} & \mathbf{0} \\ \tilde{\mathbf{K}}_{\mathbf{bd}}^{(h)} & \tilde{\mathbf{K}}_{\mathbf{bb}}^{(h)} & -\tilde{\mathbf{K}}_{\mathbf{be}}^{(h)} \\ \mathbf{0} & \tilde{\mathbf{K}}_{\mathbf{eb}}^{(h)} & \mathbf{K}_{\mathbf{ee}} \end{bmatrix} \begin{Bmatrix} \tilde{\mathbf{q}}_{\mathbf{d}}^{(h)} \\ \tilde{\mathbf{q}}_{\mathbf{b}}^{(h)} \\ \mathbf{q}_{\mathbf{e}} \end{Bmatrix} = \begin{Bmatrix} \mathbf{0} \\ \mathbf{0} \\ \mathbf{F}_{\mathbf{e}} \end{Bmatrix} \tag{5.167}
$$

Next, perform a transformation to the modal domain using the eigenvectors $\mathbf{V}_0^{(h)}$ obtained from solving the bare-blisk eigenproblem

$$\left\{ \begin{array}{c} \tilde{\mathbf{q}}_{\mathbf{d}}^{(h)} \\ \tilde{\mathbf{q}}_{\mathbf{b}}^{(h)} \end{array} \right\} = \left\{ \begin{array}{c} \mathbf{V}_{0,\mathbf{d}}^{(h)} \\ \mathbf{V}_{0,\mathbf{b}}^{(h)} \end{array} \right\} \boldsymbol{\eta} \tag{5.168}$$

and premultiply Eq. 5.167 by $\mathbf{V}_0^{(h)^t}$ to obtain the modal equations of motion

$$\begin{bmatrix} \mathbf{I} + \hat{\mathbf{M}}_{\mathbf{p}}^{(h)} & \mathbf{0} \\ \mathbf{0} & \mathbf{0} \end{bmatrix} \left\{ \begin{array}{c} \ddot{\boldsymbol{\eta}} \\ \ddot{\mathbf{q}}_{\mathbf{e}} \end{array} \right\} + \begin{bmatrix} \boldsymbol{\Omega}_0^{(h)} + \hat{\mathbf{K}}_{\mathbf{p}}^{(h)} & -\hat{\boldsymbol{\Theta}}^{(h)^t} \\ \hat{\boldsymbol{\Theta}}^{(h)} & \mathbf{K}_{\mathbf{ee}} \end{bmatrix} \left\{ \begin{array}{c} \boldsymbol{\eta} \\ \mathbf{q}_{\mathbf{e}} \end{array} \right\} = \left\{ \begin{array}{c} \mathbf{0} \\ \mathbf{F}_{\mathbf{e}} \end{array} \right\} \tag{5.169}$$

where $\boldsymbol{\Omega}_0$ is a diagonal matrix containing the squared natural frequencies of the bare blisk and the piezoelectric matrices are

$$\hat{\mathbf{M}}_{\mathbf{p}}^{(h)} = \mathbf{V}_{0,\mathbf{b}}^{(h)^t} \tilde{\mathbf{M}}_{\mathbf{bb,p}}^{(h)} \mathbf{V}_{0,\mathbf{b}}^{(h)} \tag{5.170}$$

$$\hat{\mathbf{K}}_{\mathbf{p}}^{(h)} = \mathbf{V}_{0,\mathbf{b}}^{(h)^t} \tilde{\mathbf{K}}_{\mathbf{bb,p}}^{(h)} \mathbf{V}_{0,\mathbf{b}}^{(h)} \tag{5.171}$$

$$\hat{\boldsymbol{\Theta}}^{(h)^t} = \mathbf{V}_{0,\mathbf{b}}^{(h)^t} \left[\mathbf{F}^{(h)^t} \otimes \mathbf{K}_{\mathbf{be,1,0}} \cdots \mathbf{F}^{(h)^t} \otimes \mathbf{K}_{\mathbf{be,N_p,0}} \right] \tag{5.172}$$

In the short-circuit state, the modal equations become

$$[\mathbf{I} + \hat{\mathbf{M}}_{\mathbf{p}}^{(h)}] \ddot{\boldsymbol{\eta}} + [\boldsymbol{\Omega}_0^{(h)} + \hat{\mathbf{K}}_{\mathbf{p}}^{(h)}] \boldsymbol{\eta} = \mathbf{0} \tag{5.173}$$

161

whereas in the open-circuit state, the piezoelectric voltage is proportional to the modal response such that

$$\mathbf{q_e} = -\mathbf{K_{ee}^{-1}}\hat{\boldsymbol{\Theta}}^{(h)}\boldsymbol{\eta} \tag{5.174}$$

and the modal equations become

$$[\mathbf{I} + \hat{\mathbf{M}}_{\mathbf{p}}^{(h)}]\ddot{\boldsymbol{\eta}} + [\boldsymbol{\Omega}_{\mathbf{0}}^{(h)} + \hat{\mathbf{K}}_{\mathbf{p}}^{(h)} + \boldsymbol{\Delta}\hat{\mathbf{K}}_{\mathbf{p}}^{(h)}]\boldsymbol{\eta} = \mathbf{0} \tag{5.175}$$

where $\boldsymbol{\Delta}\hat{\mathbf{K}}_{\mathbf{p}}^{(h)}$ is the switch-induced stiffness perturbation matrix

$$\boldsymbol{\Delta}\hat{\mathbf{K}}_{\mathbf{p}}^{(h)} = \hat{\boldsymbol{\Theta}}^{(h)^t}\mathbf{K_{ee}^{-1}}\hat{\boldsymbol{\Theta}}^{(h)} \tag{5.176}$$

If the harmonic under consideration corresponds to $h = 0, N_s/2$, the piezoelectric matrices are

$$\hat{\mathbf{M}}_{\mathbf{p}}^{(h)} = \mathbf{V}_{\mathbf{0,b}}^{(h)^t}\mathbf{M_{bb,p}}\mathbf{V}_{\mathbf{0,b}}^{(h)} \tag{5.177}$$

$$\hat{\mathbf{K}}_{\mathbf{p}}^{(h)} = \mathbf{V}_{\mathbf{0,b}}^{(h)^t}\mathbf{K_{bb,p}}\mathbf{V}_{\mathbf{0,b}}^{(h)} \tag{5.178}$$

$$\hat{\boldsymbol{\Theta}}^{(h)^t} = \left[\mathbf{F}^{(h)^t}\otimes\mathbf{V}_{\mathbf{0,b}}^{(h)^t}\mathbf{K_{be,1,0}}\cdots\mathbf{F}^{(h)^t}\otimes\mathbf{V}_{\mathbf{0,b}}^{(h)^t}\mathbf{K_{be,N_p,0}}\right] \tag{5.179}$$

$$= \left[\mathbf{F}^{(h)^t}\otimes\hat{\boldsymbol{\Theta}}_{\mathbf{1,0}}^{(h)^t}\cdots\mathbf{F}^{(h)^t}\otimes\hat{\boldsymbol{\Theta}}_{\mathbf{N_p,0}}^{(h)^t}\right] \tag{5.180}$$

$$\boldsymbol{\Delta}\hat{\mathbf{K}}_{\mathbf{p}}^{(h)} = \frac{1}{K_{ee,1,0}}\hat{\boldsymbol{\Theta}}_{\mathbf{1,0}}^{(h)t}\hat{\boldsymbol{\Theta}}_{\mathbf{1,0}}^{(h)}+\cdots+\frac{1}{K_{ee,N_p,0}}\hat{\boldsymbol{\Theta}}_{\mathbf{N_p,0}}^{(h)t}\hat{\boldsymbol{\Theta}}_{\mathbf{N_p,0}}^{(h)} \tag{5.181}$$

For the assumed-modes model under consideration here, the inclusion of $\mathbf{V}_{\mathbf{0,b}}^{(h)}$ in the above modal matrices enables the generation of the piezoelectric-based matrices using the truncated set of bare-

blisk mode shapes of the reference sector, rather than using the full set of assumed mode shapes; i.e., replace $\mathbf{\Psi_b}$ with $\mathbf{\Phi}_{0,b}^{(h)} = \mathbf{\Psi_b} \mathbf{V}_{0,b}^{(h)}$ in the integrals of Eq. 5.67, Eq. 5.77, and Eq. 5.118. Specifically, the modal electromechanical coupling matrix $\hat{\mathbf{\Theta}}_{k,0}^{(h)^t}$ for the kth patch becomes

$$
\begin{aligned}
\hat{\mathbf{\Theta}}_{k,0}^{(h)^t} &= \mathbf{V}_{0,b}^{(h)^t} \mathbf{K}_{be,k,0} \\
&= \mathbf{V}_{0,b}^{(h)^t} \int_{V_{p,k,j}} \frac{\bar{e}_{31,k,0} z}{z_{p2,k,0} - z_{p1,k,0}} \left(\frac{\partial^2 \mathbf{\Psi}_b^t}{\partial r^2} + \frac{1}{r} \frac{\partial \mathbf{\Psi}_b^t}{\partial r} + \frac{1}{r^2} \frac{\partial^2 \mathbf{\Psi}_b^t}{\partial \theta^2} \right) dV \\
&= \int_{V_{p,k,0}} \frac{\bar{e}_{31,k,0} z}{z_{p2,k,0} - z_{p1,k,0}} \left(\frac{\partial^2 \mathbf{\Phi}_{0,b}^{(h)^t}}{\partial r^2} + \frac{1}{r} \frac{\partial \mathbf{\Phi}_{0,b}^{(h)^t}}{\partial r} + \frac{1}{r^2} \frac{\partial^2 \mathbf{\Phi}_{0,b}^{(h)^t}}{\partial \theta^2} \right) dV
\end{aligned}
\tag{5.182}
$$

As the above equation shows, the kth patch contributes to the electromechanical coupling that depends on the sum of the modal strains integrated over the patch area. As such, maximizing the coupling requires sizing and locating the patch in a region of that encompasses large modal strains; however, if the patch covers an area where the structure is in tension and compression, the modal strains are opposite in sign. In such cases, the charge generated on the patch cancels, thereby contributing minimal electromechanical coupling to the mode in question and, consequently, resulting in a minimal variation in the modal stiffness.

For the harmonics where $h \neq 0, N_s/2$, the piezoelectric modal matrices include contributions from both cosine and sine components and are

$$\hat{\mathbf{M}}_{\mathbf{p}}^{(h)} = \mathbf{V}_{\mathbf{0,b}}^{(h,c)^t} \mathbf{M}_{\mathbf{bb,p}} \mathbf{V}_{\mathbf{0,b}}^{(h,c)} + \mathbf{V}_{\mathbf{0,b}}^{(h,s)^t} \mathbf{M}_{\mathbf{bb,p}} \mathbf{V}_{\mathbf{0,b}}^{(h,s)} \tag{5.183}$$

$$\hat{\mathbf{K}}_{\mathbf{p}}^{(h)} = \mathbf{V}_{\mathbf{0,b}}^{(h,c)^t} \mathbf{K}_{\mathbf{bb,p}} \mathbf{V}_{\mathbf{0,b}}^{(h,c)} + \mathbf{V}_{\mathbf{0,b}}^{(h,s)^t} \mathbf{K}_{\mathbf{bb,p}} \mathbf{V}_{\mathbf{0,b}}^{(h,s)} \tag{5.184}$$

$$
\begin{aligned}
\hat{\mathbf{\Theta}}^{(h)^t} &= \left[\mathbf{F}^{(h,c)^t} \otimes \mathbf{V}_{\mathbf{0,b}}^{(h,c)^t} \mathbf{K}_{\mathbf{be,1,0}} \cdots \mathbf{F}^{(h,c)^t} \otimes \mathbf{V}_{\mathbf{0,b}}^{(h,c)^t} \mathbf{K}_{\mathbf{be,N_p,0}} \right] \\
&\quad + \left[\mathbf{F}^{(h,s)^t} \otimes \mathbf{V}_{\mathbf{0,b}}^{(h,s)^t} \mathbf{K}_{\mathbf{be,1,0}} \cdots \mathbf{F}^{(h,s)^t} \otimes \mathbf{V}_{\mathbf{0,b}}^{(h,s)^t} \mathbf{K}_{\mathbf{be,N_p,0}} \right] \\
&= \left[\mathbf{F}^{(h,c)^t} \otimes \hat{\mathbf{\Theta}}_{\mathbf{1,0}}^{(h,c)^t} \cdots \mathbf{F}^{(h,c)^t} \otimes \hat{\mathbf{\Theta}}_{\mathbf{N_p,0}}^{(h,c)^t} \right] \\
&\quad + \left[\mathbf{F}^{(h,s)^t} \otimes \hat{\mathbf{\Theta}}_{\mathbf{1,0}}^{(h,s)^t} \cdots \mathbf{F}^{(h,s)^t} \otimes \hat{\mathbf{\Theta}}_{\mathbf{N_p,0}}^{(h,s)^t} \right]
\end{aligned}
\tag{5.185}
$$

$$
\begin{aligned}
\Delta \hat{\mathbf{K}}_{\mathbf{p}}^{(h)} &= \frac{1}{K_{ee,1,0}} \left[\hat{\mathbf{\Theta}}_{\mathbf{1,0}}^{(h,c)t} \hat{\mathbf{\Theta}}_{\mathbf{1,0}}^{(h,c)} + \hat{\mathbf{\Theta}}_{\mathbf{1,0}}^{(h,s)t} \hat{\mathbf{\Theta}}_{\mathbf{1,0}}^{(h,s)} \right] + \cdots \\
&\quad + \frac{1}{K_{ee,N_p,0}} \left[\hat{\mathbf{\Theta}}_{\mathbf{N_p,0}}^{(h,c)t} \hat{\mathbf{\Theta}}_{\mathbf{N_p,0}}^{(h,c)} + \hat{\mathbf{\Theta}}_{\mathbf{N_p,0}}^{(h,s)t} \hat{\mathbf{\Theta}}_{\mathbf{N_p,0}}^{(h,s)} \right]
\end{aligned}
\tag{5.186}
$$

With expressions developed for both the open- and short-circuit states of the blisk, solving the eigenproblems generates the estimates of the natural frequencies required for calculating the electromechanical coupling coefficients for the specified harmonic.

5.2.2 Evaluation of the Coupling Coefficients Neglecting the Mechanical Influence of the Patches

Next, consider the case where the patch thickness is much smaller than the blade thickness such that the patches do not appreciably contribute to the blade mass and stiffness. As such, $\hat{\mathbf{M}}_{\mathbf{p}}^{(h)} = \hat{\mathbf{K}}_{\mathbf{p}}^{(h)} = \mathbf{0}$

and the short-circuit modal equations reduce to the bare-blisk modal equations:

$$\mathbf{I}\ddot{\boldsymbol{\eta}} + \boldsymbol{\Omega}_0^{(h)}\boldsymbol{\eta} = \mathbf{0} \tag{5.187}$$

and the short-circuit natural frequencies are the same as the bare-blisk natural frequencies. Also, the open-circuit modal equations reduce to

$$\mathbf{I}\ddot{\boldsymbol{\eta}} + [\boldsymbol{\Omega}_0^{(h)} + \Delta\hat{\mathbf{K}}_\mathbf{p}]\boldsymbol{\eta} = \mathbf{0} \tag{5.188}$$

In general, $\Delta\hat{\mathbf{K}}_\mathbf{p}$ is not diagonal and the open-circuit modal stiffness has off-diagonal components that lightly couple the modes; however, the diagonal terms dominate and closely approximate the open-circuit natural frequencies. For the $h = 0, N_s/2$ harmonics, this approximation yields the rth open-circuit natural frequencies and coupling coefficients

$$\omega_{0,\text{oc},r}^{(h)^2} \approx \omega_{0,\text{sc},r}^{(h)^2} + \sum_{k=1}^{N_p} \frac{\hat{\theta}_{k,0,r}^{(h)^2}}{K_{ee,k,0}} \tag{5.189}$$

$$k_{\text{eff},r}^{(h)^2} \approx \frac{\sum_{k=1}^{N_p} \frac{\hat{\theta}_{k,0,r}^{(h)^2}}{K_{ee,k,0}}}{\omega_{0,\text{sc},r}^{(h)^2} + \sum_{k=1}^{N_p} \frac{\hat{\theta}_{k,0,r}^{(h)^2}}{K_{ee,k,0}}} \tag{5.190}$$

and for all other harmonics:

$$\omega_{0,\text{oc},r}^{(h)2} \approx \omega_{0,\text{sc},r}^{(h)2} + \sum_{k=1}^{N_p} \frac{\hat{\theta}_{k,0,r}^{(h,c)2} + \hat{\theta}_{k,0,r}^{(h,s)2}}{K_{ee,k,0}} \tag{5.191}$$

$$k_{\text{eff},r}^{(h)2} \approx \frac{\sum_{k=1}^{N_p} \frac{\hat{\theta}_{k,0,r}^{(h,c)2} + \hat{\theta}_{k,0,r}^{(h,s)2}}{K_{ee,k,0}}}{\omega_{0,\text{sc},r}^{(h)2} + \sum_{k=1}^{N_p} \frac{\hat{\theta}_{k,0,r}^{(h,c)2} + \hat{\theta}_{k,0,r}^{(h,s)2}}{K_{ee,k,0}}} \tag{5.192}$$

In the above equation, for either the cosine or sine mode, the opposing mode has zero electromechanical coupling (i.e., when $\hat{\theta}_{k,0,r}^{(h,c)} \neq 0$, $\hat{\theta}_{k,0,r}^{(h,s)} = 0$). This analytical estimation of the electromechanical coupling coefficient can be useful tool for the initial patch sizing and placement for any piezoelectric-based system. The estimate derived here only uses the natural frequencies and mode shapes of the tuned blisk, thus enabling a rapid means of estimating the coupling for any configuration of patches.

As an example, consider the 8-sector tuned blisk discussed previously in Section 5.1.9.3, but with rectangular piezoelectric patches arbitrarily sized and located at each blade root. Figure 5.8 shows two of the 4ND bare-blisk modes that correspond to the first bending (1B) and third torsion (3T) mode families and with the color scheme corresponding to the modal displacement. Figure 5.9 shows the same two modes but with the color scheme corresponding to the sum of the modal strains at each spatial location. For the 1B/4ND mode, the rectangular patch encloses an area of high modal strain near the blade root, whereas for the 3T/4ND mode, the rectangular patch encloses an area where the blade is in both tension and compression with modal strains that are equal in magnitude but opposite in sign.

166

Figure 5.10 shows the effect that increasing the patch thickness (normalized by the blade stiffness) has on the coupling coefficients for both the 1B/4ND and 3T/4ND modes. For each mode, this figure shows the coupling coefficients generated using the full set of assumed modes that includes 96 modes for the disk and 64 modes for the blades, the truncated set of 20 bare-blisk modes per harmonic, and the analytical estimation from Eqs. 5.190 and 5.192. For small patch thicknesses ($<$ 10% blade thickness), the coupling coefficients for the 1B/4ND modes converge to the analytical estimate as the patch contributes negligible mass and stiffness to each blade. Increasing the patch thickness causes the coupling coefficients generated from the first two methods to diverge from the analytical estimate, thus indicating that there is an appreciable influence on the blade mass and stiffness contributed by the patch. For all thickness values, the coefficients obtained used the truncated set of modes show good agreement with those obtained using the full set of assumed modes, but with a fraction of the computational cost. Increasing the number of modes included in the truncated set can diminish the slight overestimation of the coupling coefficients, but at the expense of an increased computation time. Furthermore, the coupling coefficients for the 3T/4ND modes are zero for all patch thickness values. As the blades are in both tension and compression within the area enclosed by the patches, the generated charge cancels, thus resulting in the minimal coupling.
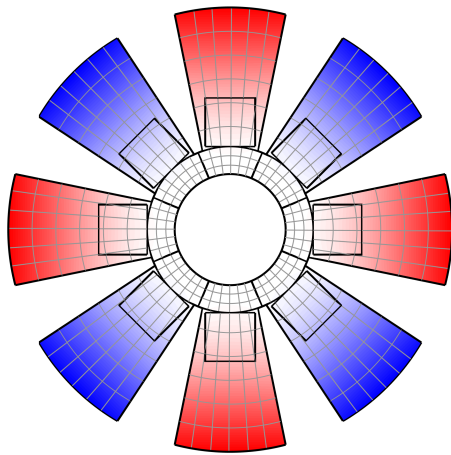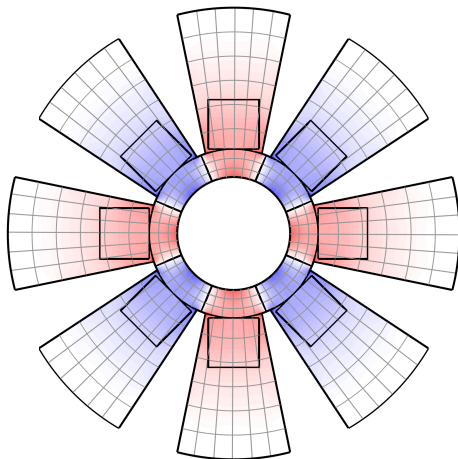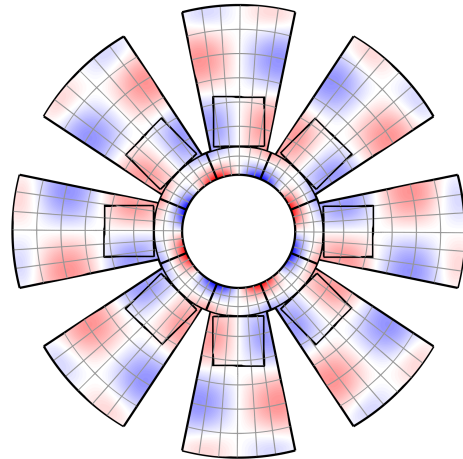
(a) 1B/4ND mode shape.
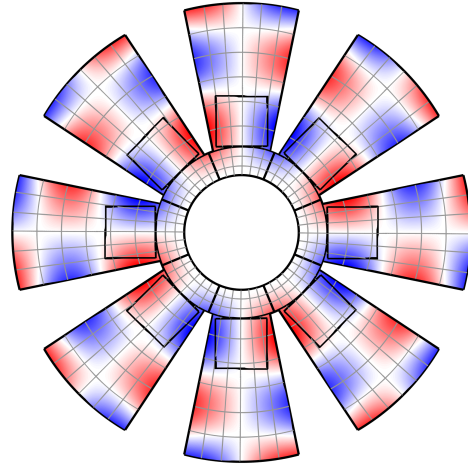
(b) 3T/4ND mode shape.

Figure 5.8: Example mode shapes of the blisk with the blade-mounted piezoelectric patches where the color scheme corresponds to the modal displacements.

(a) 1B/4ND mode shape.

(b) 3T/4ND mode shape.

Figure 5.9: Example mode shapes of the blisk with the blade-mounted piezoelectric patches where the color scheme corresponds to the sum of the modal strains.
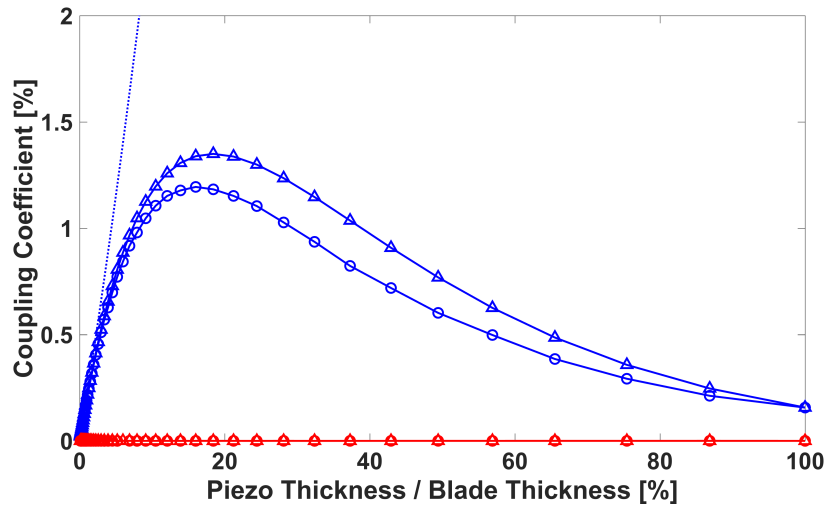
Figure 5.10: Effect of piezoelectric thickness on the electromechanical coupling coefficients for the 1B/4ND mode (blue) and 3T/4ND (red). For each mode, the figure shows the coupling coefficients obtained using the full set of assumed modes (solid with circles), a truncated set of bare-blisk modes (solid with triangles), and the analytical estimation utilizing the bare-blisk natural frequencies and mode shapes (dashed).

5.2.3 Multi-Objective Optimization

Designing a piezoelectric-based system with the piezoelectric materials functioning as actuators, sensors, or vibration-reduction mechanisms, often requires a design that targets multiple vibration modes. As the preceding section showed, the electromechanical coupling largely depends on the modal strain distribution throughout the patch volume. As such, locating and sizing a network of piezoelectric materials to generate strong electromechanical coupling in some modes can lead to weak coupling in others, thus resulting in a trade-off between maximizing the coupling of the various target modes. Furthermore, the design may also require minimizing the total patch volume such that the patches do not significantly alter the dynamics of the initial system. As with any optimization problem, optimizing the piezoelectric patches requires defining an appropriate objective

169

function. Considering the maximization of the electromechanical coupling over multiple modes and the simultaneous minimization of the patch volume, the objective function to minimize is

$$J = w_1 V_p - \sum_{r=1}^{N_r} w_{r+1} k_{\text{eff},r}^2 \qquad (5.193)$$

The inclusion of multiple objectives within the objective function can lead to multiple optimal solutions depending on the assignment of the weights. As such, this type of optimization problem is an ideal candidates for application of a multi-objective optimization procedure. Rather than optimizing a single objective function, multi-objective optimization considers multiple objectives

$$J_1 = V_p, \quad J_2 = -k_{\text{eff},1}^2, \quad \cdots \quad J_{N_r+1} = -k_{\text{eff},N_r}^2 \qquad (5.194)$$

and produces so-called Pareto-optimal fronts composed of the Pareto-optimal solutions. These Pareto-optimal fronts can visually aid the designer in choosing designs with acceptable tradeoffs between the various objectives. A solution is weakly Pareto-optimal, or non-dominated, if there does not exist any other solutions that improve all objectives; i.e., all other solutions degrade at least one objective [104]. The multi-objective optimization procedure used here is the non-dominated sorting genetic algorithm (NSGA-II). [105] This procedure has recently been applied for a piezoelectric-based system that required the optimization of sets of patches for active vibration control of stationary and rotating cantilever beams using controllability as the performance measure. [106] NSGA-II incorporates a rapid-sorting algorithm to sort each solution based on their non-dominance ranking and incorporates this ranking into the solution's fitness measure. The

candidate solutions with a non-dominance rank of zero correspond to the Pareto-optimal front that consists of all non-dominated solutions. A non-dominance rank of one corresponds to candidates that, after removing the rank-zero candidates from the population pool, are non-dominated with respect to all remaining candidates, and so on. NSGA-II also incorporates a crowding-distance measure into the candidate's fitness to preserve genetic diversity within the population, thereby enabling a better spread within the Pareto-optimal front. After creating an initial population of N_{pop} total candidates and assigning a fitness based on the aforementioned criteria, a binary tournament selection procedure identifies two candidates for mating and performs a genetic crossover at a probability of P_{cross} and a mutation at a probability P_{mut}. The process then inserts the generated offspring into the parent population and sorts the updated population again by the non-dominance ranking and retains only the N_{pop} most fit candidates. The process then iterates over N_{gen}, or until satisfying a specified threshold.

In general, the optimization procedure can optimize the piezoelectric patch's geometric parameters and location/orientation on the blade; often times, however, test prototypes utilize off-the-shelf piezoelectric patches that have fixed dimensions. This analysis simplifies the optimization by only considering a single patch per blade with fixed dimensions. As such, the only parameters to optimize are the patch's location and orientation (either 0° or 90°). Furthermore, the optimization procedure seeks to maximize the coupling for the 4ND modes of the blisk examined in Section 5.1.9.3 and for the mode families associated with the blade's 1st bending (1B) mode, 2nd bending (2B) mode, and the mode showing a mixture of 3rd bending and 1st chord-wise bending (3B1CB), producing a "saddle" shape. Each patch consists of a piezoceramic (PZT-5H) with the

parameters shown in Table 5.3. The optimization begins by first generating an initial population with parameters that confine the patches within the blade boundaries. After identifying two candidates for mating, performing an arithmetic crossover ensures the offspring generation includes patches with dimensions that satisfy the system constraints. Furthermore, if the offspring undergoes a mutation, randomly selecting the mutated value from a list of feasible values that satisfy the system constraints will ensure the feasibility of the mutated offspring. After some experimentation, the algorithm parameters $N_{pop} = 150$, $N_{gen} = 150$, $P_{cross} = 0.9$, and $P_{mut} = 0.05$ showed satisfactory performance.

Figure 5.11 shows the Pareto-optimal fronts obtained from the optimization that exhibit the tradeoffs between the coupling coefficients for the 1B/4ND, 2B/4ND, and 3B/1CB modes. For patch configurations that maximize coupling for the 1B mode, there is a reduced coupling for the other two modes. Consider the patch configuration A identified with a red square in the figures. Figure 5.12 shows the blisk mode shapes with the color scheme corresponding to the sum of the modal strains at each spatial location. The left plots correspond to patch configuration A and show that the patch resides near the blade root where there is maximum modal strain for the 1B/4ND mode, thus producing $k^2_{1B} = 1.15\%$. For the 2B/4ND and 3B1CB/4ND modes, patch A is located away from the region of maximum modal strain that exists near the center of the blade; however, some strain is still present, thus producing $k^2_{2B} = 0.75\%$ and $k^2_{3B1CB} = 0.95\%$. Next, consider patch configuration B identified with a gold circle in Fig. 5.11; this configuration shows increased coupling for the 2B/4ND and 3B1CB/4ND modes, but reduced coupling for the 1B/4ND mode. The right plots in Fig. 5.12 correspond to patch configuration B and show that locating the patches

near the middle of the blades increases the coupling for the 2B/4ND and 3B1CB/4ND modes to $k_{2B}^2 = 1.97\%$ and $k_{3B1CB}^2 = 3.13\%$, respectively. At this location, minimal strain exists for the 1B/4ND mode, thus reducing the coupling to $k_{1B}^2 = 0.11\%$. The blisk manufactured and utilized for the experimental analysis in Ch. 6 utilizes patch configuration B due to the large coupling that exists for the 2B and 3B1CB modes.

Table 5.3: Piezoelectric patch parameters.

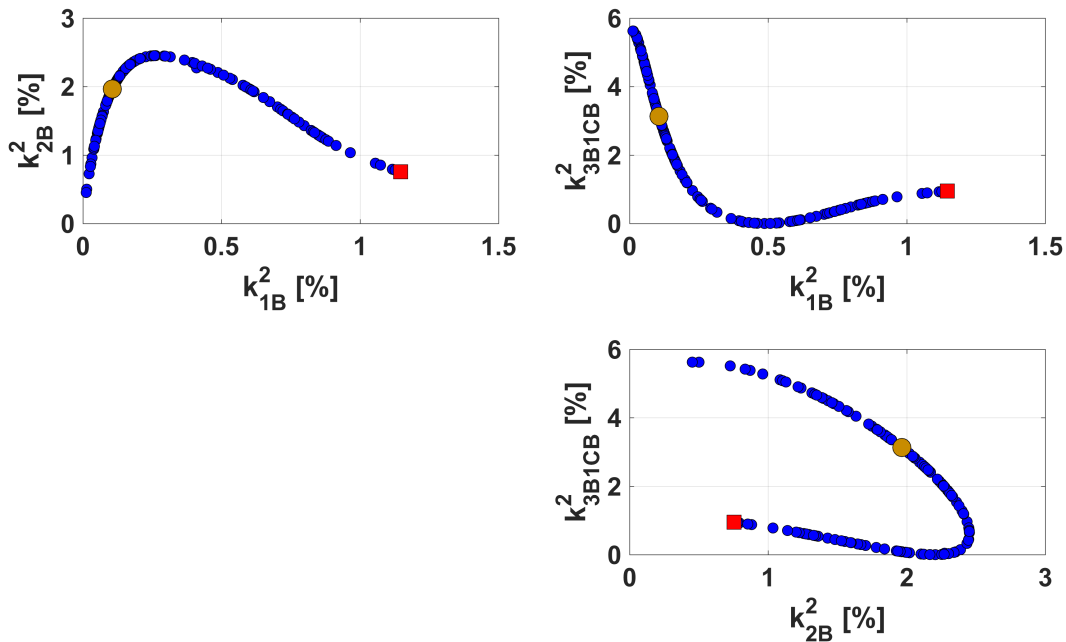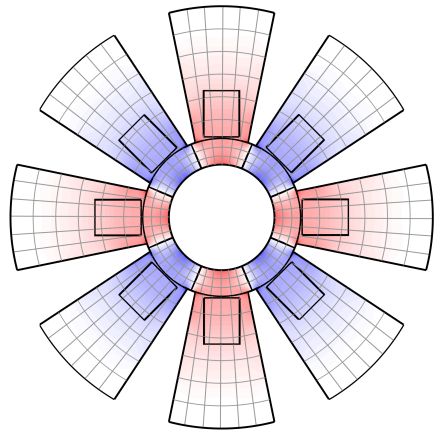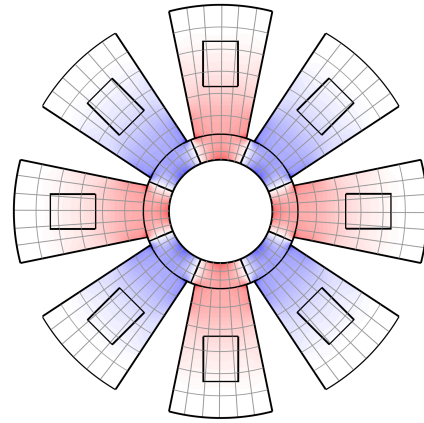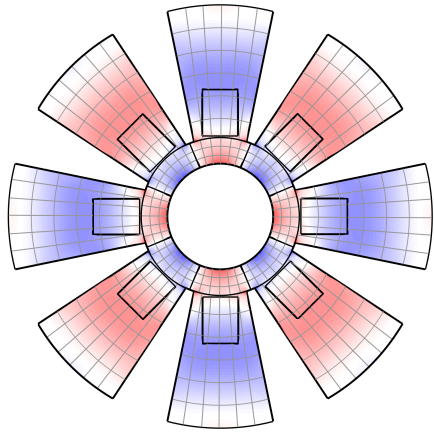| Piezoceramic (PZT-5H)	
Length [mm]	44.50
Width [mm]	34.29
Thickness [mm]	0.27
% Blade Vol.	2.65

Figure 5.11: Pareto-optimal fronts (blue circles) showing the tradeoffs between the three objectives. Also shown are the solutions for patch configuration A (red square) and patch configuration B (gold circle).
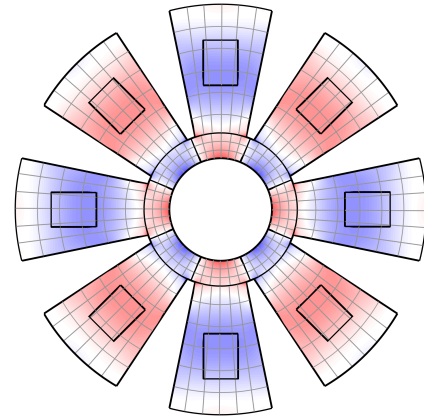
(a) 1B mode shape: Piezo A.

(b) 1B mode shape: Piezo B.

(c) 2B mode shape: Piezo A.

(d) 2B mode shape: Piezo B.
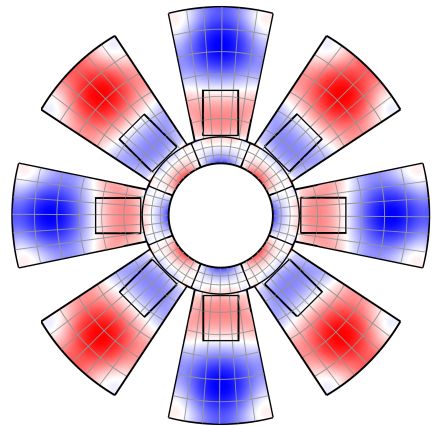
(e) 3B1CB mode shape: Piezo A.
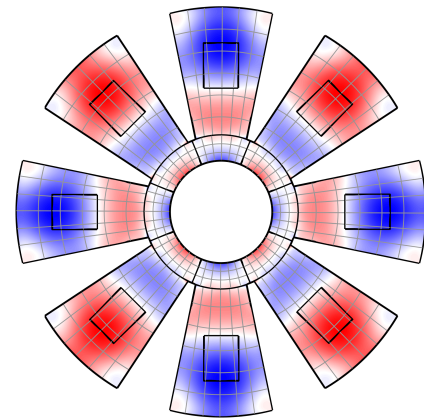
(f) 3B1CB mode shape: Piezo B.

Figure 5.12: The 4ND mode shapes targeted to optimize the electromechanical coupling with the color scheme corresponding to the sum of the modal strains at each spatial position. The left figures correspond to patch configuration A (red square in Fig. 5.11), whereas the right figures correspond to patch configuration B (gold circle in Fig. 5.11).

Finally, a finite-element model developed in NX 12.0 provides a source of validation for the assumed-modes model that includes the influence of the blade-mounted piezoelectric patches; both models consider patch configuration B obtained from the optimization. The finite-element model is similar to that utilized in Section 5.1.9.3, but includes the piezoelectric pacthes. Although NX 12.0 does not explicitly contain piezoelectric elements to model these patches, defining an anisotropic material with the material properties corresponding to PZT-5H poled through the thickness enables the simulation of both the open- and short-circuit cases. For the short-circuit case, this requires utilizing the stiffness matrix at a constant electric field ($\mathbf{c}^E$ in Eq. 2.1); whereas for the open-circuit case, this requires utilizing the stiffness matrix at a constant electric displacement ($\mathbf{c}^D$ in Eq. 2.3). Figure 5.13 shows the nodal-diameter map of the tuned blisk with all piezoelectric patches operating in the short-circuit state and shows that both solutions obtained from the assumed-modes model and the finite-element model show excellent agreement. The frequency curves show a slight upward shift compared to the curves obtained from the bare blisk and shown in Fig. 5.4, thus indicating that the patches slightly stiffen each blade.

Figure 5.14 shows the coupling coefficient as a function of nodal diameter for each mode family. As the patch parameters obtained from the optimization target both the 2B and 3B1CB mode families, these families exhibit the largest coupling, especially for the 4ND modes. These modes also exhibit a slight increase in coupling for increasing nodal diameter. This effect indicates that for each nodal diameter, there are slight variations in the mode shape that alter the modal strain distribution. Although for these two mode families, the coupling remains large over all nodal diameters, the two-stripe (2S) mode family exhibits a strong nodal-diameter dependence

for the coupling where the coupling vanishes for the 3ND and 4ND modes. This nodal-diameter-dependent coupling demonstrates the importance in performing the optimization for the entire blisk, rather than for the stand-alone blades.

Figure 5.14 also shows the coupling coefficients obtained from both the assumed-modes and finite-element models. The coupling coefficients obtained from both approaches show the same general trends; however, the ones obtained from the assumed-modes model slightly overestimate the ones obtained from the finite-element model. An experimental analysis undertaken by Kauffman for a cantilevered blade, idealized as a trapezoidal plate, showed a similar overestimation in the coupling coefficients [80]. As the coupling largely depends on the modal strain distribution, and, hence, the mode shapes, increasing the number of modes in the model should increase the accuracy of the coupling estimates, but showed little effect. This result may indicate that the assumed-modes model is not fully capable of converging to the true mode shapes, or that the model requires inclusion of a significantly larger number of assumed modes that is not computationally feasible. [107] Another source of discrepancy may arise in the thin-plate assumption utilized by the assumed-modes model that neglects the out-of-plane stresses, whereas the finite-element model incorporates the full three-dimensional stress field. As such, the in-plane strains induced in the patches may be larger for the assumed-modes model, thus resulting in the larger coupling coefficients.
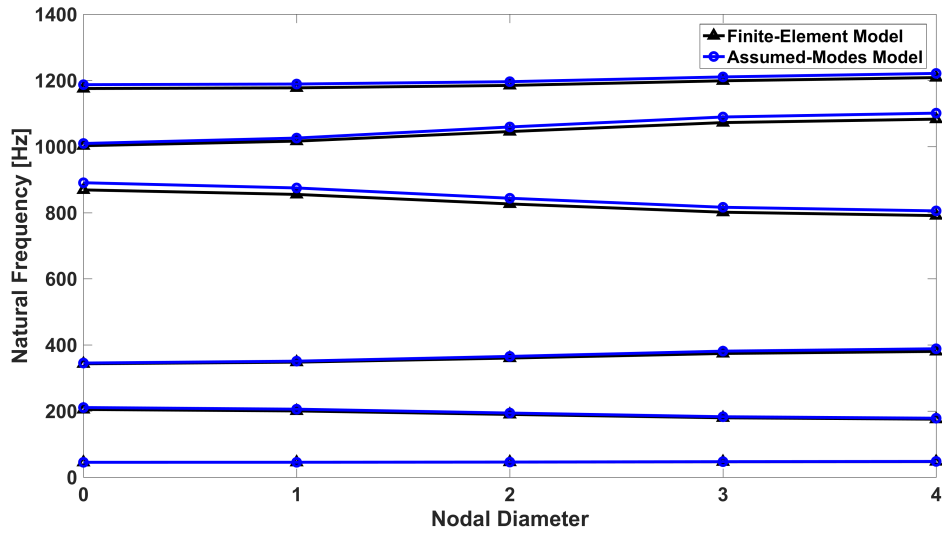
Figure 5.13: Nodal diameter map of the tuned blisk with all piezoelectric patches operating in the short-circuit state for the first six mode families.
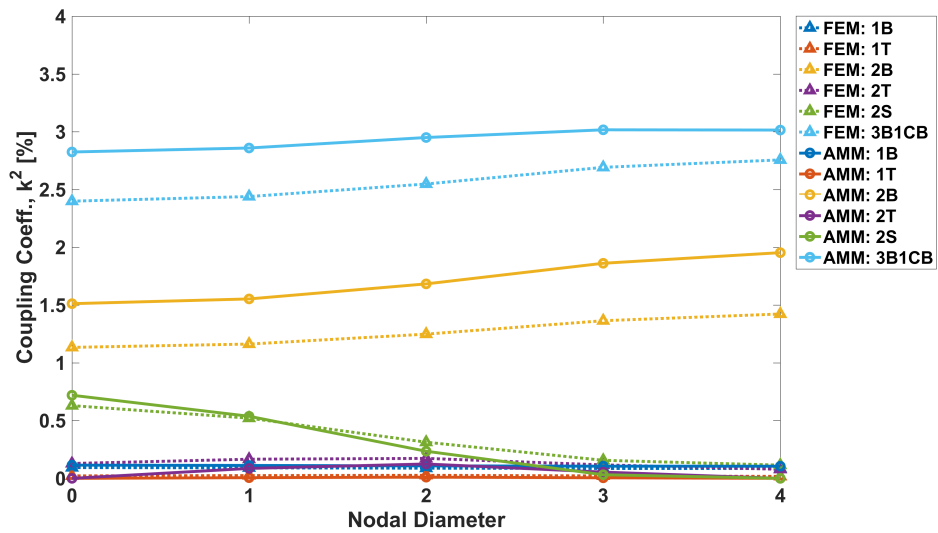

Figure 5.14: Tuned-blisk coupling coefficients as a function of the nodal diameter for the first six mode families.

CHAPTER 6
APPLICATION TOWARDS AN ACADEMIC BLISK—PART 2:

EXPERIMENTAL ANALYSIS

This chapter provides the results from the experimental analysis used to validate the RFD concept. This analysis incorporates the blisk and optimal piezoelectric parameters identified in Ch. 5. Section 6.1 details the 8-blade blisk experimental setup. Section 6.2 details the modal tests performed to experimentally characterize the blisk. It presents the modal parameters for the blisk in both the open- and short-circuit operating states. Section 6.3 describes the development of a hybrid numerical model that utilizes the experimental modal data; this model enables the application of the genetic algorithm previously developed in Ch. 4 to identify the optimal triggers. This section also presents a comparison between numerical simulations and the experimental tests for several engine-order excitations.

6.1   Hardware Setup

The experimental setup consists of the same academic blisk described in the preceding chapter. Figure 6.1 shows the 8-blade academic blisk machined from a single sheet of aluminum and clamped on both sides of the central hub. The overhang between the blades and the clamped

region of the hub facilitated the mechanical coupling between neighboring blades. This figure also shows the piezoelectric patches (Piezo Systems, Inc. T110-H4E-602) bonded on both sides of the blades in a collocated manner, and the accelerometers (PCB Piezotronics 352A21) mounted with wax on each blade tip used to measure the tip response.
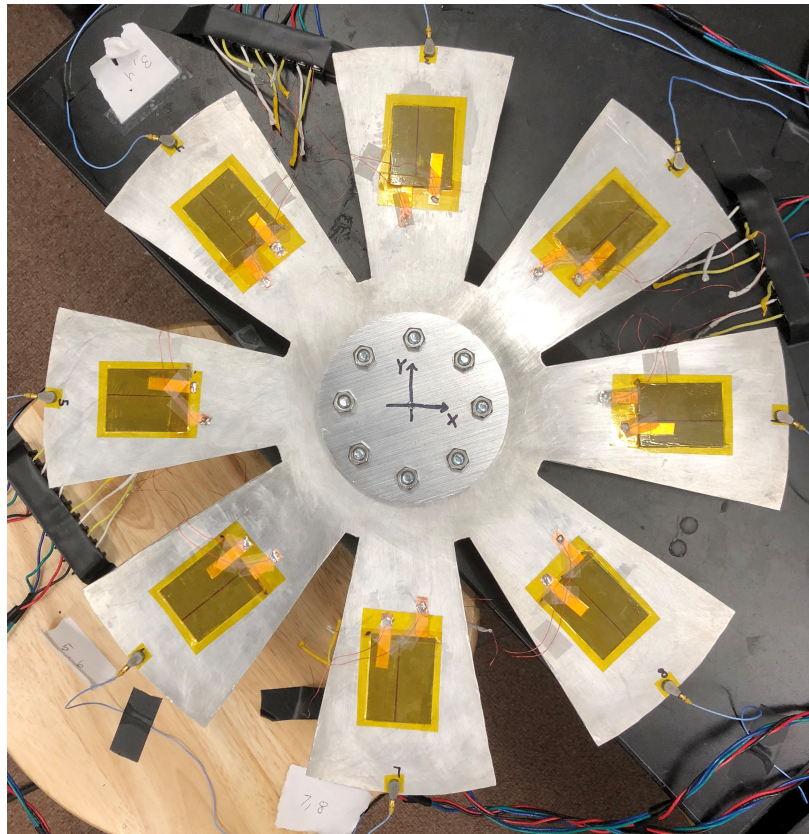
Figure 6.1: Academic blisk with blade-mounted piezoelectric patches used in the experimental study.

The sets of patches located on the top and bottom surfaces operated in two separate manners: 1) The patches on one surface operated as actuators to generate the traveling-wave excitation for a user-defined engine order. A digital-to-analog converter (National Instruments 9263) connected to these actuator patches provided a constant amplitude, sinusoidal voltage with a blade-dependent phase governed by Eq. 3.13. 2) The patches on the opposite surface provided the stiffness-state

modulation by attaching each patch to a shunt circuit containing a single reed relay (Coto Technology 9007-05-00). A similar digital-to-analog converter provided a single "on/off" voltage command, amplified by a transistor, to all relays to enforce the simultaneous switching of all patches between the open- and short-circuit states.

6.2 Modal Parameters

Identification of the optimal triggers via the genetic algorithm presented in Ch. 4 requires a model that accurately represents the experimental blisk and includes obtaining the blisk's modal parameters (i.e., natural frequencies, modal damping values, and mode shapes). As the blisk already incorporates piezoelectric patches functioning as dedicated actuators, these same patches can also provide the forcing mechanism to excite the blisk over a frequency spectrum containing the vibration modes of interest.

One such method to control the frequency content is to send a Gaussian-shaped pulse to one of the patches, effectively exciting the system in a similar manner as in typical modal-hammer tests [108]. Due to the light coupling between blades, to excite all blades sufficiently using only a single patch required a large actuation voltage; however, this large voltage induced a nonlinear response for the blade where the actuator patch was mounted. Instead, exciting the blisk with all patches simultaneously distributes the actuation energy around the blisk, rather than localizing the actuation energy on a single blade, thus preserving the operation of all blades within the linear regime. Furthermore, as the mistuned nature of the blisk causes each mode shape to contain a

distribution of spatial harmonic content, actuating the blades with engine-order excitation supplied through the actuator patches will excite all modes, provided they contain some spatial-harmonic content equal to the chosen engine order. Figure 6.2 shows that forcing the blisk with 1EO excitation sufficiently excites all modes within 1050-1250 Hz frequency band that corresponds to the 3B1CB mode family. This figure shows the frequency response for both the open- (blue curves) and short-circuit (red curves) states. It also shows the response of all blades (light, thin curves), and the maximum blade response (dark, thick curves) at each frequency line. When operating in either the open- or short-circuit state, there is a near identical response, but with a clear downwards shift in resonance frequencies for the short-circuit state compared to the open-circuit state.

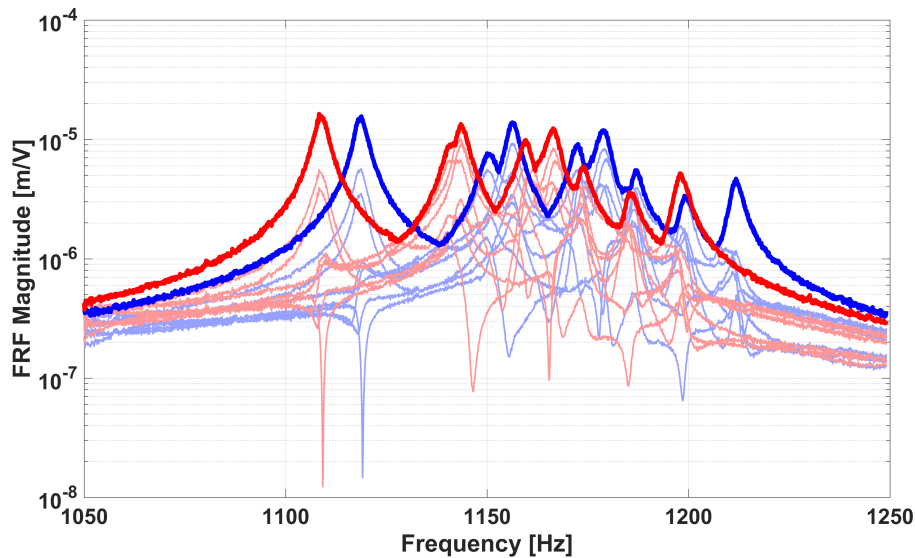Figure 6.2: Experimental frequency response for all blades subjected to 1EO excitation supplied by the piezoelectric patches. This figure shows the response for both the open-circuit (blue) and short-circuit (red) states.

The frequency response of the system subjected to the engine-order excitation supplied by the patches occurs in a similar form to that of an input force, thus enabling the use of typical frequency

domain methods to extract the blisk's modal parameters. For example, consider the equations of motion for a blisk including piezoelectric materials, the equations of motion in matrix form are

$$\mathbf{M\ddot{x}} + \mathbf{C\dot{x}} + \mathbf{Kx} - \mathbf{\Theta}^t \mathbf{V_A} = \mathbf{f_m} \tag{6.1}$$

where $\mathbf{V_A}$ is a vector piezoelectric actuation voltages and $\mathbf{K}$ is the blisk stiffness matrix in either the open- or short-circuit states. As one set of piezoelectric patches provide the excitation rather than an external mechanical force, these equations become

$$\mathbf{M\ddot{x}} + \mathbf{C\dot{x}} + \mathbf{Kx} = \mathbf{\Theta}^t \mathbf{V_A} \tag{6.2}$$

Using the modal transformation

$$\mathbf{x} = \mathbf{\Phi\eta} \tag{6.3}$$

and premultiplying the equations of motion by $\mathbf{\Phi}^t$, the modal equations of motion are

$$\mathbf{\hat{M}\ddot{\eta}} + \mathbf{\hat{C}\dot{\eta}} + \mathbf{\hat{K}\eta} = \mathbf{\hat{\Theta}}^t \mathbf{V_A} \tag{6.4}$$

Considering only a single mode, the modal equation is

$$\ddot{\eta}_r + 2\zeta_r \omega_r \dot{\eta}_r + \omega_r^2 \eta_r = \frac{1}{\hat{m}_r} \sum_{j=0}^{N_s-1} \hat{\theta}_{j,r} V_{A,j} \tag{6.5}$$

For engine-order excitation supplied through the piezoelectric patches, the magnitude of the voltage is constant with a blade-dependent phase. In complex form, the voltage supplied by the piezoelectric patch on the jth blade is

$$V_{A,j} = V_{A0}e^{i\omega t}e^{i\gamma_j} \tag{6.6}$$

Assuming the rth modal response is also sinusoidal such that

$$\eta_r = \eta_{0,r}e^{i\omega t} \tag{6.7}$$

the frequency response of this mode with respect to the voltage supplied by the patch on the reference sector is

$$H_{\eta,r}(\omega) = \frac{\eta_{0,r}}{V_{A0}} = \frac{\frac{1}{\hat{m}_r}\sum_{j=0}^{N_s-1}\hat{\theta}_{j,r}e^{i\gamma_j}}{\omega_r^2 - \omega^2 + i2\zeta_r\omega_r\omega} \tag{6.8}$$

Summing over all modes and including the effects of any residual modes outside the frequency band of interest, the frequency response of the jth blade tip is

$$H_j(\omega) = \frac{x_j}{V_{A0}} = \sum_{r=1}^{N_r} \frac{A_{j,r}}{\omega_r^2 - \omega^2 + i2\zeta_r\omega_r\omega} - \frac{LR_j}{\omega^2} + UR_j \tag{6.9}$$

where $A_{j,r}$ is the modal amplitude that represents the contribution of the rth mode to the jth blade's response such that

$$A_{j,r} = \frac{1}{\hat{m}_r}\phi_{j,r}\sum_{j=0}^{N_s-1}\hat{\theta}_{j,r}e^{i\gamma_j} \tag{6.10}$$

The above form of the frequency response function is similar to that of the response function corresponding to mechanical excitation [109]. As such, the utilization of typical frequency-domain

methods enables the estimation of the blisk's modal parameters. The method chosen here is the polyreference least-squares complex frequency-domain method, also referred to as the PolyMAX method [110, 111]. Of particular interest here, one of the strengths of the PolyMAX method is its ability to estimate modal-participation factors along with the poles (natural frequencies and modal damping ratios) when constructing the stabilization diagram. This feature enables the PolyMAX method to more easily resolve the closely-spaced modes expected in mistuned blisks.

Table 6.1 shows the modal parameters for the 3B1CB mode family obtained from the Poly-MAX method implemented in MATLAB. This table also shows the modal parameters for the blisk with all blades operating in either the open- or short-circuit state. The blisk is lightly damped with all damping values equal to or below 0.2% critical damping. The damping for each mode is also relatively constant between the open- and short-circuit states suggesting that the switch between stiffness states has a negligible effect.

Table 6.1: Blisk modal parameters for the 3B1CB mode family.

Mode	Freqs. [kHz]		Damping [%]		k^2_{eff} [%]
	OC	SC	OC	SC	
1	1.119	1.109	0.13	0.14	1.80
2	1.151	1.141	0.20	0.18	1.68
3	1.156	1.143	0.10	0.09	2.23
4	1.173	1.160	0.13	0.14	2.16
5	1.179	1.167	0.13	0.14	2.15
6	1.187	1.174	0.09	0.11	2.19
7	1.199	1.186	0.11	0.14	2.23
8	1.212	1.198	0.11	0.13	2.28

Furthermore, this mode family exhibits excellent electromechanical coupling with a coupling coefficient of $k^2_{\text{eff,avg}} = 2.09\%$ averaged over all modes of the family; however, the average coupling

coefficient obtained from the tuned numerical model for the same mode family is $k_{\text{eff,avg}}^2 = 2.93\%$.

Taking the experiment as truth, the average coupling coefficient obtained by the model overestimates the experimental coupling coefficient by 40.9%. These discrepancies in the measured coupling may arise from multiple sources. A first source is the limitations of the assumed-modes model as discussed previously in Section 5.2.3. A second source is the existence of the bond layer between the patch and the blade surfaces. The numerical model assumed an ideal bond between the patch and blade surface that results in the transmission of the entire strain from the the blade to the patch. Realistically, a thin bond layer exists between these two surfaces and contributes shear-lag losses that result in a less-efficient transmission of strain [112]. As the electromechanical coupling for a particular mode depends largely on the modal strain, any reduction in the strain transmitted to the patches will result in a loss of electromechanical coupling. A third source of discrepancy may arise due to the presence of the accelerometers and associated cabling in the experimental setup. The blisk utilized here is relatively thin such that the added mass contributed by the sensors may not be negligible. This mass loading can not only drive down the observed natural frequencies, but it can also alter the mode shapes and, consequently, the modal strain distribution, thus affecting the electromechanical coupling.

Figure 6.3 shows both the the experimental mode shapes (normalized by the component of the mode shape with the largest magnitude) for each mode of the 3B1CB mode family (left plots), and also as the associated Fourier coefficients (right plots). This figure also shows these quantities corresponding to the open- (blue) and short-circuit (red) states. The mistuning spreads the spatial-harmonic content to all modes with varying degrees. Furthermore, the mode shapes between both

185

the open- and short-circuit states are nearly identical indicating the stiffness increase across all

blades on the blisk is also nearly identical; however, there are some slight discrepancies, especially

distinguishable in the 2nd and 3rd modes. These discrepancies most likely arise due to the addi-

tional mistuning stemming from patch implementation. These mistuning sources may include the

manufacturing of the piezoelectric patches themselves, the mounting locations, and even the size

of the bond layer at each mounting location. This mistuning, however, is small compared to the

overall mistuning present for the blisk, thereby resulting in only small discrepancies between the

mode shapes between the two stiffness states.

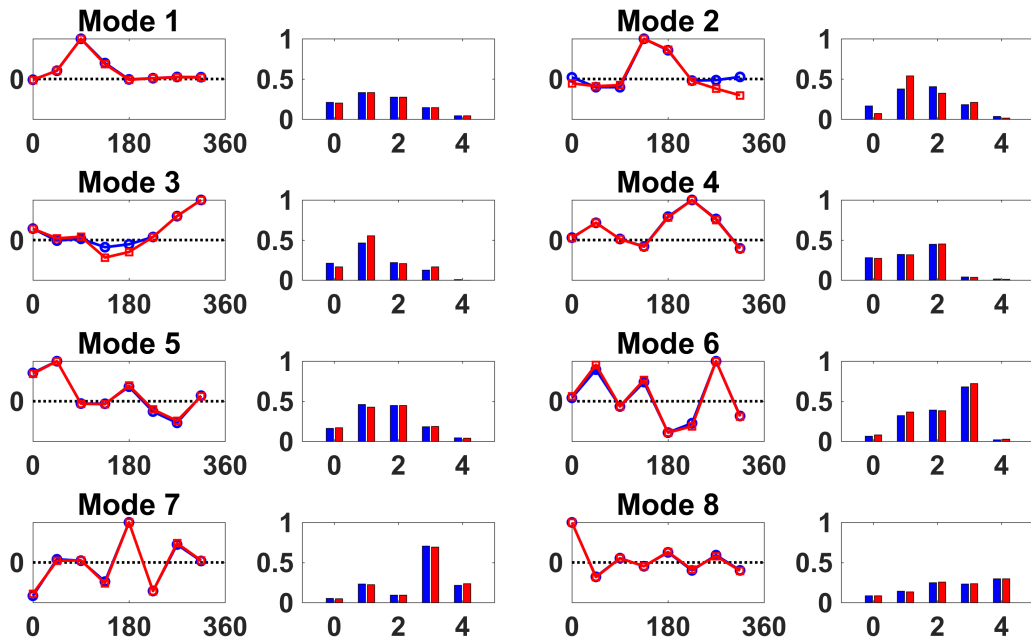Figure 6.3: Unwrapped mistuned mode shapes (left plots) where the ordinate corresponds to the blade number. Also shown is the magnitude of the Fourier components for each mode shape (right stem plots) where the ordinate corresponds to the spatial harmonic number (nodal diameter). All plots include quantities corresponding to the blades operating in the open-circuit (blue) and short-circuit (red) states.

6.3 RFD Application

As it currently stands, application of RFD requires a model to identify the optimal sets of switch triggers. As such, the experimental characterization of the blisk enables the generation of a hybrid model utilizing the lumped-parameter model developed in Section 3.1 with the experimental modal data. Furthermore, the optimal trigger identification only requires relative quantities, thereby enabling the use of the nondimensional form of the equations of motion. The nondimensional variables are the same as defined in Eqs. 3.15-3.21 but with time nondimensionalized by the mean natural frequency of the mode family. Also, one set of the piezoelectric patches functions as actuators that generates the traveling-wave excitation and requires the replacement of the mechanical force in the nondimensionalization procedure by the force generated by the actuation voltage such that $f_{m,0} = \theta_A V_{A0}$. The resulting nondimensional equations of motion for an 8-sector blisk are

$$\bar{\mathbf{M}}\bar{\mathbf{x}}'' + \bar{\mathbf{C}}\bar{\mathbf{x}}' + \bar{\mathbf{K}}\bar{\mathbf{x}} = \bar{\mathbf{V}}_{\mathbf{A}} + \bar{\mathbf{F}}_{\mathbf{sw}} \tag{6.11}$$

where the mass, damping, and stiffness matrices, as well as the piezoelectric forcing vector and the switch-induced forcing vector are

$$\bar{\mathbf{M}} = \mathbf{I} + \Delta\bar{\mathbf{M}}_{\mathbf{exp}} \tag{6.12}$$

$$\bar{\mathbf{C}} = 2\zeta_0\mathbf{I} + \Delta\bar{\mathbf{C}}_{\mathbf{exp}} \tag{6.13}$$

$$\bar{\mathbf{K}} = \bar{\mathbf{K}}_{\mathbf{oc}} + \Delta\bar{\mathbf{K}}_{\mathbf{oc,exp}} - (\mathbf{I} - \mathbf{S})(\Delta\bar{\mathbf{K}}_{\mathbf{p}} + \Delta\bar{\mathbf{K}}_{\mathbf{p,exp}}) \tag{6.14}$$

$$\bar{\mathbf{V}}_{\mathbf{A}} = \begin{bmatrix} \bar{V}_{A,0} & \cdots & \bar{V}_{A,N_s-1} \end{bmatrix}^t \tag{6.15}$$

$$\bar{\mathbf{F}}_{\mathbf{sw}} = \mathbf{S}(\Delta\bar{\mathbf{K}}_{\mathbf{p}} + \Delta\bar{\mathbf{K}}_{\mathbf{p,exp}})\bar{\mathbf{x}}_{\mathbf{sw}} \tag{6.16}$$

These modal matrices also include the variations to the lumped-parameter model introduced by the experiment that are unknown. Furthermore, the experiment constrains all blades to switch stiffness states simultaneously such that $\mathbf{S} = s_0\mathbf{I}$. Using the measured open-circuit mode shapes enables a transformation to the modal domain with respect to the open-circuit state such that

$$\bar{\mathbf{x}} = \mathbf{\Phi}_{\mathbf{oc}}\boldsymbol{\eta} \tag{6.17}$$

Premultiplying the nondimensional equations of motion by $\mathbf{\Phi}_{\mathbf{oc}}^t$ results in the modal equations of motion

$$\hat{\mathbf{M}}\boldsymbol{\eta}'' + \hat{\mathbf{C}}\boldsymbol{\eta}' + \hat{\mathbf{K}}\boldsymbol{\eta} = \hat{\mathbf{V}}_{\mathbf{A}} + \hat{\mathbf{F}}_{\mathbf{sw}} \tag{6.18}$$

where the modal matrices and modal forcing vectors are

$$\hat{\mathbf{M}} = \boldsymbol{\Phi}_{\mathbf{oc}}^t(\mathbf{I} + \boldsymbol{\Delta}\bar{\mathbf{M}}_{\mathbf{exp}})\boldsymbol{\Phi}_{\mathbf{oc}} = \mathbf{I} \tag{6.19}$$

$$\hat{\mathbf{C}} = \boldsymbol{\Phi}_{\mathbf{oc}}^t(2\zeta_0\mathbf{I} + \boldsymbol{\Delta}\bar{\mathbf{C}}_{\mathbf{exp}})\boldsymbol{\Phi}_{\mathbf{oc}} = \mathbf{diag}(2\zeta_1\bar{\omega}_{\mathrm{oc},1},\cdots,2\zeta_{N_s}\bar{\omega}_{\mathrm{oc},N_s}) \tag{6.20}$$

$$\hat{\mathbf{K}} = \boldsymbol{\Phi}_{\mathbf{oc}}^t[\bar{\mathbf{K}}_{\mathbf{oc}} + \boldsymbol{\Delta}\bar{\mathbf{K}}_{\mathbf{oc,exp}} - (1-s_0)(\boldsymbol{\Delta}\bar{\mathbf{K}}_{\mathbf{p}} + \boldsymbol{\Delta}\bar{\mathbf{K}}_{\mathbf{p,exp}})]\boldsymbol{\Phi}_{\mathbf{oc}}$$
$$= \mathbf{diag}(\bar{\omega}_{\mathrm{oc},1}^2,\cdots,\bar{\omega}_{\mathrm{oc},N_s}^2) - (1-s_0)\boldsymbol{\Delta}\hat{\mathbf{K}}_{\mathbf{p}} \tag{6.21}$$

$$\hat{\mathbf{V}}_{\mathbf{A}} = \boldsymbol{\Phi}_{\mathbf{oc}}^t\bar{\mathbf{V}}_{\mathbf{A}} \tag{6.22}$$

$$\hat{\mathbf{F}}_{\mathbf{sw}} = s_0\boldsymbol{\Phi}_{\mathbf{oc}}^t(\boldsymbol{\Delta}\bar{\mathbf{K}}_{\mathbf{p}} + \boldsymbol{\Delta}\bar{\mathbf{K}}_{\mathbf{p,exp}})\boldsymbol{\Phi}_{\mathbf{oc}}\boldsymbol{\eta}_{\mathbf{sw}} = s_0\boldsymbol{\Delta}\hat{\mathbf{K}}_{\mathbf{p}}\boldsymbol{\eta}_{\mathbf{sw}} \tag{6.23}$$

Here, $\bar{\omega}_{\mathrm{oc},r}$ is the rth open-circuit natural frequency normalized by the mean open-circuit natural frequency of the mode family. Furthermore, the modal-parameter extraction that utilizes the data obtained from the engine-order excitation does not yield mass-normalized mode shapes, thus requiring the scaling of the mode shapes in a different manner. Distributing the terms in the modal mass matrix results in

$$\boldsymbol{\Phi}_{\mathbf{oc}}^t\boldsymbol{\Phi}_{\mathbf{oc}} + \boldsymbol{\Phi}_{\mathbf{oc}}^t\boldsymbol{\Delta}\bar{\mathbf{M}}_{\mathbf{exp}}\boldsymbol{\Phi}_{\mathbf{oc}} = \mathbf{I} \tag{6.24}$$

Assuming that the experiment only introduces small variations to the mass matrix, the components of $\boldsymbol{\Delta}\bar{\mathbf{M}}_{\mathrm{exp}}$ are much less than one, thus resulting in the diagonal components of $\boldsymbol{\Phi}_{\mathbf{oc}}^t\boldsymbol{\Phi}_{\mathbf{oc}}$ approximately equal to one. This assumption enables the scaling of each mode shape such that $\boldsymbol{\phi}_{\mathbf{oc,r}}^t\boldsymbol{\phi}_{\mathbf{oc,r}} \approx 1$. Furthermore, as the mode shapes between the open- and short-circuit states are nearly identical, the matrix $\boldsymbol{\Delta}\hat{\mathbf{K}}_{\mathbf{p}}$ is approximately diagonal where the diagonal components are the

differences between the open- and short-circuit squared natural frequencies

$$\mathbf{\Delta \hat{K}_p} = \mathbf{diag}(\omega_{\mathrm{oc},1}^2, \cdots, \omega_{\mathrm{oc},N_s}^2) - \mathbf{diag}(\omega_{\mathrm{sc},1}^2, \cdots, \omega_{\mathrm{sc},N_s}^2) \qquad (6.25)$$

Using the above model with the solutions to transient excitation developed in Section 3.2.3 enables the identification of the optimal switch triggers via the genetic algorithm presented in Section 4.1.2.

For the first experimental test, consider the blisk subjected to 1EO excitation sweeping through the 1050 Hz – 1250 Hz frequency band at $f_{\mathrm{rate}} = 10$ Hz/s ($\omega_{\mathrm{rate}} = 62.8$ rad/s), or $\bar{\omega}_{\mathrm{rate}} \approx 10^{-6}$. Figure 6.4 shows the results for RFD considering 8 optimized triggers. Each plot shows quantities corresponding to the open-circuit case (blue), the short-circuit case (red), and the optimal case (gold). Figure 6.4a shows the response envelopes at each time instant obtained from the numerical simulation. As the last three modes contain the smallest amount of 1ND harmonic content, the 1EO excitation does not excite them as strongly as the first five modes. The optimal triggers primarily occur between the open- and short-circuit peaks, resulting in a 51.6% decrease in the maximum blade response. Figure 6.4b shows each blade's maximum response obtained from the simulation. RFD shows the greatest benefit for the largest responding blades (i.e., blade 3, 7, and 8) where there are significant decreases in the maximum blade response. Figure 6.4c shows the response envelopes obtained from the experiment. Similar to the numerical simulation, the last three modes are not excited as strongly as the first five modes; however, the third mode responds at a smaller amplitude in the experiment compared to the simulation. As such, RFD reduces the maximum blade response by 31.2%, which is smaller than the numerical prediction. This discrepancy most

190

likely arises from errors in the measurement and curve-fitting process, as well as the mode-shape-scaling process. Figure 6.4d shows each blade's maximum response obtained from the experiment. The experiment shows similar trends as the simulation with RFD providing the greatest benefit for the largest responding blades.

For the second experimental test, consider the blisk subjected to 4EO excitation and again sweeping through at $f_{\text{rate}} = 10$ Hz/s, or $\bar{\omega}_{\text{rate}} \approx 10^{-6}$. Figure 6.5a shows the response envelopes obtained from the numerical simulation. The 4EO excitation most strongly excites the 7th and 8th modes as these modes contained the largest amount of 4ND content. One of the optimal triggers occurs between the two largest response peaks in the open- and short-circuit states and results in a 59.2% reduction in the maximum response. A trigger also occurs between the first two smaller peaks that reduces the vibration further. There are also several triggers that are redundant and provide no benefit; for example, the first two triggers occur nearly simultaneously such that the system essentially remains operating in the open-circuit state. Figure 6.5b shows each blade's maximum response obtained from the simulation. As the last mode shape shows vibration primarily localized in the 1st blade, the 4EO excitation causes this same blade to respond with the largest amplitude. Consequently, RFD provides the greatest benefit for this blade. Figure 6.5c shows the response envelopes obtained from the experiment that closely resemble the simulation and where RFD provides a 45.3% reduction in the maximum response. Figure 6.5d shows each blade's maximum response obtained from the experiment where the overall trends closely resemble those observed in the simulation.

Although not presented here, RFD was tested for the remaining engine orders. Figure 6.6 shows two bar graphs summarizing the results for both the numerical simulations and the experiments. Figure 6.6a shows the maximum amplitude of all blades for the optimal case normalized by the maximum amplitude in the un-switched, open-circuit case. Both the simulations and the experiments show good agreement. In all cases, there is at least a 20% reduction in the maximum system response, except for 3EO excitation, where there is less than a 10% reduction. Figure 6.6b shows the total area under the maximum response envelope for the optimal case normalized by the total area under the maximum response envelope for the open-circuit baseline. RFD provides at least a 25% decrease in total area for all engine orders, include the case of 3EO excitation. As such, RFD still provides benefit by reducing the total strain energy generated during resonance passages, even if there is not an ample reduction in the maximum response.
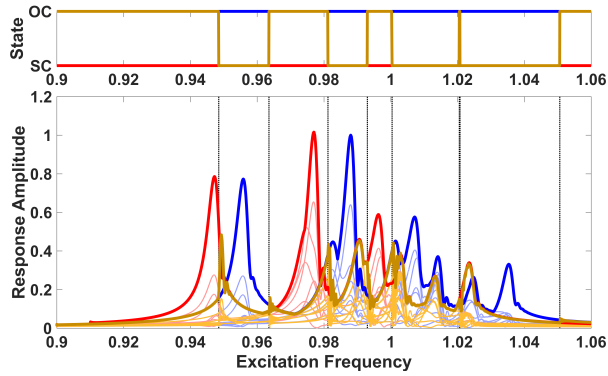
(a) Time response obtained numerically.
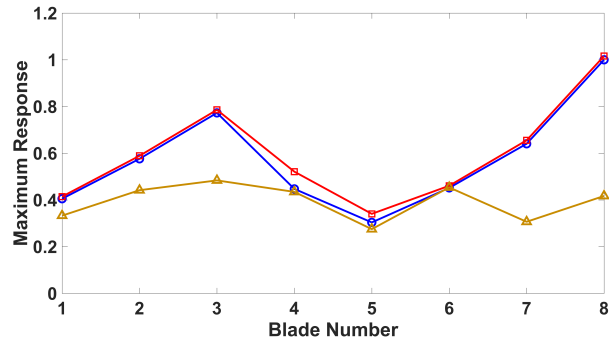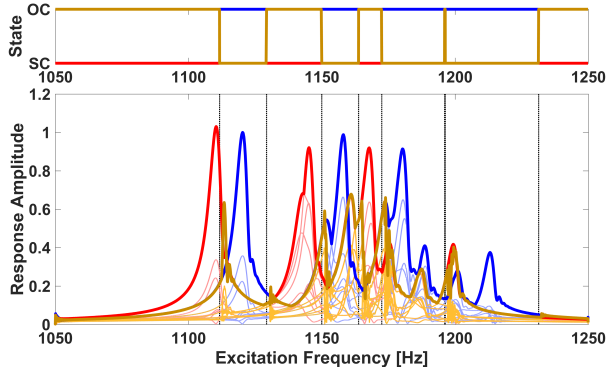
(b) Max blade response obtained numerically.

(c) Time response obtained experimentally.

(d) Max blade response obtained experimentally.

Figure 6.4: RFD performance for the blisk subjected to 1EO excitation. Each plot shows the quantities obtained for the open-ciruit (blue), short-circuit (red), and optimal (cases), all normalized by the maximum response of the un-switched, open-circuit baseline.
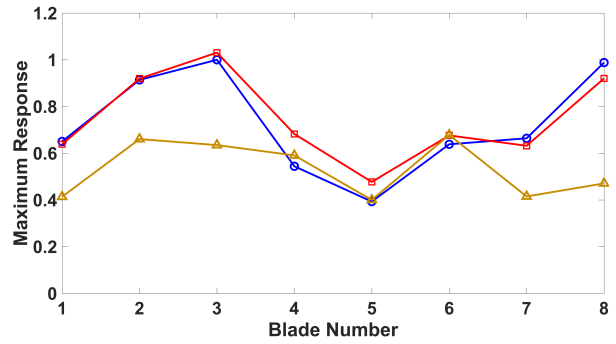
(a) Time response obtained numerically.

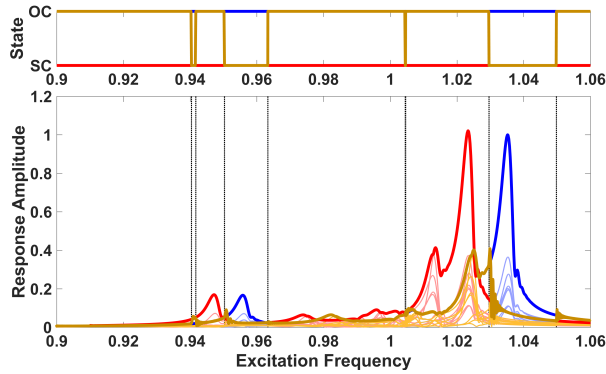(b) Max blade response obtained numerically.
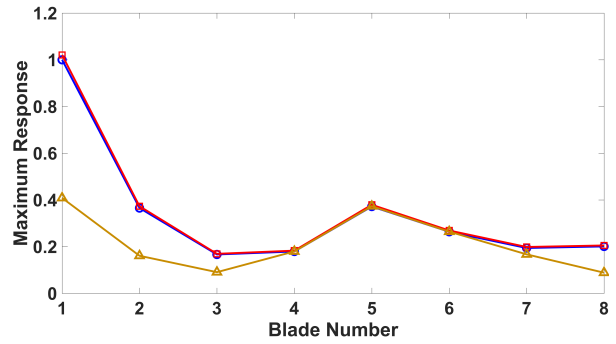

(c) Time response obtained experimentally.

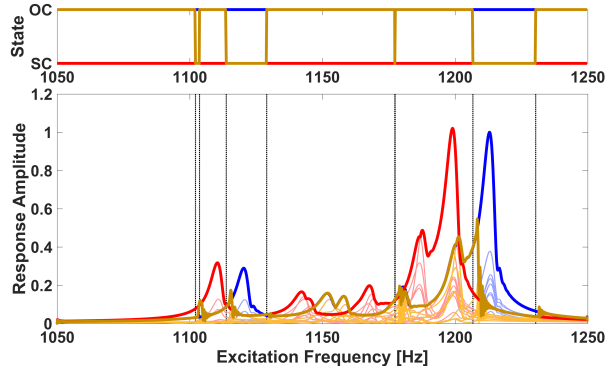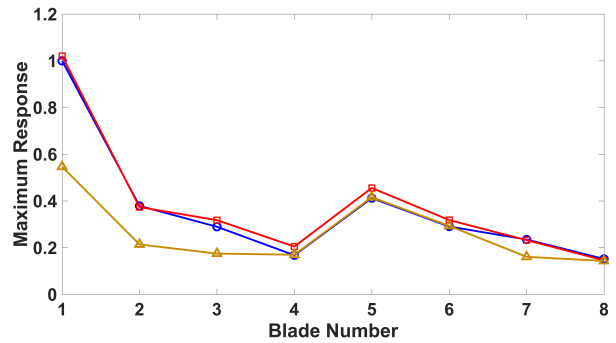(d) Max blade response obtained experimentally.

Figure 6.5: RFD performance for the blisk subjected to 4EO excitation. Each plot shows the quantities obtained for the open-ciruit (blue), short-circuit (red), and optimal (cases), all normalized by the maximum response of the un-switched, open-circuit baseline.
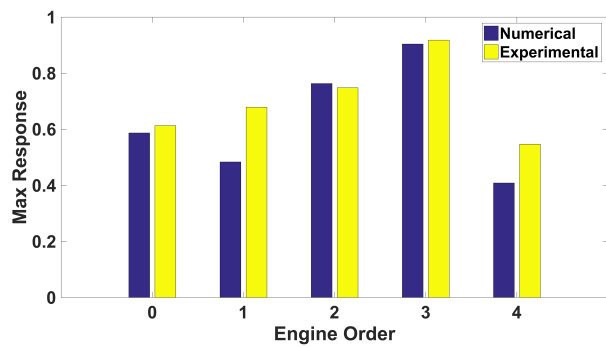
(a) Maximum response of the entire blade set.
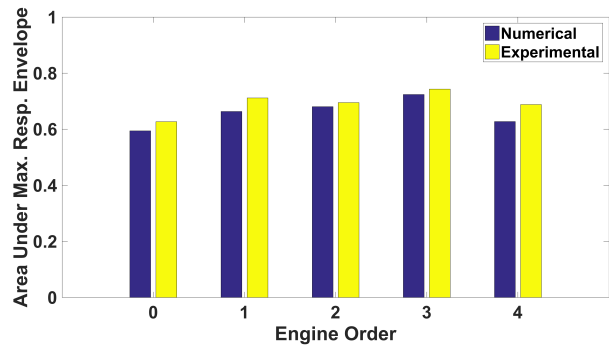
(b) Area under the maximum response envelope.

Figure 6.6: Numerical and experimental performance comparison for all engine orders. Each plot shows the quantities obtained for the optimal RFD performance normalized by the quantities obtained for the baseline, open-circuit case with no switch application.

CHAPTER 7
CONCLUDING REMARKS AND FUTURE RESEARCH DIRECTIONS

The primary focus of this research effort is to reduce excessive vibrations of mistuned blisks undergoing transient excitation. Reducing blade vibrations and increasing blade life has long been a focus of researchers for many decades. Many of the previously investigative approaches have their own associated advantages and drawbacks, one of which requires careful design considerations and tight tuning of certain parameters that exhibit sensitivity to any variations induced by operational wear and damage over the lifespan of the engine. Furthermore, many of these approaches can only effectively target a single resonance crossing without increasing the size and complexity of the vibration reduction system, thus leading to designs that may be difficult, or physically infeasible, to implement due to the stringent constraints imposed by a turbomachinery environment. As such, this research effort focused on extending the RFD approach to reduce blisk vibrations by developing the theoretical framework required to analyze these complex systems, as well as providing experimental validation to further prove the viability of the approach.

This research effort contributed several novel and significant aspects, the first of which included the natural extension of RFD from systems with well-separated modes, to more complex systems exhibiting closely-spaced modes, such as those typically encountered in mistuned blisks. The models utilized here consisted of lumped-parameter elements to qualitatively capture the complex dy-

namics stemming from mistuned blisks with blade-mounted piezoelectric elements, thus enabling parametric studies provided by Monte Carlo simulations to identify the key parameters that dictate RFD performance. Performing such a large-scale statistical analysis required a computationally efficient methodology to obtain the response to transient excitation and to identify the optimal sets of switch triggers. To address the former, this research adapted a semi-analytical procedure to solve for the blisk's response to transient excitation associated with a specified engine order; to address the latter, this research also incorporated an optimization procedure to identify the optimal triggers. Another significant aspect of this work is the development of an electromechanical assumed-modes model that accurately represents a blisk with blade-mounted piezoelectric patches. Stemming from this model was the application of a multi-objective optimization procedure used to optimize the piezoelectric patch parameters that maximize the electromechanical coupling for the vibration modes of interest. The final significant aspect of this work was the experimental validation of the RFD concept as applied to a mistuned blisk.

Although this research effort built the fundamental framework necessary for extending the RFD concept to mistuned blisks, this concept requires further development before a successful physical implementation on real turbomachinery blades. First and foremost, significant implementation questions remain, as outlined by Kauffman [80]. One of the key implementation limitations is the requirement of a system model to identify the optimal sets of switch triggers; instead, the development of a model-independent switching control law utilizing a readily measurable quantity, such as the piezoelectric voltage, would provide the robustness and versatility required by the inherently random nature of mistuning. Future research should also extend the concepts developed

in this work to more complex models. Specifically, the numerical analysis only considered the application of RFD to lumped-parameter models, thus necessitating the extension, albeit straightforward, to more complex models, including both the assumed-modes model developed here, and more industrial, finite-element models. Finally, further development and refinement of assumed-modes model would be a fruitful endeavor as this model is a computationally cheap alternative to finite-element models, thus enabling the utilization for identifying general trends in turbomachinery blade design.

7.1 Key Research Findings

7.1.1 Resonance Frequency Detuning

Examining the viability of RFD to reduce vibrations present in mistuned blisks first requires a fundamental model to adequately capture the underlying response dynamics. As such, this research incorporated piezoelectric elements into a lumped-parameter blisk model to analyze RFD. This model enabled the analysis of both tuned and mistuned systems and when considering the operation of all blades in either the open- or short-circuit stiffness states. By switching all blades simultaneously, there is a uniform increase/decrease in the stiffness around the blisk, resulting in identical mode shapes between the two operating states, and a relatively constant electromechanical coupling coefficient for all modes. Furthermore, the forced response for both operating states

are nearly identical, but with the short-circuit response exhibiting a downward shift in all resonance frequencies due to the softening effect provided the reduced blade stiffness.

Successful RFD application requires the identification of the optimal sets of switch triggers to reduce vibration. When considering harmonic excitation, the sole optimal trigger for the tuned system depends on the electromechanical coupling coefficient and the engine order; conversely, the optimal triggers for a mistuned system with decoupled blades depend on the mistuning associated with each of the individual blades and also the coupling coefficient. Mistuned systems that include the interblade coupling operate within these two limiting cases, thus the complex dynamics require a separate approach to identify the optimal triggers. This analysis applied a genetic algorithm to identify these optimal triggers when considering both the reduction of the maximum response and the total area under the response envelopes as the performance measures. Furthermore, RFD is a transient approach that requires a computationally efficient means of solving for the response. This analysis utilized a previously developed, semi-analytical approach, and adapted it to include the effects of switching between the available stiffness states provided by the piezoelectric elements.

The inherently random nature of mistuning requires a parametric study that utilizes Monte Carlo simulations to identify the general trends accompanying the various design parameters; such parameters include the mistuning strength, the excitation sweep rate, the modal damping, and the difference between the open- and short-circuit states (i.e., the electromechanical coupling). The parametric study showed that RFD provides the greatest benefit for systems with light mistuning, light damping, large electromechanical coupling, and subjected to slow and moderate sweep rates. The parametric study also showed that RFD performed successfully when only considering a sin-

gle switch between the open- and short-circuit state, whereas multiple switches showed marginal benefit, except in highly mistuned systems.

This research effort also provided experimental validation using an academic blisk manufactured from a single sheet of aluminum. One set of piezoelectric patches functioned as actuators that simulated the engine-order excitation, while a second set provided the stiffness-state modulation to reduce vibration. Identifying the optimal triggers required the application of the genetic algorithm to a hybrid model consisting of the lumped-parameter model with the experimentally identified modal parameters (i.e., natural frequencies, modal damping ratios, and mode shapes). For engine-order excitation sweeping through the resonances of a single mode family, both numerical simulations and experimental tests exhibited the potential of RFD to reduce vibration for all engine orders. When considering the reduction of the peak response as the performance metric, RFD performed better for some engine orders compared to others; however, when considering the reduction of area under the maximum response envelope, RFD performed comparably for all engine orders.

7.1.2   Assumed-Modes Blisk Model and Piezoelectric Optimization

As a step taken towards applying RFD to more complex systems, this research developed an electromechanical blisk model utilizing the energy-based, assumed-modes approach. Comparisons to a finite-element model provided validation of the modeling strategy for both the tuned and mistuned cases. In a similar manner to finite-element models, the developed model can also decrease

the computational expense when analyzing a tuned blisk by only requiring the system matrices for a single sector. Furthermore, the resulting tuned-system equations of motion only couple for similar harmonics, thus reducing the size of the associated eigenvalue problems. When including the piezoelectric patches, the model showed that the coupling coefficients for some mode families largely depend on the spatial harmonic, or nodal diameter number, due to the altered distribution of modal strains.

Designing a piezoelectric-based system requires appropriately sizing and locating the piezoelectric patches to achieve the desired function, whether that be for actuating, sensing, reducing vibration, or harvesting vibration energy. Often times, these piezoelectric-based systems also require performing these functions across multiple modes. As such, this research incorporated a multi-objective optimization algorithm to optimize the patch parameters using the patch volume and the electromechanical coupling as the performance metrics. This optimization procedure requires application towards the full blisk model, rather than a stand-alone blade, due to the nodal-diameter dependency exhibited by the coupling coefficients. As this optimization requires calculating the coupling for a large number of systems, the procedure optimizes the parameters for a tuned blisk to exploit the computational savings. Utilizing a reduced number of bare-blisk mode shapes to transform the system equations to the modal domain before including the influence of the patches further reduces the computational cost. Also presented was an analytical derivation for the coupling coefficient that largely depends on the sum of the bare-blisk modal strains integrated over the patch area, as well as the patch material parameters. For patches that are thin compared to the host blade, this analytical coupling coefficient provides a good indicator of the optimal patch

location. Lastly, while this research developed these concepts for use with the assumed-modes model, extension to finite-element models should be straightforward.

7.1.3 Experimental Testing of a Mistuned Blisk

Stemming from the experimental component of this research was the development of testing methods that benefit the turbomachinery community as a whole. Recently, researchers have utilized piezoelectric actuators in modal tests as an alternative to produce Gaussian-shaped pulses typical of modal-hammer tests; using the piezoelectric actuators in this manner enables more control over the frequency content associated with the pulse [108]. When attempting to incorporate this approach to experimentally characterize the blisk used in this research, the light coupling between blades dictated large actuation voltages supplied to the blade-mounted patch to sufficiently excite all blades on the blisk; however, these large voltages caused nonlinearities in the response of the blade containing the actuator. As such, this research developed a separate testing procedure for blisks that recruits the piezoelectric actuators located on all of blades to distribute the actuation energy around the blisk. The form of the frequency response function when considering engine-order excitation is similar to that of an applied point force, thus enabling the use of typical modal-parameter estimation routines. This research also developed a hybrid model that utilized the lumped-parameter blisk model in conjunction with the experimentally obtained modal data. Simulations using this model closely resembled the experimental response when considering the transient excitation provided by the specified engine order, thus enabling the application of the

genetic algorithm to identify the optimal triggers. A similar semi-empirical blisk model exists, but only considers harmonic excitation [96].

7.2 Recommendations for Future Research Directions

7.2.1 Model-Independent Switching Law

In this research, identification of the optimal triggers required the use of a genetic algorithm with a blisk model. Although this method of identifying the optimal trigger sets offers invaluable insight into the fundamental aspects of RFD and the expected vibration reduction performance, such an approach may not be feasible for a physical implementation. Blisks are highly sensitive to mistuning that causes significant distortions in the mode shapes and, consequently, the forced response. The harsh environments experienced by these systems can constantly alter the mistuning pattern through uneven operational wear and foreign-object damage, thus constantly requiring the identification of updated sets of optimal triggers and the computational resources needed to do so. As such, progression towards a successful physical implementation most likely requires a model-independent switching law that can adapt to the changing dynamics expected in these systems. One such strategy performs this switch based on a measurement of the piezoelectric voltage, and its corresponding derivatives, that signal an approaching resonance; however, the analysis of this switching law focused only on a single, well-separated mode [113]. The extension of this switching law to mistuned blisks that contain regions of closely-spaced modes requires further investigation.

Specifically, if there are any overlapping open- and short-circuit resonances, such as in the example shown in Fig.4.6, updates to the switching logic may require the application of several consecutive switches after triggering the initial switch.

Considering that the analysis provided here constrained the blades to switch simultaneously, physically satisfying this constraint would require a means of communication between the patches located on the various blades. One method would be to attach leads to the patches that run to the root of the blades and onto the disk, where the patches could then be connected to a single relay. A second method considers each of the patches as stand-alone systems connected to independent switching circuits. As all the blades of a mistuned blisk experience resonances simultaneously, the voltage-based switching logic should also cause the patches to switch simultaneously; however, if the modal participation is small for some of the blades, the amplitudes of the associated resonance peaks may also be too small to trigger a switch. In such situations, the minimal deflection experience by the blades will prohibit any strain from developing within the patches and they will not appreciably add to the electromechanical coupling for the mode in question; therefore, switching these patches would not be necessary for resonance avoidance.

7.2.2 Further Development of the Assumed-Modes Blisk Model

As RFD progresses, the need arises for investigations on more complex blisk models. The low-order assumed-modes model provides an initial stepping stone towards achieving this goal. The model developed here, however, neglects the effects of the rotation-based centrifugal forces. These

rotation-based effects can alter the modal strain distribution of the blades and, consequently, influence the associated electromechanical coupling coefficients. [80, 114] Inclusion of these rotation-based effects is paramount, especially when considering the optimization of the patches. Further developments of the assumed-modes model may also include such features as the blade pre-twist and stagger angles, both of which have been previously modeled using similar energy-based methods [85, 86, 87]. At some point, however, further increasing the complexity will render the assumed-modes approach inadequate, thus necessitating the progression to higher-fidelity finite-element models.

LIST OF REFERENCES

[1] T. Nicholas, "Critical issues in high cycle fatigue," *International Journal of Fatigue*, vol. 21, pp. S221 – S231, 1999.

[2] M. P. Castanier and C. Pierre, "Modeling and analysis of mistuned bladed disk vibration: Status and emerging directions," *Journal of Propulsion and Power*, vol. 22, no. 2, pp. 384–396, 2006.

[3] J. L. Kauffman and G. A. Lesieutre, "Piezoelectric-based vibration reduction of turbomachinery bladed disks via resonance frequency detuning," *AIAA Journal*, vol. 50, no. 5, pp. 1137–1144, 2012.

[4] O. Younossi, M. V. Arena, R. M. Moore, M. Lorell, J. Mason, and J. C. Graser, *Military Jet Engine Acquisition : Technology Basics and Cost-Estimating Methodology*. Santa Monica, CA: Rand, Project Air Force, 2002.

[5] G. Electric. (2013). [Online]. Available: http://generalelectric.tumblr.com/post/56364254531/this-stunning-looking-engine-blisk-is-part-of-a-ge

[6] *The jet engine*. London: Rolls-Royce, 2005.

[7] J. A. Beck, J. M. Brown, B. Runyon, and O. E. Scott-Emuakpor, "Probabilistic study of integrally bladed rotor blends using geometric mistuning models," in *58th AIAA/ASCE/AHS/ASC Structures, Structural Dynamics, and Materials Conference, AIAA SciTech Forum*, vol. AIAA 2017-0860. Grapevine, TX: AIAA, January 2017.

[8] B. A. Cowles, "High cycle fatigue in aircraft gas turbines – an industry perspective," *International Journal of Fracture*, vol. 80, no. 2, pp. 147–163, 1996.

[9] D. L. Thomas, "Dynamics of rotationally periodic structures," *International Journal for Numerical Methods in Engineering*, vol. 14, no. 1, pp. 81–102, 1979.

[10] D. J. Ewins, "The effects of detuning upon the forced vibration of bladed disks," *Journal of Sound and Vibration*, vol. 9, no. 1, pp. 65–79, 1969.

[11] D. Whitehead, "Effect of mistuning on the vibration of turbo-machine blades induced by wakes," *Journal of Mechanical Engineering Science*, vol. 8, no. 1, pp. 15–21, 1966.

[12] R. J. Wischt and N. G. Garafolo, "Variable stiffness technique for turbomachinery using shape memory alloys," in *Proceedings of the AIAA SciTech Forum*. Kissimmee, FL: AIAA, January 2015.

[13] N. G. Garafolo and R. Collard, "Active stiffness method for high cycle fatigue mitigation using topical thin foil shape memory alloy," *Journal of Mechanical Design and Vibration*, vol. 5, no. 1, pp. 11–20, 2017.

[14] G. K. Lopp and J. L. Kauffman, "Switch triggers for optimal vibration reduction via resonance frequency detuning," *Journal of Vibration and Acoustics*, vol. 138, no. 1, 2015.

[15] J. H. Griffin, "A review of frictiondamping of turbine blade vibration," *Internation Journal of Turbo and Jet-Engines*, vol. 7, no. 3–4, pp. 297–308, 1990.

[16] K. Y. Sanliturk, D. J. Ewins, and A. B. Stanbridge, "Underplatform dampers for turbine blades: Theoretical modeling, analysis, and comparison with experimental data," *Journal of Engineering for Gas Turbines and Power*, vol. 123, no. 4, pp. 919–929, 2001.

[17] D. Laxalde, F. Thouverez, and J.-P. Lombard, "Forced response analysis of integrally bladed disks with friction ring dampers," *Journal of Vibration and Acoustics*, vol. 131, no. 1, pp. 011 013–1–011 013–9, 2010.

[18] D. Laxalde, F. Thouverez, J. J. Sinou, and J. P. Lombard, "Qualitative analysis of forced response of blisks with friction ring dampers," *European Journal of Mechanics -A/Solids*, vol. 26, no. 4, pp. 676–687, 2007.

[19] J. J. Hollkamp, R. L. Bagley, and R. W. Gordon, "A centrifugal pendulum absorber for rotating, hollow engine blades," *Journal of Sound and Vibration*, vol. 219, no. 3, pp. 539–549, 1999.

[20] K. P. Duffy, R. L. Bagley, and O. Mehmed, "On a self-tuning impact vibration damper for rotating turbomachinery," in *Proceedings of the 36th AIAA/ASME/SAE/ASEE Joint Propulsion Conference and Exhibit*. Las Vegas, NV: AIAA, 2000.

[21] S. W. Shaw and C. Pierre, "The dynamic response of tuned impact absorbers for rotating flexible structures," *Journal of Computational and Nonlinear Dynamics*, vol. 1, no. 1, pp. 13–24, 2006.

[22] S. Gozen, B. J. Olsen, S. W. Shaw, and C. Pierre, "Resonance suppresion in multi-degree-of-freedom rotating flexible structures using order-tuned absorbers," *Journal of Vibration and Acoustics*, vol. 134, no. 6, pp. 061 016–1–061 016–7, 2012.

[23] A. Hartung, U. Retze, and H.-P. Hackenberg, "Impulse mistuning of blades and vanes," *Journal of Engineering for Gas Turbines and Power*, vol. 139, no. 7, 2017.

[24] M. D. Rao, "Recent applications of viscoelastic damping for noise control in automobiles and commercial airplanes," *Journal of Sound and Vibration*, vol. 262, no. 3, pp. 457–474, 2003.

[25] J. B. Kosmatka, A. J. Lapid, and O. Mehmed, "Passive vibration reduction of advanced composite pretwisted plates using integral damping materials," in *Proceedings of the SPIE Conference on Smart Structures and Materials 1995*, vol. 2445.   San Diego, CA: SPIE, May 1995, pp. 72–83.

[26] ——, "Vibration reduction in advanced composite turbo-fan blades using embedded damping materials," in *Proceedings of the SPIE Conference on Smart Structures and Materials 1996*, vol. 2720.   San Diego, CA: SPIE, May 1996, pp. 13–24.

[27] J. B. Kosmatka and O. Mehmed, "Vibrational reduction in integral damped composite fan blades: Experimental results," in *Proceedings of the SPIE Conference on Smart Structures and Materials 1998*, vol. 3327.   San Diego, CA: SPIE, March 1998, pp. 115–127.

[28] ——, "Development of an integral damping treatment for nasa's next-generation hollow fan blades," in *Proceedings of the SPIE Conference on Smart Structures and Materials 2002*, vol. 4697.   San Diego, CA: SPIE, June 2002, pp. 15–24.

[29] J. M. Biggerstaff and J. B. Kosmatka, "Damping performance of cocured graphite/epoxy composite laminates with embedded damping materials," *Journal of Composite Materials*, vol. 33, no. 15, pp. 1457–1469, 1999.

[30] G. A. Lesieutre, "How membrane loads influence the modal damping of flexural structures," *AIAA Journal*, vol. 47, no. 7, pp. 1642–1646, 2009.

[31] K. E. Graves, D. Toncich, and P. G. Iovenitti, "Theoretical comparison of motional and transformer emf device damping efficiency," *Journal of Sound and Vibration*, vol. 233, no. 3, pp. 441–453, 2000.

[32] J.-S. Bae, M. K. Kwak, and D. J. Inman, "Vibration suppression of a cantilever beam using eddy current damper," *Journal of Sound and Vibration*, vol. 284, no. 3–5, pp. 805–824, 2005.

[33] H. A. Sodano, J.-S. Bae, D. J. Inman, and W. K. Belvin, "Concept and model of eddy current damper for vibration suppression of a beam," *Journal of Sound and Vibration*, vol. 288, no. 4–5, pp. 1177–1196, 2005.

[34] H. A. Sodano and J.-S. Bae, "Eddy current damping in stuctures," *The Shock and Vibration Digest*, vol. 36, no. 6, pp. 469–478, 2004.

[35] J. Laborenz, C. Siewert, L. Panning, J. Wallaschek, C. Gerber, and Pierre-Alain, "Eddy current damping: A concept study for steam turbine blading," *Journal of Engineering for Gas Turbines and Power*, vol. 132, no. 5, pp. 052 505–1–052 505–7, 2010.

[36] J. H. Griffin and T. M. Hoosac, "Model development and statistical investigation of turbine blade mistuning," *Journal of Vibration, Acoustics, Stress, and Reliability in Design*, vol. 106, no. 2, pp. 204–210, 1984.

[37] M. P. Castanier and C. Pierre, "Using intentional mistuning in the design of turbomachinery rotors," *AIAA Journal*, vol. 40, no. 10, pp. 2077–2086, 2002.

[38] B.-K. Choi, J. Lentz, A. J. Rivas-Guerra, and M. P. Mignolet, "Optimization of intentional mistuning patters for the reduction of the forced response effects of unintentional mistuning: Formulation and assessment," *Journal of Engineering for Gas Turbines and Power*, vol. 125, no. 1, pp. 131–140, 2003.

[39] W. P. Mason, "Piezoelectricity, its history and applications," *The Journal of the Acoustical Society of America*, vol. 70, no. 6, pp. 1561–1566, 1981.

[40] S. R. Moheimani and A. J. Fleming, *Piezoelectric Transducers for Vibration Control and Damping*. London: Springer, 2006.

[41] N. W. Hagood and A. von Flotow, "Damping of structural vibrations with piezoelectric materials and passive electrical networks," *Journal of Sound and Vibration*, vol. 146, no. 2, pp. 243–268, 1991.

[42] Institute of Electrical and Electronics Engineers, "IEEE Standard on Piezoelectricity," IEEE, New York, NY, ANSI/IEEE Std. 176-1987, 1987.

[43] R. L. Forward, "Electronic damping of vibrations in optical structures," *Applied Optics*, vol. 18, no. 5, 1979.

[44] C. J. Cross and S. Fleeter, "Shunted piezoelectrics for passive control of turbomachine blading flow-induced vibrations," *Smart Material and Structures*, vol. 11, pp. 239–248, 2002.

[45] S. M. Schwarzendahl, J. Szwedowicz, M. Neubauer, L. Panning, and J. Wallaschek, "On blade damping technology using passive piezoelectric dampers," in *Proceedings ASME Turbo Expo 2012: Turbine Technical Conference and Exposition*, vol. Volume 7: Structures and Dynamics, Parts A and B. Copenhagen, Denmark: ASME, June 2012.

[46] H. Yu and K. W. Wang, "Piezoelectric networks for vibration suppression of mistuned bladed disks," *Journal of Vibration and Acoustics*, vol. 129, no. 5, pp. 559–566, 2007.

[47] ——, "Vibration suppression of mistuned coupled-blade-disk systems using piezoelectric circuitry network," *Journal of Vibration and Acoustics*, vol. 131, no. 2, 2009.

[48] A. Hohl, M. Neubauer, S. M. Schwarzendahl, L. Panning, and J. Wallaschek, "Active and semiactive vibration damping of turbine blades with piezoceramics," in *Proceedings of SPIE 7288, Active and Passive Smart Structures and Integrated Systems 2009*, vol. 7288. SPIE, April 2009.

[49] B. Mokrani, R. Bastaits, M. Horodinca, I. Romanescu, I. Burda, R. Viguié, and A. Preumont, "Parallel piezoelectric shunt damping of rotationally periodic structures," *Advances in Materials Science and Engineering*, vol. 2015, 2015.

[50] B. Zhou, F. Thouverez, and D. Lenoir, "Vibration reduction of mistuned bladed disks by passive piezoelectric shunt damping techniques," *AIAA Journal*, vol. 52, no. 6, pp. 1194–1206, 2014.

[51] J. J. Hollkamp, "Multimodal passive vibration suppression with piezoelectric materials and resonant shunts," *Journal of Intelligent Material Systems and Structures*, vol. 5, no. 1, pp. 49–57, 1994.

[52] S.-Y. Wu, "Method for multiple-mode shunt damping of structural vibration using a single pzt transducer," in *Proceedings of the SPIE Conference on Smart Structures and Materials 1998*, vol. 3327.   San Diego, CA: SPIE, mar 1998, pp. 159–168.

[53] W. W. Clark, "Semi-active vibration control with piezoelectric materials as variable-stiffness actuators," in *Proceedings of SPIE 3672, Smart Structures and Materials 1999: Passive Damping and Isolation*.   Newport Beach, CA: SPIE, June 1999.

[54] ——, "Vibration control with state-switched piezoelectric materials," *Journal of Intelligent Material Systems and Structures*, vol. 11, no. 4, pp. 263–271, 2000.

[55] C. Richard, D. Guyomar, D. Audigier, and G. Ching, "Semi-passive damping using continuous switching of a piezoelectric device," in *Proceedings of the SPIE Conference on Smart Structures and Materials 1999*, vol. 3672.   Newport Beach, CA: SPIE, mar 1999, pp. 104–111.

[56] C. Richard, D. Guyomar, D. Audigier, and H. Bassaler, "Enhanced semi-passive damping using continuous switching of a piezoelectric device on an inductor," in *Proceedings of the SPIE Conference on Smart Structures and Materials 2000*, vol. 3989.   Newport Beach, CA: SPIE, mar 2000, pp. 288–299.

[57] E. Lefeuvre, A. Badel, L. Petit, C. Richard, and D. Guyomar, "Semi-passive piezoelectric structural damping by synchronized switching on voltage sources," *Journal of Intelligent Material Systems and Structures*, vol. 17, no. 8–9, pp. 653–660, 2006.

[58] A. Badel, G. Sebald, D. Guyomar, M. Lallart, E. Lefeuvre, C. Richard, and J. Qiu, "Piezoelectric vibration control by synchronized switching on adaptive voltage sources: Towards wideband semi-active damping," *Journal of Acoustical Society of America*, vol. 119, no. 5, pp. 2815–2825, 2006.

[59] H. Ji, J. Qiu, J. Cheng, and D. Inman, "Application of a negative capacitance circuit in synchronized switch damping techniques for vibration suppression," *Journal of Vibration and Acoustics*, vol. 133, no. 4, 2011.

[60] J. Liu, L. Li, X. Huang, and L. Jezequel, "Dynamic characteristics of the blisk with synchronized switch damping based on negative capacitor," *Mechanical Systems and Signal Processing*, vol. 95, pp. 425–445, October 2017.

[61] J. Liu, L. Li, Y. Fan, and X. Huang, "A modified nonlinear modal synthesis scheme for mistuned blisks with synchronized switch damping," *International Journal of Aerospace Engineering*, vol. 2018, July 2018.

[62] G. D. Larson, P. H. Rogers, and W. Munk, "State switched transducers: A new approach to high-power, lower-frequency, underwater projectors," *Journal of Acoustical Society of America*, vol. 103, no. 1428, 1998.

[63] K. A. Cunefare, S. D. Rosa, N. Sadegh, and G. Larson, "State-switched absorber for semi-active structural control," *Journal of Intelligent Material Systems and Structures*, vol. 11, no. 4, pp. 300–310, 2000.

[64] J. L. Kauffman and G. A. Lesieutre, "Performance of piezoelectric-based damping techniques for structures with changing excitation frequencies," in *Proceedings of SPIE Smart Structures / NDE 2011*, vol. 7977.   San Diego, CA: SPIE, mar 2011, SPIE 7977-12.

[65] S. Zhang, R. Xia, L. Lebrun, D. Anderson, and T. R. Shrout, "Piezoelectric materials for high power, high temperature applications," *Materials Letters*, vol. 59, no. 27, pp. 3471–3475, nov 2005.

[66] A. A. Bent and N. W. Hagood, "Piezoelectric fiber composites with interdigitated electrodes," *Journal of Intelligent Material Systems and Structures*, vol. 8, no. 11, pp. 903–919, 1997.

[67] W. K. Wilkie, R. G. Bryant, J. W. High, R. L. Fox, R. F. Hellbaum, A. Jalink, B. D. Little, and P. H. Mirick, "Low-cost piezocomposite actuator for structural control applications," in *Proceedings Volume 3991, Smart Structures and Materials 2000: Industrial and Commercial Applications of Smart Structures Technologies*, vol. 3991.   Newport Beach, CA: SPIE, June 2000.

[68] Y. Lin and H. A. Sodano, "Fabrication and electromechanical characterization of a piezoelectric structural fiber for multifunctional composites," *Advanced Functional Materials*, vol. 19, no. 4, pp. 592–598, feb 2009.

[69] L. M. Amoo, "On the design and structural analysis of jet engine fan blade structures," *Progress in Aerospace Sciences*, vol. 60, pp. 1–11, 2013.

[70] T. Wollmann, N. Modler, M. Dannemann, A. Langkamp, S. Nitschke, and A. Filippatos, "Design and testing of composite compressor blades with focus on the vibration behaviour," *Composites: Part A*, vol. 92, pp. 183–189, 2017.

[71] Y. Lin and H. A. Sodano, "Concept and model of a piezoelectric structural fiber for multifunctional composites," *Composites Science and Technology*, vol. 68, no. 7–8, pp. 1911–1918, June 2008.

[72] L. R. Corr and W. W. Clark, "A novel semi-active multi-modal vibration control law for a piezoceramic actuator," *Journal of Vibration and Acoustics*, vol. 125, no. 2, pp. 214–222, 2003.

[73] G. D. Larson and K. A. Cunefare, "Quarter-cycle switching control for switch-shunted dampers," *Journal of Vibration and Acoustics*, vol. 126, no. 2, pp. 278–283, 2004.

[74] C. Kelley, "Optimal switch timing for piezoelectric-based semi-active vibration reduction techniques," Master's thesis, University of Central Florida, Orlando, FL, 2016.

[75] G. K. Lopp, C. R. Kelley, and J. L. Kauffman, "On the transient dynamics of piezoelectric-based, state-switched systems," *Applied Physics Letters*, vol. 112, no. 054102, 2018.

[76] B. J. Olson, S. W. Shaw, C. Shi, C. Pierre, and R. G. Parkeri, "Circulent matrices and their application to vibration analysis," *Applied Mechanics Reviews*, vol. 66, no. 4, June 2014.

[77] R. Markert and M. Seidler, "Analytically based estimation of the maximum amplitude during passage through resonance," *International Journal of Solids and Structures*, vol. 38, no. 10–13, pp. 1975–1992, 2001.

[78] M. Bonhage, L. Pohle, L. P. von Scheidt, and J. Wallaschek, "Transient amplitude amplification of mistuned blisks," *Journal of Engineering for Gas Turbines and Power*, vol. 137, no. 11, pp. 1–8, 2015.

[79] M. Bonhage, J. T. Adler, C. Kolhoff, O. Hentschel, K.-D. Schlesier, L. P. von Scheidt, and J. Wallaschek, "Transient amplitude amplification of mistuned structures: An experimental validation," *Journal of Sound and Vibration*, vol. 436, pp. 236–252, 2018.

[80] J. L. Kauffman, "Vibration reduction of integrally bladed rotors using piezoelectric materials," Ph.D. dissertation, Pennsylvania State University, December 2012.

[81] S. T. Wei and C. Pierre, "Localization phenomena in mistuned assemblies with cyclic symmetry part 1: Free vibrations," *Journal of Vibration, Acoustics, Stress, and Reliability in Design*, vol. 110, no. 4, pp. 429–438, 1988.

[82] ——, "Localization phenomena in mistuned assemblies with cyclic symmetry part 2: Forced vibrations," *Journal of Vibration, Acoustics, Stress, and Reliability in Design*, vol. 110, no. 4, pp. 439–449, 1988.

[83] Z. Michalewicz and C. Janikow, "Handling constraints in genetic algorithms," in *Proceedings of the Fourth Internation Conference on Genetic Algorithms*. Los Altos, CA: Morgan Kaufmann Publishers, 1991.

[84] R. Bladh, C. Pierre, M. P. Castanier, and M. J. Kruse, "Dynamic response predictions for a mistuned industrial turbomachinery rotor using reduced-order modeling," *Journal of Engineering for Gas Turbines and Power*, vol. 124, no. 2, pp. 311–324, 2002.

[85] V. Omprakash and V. Ramamurti, "Natural frequencies of bladed disks by a combined cyclic symmetry and rayleigh-ritz method," *Journal of Sound and Vibration*, vol. 125, no. 2, pp. 357–366, September 1988.

[86] T. Tomioka, Y. Kobayashi, and G. Yamada, "Analysis of free vibration of rotating disk-blade coupled systems by using artificial springs and orthogonal polynomials," *Journal of Sound and Vibration*, vol. 191, no. 1, pp. 53–73, 1996.

[87] S.-B. Chun and C.-W. Lee, "Vibration analysis of shaft-bladed disk system by using substructure synthesis and assumed modes method," *Journal of Sound and Vibration*, vol. 189, no. 5, pp. 587–608, 1996.

[88] A. Erturk, "Assumed-modes modeling of piezoelectric energy harvesters: Euler–bernoulli, rayleigh, and timoshenko models with axial deformations," *Computers and Structures*, vol. 106–107, pp. 214–227, 2012.

[89] A. Erturk and D. J. Inman, *Piezoelectric Energy Harvesting*. John Wiley & Sons, Ltd, 2011.

[90] L. Cheng and J. Nicolas, "Free vibration analysis of a cylindrical shell—circular plate system with general coupling and various boundary conditions," *Journal of Sound and Vibration*, vol. 155, no. 2, pp. 231–247, 1992.

[91] J. Yuan and S. M. Dickinson, "The flexural vibration of rectangular plate systems approached by using artificial springs in the rayleigh-ritz method," *Journal of Sound and Vibration*, vol. 159, no. 1, pp. 39–55, 1992.

[92] A. Sternchuss, "Multi-level parametric reduced models of rotating bladed disk assemblies," Ph.D. dissertation, Ecole Centrale Paris, 2009.

[93] B. Zhou, "Study of piezoelectric shunt damping applied to mistuned bladed disks," Ph.D. dissertation, Ecole Centrale de Lyon, December 2012.

[94] G. M. Oosterhout, P. J. M. van de Hoogt, and R. M. E. J. Spiering, "Accurate calculation methods for natural frequencies of plates with special attention to the higher modes," *Journal of Sound and Vibration*, vol. 183, no. 1, pp. 33–47, May 1995.

[95] R. Bhat, "Natural frequencies of rectangular plates using characteristic orthogonal polynomials in rayleigh-ritz method," *Journal of Sound and Vibration*, vol. 102, no. 4, pp. 493–499, 1985.

[96] J. A. Fabunmi, "Forced vibrations of a single stage axial compressor rotor," *Journal of Engineering for Power*, vol. 102, no. 2, pp. 322–328, 1980.

[97] T. R. Jeffers, J. J. Kielb, and R. S. Abhari, "A novel technique for the measurements of blade damping using piezoelectric actuators," in *ASME Turbo Expo 2000: Power fo Land, Sea, and Air*, vol. Volume 4: Manufacturing Materials and Metallurgy; Cermics; Structures and Dynamics; Controls, Diagnostics, and Instrumentation; Education. Munich, Germany: ASME, May 2000, pp. 1–11.

[98] J. Belz, M. May, J. Siemann, J. R. Seume, C. Voigt, H. Böhmer, and B. Grüber, "Excited blade vibration for aeroelastic investigations of a rotating blisk using piezo-electric macro fiber composites," in *ASME Turbo Expo 2013: Turbine Technical Conference and Exposition*, vol. Volume 7B: Structures and Dynamics. San Antonio, Texas: ASME, June 2013, pp. 1–9.

[99] J. Sirohi and I. Chopra, "Fundamental understanding of piezoelectric strain sensors," *Journal of Intelligent Material Systems and Structures*, vol. 11, no. 4, pp. 246–257, 2000.

[100] T. M. Pickering, "Methods for validation of a turbomachinery rotor blade tip timing system," Ph.D. dissertation, Virginia Polytechnic Institute and State University, March 2014.

[101] V. Gupta, M. Sharma, and N. Thakur, "Optimization criteria for optimal placement of piezo-electric sensors and actuators on a smart structure: A technical review," *Journal of Intelligent Material Systems and Structures*, vol. 21, pp. 1227–1243, 2010.

[102] A. Sénéchal, O. Thomas, and J.-F. Deü, "Optimization of shunted piezoelectric patches for vibration reduction of complex structures - application to a turbojet fan blade," in *Proceedings ASME 2010 International Design Engineering Technical Conference and Computers and Information in Engineering Coneference*, vol. Volume 5: 22nd International Conference on Design Theory and Methodology; Special Conference on Mechanical Vibration and Noise. Montreal, Quebec: ASME, August 2010.

[103] C. R. Kelley and J. L. Kauffman, "Optimal placement and sizing of piezoelectric material for multiple-mode vibration," in *Proceedings ASME 2018: Turbomachinery Technical Conference and Exposition*, vol. Volume 7C: Structures and Dynamics. Oslo, Norway: ASME, June 2018.

[104] R. T. Marler and J. S. Arora, "Survey of multi-objective optimization methods for engineering," *Structural and Multidisciplinary Optimization*, vol. 26, no. 26, pp. 369–395, 2004.

[105] K. Deb, A. Pratap, S. Agarwal, and T. Meyarivan, "A fast and elitist multiobjective genetic algorithm: Nsga-ii," *IEEE Transactions on Evolutionary Computation*, vol. 6, no. 2, pp. 182–197, 2002.

[106] K. Dhuri and P. Seshu, "Multi-objective optimization of piezo actuator placement and sizing using genetic algorithm," *Journal of Sound and Vibration*, vol. 323, no. 3–5, pp. 495–514, 2009.

[107] L. Meirovitch, *Principles and Techniques of Vibrations*. Prentice Hall, 1997.

[108] V. Ruffini, T. Nauman, and C. W. Schwingshackl, "Impulse excitation of piezoelectric patch actuators for modal analyis," *Topics in Modal Analysis & Testing*, vol. 10, pp. 97–106, 2017.

[109] D. J. Ewins, *Modal testing : theory, practice, and application*. Research Studies Press, 2000.

[110] P. Guillaume, P. Verboven, S. Vanlanduit, H. V. der Auweraer, and B. Peeters, "A poly-reference implementation of the least-squares complex frequency-domain estimator," in *Proceedings of the 21st International Modal Analysis Conference*, Kissimmee, FL, 2003.

[111] B. Peeters, H. V. der Auweraer, P. Guillaume, and J. Leuridan, "The polymax frequency-domain method: A new standard for modal parameter estimation?" *Shock and Vibration*, vol. 11, no. 3–4, pp. 395–409, 2004.

[112] E. F. Crawley and J. D. Luis, "Use of piezoelectric actuators as elements of intelligent structures," *AIAA Journal*, vol. 25, no. 10, pp. 1373–1385, 1987.

[113] G. K. Lopp and J. L. Kauffman, "Optimal resonance frequency detuning switch trigger determination using measurable response characteristics," in *Proceedings of AIAA Scitech 2015*. Kissimmee, Florida: AIAA, 2015.

[114] K. P. Duffy, B. B. Choi, A. J. Provenza, J. B. Min, and N. Kray, "Active piezoelectric vibration control of subscale composite fan blades," *Journal of Engineering for Gas Turbines and Power*, vol. 106–107, 2013.